UNIVERSITÉ DE STRASBOURG

ÉCOLE DOCTORALE DE PHYSIQUE ET PHYSIQUE CHIMIE (ED 182)

Institut Pluridisciplinaire Hubert Curien – IPHC (UMR 7178)

THÈSE présentée par :

Antoine Syx

Soutenue le : **1er octobre 2024**

pour obtenir le grade de : **Docteur de l'université de Strasbourg**

Discipline/ Spécialité : Physique des particules et astroparticules

Calibration of the Virgo gravitational waves detector using a Newtonian Calibrator for the observing run O4

THÈSE dirigée par :

M. MOURS Benoît	Directeur de recherche, IPHC Strasbourg

RAPPORTEURS :

M. BARSUGLIA Matteo	Directeur de recherche, APC Paris
M. VERKINDT Didier	Chargé de recherche, LAPP Annecy

AUTRES MEMBRES DU JURY :

Mme. OERTEL Micaela	Directrice de recherche, ObAs Strasbourg
M. AUBERT Dominique	Professeur des universités, ObAs Strasbourg

Remerciements

Je tiens tout d'abord à remercier mon superviseur de thèse, Benoît, pour son soutien et ses conseils tout au long de ces trois années.

Merci aux membres d'OGMA à l'IPHC : Dimitri pour son aide précieuse durant mes deux premières années, Florian pour ses précieux conseils lors de ma dernière année, ainsi que Vincent, Thomas, Pierre et Thierry pour leurs contributions.

Un grand merci aux membres de l'atelier de l'IPHC, Eddy, Mehmet et Dominique, pour leur expertise technique. Merci également aux membres du LAPP avec qui j'ai eu l'occasion d'échanger et d'apprendre tout au long de mon travail.

Je tiens à exprimer mon éternelle gratitude à ma famille : mes parents, mon frère, mon oncle et mes grands-parents, qui m'ont soutenu depuis le début de mon parcours en physique. Un merci tout particulier à ma chère Mobina pour son soutien indéfectible, même dans les moments les plus difficiles.

Je souhaite aussi remercier mes amis, ceux qui m'accompagnent depuis le collège, lycée et les études, les bougs ; ainsi que ceux rencontrés à Block'Out Strasbourg pendant la grimpe : Rémi, Karim, Corentin, Alix, Hugo, Adrien, Alexis, Chloé et Judi. Merci aussi à Irene, Zara et Celina pour leur présence.

Enfin, je remercie les membres de mon jury : Dominique Aubert, président du jury, Micaela Oertel, Matteo Barsuglia, et Didier Verkindt qui a fait le déplacement depuis Annecy pour participer à la soutenance.

Contents

Introduction

Since the first direct detection of a gravitational wave signal in 2015 with a binary black hole merger, the LIGO Virgo Collaboration recently joined by KAGRA has seen an increasing number of events at every new observing run. These detections serve as a validation of the 1916 theory of general relativity by Albert Einstein as well as a new tool to understand our universe. Among other things, they can be used to determine the value of the Hubble constant H_0, at the moment with larger uncertainty than the difference between the SH0ES and Planck measurements.

The detection of such waves is done by measuring the length variations between suspended free test masses, the mirrors of kilometers long interferometers. These length variations are induced by gravitational waves travelling in space and passing through the detectors, resulting in a signal called $h(t)$. However, their detection is a challenge that requires measuring length variations of the order of 10^{-18} meters. The accuracy of a detector relies on its calibration process and is important in constraining the measurement uncertainties. The calibration of an instrument such as the Virgo interferometer is performed by slightly moving one end mirror of the 3 km long arms by a known amount. Then, to calibrate the $h(t)$ signal, we adjust the first estimate of the reconstructed signal h_{rec} to match the known injected signal h_{inj}.

This PhD work which started in October 2021, is the development of a new and more accurate calibration actuator: the Newtonian calibrator or NCal. After a brief introduction of the concept of gravitational waves and their detection method in chapter 1, chapter 2 presents the different calibration methods used for the Virgo interferometer. Until the end of O3 in 2020, this process was mainly performed using the Photon Calibrator (PCal) method which uses the radiation pressure of an auxiliary laser to move a mirror. The PCal uncertainty on the injected signal was 1.4% at the end of O3. A new system was developped for the O4 run that started at the end of May 2023 for the LIGO interferometers, joined by Virgo in April 2024 for O4b. This new calibration device, the NCal, generates a variable gravitational field to move a mirror. Each NCal is a rotor with two massive sectors modulating its gravitational field at twice the rotor operating frequency. NCal prototypes were first tested in Virgo with also a 1.4% uncertainty on the injected signal achieved at the end of O3, a result motivating the development of a new NCal system.

The signal generated by a rotor mainly relies on its geometry and its distance to the mirror. Multiple NCals can be used to measure the mirror position. Therefore the O4 NCal system is composed of three setups, located around one mirror. Each setup can host up to two NCals for a total of six NCals operating simultaneously. A total of eight aluminum rotors and eight Polyvinyl Chloride (PVC) rotors have been machined at the IPHC followed by a careful metrology work. The material was first shaped into cylinders in order to ease the determination of the material density, this is discussed in detail in chapter 3.

Chapter 4 covers the characteristics of the rotors once machined into their final shape. A detailed description on the measurements and the method to characterize the geometry of the rotors is shown. The rotor geometry was then implemented in a finite element analysis program named "FROMAGE" which was used to compute the signal of each rotor on the mirror.

Chapter 5 discusses various tests performed on the rotor such as their balancing to reduce vibrations as well as their thermal and elastic properties when operating.

As pairs and triplets of NCals are used, their relative position is discussed in chapter 6. It starts by describing the installation procedure of reference plates and their survey by the European Gravitational Observatory (EGO) infrastructure team. The presentation of the installation of the suspended plates and the NCals followed.

Chapter 7 discusses the commissioning of the NCal system. We present the improvements made on the real time control of the NCals. Studies on the reliability of the system have been performed as well as the parasitic couplings of the NCals with the mirror. It was discovered that a magnetic coupling between the aluminum rotors and the mirror induced a slight bias in the calibration signal. Further investigations lead us to apply a magnetic shielding on the NCals and later to use PVC as a material for the rotors. Chapter 7 also presents the process which monitors the NCal lines and the alert system which was implemented to warn the operators in case of an NCal malfunction. Then, we include the first measurements on the mirror-to-NCals distance. For this, we used pairs of NCals on the North-South axis.

Chapter 8 is dedicated to the NCal activities during the three weeks of the engineering run ER16 before the start of O4b. We present more measurements on the mirror position using multiple NCals. During ER16, we also continued the investigations on other possible parasitic couplings. We present the NCal calibration uncertainty achieved at the end of ER16. At that time, the PCal measurements had a larger difference between the West End and North End PCals. It was therefore decided to use the NCal as the absolute reference for the PCal at low frequency and then use the PCal at higher frequencies to calibrate the Virgo signal.

Chapter 9 covers the first three months of O4b which started just at the end of ER16 on April 10, 2024. Here we start by presenting the conditions of the NCal system and their operating frequencies through this period and the change of two aluminum rotors by PVC ones. We present comparisons between the NCal-to-mirror distances computed with ER16 and O4b data, and the uncertainty obtained three months after the start of O4b.

Finally, chapter 10 summarizes the work described in this thesis.

For accessibility purposes, this thesis was mainly written in English. However, the Doctoral College of Physics (ED182) of Strasbourg University requests at least 10% of the thesis to be written in French. Therefore, the first chapter which introduces general concepts has been written in French.

Chapter 1

La détection des ondes gravitationnelles

Contents

Introduction

Ce chapitre a pour objectif de discuter le phénomène d'ondes gravitationnelles et leur méthode de détection. Nous commencerons par introduire la base théorique, la théorie de la relativité générale d'Albert Einstein de 1916, qui prédit l'existence de ces ondes. En second lieu, nous nous intéresserons aux différentes sources astrophysiques d'ondes gravitationnelles. Ensuite, nous discuterons de la méthode de détection de ces ondes avec le réseau de détecteur planétaire constituant la collaboration LIGO-Virgo-KAGRA. Puis, nous nous focaliserons sur le détecteur d'ondes gravitationnelles Virgo, construit en Italie. Finalement, nous discuterons des enjeux de l'étalonnage de ces détecteurs.

1.1 Les ondes gravitationnelles

1.1.1 Relativité générale

Contrairement à la théorie Newtonienne de la gravitation où cette dernière est considérée comme une force, la theorie de la relativité générale [1] d'Albert Einstein décrit la gravitation comme un résultat de la courbure de l'espace-temps. Cette courbure est induite par la présence de matière ou d'énergie dans l'espace. La géométrie de cet espace-temps obéit aux équations d'Einstein:

$$R_{\mu\nu} - \frac{1}{2}g_{\mu\nu}R = -\frac{8\pi G}{c^4}T_{\mu\nu} \tag{1.1}$$

avec $R_{\mu\nu}$ le tenseur de Ricci, $g_{\mu\nu}$ le tenseur métrique, R la courbure scalaire, G la constante gravitationnelle, c la vitesse de la lumière dans le vide et $T_{\mu\nu}$ le tenseur énergie-impulsion. Dans ce jeu d'équations, le terme de gauche défini la géométrie de l'espace-temps en présence d'une masse ou d'énergie dans cet espace décrit par le terme de droite.

Dans l'approximation d'un champ gravitationnel faible, la métrique peut s'écrire comme la somme d'une métrique plate η (tenseur de Minkowski) et d'une perturbation h:

$$g_{\mu\nu} = \eta_{\mu\nu} + h_{\mu\nu} \tag{1.2}$$

En développant l'équation 1.1 à l'aide de l'équation 1.2, on obtient pour une source lointaine ($T_{\mu\nu} = 0$):

$$\Box(h_{\mu\nu} - \frac{1}{2}\eta_{\mu\nu}h) = 0 \tag{1.3}$$

avec $\Box = \eta^{\mu\nu}\partial_\mu\partial\nu$ l'opérateur d'Alembertien. Le terme $(h_{\mu\nu} - \frac{1}{2}\eta_{\mu\nu}h)$ représente la perturbation de la métrique lors de la propagation d'une onde gravitationnelle. On peut réécrire les solutions de l'eq. (1.3) comme une combinaison d'ondes planes monochromatiques se propageant à la vitesse de la lumière dans le vide:

$$\tilde{h}_{\mu\nu}(x) = \mathrm{Re}(A_{\mu\nu}e^{ik_\alpha x^\alpha}) \tag{1.4}$$

avec $\tilde{h}_{\mu\nu} = h_{\mu\nu} - \frac{1}{2}\eta_{\mu\nu}h$, $A_{\mu\nu}$ le tenseur amplitude de l'onde et k_α le vecteur d'onde.

Le tenseur amplitude de l'onde gravitationnelle peut s'écrire à l'aide des deux polarisations possibles de l'onde h_+ et $h_\times$, l'une tournée de $\pi/4$ par rapport à l'autre:

$$A_{\mu\nu} = \begin{pmatrix} 0 & 0 & 0 & 0 \\ 0 & h_+ & h_\times & 0 \\ 0 & h_\times & -h_+ & 0 \\ 0 & 0 & 0 & 0 \end{pmatrix}$$

La fig. 1.1 montre les effets des polarisations + et × d'une onde gravitationnelle sur des masses libres transverses à la direction de propagation de l'onde. La variation de distance ΔL induite entre deux masses libres est proportionnelle à l'amplitude h de l'onde gravitationnelle et s'écrit:

$$\Delta L = h\frac{L_0}{2} \tag{1.5}$$

avec L_0 la distance au repos entre les masses libres.

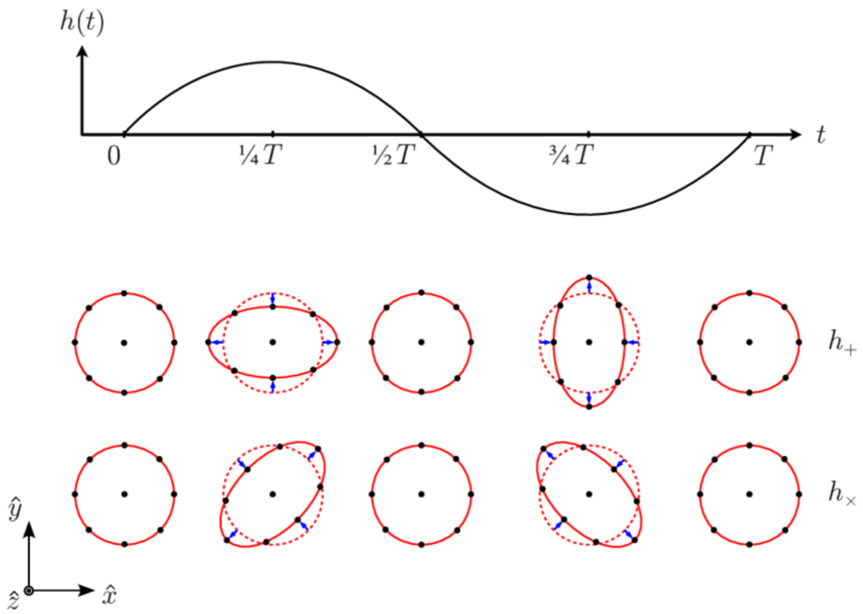

FIGURE 1.1: En haut, l'amplitude d'une onde gravitationnelle monochromatique de pulsation $\omega = 2\pi/T$ se propageant selon z. En bas, les effets des polarisations + et × de l'onde sur un anneau de masses libres. Source: [2].

1.1.2 Sources astrophysiques

Les sources astrophysiques d'ondes gravitationnelles peuvent être classées selon le type de signal qu'elles émettent. On dénombre trois principales types de signaux: transitoire, continu et stochastique.

Sources transitoires

Les sources de signaux transitoires sont de durées relativement courtes, allant de quelques millisecondes à plusieurs minutes. Ces signaux peuvent êtres générés par des événements astrophysiques de courte durée tel que:

- Les signaux *burst*, provenant par exemple de l'explosion d'une étoile en supernova ou de l'activité intense de magnétars, étoiles à neutrons possédant un fort champ magnétique [3].

Une autre catégorie de sources est à l'origine de ces signaux, de période plus longue mais dont seulement l'étape finale peut être détectée, les coalescences de systèmes binaires compacts (CBC). Un catalogue cumulatif des détections de CBC, GWTC-3 [4], a été publié à la fin de la troisième période d'observation O3 regroupant un total de 90 détections. On distingue trois types de CBC:

- Les binaires de trous noirs (BBH), coalescence d'une paire de trous noirs. Ce type de source est l'événement le plus observé dont la première détection a été réalisée par les interféromètres LIGO en 2015 (GW150914) [5].
- Les binaires d'étoiles à neutrons (BNS), coalescence d'une paire d'étoiles à neutrons. Ce type de source est moins observé que les BBH, dû à la masse inférieure des étoiles à neutrons. La première détection de BNS a été réalisée en 2017 avec pour la première fois une contrepartie électromagnétique (GW170817) [6].
- Les binaires de trou noir et étoile à neutrons (NSBH), coalescence d'une paire composée d'un trou noir et d'une étoile à neutrons. La première détection a été réalisée en 2020 (GW200105).

La fig. 1.2 présente le processus de coalescence d'une CBC (ici la première BBH GW150914), se divisant en trois étapes successives:

- La phase spiralante (*inspiral*) où la distance séparant les deux objets orbitant l'un autour de l'autre diminue en raison de la perte d'énergie provenant du rayonnement des ondes gravitationnelles.
- La phase de fusion (*merger*) où les deux objets fusionnent en un seul.
- La phase de désexcitation (*ringdown*) où le système tend vers un état stable.

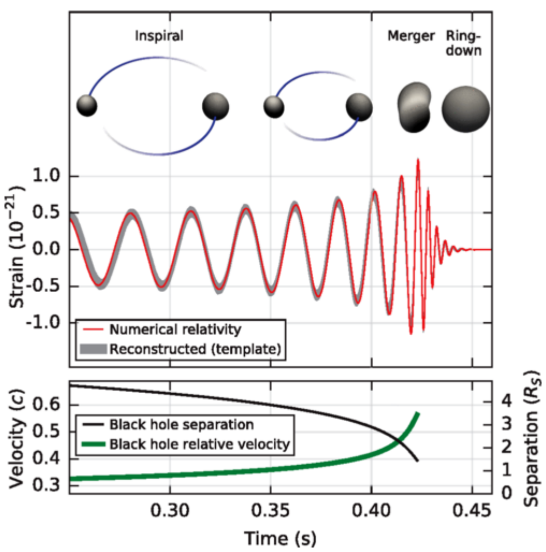

FIGURE 1.2: Dans le panneau du haut est montré le schéma de la phase spiralante, de fusion et de désexcitation pour une coalescence de binaire de trous noirs, ainsi que la forme des ondes émises au cours du processus. Dans le panneau du bas est montré l'évolution de la distance séparant les trous noirs et de leur vitesse relative au cours du temps. Source: [5].

Sources continues

Les sources continues peuvent générer des ondes gravitationnelles pendant des mois voire des années. Les signaux générés sont d'amplitude constante mais plus faible que pour les CBC. Néanmoins, leur durée permet l'accumulation de données et donc accroît leur chance de détection. Les sources attendues d'émission de signaux continus dans la bande de fréquence des détecteurs actuels sont:

- Les pulsars, étoiles à neutrons en rotation. Avec leur importante vitesse de rotation, une éventuelle asymétrie de distribution de la masse de l'étoile génère un signal d'ondes gravitationnelles [7].

Bruit de fond stochastique

Le bruit de fond stochastique regroupe différentes sources de signaux incohérents dont l'amplitude est trop faible pour être détectée individuellement [8].

1.1.3 Les enjeux de leur détection

La détection des ondes gravitationnelles bénéficie à différents domaines de la physique:

- Dans le domaine de la physique fondamentale, leur détection permet de tester les limites de la relativité générale [9].
- D'un point de vue astrophysique, la détection de CBC permet d'étudier leur formation et leur population dans l'Univers [5, 6]. De plus, la recherche de détection conjointe avec une contrepartie électromagnétique, ouvrant la porte à l'astronomie multi-messagers, permet de mieux comprendre les origines d'événements tels que les sursauts gamma [10]. Avec l'amélioration de la sensibilité des détecteurs, on espère pouvoir étudier les émissions d'ondes gravitationnelles provenant d'événements tels que les supernovae [11]. L'étude des BNS permet aussi de renseigner sur la structure composant les étoiles à neutrons [12].
- Dans le domaine de la cosmologie, la détection de CBC permet d'effectuer des mesures de distance, et donc, de la constante de Hubble H_0 avec une méthode indépendante de *SH0ES* et *Planck* [13–16]. Cette dernière sera approfondie en fin de chapitre.

1.2 La détection d'ondes gravitationnelles

Comme introduit dans la section précédente, la propagation d'une onde gravitationnelle induit une variation des distances entre des masses libres. Cette variation est proportionnelle à la distance au repos entre ces masses. Un détecteur d'ondes gravitationnelles doit être sensible à des variations de distance entre des masses libres. Dans le cas d'un interféromètre de Michelson, les masses libres sont les miroirs suspendus à un pendule en bout de bras. La mesure de distance est faite à l'aide d'un laser, une variation de distance est convertie en variation de puissance du laser observable en sortie de l'interféromètre.

1.2.1 Le principe d'interféromètre de Michelson

Un interféromètre de Michelson est un système composé d'une source laser frappant une lame séparatrice réfléchissant la moitié de sa lumière dans une direction à

90°, laissant passer l'autre. Les deux faisceaux résultant sont réfléchis vers la lame séparatrice par des miroirs situés au bout des bras de l'interféromètre. L'intensité du faisceau recombiné qui est monitoré par un jeu de photodiodes, dépend de la différence de longueur des deux bras, et donc de l'éventuel passage d'une onde gravitationnelle.

1.2.2 Un réseau de détecteur planétaire

La fig. 1.3 montre la localisation des interféromètres en opération, LIGO, Virgo, KAGRA et GEO600, ainsi que LIGO-India dont la construction devrait être achevée d'ici 2030.

Virgo, installé en Italie, près de Pise, est un interféromètre dont les bras font 3 km de long.

Il y a deux interféromètres LIGO installés aux États-Unis. L'un est situé à Hanford, dans l'État de Washington, et le second est situé à Livingston, dans l'État de Louisiane. Les deux détecteurs sont des interféromètres dont les bras font 4 km de long. Les deux interféromètres sont alignés de façon à maximiser l'intersection des diagrammes d'antenne des deux détecteurs, c'est à dire privilégier les observations en coïncidences. En 2015, les collaborations LIGO et Virgo observent dans les deux détecteurs LIGO la première détection directe des ondes gravitationnelles issues d'une fusion de BBH [5], menant au prix Nobel de physique 2017.

KAGRA est un interféromètre, dont les bras font 3 km de long, construit sous terre dans la mine de Kamioka au Japon pour minimiser le bruit sismique. Il possède la particularité d'avoir ses miroirs refroidis à une température de 20 Kelvin, réduisant le bruit thermique. La fin de la construction de KAGRA est encore récente (fin de la période d'observation O3), ce qui fait que sa sensibilité reste encore limitée.

LIGO-India est un projet d'interféromètre de 4 km de long, similaire aux détecteurs LIGO, actuellement en construction en Inde. Il est prévu d'être opérationnel avant 2030.

GEO600 est l'un des plus anciens detétecteur d'ondes gravitationnelles par interférométrie. Malgré une envergure plus petite avec des bras de 600 mètres réduisant sa sensibilité comparé aux autres projets, il joue un rôle en tant que banc d'essai de nouvelles technologies développée pour les interféromètres.

Ces interféromètres composent un réseau de détecteurs planétaire. L'objectif est la détection d'événements en coïncidence, pour comparer les temps d'arrivée et amplitudes d'un signal. L'utilisation de plusieurs détecteurs permet notamment d'améliorer la localisation d'un événement astrohysique en triangulant la source du signal.

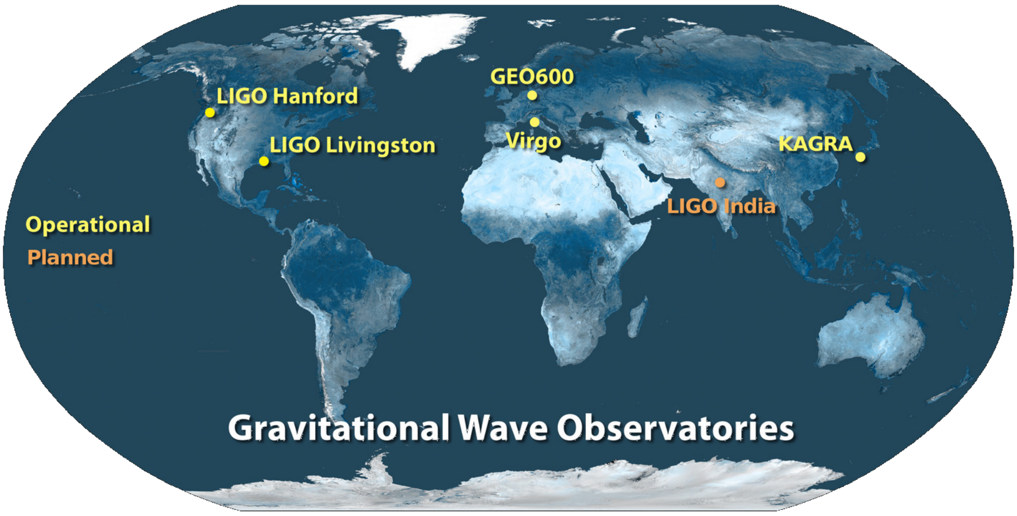

FIGURE 1.3: Carte du réseau d'interféromètres terrestres pour la détection d'ondes gravitationnelles.

1.2.3 Les périodes d'observation

La fig. 1.4 présente le calendrier des périodes d'observation pour les détecteurs d'ondes gravitationnelles. Entre chaque périodes, un temps d'arrêt est prévu pour diverses améliorations et phases de tests. La sensibilité d'un détecteur est caractérisée par sa portée d'observation. Étant donné que les fusions BNS sont une classe bien étudiée de signaux à ondes gravitationnelles, cette portée est définie comme la distance d'observation de BNS par un seul détecteur pour un rapport signal sur bruit (SNR) de 8 moyennée sur toutes les directions possibles.

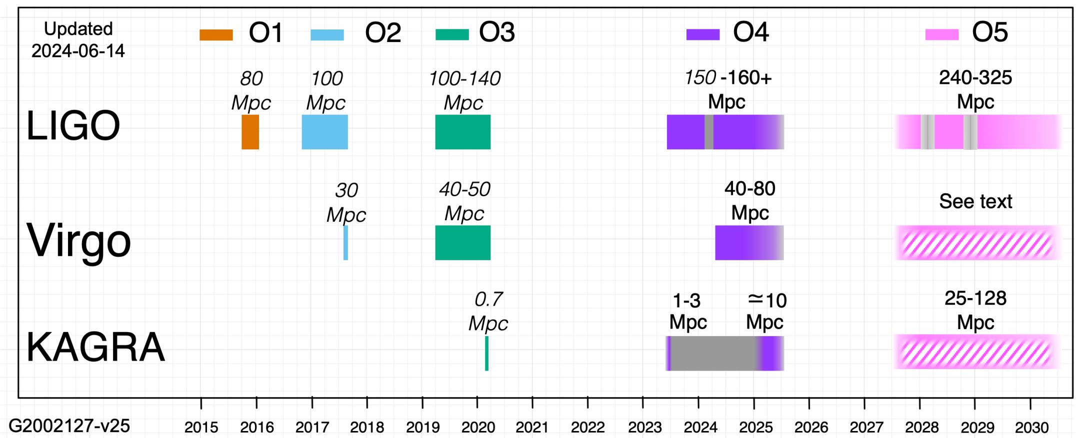

FIGURE 1.4: Calendrier des périodes d'observation de la collaboration LIGO-Virgo-KAGRA. Les portées effectives pour les prises de données passées et estimées pour le futur sont données. Source: Collaboration LIGO-Virgo-KAGRA

1.3 Le détecteur Advanced Virgo plus

Le détecteur Advanced Virgo plus (AdV+), localisé à Cascina en Italie, est un détecteur d'ondes gravitationnelles dont la bande de fréquence est comprise entre 10 Hz et quelques kHz. Le détecteur est un interféromètre de Michelson à recyclage de puissance et de signal avec des cavités de Fabry-Pérot de 3 km de long. La fig. 1.5 montre une vue aérienne de Virgo.

FIGURE 1.5: Vue aérienne du détecteur Virgo.

1.3.1 Vue d'ensemble du détecteur

La fig. 1.6 montre un schéma de la disposition optique de Virgo. L'essentiel des éléments constituant l'interféromètre est sous vide afin d'éviter le bruit acoustique, les variations de l'indice de réfraction de l'air dans le système et le bruit lié aux molécules d'air entrant en contact avec les miroirs. Ces principaux éléments sont:

Les masses tests

L'objectif de Virgo est de comparer deux distances et de mesurer leur variation relative. Ces distances sont les longueurs des deux bras de l'interféromètre qui sont matérialisées par des masses tests que sont les miroirs d'entrée (NI ou WI) et d'extrémité (NE ou WE) des cavités Fabry-Perrot de chaque bras. Ces masses tests sont suspendues à un superatténuateur (décrit plus tard dans cette section) pour limiter les perturbations environnementales et accéder ainsi aux déformations de l'espace engendrées par les ondes gravitationnelles. Ces miroirs ont une masse de 42 kg pour un diamètre de 350 mm et une épaisseur de 200 mm. Afin de limiter les pertes optiques, ils sont en silice amorphe très pure, revêtus de traitements multicouches pour obtenir les transmissions et réflexions souhaitées. Leurs défauts de surfaces sont réduits au maximum pour minimiser les effets de dispersion de la

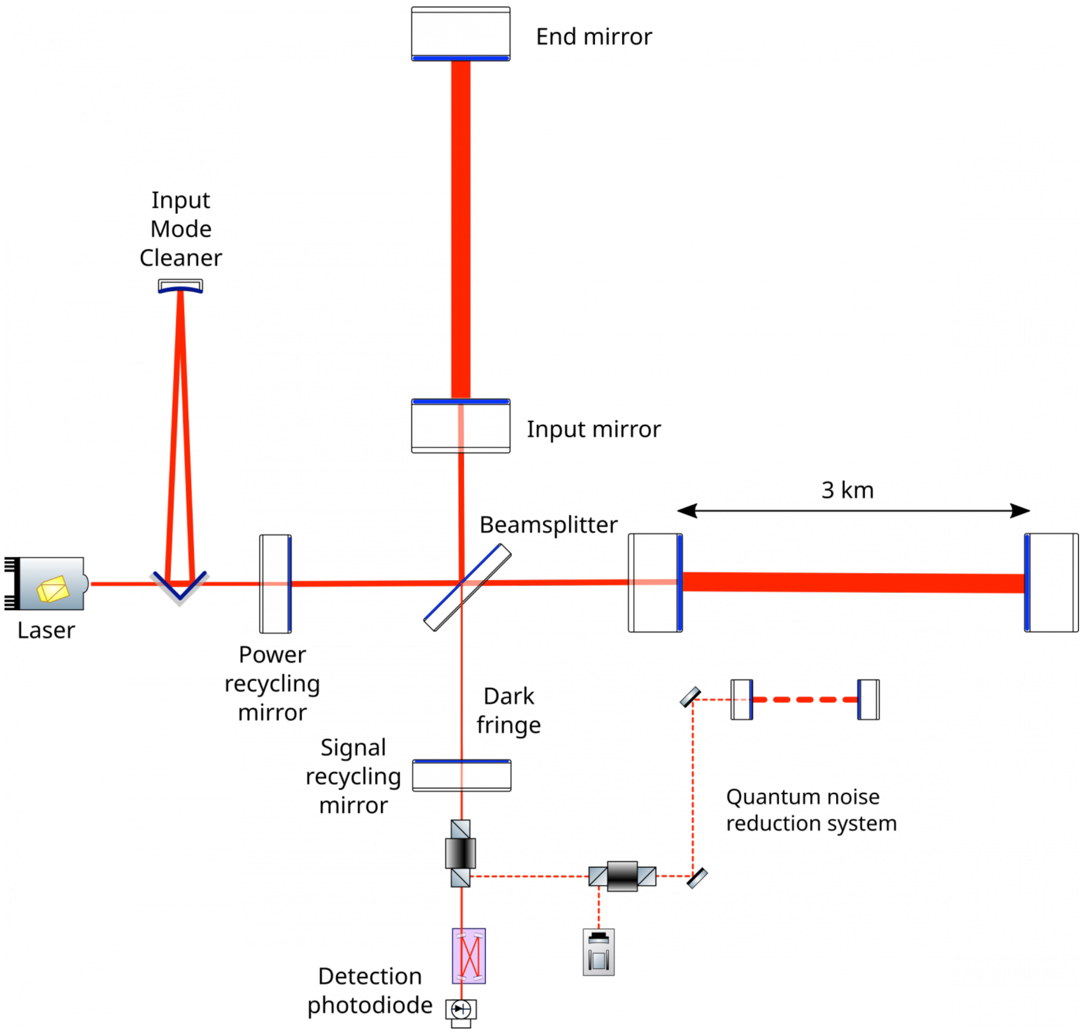

FIGURE 1.6: La disposition optique du détecteur Advanced Virgo. Schéma issu de la collaboration Virgo.

lumière et donc les pertes optiques. De plus, des systèmes de compensation thermiques (TCS) sont utilisés pour corriger leurs imperfections ainsi que leurs déformations due à leur échauffement par la centaine de kilowatt de lumière circulant dans les bras de l'interféromètre.

La source laser

La source laser d'AdV+ est un laser (Nd:YAG) d'une longueur d'onde de 1064 nm. La puissance injectée dans l'interféromètre au début de O4 est d'environ 18 W. Le faisceau est modulé en phase pour fournir des bandes latérales (c'est à dire plusieurs longueur d'ondes très proches) et contrôler les différentes parties de l'interféromètre.

Cavité de nettoyage de mode d'entrée

La cavité de nettoyage de mode d'entrée (*Input Mode Cleaner*) purifie le faisceau laser avant qu'il n'entre dans l'interféromètre. Elle filtre les modes transversaux indésirables, ne laissant passer que le mode fondamental, stabilise la fréquence du laser pour réduire le bruit en fréquence, améliore la qualité du faisceau en éliminant les fluctuations d'intensité, et fixe la polarisation du faisceau.

Miroir de recyclage de puissance

Pour un fonctionnement optimal, l'interféromètre est réglé sur la frange sombre. L'essentiel de la puissance injectée est donc réfléchie par l'interféromètre. Le miroir de recyclage (PR), placé en entrée de l'interféromètre, réinjecte cette lumière, augmentant la puissance qui circule dans l'interféromètre et donc la sensibilité du détecteur.

Cavités de Fabry-Pérot

Les deux bras perpendiculaires de l'interféromètre ont chacun une longueur de 3 km. Ces bras contiennent chacun une cavité résonnante de Fabry-Pérot qui augmente la distance de parcours de la lumière en la faisant rebondir plusieurs fois entre les masses tests, ce qui augmente la sensibilité du détecteur.

Miroir de recyclage de signal

Le miroir de recyclage de signal (SR) est situé en sortie de l'interféromètre. Il réinjecte le signal d'onde gravitationnelle pour l'amplifier optiquement, ce qui améliore la sensibilité de l'interféromètre.

Cavité de nettoyage de mode de sortie

La cavité de nettoyage de mode de sortie (*Output Mode Cleaner*) filtre le faisceau sortant de l'interféromètre. Elle sert à réduire les modes d'ordres supérieurs induits par les défauts de l'interféromètre et à éliminer les bandes latérales utilisées pour son contrôle.

Détection

La détection du signal s'effectue à l'aide de photodiodes à haute efficacité quantique.

Squeezing

Un système de lumière compressée (*squeezing*) a été installé près des bancs de détection de l'interféromètre pour O3. Il génère un état de lumière compressée, qui, une fois injecté dans l'interféromètre, permet de réduire le bruit quantique en sortie. Il a été complété pour O4 avec une cavité de filtrage qui permet de contrôler l'état de la lumière compressée en fonction de la fréquence. Étant donné les ajustements à la configuration optique de Virgo réquises pour son fonctionnement pendant O4 et des pertes optiques plus importantes que prévues, l'apport de ce système reste relativement modeste pour la prise de données O4.

1.3.2 Le système de suspension

Les miroirs sont suspendus par de fines fibres de silices à une structure appelée marionette, elle-même suspendue à une série de filtres appelé le superatténuatteur dont les fréquences de résonance sont de l'ordre ou inférieur au Hz. Cela permet de réduire le bruit sismique. Un schéma du superatténuateur de Virgo issu de [17] est montré dans la fig. 1.7. Chacun des filtres du superatténuateur fonctionne dans les six degrés de liberté. Les déplacements longitudinaux du miroir sont atténués par les filtres d'un facteur $(f_r/f)^{2N}$. La série de $N = 7$ filtres réduit donc le bruit sismique d'un facteur $(f_r/f)^{14}$. La position de la marionnette et du miroir est contrôlée grâce à des actionneurs électromagnétiques.

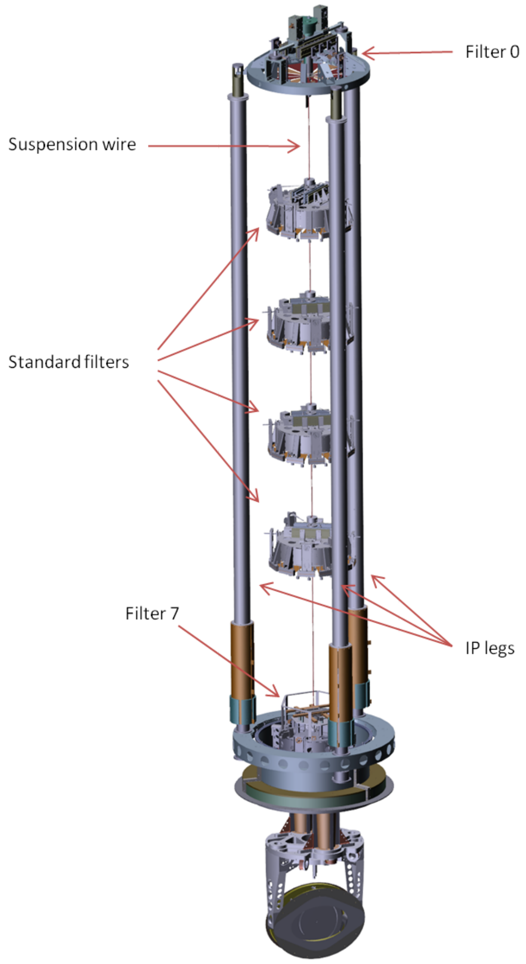

FIGURE 1.7: Schéma d'un superatténuateur de Virgo. Source: [17].

1.3.3 Les actionneurs électomagnétiques (EM)

Les actionneurs ont pour but d'induire un déplacement contrôlé, en agissant directement sur le miroir et sur la marionette à laquelle il est suspendu. Pour cela, on utilise un système appelé actionneurs électromagnétiques. En pratique, des bobines, dans lesquels un courant est injecté, agissent sur des aimants fixés sur la marionette et le dos du miroir. La fig. 1.8 montre le miroir et la marionette Nord (NE) de Virgo.

Sachant que les déplacements de la marionette sont filtrés par le pendule que constitue le miroir suspendu, les actions au niveau de la marionette sont limitées à quelques dizaines de Hz. Dans le cas des actionneurs du miroir, le contrôle du mouvement longitudinal des miroirs peut être réalisé jusqu'à plusieurs centaines de Hz. Ainsi, pour l'étalonnage, les réponses des actionneurs électromagnétiques de la marionnette et du miroir doivent être mesurées uniquement dans ces bandes de fréquences.

Lors des premières campagnes de mesures scientifiques de Virgo, VSR1 et VSR2, les actionneurs électromagnétiques ont joué un rôle essentiel dans l'étalonnage du détecteur [18, 19]. Ils étaient directement étalonnés à partir des signaux de configuration optiques simplifiés de l'interféromètre (voir section 2.1). Depuis O3, les actionneurs électromagnétiques sont étalonnés par l'action des PCals sur les miroirs

NE et WE. Pendant O3, l'incertitude d'étalonnage maximale estimée des actionneurs électromagnétiques était de 1.84% [20].

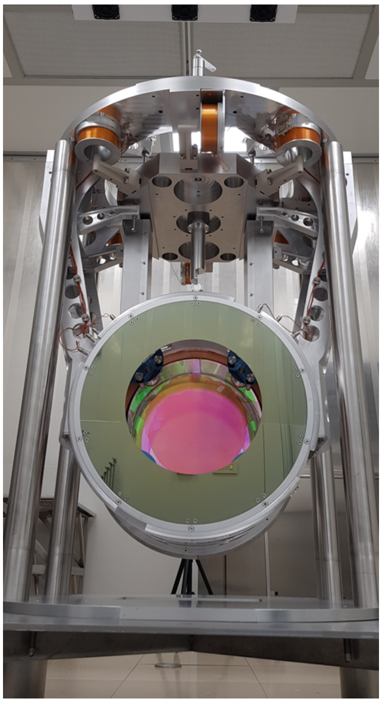

FIGURE 1.8: Photo du miroir et de la marionette NE de Virgo. Les bobines fixées à la cage d'actionnement sont utilisées pour agir sur les aimants du miroir et de la marionnette. Le diaphragme qui entoure le miroir cache en grande partie les quatres paires de bobines et aimants du miroir.

1.3.4 La reconstruction du signal d'onde gravitationnelle $h(t)$

Le signal de l'interféromètre $h(t)$ est défini comme suit:

$$h(t) = \frac{L_N(t) - L_W(t)}{L_0} \tag{1.6}$$

où L_N et L_W sont respectivement les longueurs des cavités de Fabry-Pérot Nord et Ouest de l'interféromètre, $L_0 = 3000$ m est la longueur nominale des bras de l'interféromètre.

Il est obtenu par le processus de reconstruction du signal. Ce processus part du signal de la photodiode de sortie qui mesure les déplacements d'un interféromètre contrôlé. Il faut donc lui soustraire les effets des boucles de contrôle injectées par les actionneurs électromagnétiques. Pour cela, on soustrait au signal de photodiode converti en Watts, les contributions de chaque miroir contrôlé (NE, WE, BS) le signal de control corrigé de la réponse de l'actionneur ainsi que de la réponse optique correspondante. Le résultat est ensuite multiplié par la réponse optique inverse de l'interféromètre pour passer des Watts à une variation de longueur et donc $h(t)$.

Des signaux d'étalonnage sont continuellement injectés pour suivre les réponses optiques en temps réel. Cette opération de reconstruction soustrait donc aussi ces signaux d'étalonnage. De plus, des sources de bruit variées (fréquence du laser, lumière diffusée) peuvent se coupler au signal $h(t)$. Des canaux témoins sont sélectionnés pour surveiller et soustraire ces contributions à $h(t)$ via des fonctions de transfert.

1.3.5 La sensibilité de Virgo

La fig. 1.9 issue de [17] montre la sensibilité théorique de Advanced Virgo Plus dans sa phase 1. Les principales sources de bruit sont les suivantes:

- Bruit quantique de mesure: Le niveau de ce bruit est définit par la puissance injectée dans l'interféromètre, les détails de la configuration optique (paramètres de la cavité Fabry-Pérot, miroir de recyclage de puissance et miroir de recyclage du signal) ainsi que les performances du *squeezing*.

- Bruit thermique des miroirs: Ce bruit est dominé par l'agitation thermique des revêtements des miroirs. Son amplitude est estimée à partir des caractéristiques des matériaux utilisés et du processus de dépôt.

- Bruit thermique du pendule: Ce bruit est évalué à partir des pertes connues dans les fibres de silice fondue, de celles des liaisons avec miroir ou marionette, ainsi que des pertes mécaniques de la marionnette.

- Bruit Newtonien: Ce bruit est estimé à l'aide du meilleur modèle disponible qui prend en compte l'activité sismique et la géométrie de l'environnement du miroir.

- Bruit technique: Ce bruit est difficile à prévoir et résulte principalement de la combinaison du bruit de contrôle, de la lumière diffusée, du bruit des actionneurs et des perturbations environnementales.

Ces différents types de bruit doivent être maîtrisés et réduits au mieux pour optimiser la sensibilité d'Advanced Virgo Plus.

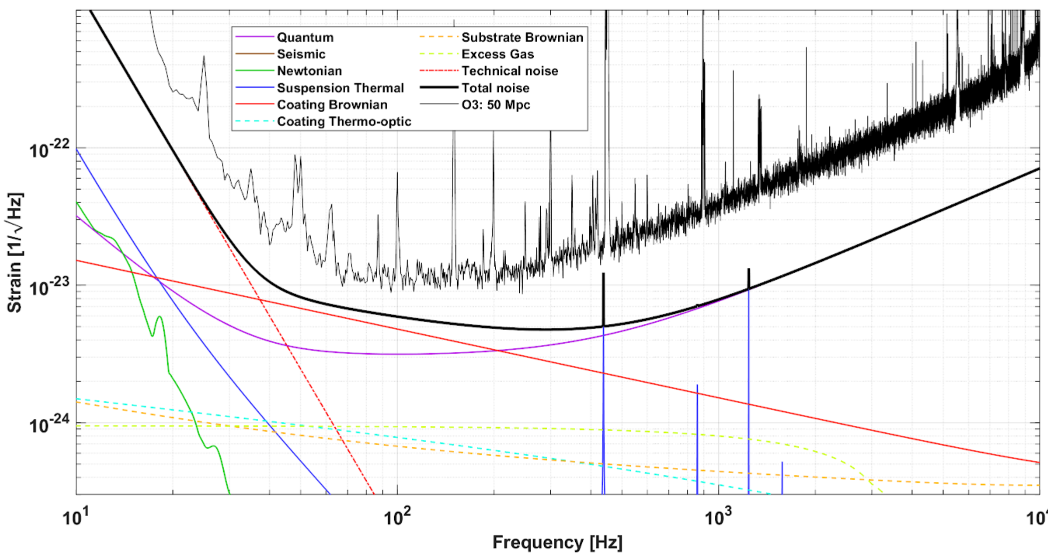

FIGURE 1.9: En noir, ligne épaisse: la sensibilité du design de Advanced Virgo Plus Phase 1. Les principales contributions des sources de bruit sont montrées. Par comparaison, la sensibilité atteinte par Virgo pendant O3 est superposée. Source: [17]

1.4 Les enjeux de l'étalonnage des détecteurs

1.4.1 Localisation des sources astrophysiques

Le réseau de détecteur terrestre permet de localiser les sources astrophysiques. En effet, contrairement à un télescope optique, le diagramme d'antenne d'un détecteur d'ondes gravitationnelles couvre une large fraction du ciel, mais avec une réponse non uniforme. Une source astrophysique peut donc être observée par l'ensemble des détecteurs situés sur Terre mais avec une très mauvaise localisation pour chaque détecteur. L'exploitation des différences de temps d'arrivée permet d'obtenir par triangulation la position de la source dans le ciel. De plus, la comparaison des amplitudes observées permet d'affiner cette localisation. La fig. 1.10 issue de [6] montre la reconstruction de la position dans le ciel de la première détection d'une BNS par les interféromètres LIGO et Virgo avec contrepartie électromagnétique (GW170817).

Sachant que le SNR le plus élevé mesuré pendant O3 est de 26, c'est-à-dire que l'amplitude du signal est mesurée avec une fluctuation statistique de 1/26, il faut donc que les incertitudes systématiques d'étalonnage d'un détecteur soient bien inférieures à cette valeur. Cela signifie que les incertitudes d'étalonnage soient inférieures au pourcent pour ne pas induire de biais dans la localisation de la source et donc ne pas rater une possible contrepartie optique.

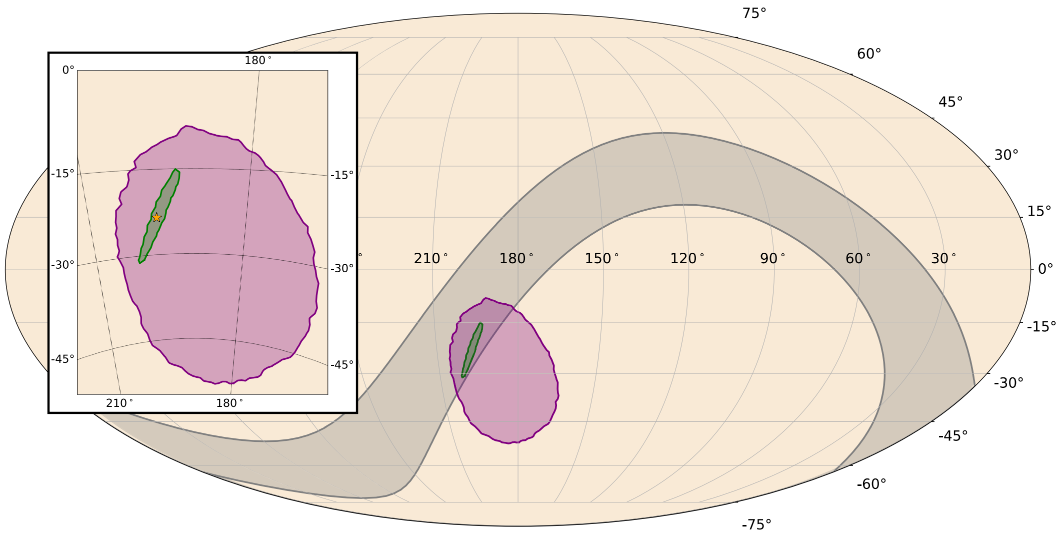

FIGURE 1.10: Reconstruction de la position dans le ciel de la source pour GW170817. Le contour à 90% de la carte finale de localisation du ciel de LIGO-Virgo est affiché en vert (LIGO et Virgo). Le contour à 90% donné par l'observation du sursaut gamma est superposé en violet. Source: [6].

1.4.2 Mesure de la constante de Hubble H_0

La constante de Hubble H_0 est une quantité primordiale en cosmologie représentant le taux d'expansion local the l'Univers. Pour des distances proches ($d < 50$ Mpc), on peut l'écrire comme suit:

$$v_H = H_0 d \tag{1.7}$$

avec v_H la vitesse de récession de la source et d la distance à la source.

Deux principales méthodes de mesure de la constante de Hubble sont utilisées depuis de nombreuses années:

- L'observation de chandelles standard, objets astronomiques de luminosité connue permettant de mesurer les distances de nombreuses galaxies proches ($d <$ 30 Mpc) combiné avec l'observation de galaxies plus lointaines par le biais de supernovae ou luminosité globale de galaxies pour des distances allant jusqu'à plusieurs centaines de Mpc. Une mesure récente faite par le télescope spatial

Hubble a donné: $H_0 = 74.03 \pm 1.42$ km/s/Mpc [13]. La difficulté de cette mesure est d'obtenir la distance de la source, ce qui se fait par étapes successives, engendrant de possibles erreurs.

- L'observation du fond diffus cosmologique (CMB) basée sur le modèle ΛCDM. Une mesure récente faite par le télescope spatial Planck a, quant à elle, donné: $H_0 = 67.4 \pm 0.5$ km/s/Mpc [14].

Comme le montrent ces chiffres, les résultats de ces deux méthodes sont en désaccord de plus de trois écarts-types.

Plus récemment, la détection d'ondes gravitationnelles a permis une mesure de la constante de Hubble indépendante des deux méthodes précédentes. En utilisant la première détection de BNS et de sa contrepartie électromagnétique, la constante de Hubble a été mesurée avec une valeur de $H_0 = 70^{+20}_{-9}$ km/s/Mpc. La fig. 1.11 montre les mesures de H_0 effectuées avec les différentes méthodes. Comme on peut le remarquer, la méthode utilisant les ondes gravitationnelles (couplée avec la contrepartie électromagnétique de GW170817) ne permet par de contraindre la valeur de H_0 dû à l'erreur de mesure trop importante car limitée à une seule observation. Comme la mesure de H_0 est directement proportionnelle à la distance de la source (voir l'eq. (1.7)), une erreur de mesure d'amplitude (inversement proportionnelle à la distance) induite par un biais d'étalonnage introduit la même erreur de mesure de la constante de Hubble. L'étalonnage de précision des détecteurs en dessous de 1% est donc nécessaire pour pouvoir contraindre la valeur de H_0 lorsque de nouvelles observations seront disponibles en nombre suffisant.

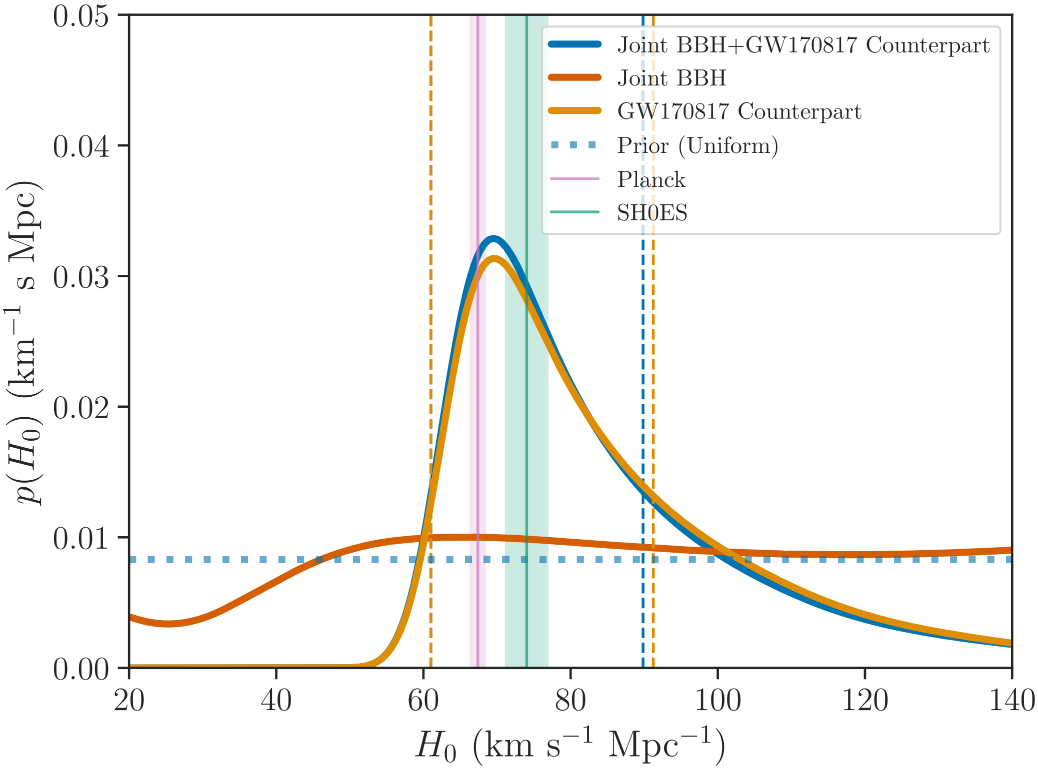

FIGURE 1.11: La mesure d'ondes gravitationnelles de H_0 (bleu foncé) à partir des détections lors des deux premières périodes d'observations de LIGO et Virgo. L'estimation GW170817 (orange) provient de l'identification de sa galaxie hôte NGC4993. La contribution complémentaire provient des BBH en association avec les catalogues de galaxies appropriés ; pour GW170814, le catalogue de galaxies DES-Y1, tandis que pour les cinq BBH restantes, GW150914, GW151226, GW170104, GW170608 et GW170809, le catalogue GLADE. Les intervalles de confiance de 68% sont indiqués par des lignes pointillées verticales. Tous les résultats supposent un préalable sur H_0 uniforme dans l'intervalle $[20, 140]$ km/s/Mpc (pointillé bleu). Les estimations de H_0 du CMB (collaboration Planck [14]) et observations de supernova (SH0ES [13]) sont également montrés. Source: [16].

1.4.3 Mesure du taux d'événements astrophysiques

Le taux d'événements astrophysiques est déterminé par le nombre de sources d'ondes gravitationnelles détectées dans un volume donné. Ce volume est défini par la distance estimée à la source. Comme expliqué dans la section précédente, une erreur de mesure de l'amplitude se traduit directement par une erreur sur la distance mesurée. En fin de compte, cette erreur sur la distance d se propage en d^3 dans le calcul du volume et donc une erreur de calibration de 1% (ce qui est moins que ce qui a été publié pour O3), se traduit par une erreur de 3% sur le taux d'événements.

1.4.4 Préparation pour les détecteurs futurs

La prochaine génération d'interféromètres terrestres, tels que Einstein Telescope (ET) et Cosmic Explorer (CE), devrait voir le jour au cours de la prochaine décennie. La sensibilité accrue de ces détecteurs permettra la détection de signaux plus faibles provenant de sources plus lointaines. Le nombre de détections sera ainsi considérablement augmenté et le volume d'observation plus étendu, rendant les enjeux abordés dans les sections précédentes encore plus cruciaux.

De plus, le SNR des événements les plus proches sera plus élevé, pouvant atteindre un millier, nécessitant un étalonnage d'une précision inférieure à 0.1%. Un étalonnage précis de ces détecteurs permettra également une meilleure estimation des paramètres des sources d'ondes gravitationnelles, tels que leurs masses, spins et distances. Cela ouvrira aussi la voie à la vérification de divers modèles théoriques de la gravitation.

Chapter 2

The detector calibration methods

Contents

Introduction

The calibration of the interferometer is done by inducing a known displacement on the mirrors and by observing the resulting signal. In this chapter we describe three calibration methods. The first method is based on the Free swinging Michelson technique which calibrates the mirror displacement induced by an actuator with respect to the wavelength of the primary laser. The second method is the Photon Calibrator (PCal) which uses the radiation pressure of an auxiliary laser hitting the surface of the mirror to induce a motion. The PCal was the calibration reference for Virgo during O3 (as well as for LIGO and KAGRA). The third method is the Newtonian Calibrator (NCal) which uses a rotor to produce a variable local gravitational field and therefore a mirror motion. The NCal started to be developped by Virgo. The first tests began during O2. The developments continued until the fourth oberving run O4 discussed in this thesis.

2.1 Free swinging Michelson

The Free Michelson technique consists in calibrating the electromagnetic actuators (see section 1.3.3) using the wavelength of the interferometer primary laser $\lambda = 1064$ nm as an etalon. The interferometer mirrors are either aligned or misaligned to setup the Free Michelson configuration. The mirrors motion is then of the order of a few wavelengths, inducing maximum and minimum observed by the output photodiodes, depending of the interference condition. Thanks to the sine-like response of the interferometer, the arm length difference could be reconstructed with the absolute scale given by the laser wavelength. It is used to compute the responses of the NI, WI and BS mirror actuators in [m/V]. These responses are then used to calibrate the NE and WE mirror actuators when the arm cavities are locked.

This method was used as the main calibration until the end of O2 and is detailed in [18–21]. During the O3 run, this method was used to crosscheck the PCal method.

2.1.1 Crosscheck with PCal during O3

Figure 2.1 from [20] shows the comparison between the Free swinging Michelson and the PCal method in modulus and phase during O3. The comparison was compatible within the uncertainties estimated from both methods on the NE mirror actuation: 1.4% using the PCal as reference and between 1% and 2% using the Free swinging Michelson technique. Therefore, the free swinging Michelson technique crosschecked the PCal based calibration within better than 2%.

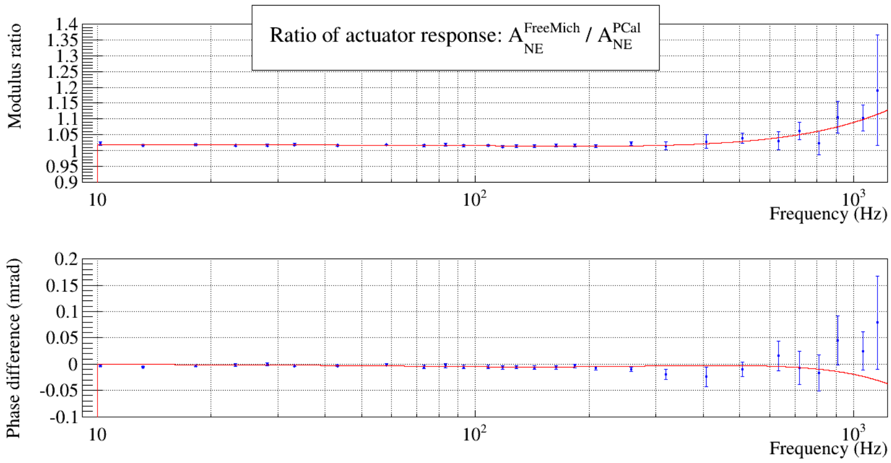

FIGURE 2.1: Comparison of the NE mirror actuator response measured with the free swinging Michelson technique to the response measured with the PCal technique. Top plot is the modulus ratio and bottom plot is the phase difference. The blue points give the ratio of the actuator response data points measured with both techniques at some frequencies in the frequency band 10-1300 Hz, with their associated statistical uncertainties. The red curve shows the ratio of the models extracted from the two independent techniques. Figure from [20].

2.2 Photon Calibrator (PCal)

For the third observing run O3, the main calibration method became the PCal [20].

2.2.1 PCal principle

The PCal uses the radiation pressure of an auxiliary laser to push the mirror. By knowing the mirror mass, the incidence angle and the reflected power P_{ref}, we can compute the radiation pressure force and the corresponding mirror displacement. Figure 2.2 shows the working principle of the PCal. The laser beam hits the end mirror with an angle of incidence $\theta = 18.5°$.

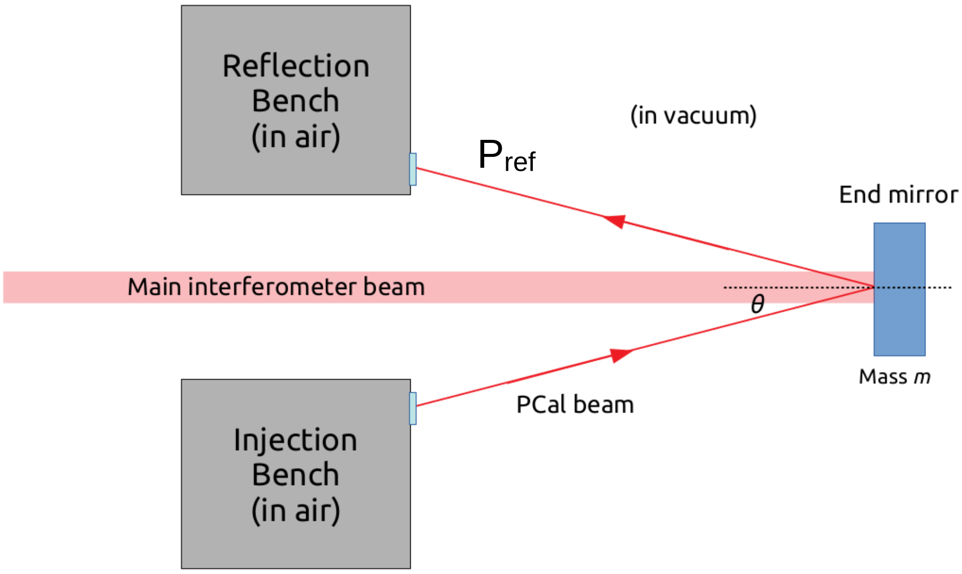

FIGURE 2.2: Drawing of the PCal principle from [22]. The force applied to the end mirror depends on the reflected power, and the angle of incidence of the beam on the mirror.

2.2.2 PCal analytical model

The relation between the displacement of the mirror and the PCal radiation pressure is shown below. The frequency dependent equation linking the force variation $\Delta F(f)$ applied on the end mirror by the laser power variation is:

$$\Delta F(f) = \frac{2\cos(\theta)}{c} \Delta P_{ref}(f) \tag{2.1}$$

The (frequency dependent) mechanical response $H_{pend}(f)$ is the displacement response $\Delta L(f)$ of the mirror to a force excitation $\Delta F(f)$. Since the mirrors are suspended, the mechanical response of the end mirror is first modeled by the mechanical response of an attenuated oscillator, with a gain G_0, a resonance frequency f_p and quality factor Q_p such that:

$$\begin{aligned} H_{pend}(f) &= \frac{\Delta L_{pend}(f)}{\Delta F(f)} \\ &= \frac{G_p}{1 + \frac{j}{Q_p}\frac{f}{f_p} - \left(\frac{f}{f_p}\right)^2} \end{aligned} \tag{2.2}$$

The end mirror has a mass of $M = 42.3$ kg and is suspended with $l_p = 0.7$ m long monolithic wires. The static gain is therefore $G_p = l_p/Mg = 1.69 \times 10^{-3}$ kg^{-1}s^2 and the resonance frequency is $f_p = \frac{1}{2\pi}\sqrt{g/l} = 0.6$ Hz. The quality factor Q_p of the pendulum is around one thousand (limited by the marionetta). If we combine the eqs. (2.1) and (2.2), we can write the displacement of the mirror due to a variation of the PCal laser power as:

$$\Delta L_{pend}(f) = \frac{G_p}{1 + \frac{j}{Q_p}\frac{f}{f_p} - \left(\frac{f}{f_p}\right)^2} \frac{2\cos(\theta)}{c} \Delta P_{ref}(f) \tag{2.3}$$

The emitted laser power $P(t)$ is modulated with an amplitude P_m, at a frequency f, around a mean power P_0 such that:

$$P(t) = P_0 + P_m \sin(2\pi f t) = P_0 + \Delta P(t) \tag{2.4}$$

The frequency of the modulation is in the bandwidth $f \in [10Hz, 10kHz]$. Therefore, the high frequency approximation $f \gg f_p$ of the pendulum can be done. Equation (2.3) can be written as:

$$\begin{aligned}\Delta L_{pend}(f) &= \frac{-G_p f_p^2}{f^2} \frac{2\cos(\theta)}{c} \Delta P_{ref}(f) \\ &= \frac{-2\cos(\theta)}{Mc(2\pi f)^2} \Delta P_{ref}(f)\end{aligned} \tag{2.5}$$

In addition to the pendulum response, the deformation of the high reflected mirror surface of the mirror due to the laser power must be included above a kHz. This deformation is seen by the interferometer as a variation of the arms length. The deformations of the surface are decomposed into a sum of internal modes of the mirror. Therefore, the total displacement of the mirror is the sum of the simple pendulum motion with all the internal modes. In practice, the PCal beam hits the center of the mirror, which excites mostly the fundamental drum modes and has the largest coupling with the interferometer beam. The expression of the mechanical response of these modes $H_{drum,tot}$ can be expressed as a sum of responses of damped harmonic oscillators $H_{drum,i}$ such that:

$$\begin{aligned}H_{drum,tot} &= \sum_i H_{drum,i}(f) \\ &= \sum_i \frac{G_{d,i}}{1 + \frac{j}{Q_{d,i}} \frac{f}{f_{d,i}} - \left(\frac{f}{f_{d,i}}\right)^2}\end{aligned} \tag{2.6}$$

Therefore, the displacement of the mirror induced by the PCal is written as:

$$\begin{aligned}\Delta L_{PCal}(f) &= \Delta L_{pend}(f) + \sum_i \Delta L_{drum,i}(f) \\ &= \Big(H_{pend}(f) + \sum_i H_{drum,i}(f)\Big) F(f)\end{aligned} \tag{2.7}$$

In practice, the calibration of the interferometer with the PCal is done in the bandwidth 10 Hz to several kHz. Only the first two resonant modes were taken into account in the model of the mirror mechanical response. The contribution of the other drum modes are neglected and eq. (2.7) becomes:

$$\begin{aligned}\Delta L_{PCal}(f) &= \Delta L_{pend}(f) + \sum_i \Delta L_{drum,i}(f) \\ &= \Big(H_{pend}(f) + \sum_i H_{drum,i}(f)\Big) F(f)\end{aligned} \tag{2.8}$$

2.3 Newtonian Calibrator (NCal)

Another option to induce a known motion of a test mass is to use a variable gravitational field produced by rotating masses. The device associated to this calibration method is named a Newtonian Calibrator (NCal) or Gravitational Calibrator (GCal for the KAGRA collaboration). The NCal method is very different from the PCal since it mainly relies on geometrical parameters such as the distance between the rotating masses and the mirror. This can lead to reduced uncertainties compared to already existing calibration methods.

2.3.1 A short NCal history

The idea of using the gravitational force as an actuator to calibrate a gravitational wave detector is an old idea. It was first developed for the resonant bar detectors, initially with a resonant system in the late 60's [23, 24] then with rotors in the 80's and 90's [25–28] with the additional purpose of studying the distance dependence of the gravitational law.

It was proposed as a calibration method for interferometric gravitational wave detector in the Virgo final conceptual design of 1992 [29] and further discussed more recently [30]. A first prototype was tested in Virgo at the end of O2 [31]. New developments were made for Virgo in O3 [32] and another prototype was first tested at LIGO during O3 as well [33]. These tests with be described in this section.

2.3.2 NCal principle

Figure 2.3 shows the layout of the NCal for Virgo. It is based on two rotating masses made of two massive sectors placed at a known distance from the mirror. When rotating, the Newtonian force produced by this device has a modulation at twice the rotor frequency. The reference frame is (O; x; y; z) with the center of the mirror in O. Due to the presence of the laser beam, the masses are not in front of the mirror. Therefore there is an angle ϕ between the beam axis of the interferometer and the rotor-to-mirror axis. The distance d is the radial distance between the center of the rotor and the center of the mirror.

The mirror is assumed to be a full cylinder of radius r_{mir} and thickness x_{mir}. The cylindrical coordinates of a point of the mirror in the reference frame are:

$$(x'; r' \cos(\beta); r' \sin(\beta))$$

where $r' \in [0; r_{mir}]$, $x' \in [-x_{mir}/2; x_{mir}/2]$ and $\beta \in [0, 2\pi]$,

The rotor parameter b is the thickness of a sector, r_{min} and r_{max} are the minimum and maximum values of the radial dimension of a sector, α is the opening angle of a sector, θ is the rotation angle of the masses around the rotor axis. The cylindrical coordinates of a point of a rotor sector $(+, -)$ in the reference frame are:

$$\begin{pmatrix} d\cos(\phi) \pm r\cos(\theta+\eta)\cos(\phi) - b'\sin(\phi) \\ d\sin(\phi) \pm r\cos(\theta+\eta)\sin(\phi) + b'\cos(\phi) \\ \pm r\sin(\theta+\psi) \end{pmatrix}$$

where $r \in [r_{min}; r_{max}]$, $\eta \in [-\alpha/2; \alpha/2]$ and $b' \in [-b/2; b/2]$

For simplicity purposes, we assume that the rotor axis is in the plane of the interferometer, with $z = 0$, but a detailed calculation when $z \neq 0$ is given in appendix A of [32].

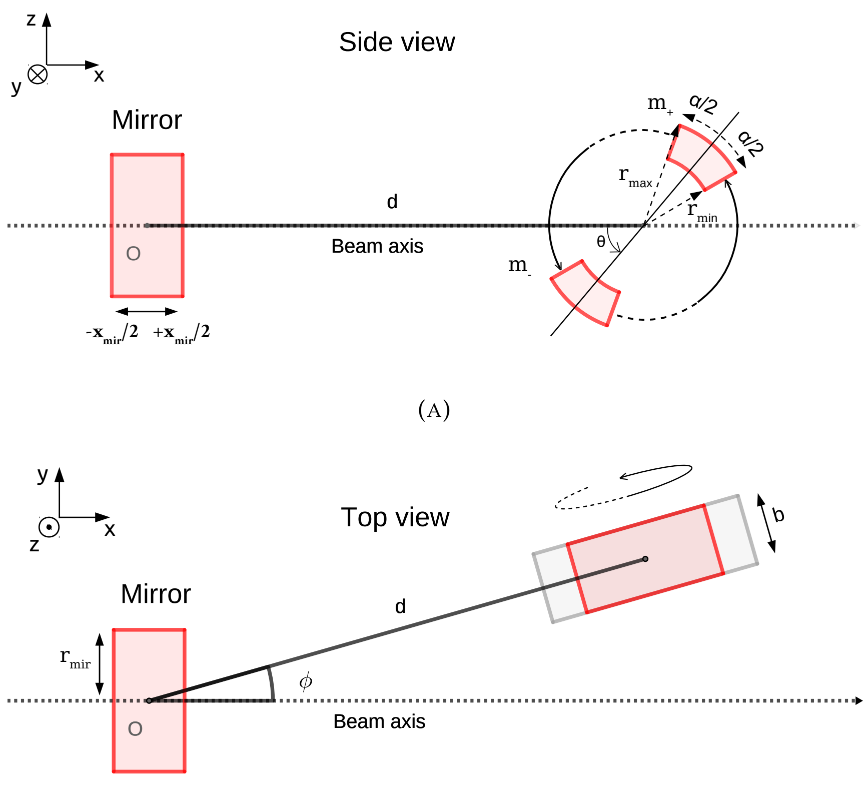

(A)

(B)

FIGURE 2.3: Schematic of the NCal rotor position with respect to a mirror of Advanced Virgo. A side view is shown in (A) and a top view in (B).

2.3.3 Analytical model of a rotor with two sectors

The analytical model of the rotor is created by describing the interaction between a small element of the mirror and the rotor. Then, it is integrated over the full rotor and mirror to form the model. The longitudinal Newtonian force induced by rotating masses on the mirror has already been established and developped in the appendix of [32], it is given in eq. (2.9). $dF_{i,x}$ is the force applied by a small element of a sector $i \in (+,-)$ at the distance d and angle ϕ. G is the gravitational constant. dm_{rot} is the mass of the sector element and dm_{mir} is the mass of the mirror element.

$$dF_{i,x} = \frac{Gdm_{rot}dm_{mir}}{d^2}\left(\cos(\phi) + \epsilon\cos(\theta+\eta)\cos(\phi) - \epsilon'''\sin(\phi) - \epsilon''\right)\left[1 + X_i\right]^{-3/2} \tag{2.9}$$

with:

$$\begin{aligned} X_i = {} & \epsilon^2 + \epsilon'^2 + \epsilon''^2 + \epsilon'''^2 \pm 2\epsilon\cos(\theta+\eta) - 2\epsilon''\cos(\phi)(1 \pm \epsilon\cos(\theta+\eta)) \\ & \mp 2\epsilon\epsilon'\sin(\beta)\sin(\theta+\eta) + 2\epsilon'''(\epsilon''\sin(\phi) - \epsilon'\cos(\phi)\cos(\beta)) \end{aligned} \tag{2.10}$$

where we defined the small quantities $\epsilon = \frac{r}{d}$, $\epsilon' = \frac{r'}{d}$, $\epsilon'' = \frac{x'}{d}$ and $\epsilon''' = \frac{b'}{d}$.

Equation (2.10) can be expanded at the fourth order using the following:

$$(1+X_i)^{-3/2} \approx \left(1 - \frac{3}{2}X_i + \frac{15}{8}X_i^2 - \frac{35}{16}X_i^3 + \frac{315}{128}X_i^4\right) \tag{2.11}$$

Then keeping only the terms at twice the rotor frequency of eq. (2.11) in eq. (2.9) and summing the longitudinal force of each small sector element, the small longitudinal force dF_x is:

$$\begin{aligned} dF_x \approx \frac{9Gdm_{rot}dm_{mir}r^2}{2d^4}\cos(\phi)\Big[1 + \frac{25}{36}\epsilon^2 + \Big(\frac{45}{2}\sin(\phi)\cos^2(\beta) - \frac{25}{6}\Big)\epsilon'^2 \\ + \Big(\frac{45}{2}\cos^2(\phi) - \frac{25}{9}\Big)\epsilon''^2 - \frac{25}{6}\epsilon'''^2\Big]\cos(2(\theta+\eta)) \end{aligned} \tag{2.12}$$

In eq. (2.12) the odd terms in $\cos(\beta)$, $\sin(\beta)$, ϵ'' and ϵ''' have been omitted since they cancel each other in the following steps.

As we consider non-point-like masses, the mass m of the rotor and M of the mirror are the integrals over the respective small massive elements dm_{rot} and dm_{mir}, assuming that ρ_{rot} and ρ_{mir} the densities of respectively the rotor and the mirror are constant within the material:

$$m = \iiint dm_{rot} = \rho_{rot}\int_{r_{min}}^{r_{max}} rdr \int_{-\alpha/2}^{\alpha/2} d\eta \int_{-b/2}^{b/2} db' \tag{2.13}$$

$$M = \iiint dm_{mir} = \rho_{mir}\int_0^{r_{mir}} r'dr' \int_0^{2\pi} d\beta \int_{\frac{-x_{mir}}{2}}^{\frac{x_{mir}}{2}} dx' \tag{2.14}$$

Integrating eq. (2.12) using eqs. (2.13) and (2.14) we obtain the total longitudinal force of an extended rotor exerted on an extended mirror. The amplitude of the mirror motion is then expressed as:

$$a(f_{2rot}) = \frac{|F_x|}{M(2\pi f_{2rot})^2} \tag{2.15}$$

where $f_{2rot} = 2f_{rot}$ with f_{rot} the rotor frequency. The mass of the mirror cancels out when computing the amplitude of the mirror motion. Finally, eq. (2.15) can be fully written as:

$$\begin{aligned} a(f_{2rot}) = \frac{9G\rho_{rot}\, b\, \sin(\alpha)(r_{max}^4 - r_{min}^4)}{32\pi^2 f_{2rot}^2 d^4}\cos(\phi)\Big[1 + \frac{25}{54d^2}\frac{(r_{max}^6 - r_{min}^6)}{(r_{max}^4 - r_{min}^4)} \\ + \Big(\frac{45}{8}\sin^2(\phi) - \frac{5}{2}\Big)\Big(\frac{r_{mir}}{d}\Big)^2 + \Big(\frac{15}{8}\cos^2(\phi) - \frac{25}{4}\Big)\Big(\frac{x_{mir}}{d}\Big)^2 - \frac{25}{72}\Big(\frac{b}{d}\Big)^2\Big] \end{aligned} \tag{2.16}$$

The first order approximation of eq. (2.16) is shown in eq. (2.17). This approximation will be used later to compute the signal uncertainty. It differs from the full computation by less than 1% for our geometry.

$$a(f_{2rot}) = \frac{9G\rho_{rot}\, b\, \sin(\alpha)(r_{max}^4 - r_{min}^4)}{32\pi^2 f_{2rot}^2 d^4}\cos(\phi) \tag{2.17}$$

The associated strain is the amplitude normalized by the interferometer arm length $L = 3$ km for Virgo and is expressed as:

$$h(f_{2rot}) = \frac{a(f_{2rot})}{L} \tag{2.18}$$

2.3.4 Analytical model of a rotor with three sectors

To reach high frequencies, one need to operate the rotor in a regime that could be challenging for the mechanical device. Another way to achieve higher frequency in $h(t)$ is to operate a rotor with more than two sectors. The resulting signal will then be at n times the rotor operating frequency with n the number of sectors. This section presents the analytical calculation of the gravitational signal from a three-sector rotor. Using the analytical equation of the newtonian force (see eq. (2.9)) we can compute the gravitational strain of a three sector rotor on the mirror at three times the rotor frequency. In eq. (2.9) $dF_{i,x}$ is the force of a small element from a sector i along the x axis, in the case of three sectors we have $i = \left[-\frac{2\pi}{3}, 0, \frac{2\pi}{3}\right]$.

We can write up to the third order the following term:

$$(1+X_i)^{-3/2} \approx 1 - \frac{3}{2}X_i + \frac{15}{8}X_i^2 - \frac{35}{16}X_i^3 \tag{2.19}$$

After computation of eq. (2.9) with eq. (2.19) we are left with the following non null component:

$$dF_{i,x} = -\frac{10Gdm_{rot}dm_{mir}}{d^2}\epsilon^3\cos(\phi)\cos^3(\theta+\eta+i) \tag{2.20}$$

The small force dF_x along x is:

$$\begin{aligned} dF_x &= \sum_i dF_{i,x} = dF_{0,x} + dF_{\frac{2\pi}{3},x} + dF_{-\frac{2\pi}{3},x} \\ &= -\frac{30}{4}\frac{Gdm_{rot}dm_{mir}}{d^2}\epsilon^3\cos(\phi)\cos(3\theta+3\eta) \end{aligned} \tag{2.21}$$

Using the following relation of the mass m of the rotor (we will consider the mirror of mass M to be a point with no dimension for this computation):

$$m = \rho_{\rm rot}\int_{r_{\rm min}}^{r_{\rm max}}\int_{-\alpha/2}^{\alpha/2}\int_{-b/2}^{b/2} r\mathrm{d}r\ \mathrm{d}\eta\ \mathrm{d}b' \tag{2.22}$$

We have:

$$\begin{aligned} F_x &= -\frac{30}{4}\frac{GM}{d^5}\cos(\phi)\rho_{\rm rot}b\int_{r_{\rm min}}^{r_{\rm max}} r^4\mathrm{d}r\int_{-\alpha/2}^{\alpha/2}\cos(3\theta+3\eta)\mathrm{d}\eta \\ &= -\frac{4}{3}\frac{GM}{d^5}\rho_{\rm rot}b\cos(\phi)\cos(3\theta)\sin(3\alpha/2)(r_{\rm max}^5 - r_{\rm min}^5) \end{aligned} \tag{2.23}$$

We can now compute the strain at 3f using the following relation:

$$\begin{aligned} h(3f_{\rm rot}) &= \frac{a(3f_{\rm rot})}{L} = \frac{|F_x|}{ML(2\pi f_{3\rm rot})^2} \\ &= \frac{G\rho_{\rm rot}\ b\ \sin(3\alpha/2)(r_{\rm max}^5 - r_{\rm min}^5)}{4\pi^2 L f_{3\rm rot}^2 d^5}\cos(\phi) \end{aligned} \tag{2.24}$$

Although it looks appealing, to reach higher frequencies, the signal generated by a three sectors rotor is 18 times smaller than a two sectors rotor for the same frequency in $h(t)$ (but with a 2/3 rotor frequency ratio) for the typical Virgo configuration at 1.7 m.

2.3.5 NCal finite element analysis with FROMAGE

The analytical model presented in section 2.3.3 considers perfect and symmetrical cylindrical shapes for the rotor and mirror but does not account for more complex geometry like mirror ears and small defects. This can be achieved by taking into account the refined geometry of both mirror and rotor via a numerical model using Finite Element Analysis (FEA). FROMAGE[1] is the simulation tool developed at IPHC for this purpose. It is written in C/C++.
The program is available at https://git.ligo.org/virgo/virgoapp/FROMAGE. The first version was released for O3 [34, 35] and was tested with the O3 NCal [32].

FROMAGE uses a grid in which the mirror and rotor elements are divided into small parts as seen in fig. 2.4 [35]. Then it computes and sums the Newtonian force between each element of the rotor and each element of the mirror.

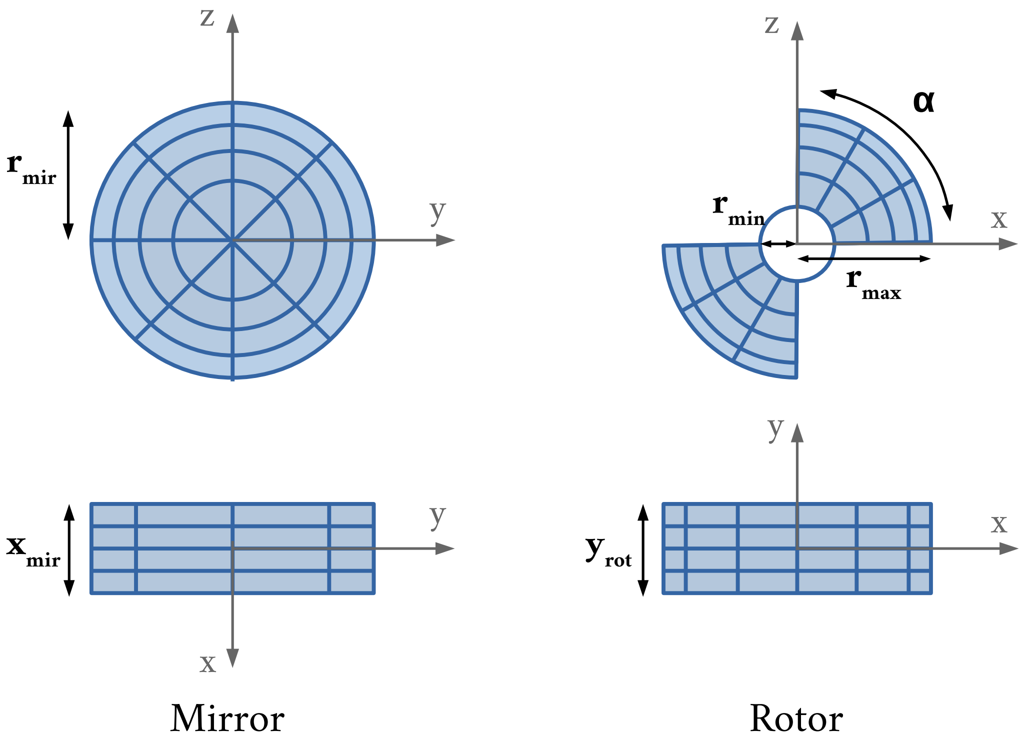

FIGURE 2.4: Principle of splitting the mirror and the rotor in FROMAGE using a grid. The splitting follows the cylindrical shape of the mirror and rotor geometry.

The total longitudinal Newtonian force applied on the mirror for a given rotation angle θ is expressed as in eq. (2.25) from [35].

$$F^{tot}_{\theta,x} = G \sum_I \sum_J \sum_\mu m_{rot,J} m_{mir,I} \frac{x_{rot\mu,J} - x_{mir,I}}{d^3_{\mu,I,J}} \tag{2.25}$$

[1]Finite element analysis of **RO**tating **MA**sses for **G**ravitational **E**ffect

Where I = (i; j; k) the elements of the mirror, J = (l; p; q) the elements of one sector of the rotor and the index μ $\in [1; n_{sectors}]$ with $n_{sectors}$ the number of sectors of the rotor.

The periodic displacement of the mirror X_θ induced by a NCal at a rotor frequency f_{rot} can be expanded in Fourier series such as in eq. (2.26) from [35] with C_k the complex Fourier coefficients, k the phase of C_k and $\theta = 2\pi f N_{rot}$.

$$X(\theta) = \frac{1}{N}\left(C_0 + 2\sum_{k=1}^{N-1} |C_k| \cos\left(k\theta + \eta_k\right)\right) \tag{2.26}$$

Figure 2.5 shows eight representations, for different angle of rotation θ, of the O4 rotor (see fig. 2.15) and mirror of Virgo where each point correspond to an element.

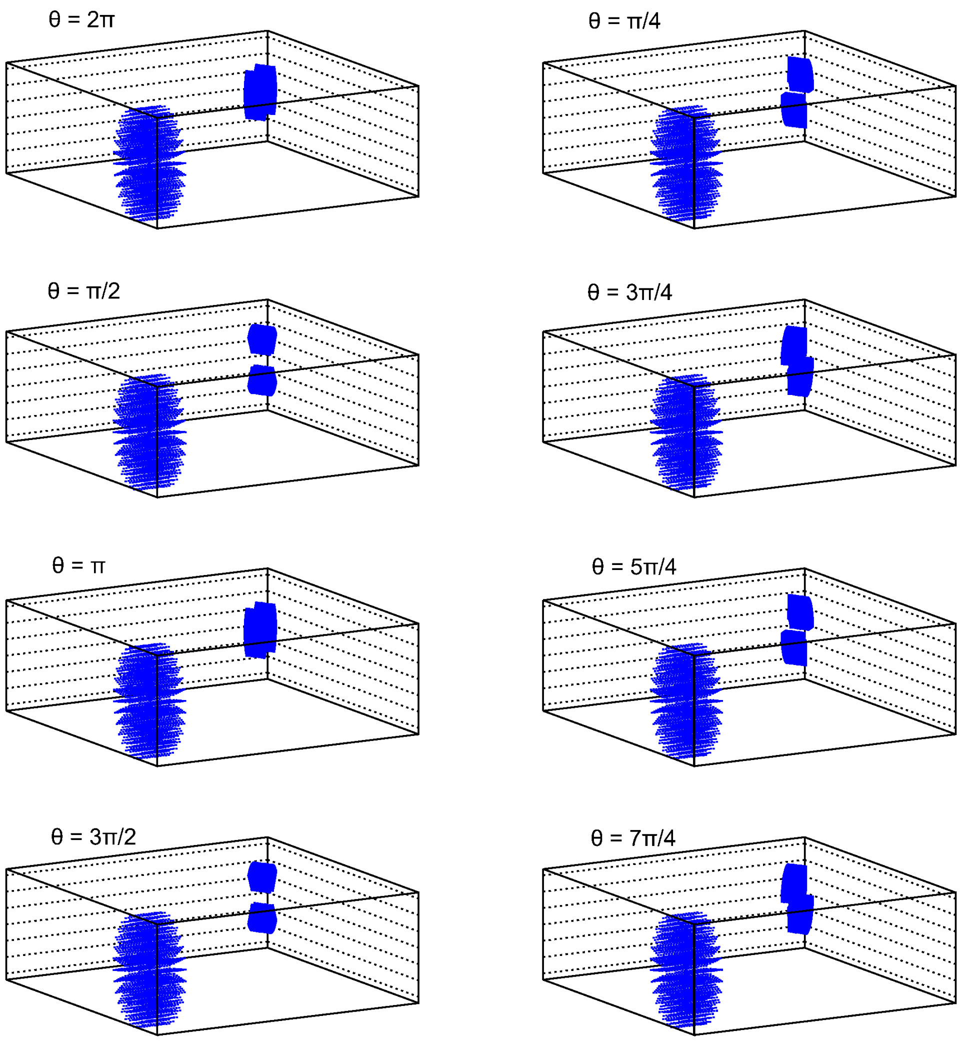

FIGURE 2.5: Representation of the mirror (foreground) and rotor (background) elements when the rotor is spinning. Each point represents an element of the rotor or mirror object computed by FROMAGE.

As the Virgo NCal rotors are made of 2 sectors, only the contribution of the quadrupole moment at twice the rotor frequency (i.e. at 2θ) is expected to be significant. In that case, the displacement X of the mirror induced by the NCal at twice the rotor frequency f_{2rot} is given by eq. (2.27).

$$X(f_{2rot}) = \frac{F_{\theta,x}^{tot}}{M_{mir}(2\pi f_{2rot})^2} \tag{2.27}$$

Where M_{mir} is the mass of the mirror.

The resolution of the grid has an impact on the computed signal. A grid of $12 \times 30 \times 8$ elements for the mirror and $8 \times 65 \times 40$ elements for each sector of the rotor was chosen to remain within 0.005% of variation from the asymptotic value for the O3 rotor (see figures 6 and 7 of [35]). As the geometry of the rotors was simplified for O4 we checked that the grid defined for the O3 rotor is still relevant for the O4 rotor so that it does not induce a significant numerical uncertainty on the results. Figure 2.6a shows the relative mirror displacement when increasing the number of elements for each grid parameter from the optimal O3 grid. We call $(n_{mir,x}; n_{mir,\alpha}; n_{mir,r})$ the mirror grid and $(n_{rot1/2,y}; n_{rot1/2,\alpha}; n_{rot1/2,r})$ the grid of a rotor sector. Summing the strain variations for each multiple of the optimized O3 grid gives the deviations shown in fig. 2.6b. Therefore, we chose to keep the O3 FROMAGE grid as it remains within 0.005% for the O4 rotor and mirror configuration.

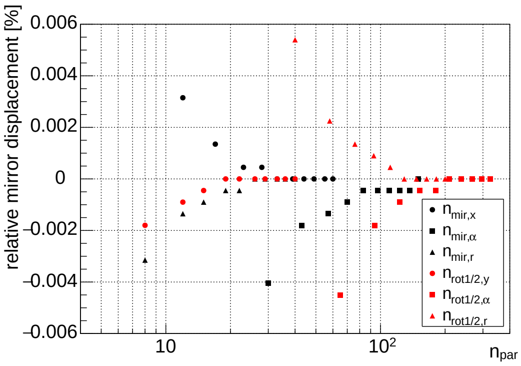

(A)

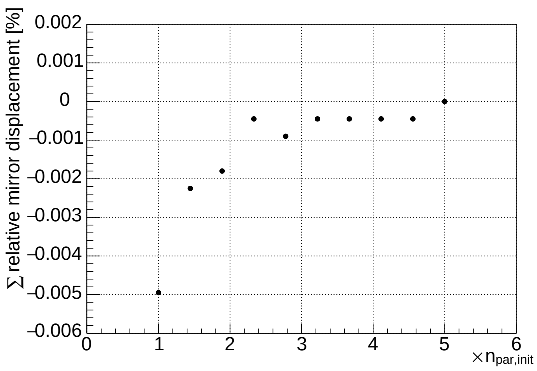

(B)

FIGURE 2.6: (A) shows the numerical variation of the relative mirror displacement for every parameter of the grid (n_{par}) starting with the O3 optimized grid for the mirror (12; 30; 8) and for a O4 rotor sector (8; 65; 40). (B) displays the sum of the relative mirror displacements on the y-axis against multiples of the initial O3 grid parameter on the x-axis.

2.4 NCal tests before O4

2.4.1 Firsts NCal tests during O2

The first tests of a NCal were performed during O2 on the Virgo interferometer and reported in [31]. The simple prototype is shown in fig. 2.7 and was produced with the objective to check that a rough NCal signal can be injected without disturbing the interferometer. Therefore, the prototype was not perfectly characterized. The rotor was made of aluminum 7075 (nominal density taken as 2800 kg.m^{-3}) with two symmetrical full sectors having an opening angle α of 45°, an inner radius r_{min} of 55.0 mm, an outer radius r_{max} of 190.0 mm and a thickness b of 52.0 mm.

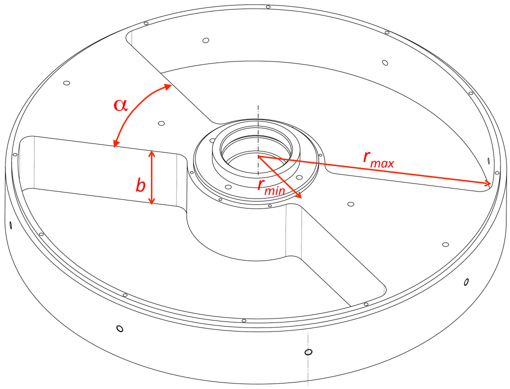

FIGURE 2.7: View of the O2 NCal rotor without its top cover.

Figure 2.8 from [31] shows the NCal lines at twice the rotating frequency around 26 Hz and 70 Hz. With an SNR of about 50, the lines were somewhat spread around their central value due to the limitations of the rough NCal control system used. When changing the NCal frequency, the sensitivity remained unchanged, except of course at the frequency of the injected line, demonstrating that the NCal did not disrupt the interferometer's operation.

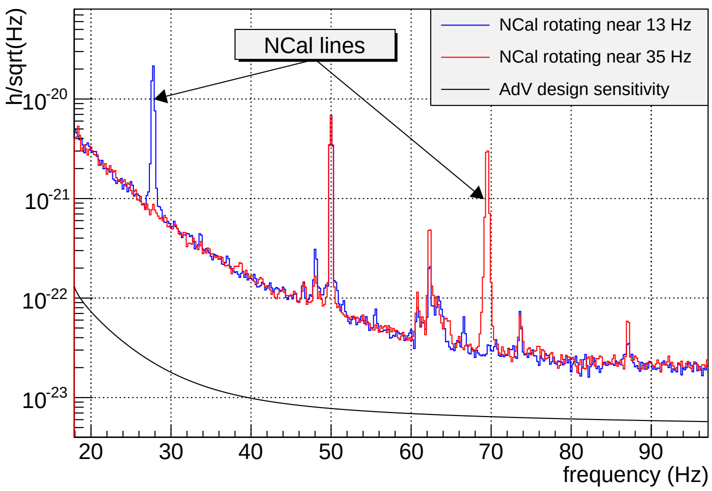

FIGURE 2.8: Measured spectrum of the $h(t)$ signal with the NCal rotating at two different speeds during O2. The NCal signal is observed at twice the NCal rotation speed.

Another check was done with the NCal position relative to the mirror. The mirror is inside a vacuum chamber and might be offset by a few mm from its expected center. To check this distance, the NCal was put at two locations, at the same distance from the mirror ($d = 1.878$ m) but on opposite sides. As the NCal amplitude in $h(t)$ varies as the fourth power of the distance at the first order, the ratio of the measured amplitudes will therefore be 8 times this mirror offset times the distance d (see eq. (8.4)). Using this method, the mirror distance offset along the NCal axis was measured to be 2.3 ± 1.4 mm which was compatible with the NCal position uncertainty. Therefore it was shown that using NCals located on opposite sides of the mirror we can measure the mirror position and reduce the corresponding uncertainty.

2.4.2 Virgo NCal during O3

Following the first tests of a Virgo NCal during O2 [31], an improved version of the NCal was built for O3 [32]. The NCal system for O3 was made of two similar rotors suspended on the South side of the mirror from a beam fixed on the structure of the tower as shown in fig. 2.9. The NCals have been labeled relative to their proximity to the mirror. The near NCal was at a distance $d_N = 1.2666$ m from the theoretical position of the mirror and the far NCal was at a distance $d_F = 1.9466$ m, both at an angle $\phi = 34.7°$ relative to the beam axis.

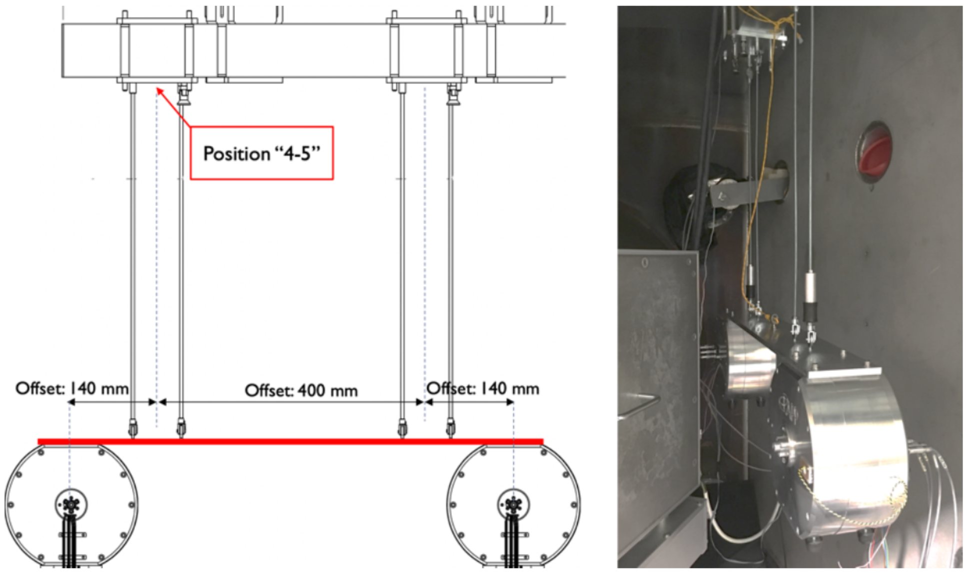

FIGURE 2.9: Left: drawing of the side of the suspended O3 NCal setup. Right: Picture of the setup installed on the South side of the North end mirror. From [36].

Rotor geometry

The O3 rotor, named NCal-200, was made of aluminum 7075 as for O2 but with two full sectors having an opening angle α of 90° to maximize the signal, an inner radius r_{min} of 32.0 mm, an outer radius r_{max} of 205.0 mm and a thickness b of 73.8 mm. As shown in fig. 2.10 two cavities were machined on each side of the rotor with a nominal outer radius of 95.0 mm and a depth of 37.0 mm. The cavities were closed with plastic covers on both sides to avoid air motion. The rotor was operated inside an aluminum casing for safety purposes. A detailed study on the safety of the NCal-200 was made in [37] and resulted in a safety factor of 20 when operating at its maximum foreseen frequency of 100 Hz. This study was performed with a naive model and confirmed by a FEA model of the rotor using ANSYS.

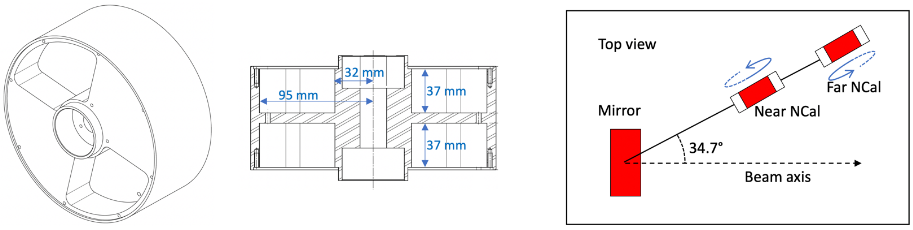

FIGURE 2.10: From left to right: 3D view of the O3 NCal-200 rotor, cross section of the rotor, sketch of the NCals locations relatve to the mirror from [32].

The amplitude of the calibration signal at twice the rotor frequency is proportional to the rotor thickness, to the density and to the fourth power of the outer radius of the rotor as derived from eq. (2.16) at first order. The relative uncertainty on the injected 2f signal from the O3 rotor geometry was 0.53% and is detailed in table 2.1.

Rotor parameter			NCal 2f signal uncertainty	
name	value	uncertainty	formula	value [%]
Density ρ [kg.m^{-3}]	2805	5	$\delta\rho/\rho$	0.18
Thickness b [mm]	74	0.2	$\delta b/b$	0.27
Outer radius r_{max} [mm]	95	0.1	$4\delta r_{max}/r_{max}$	0.42
Total uncertainty (quadratic sum)				0.53

TABLE 2.1: Uncertainties on the amplitude of the injected signal from the O3 rotor geometry. This does not include the uncertainties from the mirror to NCal distances.

NCal injections check

Several NCal injections were performed during O3, the longest test described in [32] spans over six hours of data collected in March 2020 with the Virgo interferometer running at its nominal sensitivity of 55 Mpc. Both NCals could be operated together. Figure 2.11 shows the $h(t)$ spectrum with the near NCal injecting a line at 55 Hz and the far NCal at 119 Hz (red curve). A reference spectrum taken an hour later with no NCal injection is also shown (black curve). As for O2, and despite a visible improvement relative to fig. 2.8, the NCal lines are not perfectly monochromatic due to the fluctuation of the NCal motor rotation speed. This is due to the still rough control of the NCal motor. Figure 2.8 shows that the O3 version of the NCal remains non perturbative for the interferometer.

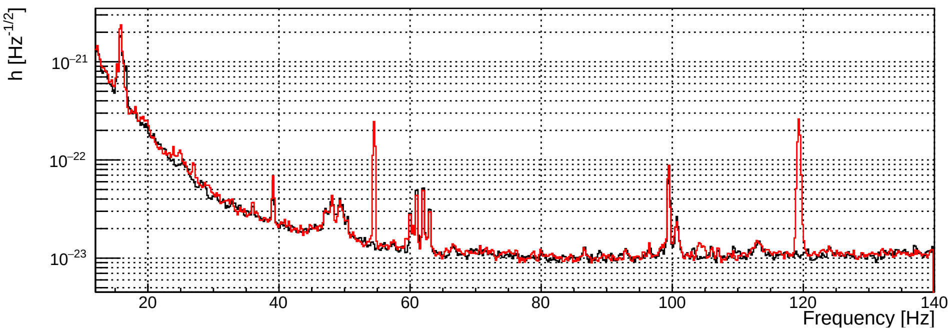

FIGURE 2.11: Red curve: $h(t)$ spectrum when the far NCal was injecting a line at 55 Hz, and the near NCal a line at 119 Hz. Black curve: spectrum when the NCal was switched off. The frequency resolution is 0.2 Hz. The FFTs are averaged over 200 seconds.

Mirror offset using two NCals

Using the amplitude of the two NCal lines and the distance between the two NCals, we can extract the mirror to NCal distance or its offset d_0 relative to the mirror-to-NCals nominal distance. This offset will then be used to correct the value of the injected signal predicted with FROMAGE. Section 6 of [32] develops the analytical formula describing the relation between the offset d_0 and the NCals amplitudes A_N (near) and A_F (far):

$$\frac{A_F}{K_F} - \frac{A_N}{K_N} \approx 4d_0 \frac{d_F - d_N}{d_F\, d_N} \approx 1.103\, d_0 \tag{2.28}$$

with $K_F = C_F d_F$ and C_F the gravitational coupling (calibration) factor of the far rotor (and near rotor for K_N).

Three offsets d_0 were computed with three different data sets. Their mean value was 7.6 ± 6.4 mm. The uncertainty on d_0 was dominated by the 0.53% rotor geometry uncertainty (see last line of table 2.1) highlighting the need for improvement on the rotor geometry knowledge.

Uncertainty on the injected signal

Table 2.2 summarizes the contributions to the O3 NCal systematic uncertainty on the expected 2f signal. A more detailed analysis of each uncertainty is provided in [32]. Overall, the systematic uncertainty on the injected NCal signal for O3 was 2.1% for the near NCal and 1.4% for the far NCal.

Parameter	uncertainty	formula	h_{rec}/h_{inj} near [%]	h_{rec}/h_{inj} far [%]
NCal to mirror distance d	6.4 mm	$4\delta d/d$	2.02	1.31
NCal to mirror angle ϕ	5.0/3.3 mrad	$\delta\phi \sin(\phi)$	0.28	0.19
NCal vertical position z	1.3 mm	$5/2(z/d)^2$	0.03	0.01
Rotor geometry	see table 2.1		0.53	
Modelling method	see end of section 4 of [31]		0.018	0.017
Mirror torque from NCal	see end of section 4 of [31]		0.05	0.03
Total uncertainty (quadratic sum)			2.1	1.4

TABLE 2.2: Uncertainties on the amplitude of the injected signal from the O3 NCal system.

NCal and PCal comparison

The NCal lines amplitudes were then averaged over some time and compared to the expected injected signal computed using the FROMAGE model. Figure 2.12 shows the ratio between the recovered (h_{rec}) and injected (h_{inj}) signal on the left and the phase difference on the right for both the NCals and the PCal. The uncertainties represented here are only statistical. For O3 the PCal uncertainty on the injected calibration lines was 1.4% [20] like for the far NCal. The overall shape of the NCal amplitude is similar to the PCal but with a difference of about 3% between both techniques, slightly larger than the combined systematic uncertainties of the two methods. However, the phase measurements from both NCal and PCal points agree in shape and absolute values.

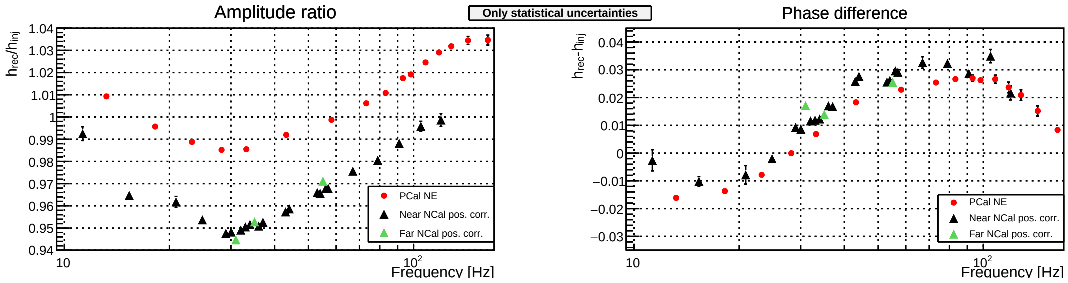

FIGURE 2.12: Comparing recovered (h_{rec}) to injected (h_{inj}) calibration lines for PCal and for NCal at the adjusted position.

2.4.3 LIGO NCal during O3

During the commisioning break of LIGO's third observing run, a NCal prototype was designed and installed at the X-end of the LIGO Hanford interferometer [33]. The prototype was placed at the base of the mirror's vacuum chamber laying on its flat side as seen on fig. 2.13. The rotor was made of an aluminum disk (25.4 cm in diameter and 5.08 cm in height) with cylindrical cavities cut into it in four-fold and six-fold symmetric patterns. Tungsten cylinders were inserted in the disk cavities to form two-fold and three-fold symmetric mass distributions. The measured force amplitudes were then measured at two and three times the rotor frequency. The NCal models predict a systematic uncertainty of 0.8% for $2f$ at 19.1 Hz and 1.1% for $3f$ at 28.7 Hz. Combining the statistical and its systematic uncertainties, the LIGO NCal reached the lowest uncertainty of 1.1% at 19.1 Hz (in $h(t)$). Overall, the NCal results align with the modeled systematic errors as seen in fig. 2.14. However, the absolute phase of the rotor could not be measured and the system was frequency-limited, operating below 10 Hz and reaching up to 29 Hz in $h(t)$.

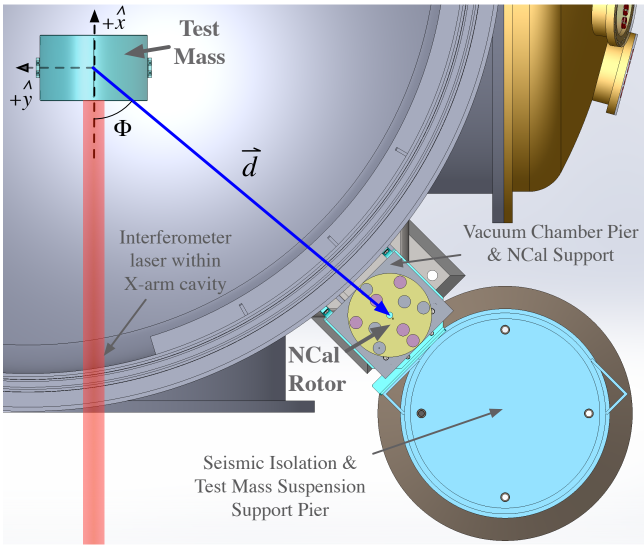

FIGURE 2.13: Top-down view of a CAD rendering of the LIGO NCal and test mass system from [33]. The NCal is shown without its enclosing frame, shell, or motor for clarity.

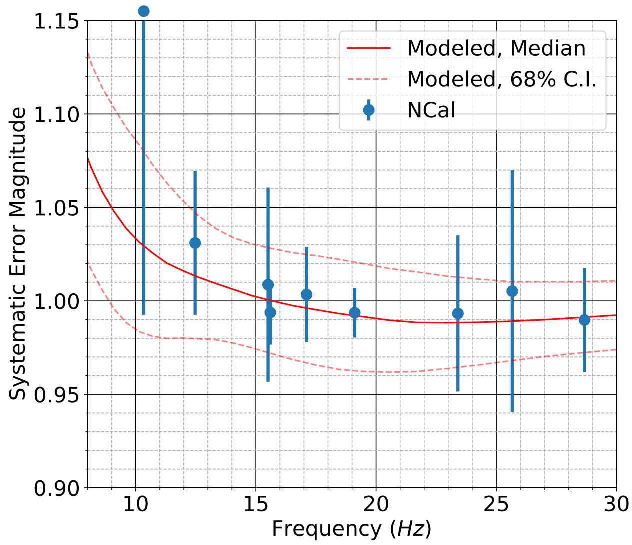

FIGURE 2.14: Comparison between the modeled systematic error magnitude and systematic error as measured by the LIGO NCal during O3 from [33].

2.5 Overview of the NCal system for O4

The goals of the NCal system for O4 were:

- To reach a total uncertainty of the system below one percent.
- To increase the frequency band compared to O3.
- To have continuous operation of the NCal system during the observing run.

Therefore, improvements were made on every aspect of the NCal system.

Given the upcoming sensitivity improvement of the Virgo detector for the following runs, as well as the much tighter requirements for the future 3G detectors, the O4 NCal system is an opportunity to study this new calibration technology. Consequently, when designing and building it, we did not limit ourselves to a predefined requirement, but did as best as we can, given the available time we had.

2.5.1 Geometry of the rotors

The geometry of the rotors has been simplified compared O3 with fully opened sectors and the removal of the rotor cavity covers. This was the opportunity to slightly increase the diameter and the thickness leading to an overall factor 2 on the amplitude of the injected signal. This should improve the accuracy of the geometrical description of the rotor since a simpler shape is easier to measure, leading to reduced uncertainties. The final geometry is shown as an isometric view in fig. 2.15 and as drawings with nominal radii, thickness and opening angle values in fig. 2.16. The detailed drawings of the rotors can be found in the technical notes [38, 39]. Let us remark that the rotors were initially designed with a 3 mm deep counterbore on a side (seen on right of fig. 2.16) foreseen to hold a cylindrical plate that will be machined as a counterweight. The geometry was later changed by adding a second counterbore on the other side (see fig. 2.15) for a second counterweight to improve the balancing as it will be discussed in section 5.1.

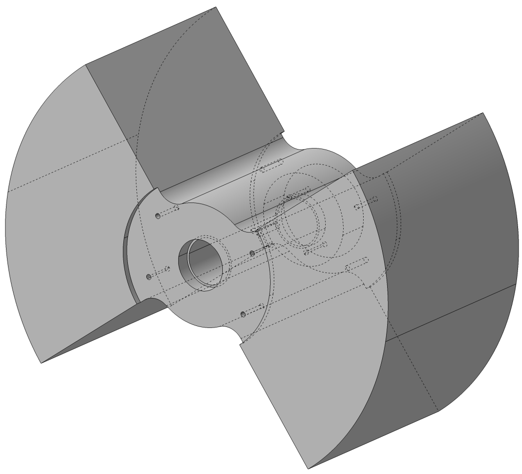

FIGURE 2.15: Isometric view of the updated O4 rotor geometry. The second counterbore seen in the back is only present in the latest rotor version.

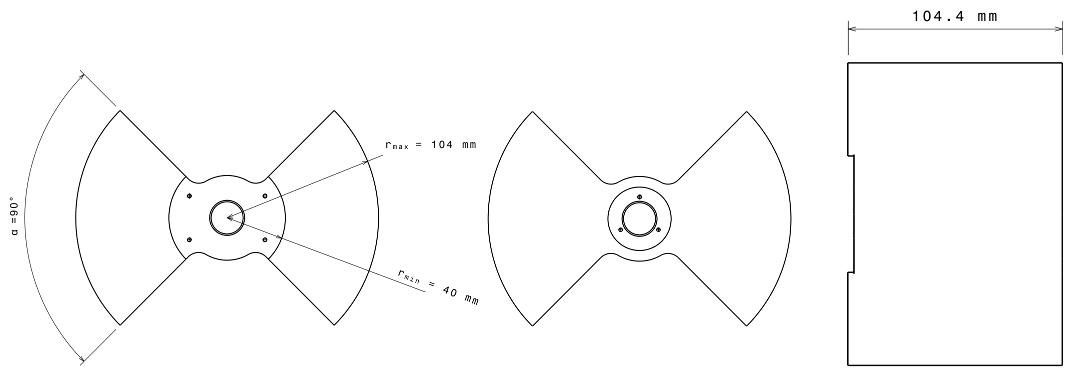

FIGURE 2.16: Drawings of the O4 rotor geometry with nominal values.

2.5.2 Material used for the rotors

It was initially foreseen that the O4 rotors would be machined using aluminum 7075-T6 as for the O3 NCal-200 [32, 37]. We use aluminum for the rotors due to its ease of machining, robustness, and low cost. Although denser materials will increase the gravitational signal, aluminum is adequate given the sensitivity achieved in the previous O3 run. Therefore, 9 rotors have been machined in aluminum 7075-T6 using two different blocks of material. But during the commissioning phase of the NCal system, a parasitic magnetic coupling between the NCal and the mirror was observed (see section 7.3.1 for more detailed discussions). Therefore eight additional rotors made of Polyvinyl Chloride (PVC) were produced.

2.5.3 Pairs of NCals around the mirror

As the distance between the NCal and the mirror was our main source of uncertainty for O3 [32], a better positioning of the NCal should allow us to lower this source of uncertainty and be more accurate on the predictions. However, as the mirror is inside a vacuum chamber, this is difficult to achieve in practice. The typical order of magnitude for the uncertainty on the mirror position is expected to be a few millimeters.

To limit the impact of positioning errors, the O4 NCal setup is equipped with pairs of rotors located on opposite sides of the mirror, and called North and South rotors. They could be used to measure the mirror location relative to the NCals, as shown during O2, or just by averaging the amplitudes of the injected signals at nearby frequencies, which removes at first order the mirror location uncertainty. This feature is shown in fig. 2.17a which presents the variation of the average strain as a function of the mirror position. Using a pair of opposite NCals (purple line) reduces by more than two orders of magnitude the uncertainty on the signal compared to a single NCal (blue line). A configuration of four NCals around the mirror was also proposed [40]. In our study, this four NCal configuration only reduces the uncertainty by a factor ~ 2 (red line). Figure 2.17b shows the variation of the strain around the theoretical mirror position centered in (0,0). For a mirror position known within 5 mm, the signal varies less than 0.02%.

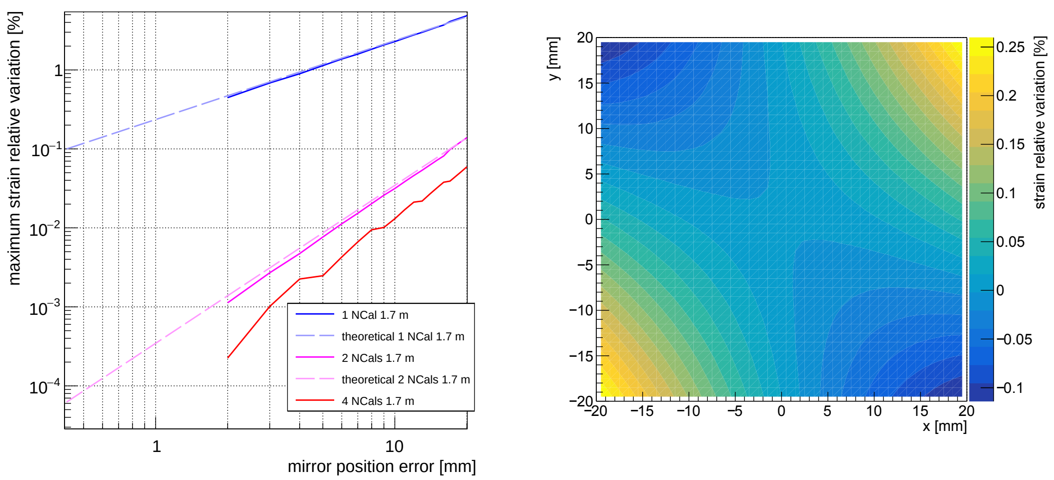

(A) (B)

FIGURE 2.17: (A) Maximum error in the injected amplitude as function of the error in mirror position, for one, two and four NCals setups. Each line connects about 30 points. (B) Relative variations of the averaged Near South and Near North NCal amplitudes as function of the mirror position. The coordinates are such that the North NCal is in the lower left corner and the South NCal in the upper right corner.

2.5.4 Adding a twist on the NCals

While studying the uncertainties of the NCal signal we investigate the effect of a rotor twist ψ around the vertical axis on the amplitude of the signal. Figure 2.18 is a top view of a twisted rotor (in red) compared to a non twisted rotor (in black) in the reference frame of the tower. The rotor is at angle ϕ with respect to the beam axis in the plane of the interferometer. The NCal system was initially designed for the rotors without twist as this effect was not studied before.

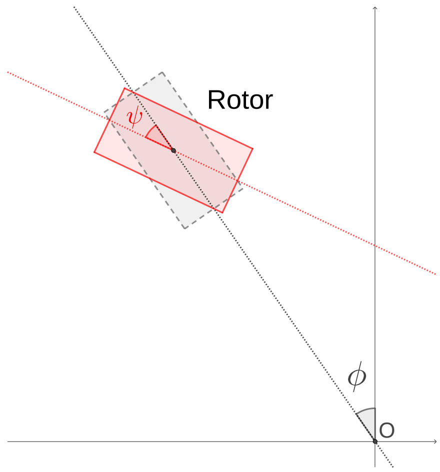

FIGURE 2.18: Top view of a rotor in the reference frame of the tower. The black rectangle shows a rotor without twist, the red one is the same rotor with a positive twist ψ. The rotor is at an angle ϕ from the beam axis. The mirror is centered on O.

Predicting the optimal rotor twist ψ in a point mass approximation

Considering a twist of the rotor in the eqs. (2.16) and (2.18) of the point mass approximation on the analytical form of the NCal strain and keeping only the second order terms at twice the rotor frequency, we have:

$$h(\phi, \psi) = \frac{G\rho_{rot}\, b\, sin(\alpha)(r_{max}^4 - r_{min}^4)}{32L\pi^2 f_{2rot}^2 d^4} \left(9\cos^2\psi\cos\phi + 6\cos\psi\sin\psi\sin\phi\right) \tag{2.29}$$

As shown in eq. (2.29) there is a coupling of the twist ψ and the angle ϕ of the rotor. Figure 2.19 left shows the optimal twist ψ_{max} to achieve a maximal strain signal as a function of ϕ. From this figure we computed that $h(\phi, \psi)$ is maximum for $\psi_{max} = 12.38°$ when $\phi = 34.7°$. This value has been checked using a point mass mirror in FROMAGE. The right plot of Figure 2.19 shows the variation of the signal for this optimal twist as a function of ϕ. If $\phi = 0°$ then the amplitude is maximum when the rotor is pointing toward the mirror with $\psi = 0°$. With $\phi = 34.7°$ at the optimal twist, the signal is 86% of this maximum signal.

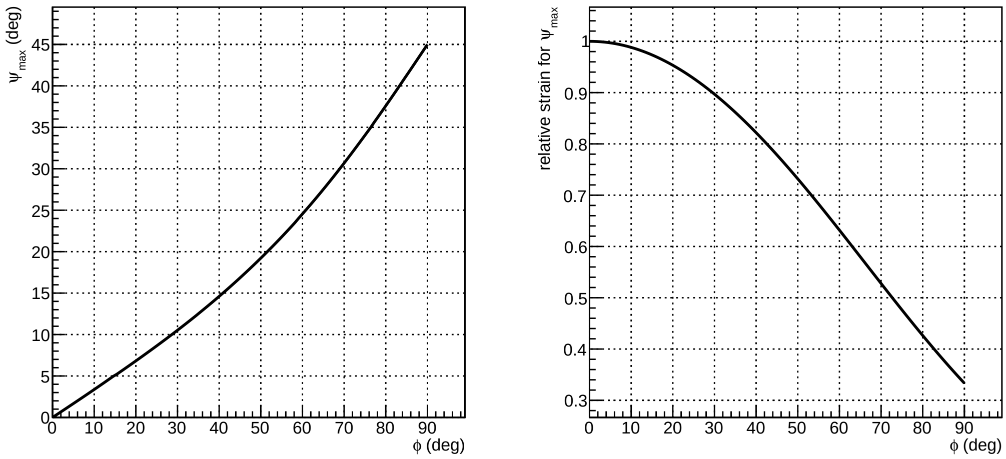

FIGURE 2.19: Left is the optimal twist ψ_{max} achieved for a maximal strain signal as a function of the angle ϕ. Right is the relative strain variation for the optimal twist ψ_{max} as a function of the angle ϕ.

Predicting the optimal rotor twist ψ using FROMAGE

Using FROMAGE v1r3 we can accurately compute the strain for an extanded rotor and mirror geometry at different angles ϕ and twists ψ. Figure 2.20 shows the NCal strain variations for a rotor at 1.7 m from the mirror normalized to the strain in $\psi = 0°$ and $\phi = 0°$. As expected from the analytical model, there is an optimal ψ value which maximizes the NCal strain when ϕ is different from 0.

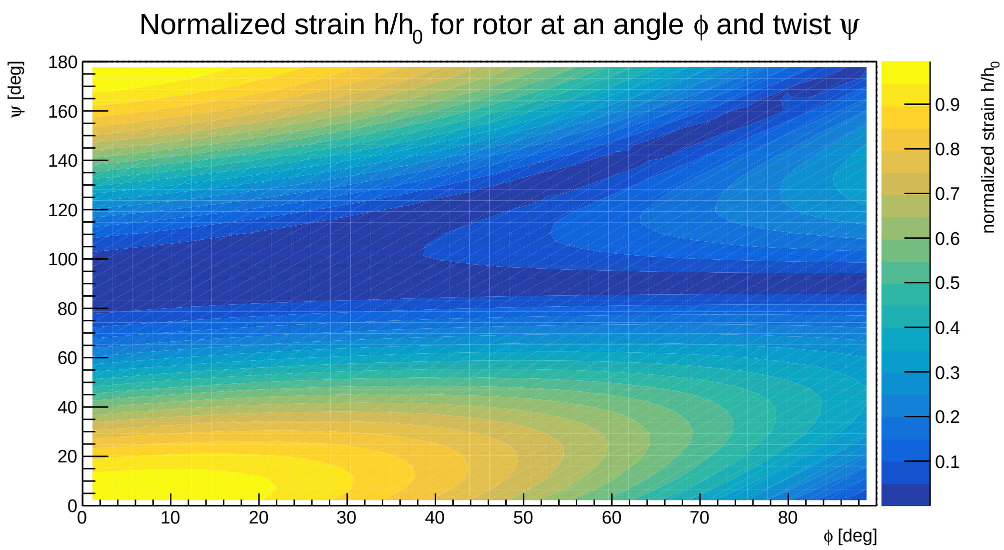

FIGURE 2.20: Normalized strain signal of a rotor at 1.7 m from the mirror for different angles ϕ and twists ψ. h_0 is the strain value for $\phi = 0°$ and $\psi = 0°$.

In fig. 2.21 we show the strain variations profiles at $\phi = 0°$ and $\phi = 34.7°$. The NCal strain is maximal for a twist $\psi = 12.1°$ when $\phi = 34.7°$. This value, computed with FROMAGE, is slightly different than the result computed with the analytical formula, thanks to the full modelling of the rotor and mirror. As a result, twisting the rotor by $\psi = 12.1°$ allows to reduce the associated uncertainty on the NCal strain as it is less sensitive to small twist variations. With this twist angle the signal improvement is 4.6%. In addition, the minimum of the strain for a twisted NCal is not at an angle $\phi = 90°$ but around $89.7°$. This is due to the finite size of the rotor and mirror taken into account in FROMAGE. It will be used when discussing parasitic couplings in section 7.3.1. The slope of the twisted rotor signal around the minimum is also given using a linear fit.

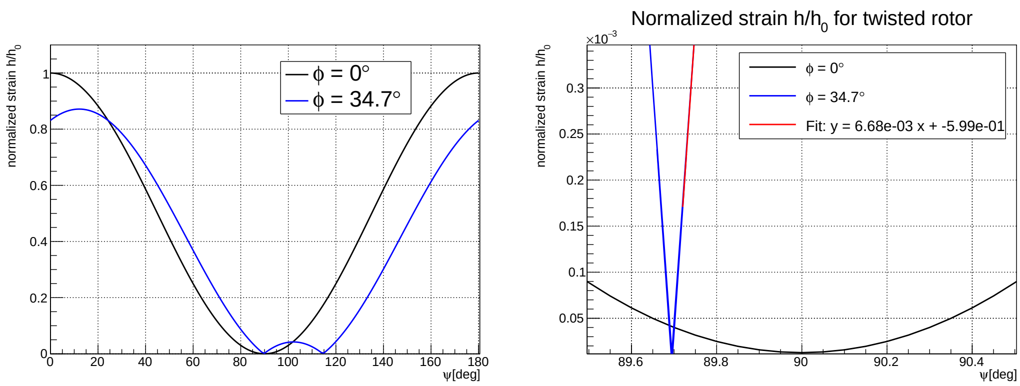

(A) (B)

FIGURE 2.21: For both graphs, normalized strain of a rotor at 1.7 m from the mirror for different twists ψ computed with FROMAGE. The black curve shows a rotor at $\phi = 0°$, the blue curve shows a rotor at $\phi = 34.7°$.(B) zooms around the minimum of (A) with a linear fit showing the slope of the twisted rotor signal.

Now that we understand the correlation between the twist and the rotor to beam axis angle we can check how the distance affects the signal of a twisted rotor (higher order terms neglected in eq. (2.16)). Figure 2.22 shows the maximum normalized signal obtained using FROMAGE for a rotor at $\phi = 34.7°$ and at distances of 1.3 m, 1.7 m, 2.1 m and 2.5 m which are the possible NCal O4 distances from the mirror. Using the fit results from fig. 2.22 we compute and report in table 2.3 the twist $\psi_{\max}$ associated to the maximum signal at $\phi = 34.7°$ for each NCal to mirror distance. Unlike eq. (2.29) which is only at the second order and does not show any distance dependancy, the computation with FROMAGE which includes the effects of all higher order terms predicts a small dependency with the distance. However, when the distance becomes large, the FROMAGE computation gets closer to the analytical result which is equivalent to a point like mirror.

Distance [m]	1.3	1.7	2.1	2.5	analytical
$\psi_{\max}$	11.89°	12.10°	12.20°	12.26°	12.38°

TABLE 2.3: Twist $\psi_{\max}$ for each NCal to mirror distance associated to the maximum signal at $\phi = 34.7°$.

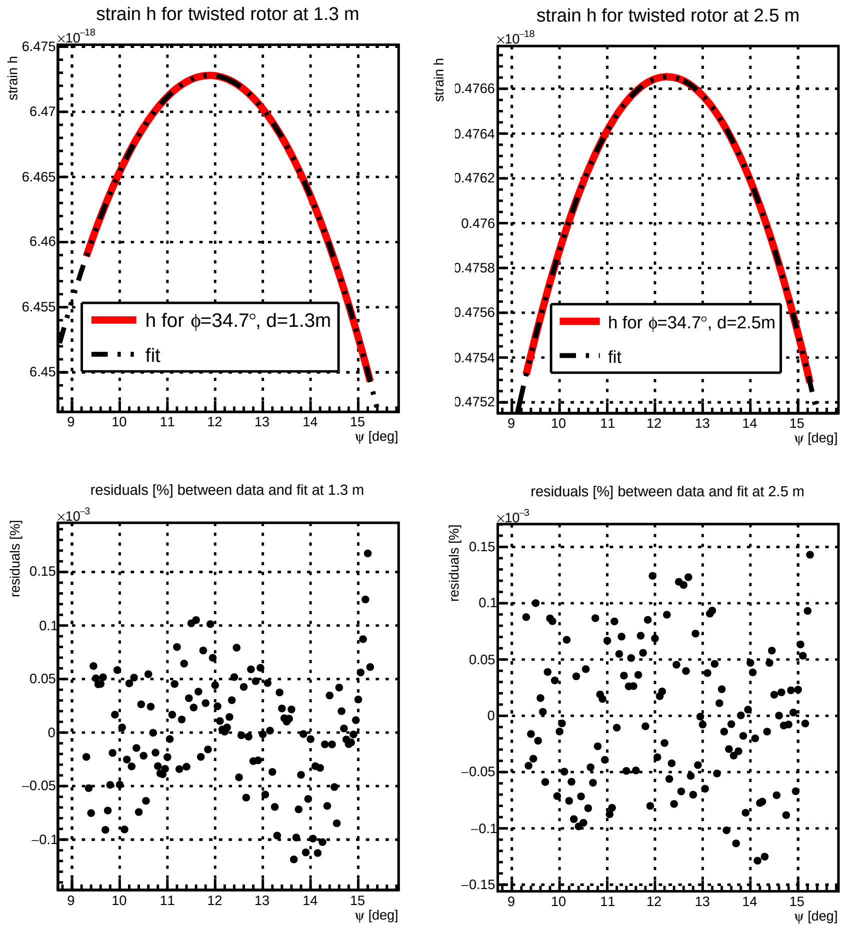

FIGURE 2.22: Top plots show the maximum signals for NCal to mirror distances of 1.3 m and 2.5 m at $\phi = 34.7°$, the red curves show the FROMAGE simulations and the black curve show quadratic fits. Bottom plots show the fit residuals which are usually smaller than 10^{-4}%.

Since it is much easier to use the same twist on every NCal we compute the amplitude variation when using a fixed ψ angle for all NCal distances. The optimal twist value would be $\psi = 12.1°$ for the NCal at 1.7 m which will be our reference distance. However for practical reasons, the implemented twist value was 12.0°. We then compute the amplitude variation for each NCal distance from fig. 2.22 around this twist, adding the alignment uncertainty $\delta\psi$, which is expected to be much lower than 0.1°. The results, in table 2.4, show that the relative amplitude deviation is of the order of 10^{-3}%. This confirms that we can use the same twist value for all rotors. This effect will be checked in chapter 6 with the actual position of the setups.

Distance [m]	1.3	1.7	2.1	2.5
Relative amplitude deviation [%]	1.67×10^{-3}	3.20×10^{-4}	9.68×10^{-4}	1.33×10^{-3}

TABLE 2.4: Relative amplitude deviations for different NCal to mirror distances at a fixed $\psi = 12.1° \pm \delta\psi = 0.1°$.

2.5.5 NCal system

As explained in the previous section, we aim to use several NCals around the mirror to minimize the uncertainty associated with its exact position in the vacuum chamber. Therefore, for O4, we placed two triplets of NCals around the North end mirror tower (see fig. 2.23). For each triplet, the NCal to mirror distance is the same. We then have a total of six NCals operating around the NE mirror. Each NCal is at an angle $\phi = 34.7°$ from the beam axis for mechanical clearance purposes and twisted by a misalignment angle $\psi = 12°$ towards the beam axis as discussed in section 2.5.4. They have been installed between spring 2023 and February 2024. At the end of the commissioning phase discussed in chapter 7, and therefore at the start of the O4b run, the configuration was the following: the far NCal triplet at a nominal distance of 2.1 m is made of aluminum rotors, the near NCal triplet at a nominal distance of 1.7 m is made of PVC rotors to limit the effect of magnetic field produced by aluminum rotors.

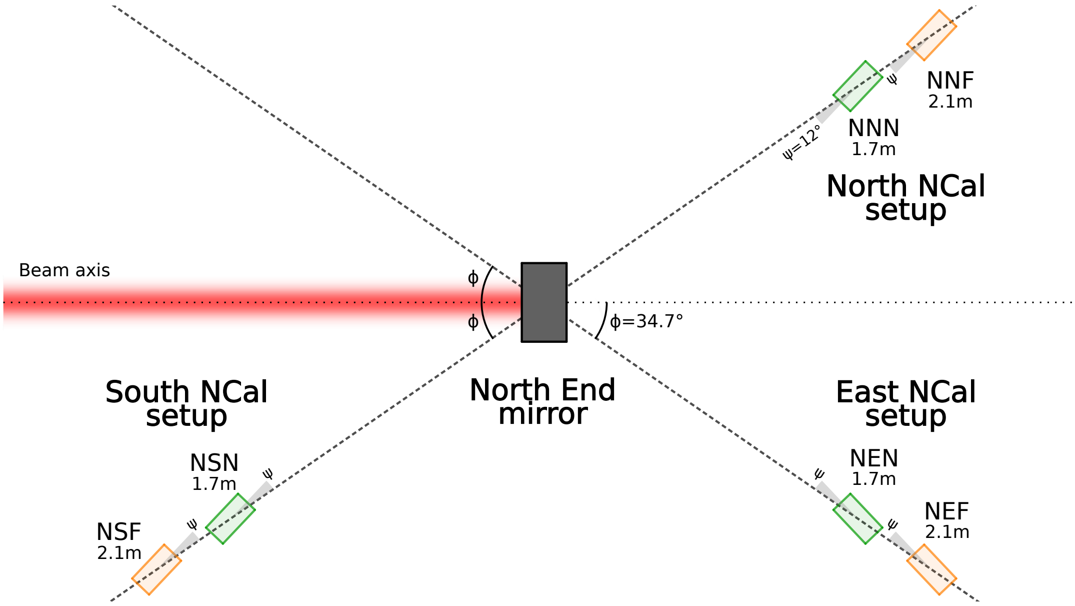

FIGURE 2.23: Layout of the Newtonian calibrator system at the start of O4b. Each rotor is identified by three letters: the main beam direction (N for north), the NCal location (N for north, S for south and E for east), and the triplet identifier (N for near and F for far). The green rotors (near) are made of PVC, while the orange rotors (far) are in aluminum.

2.5.6 NCal setup layout

Figure 2.24 shows a picture of a complete NCal setup placed on the North setup. A more detailed drawing of the NCal system around the NE tower is available at the end of the technical note [41]. Each NCal setup is suspended in six degrees of freedom by rubber springs mounted at both ends of two adjustable metal rods (1) held bellow a metal beam fixed on the tower scaffolding which does not touch the tower. These suspensions hold the vertical plate (2) where three NCals positions are available, 40 cm away from each other. Each suspended plate was equipped with the electronics to operate two out of three slots. The reference plate (5) is used to monitor the displacement of the setup and the acoustic noise over time, it is fixed at the base of the tower with a support (6). A pair of microphones is located on the reference plate to monitor the acoustic noise generated by the operating rotors and check their proper behavior.

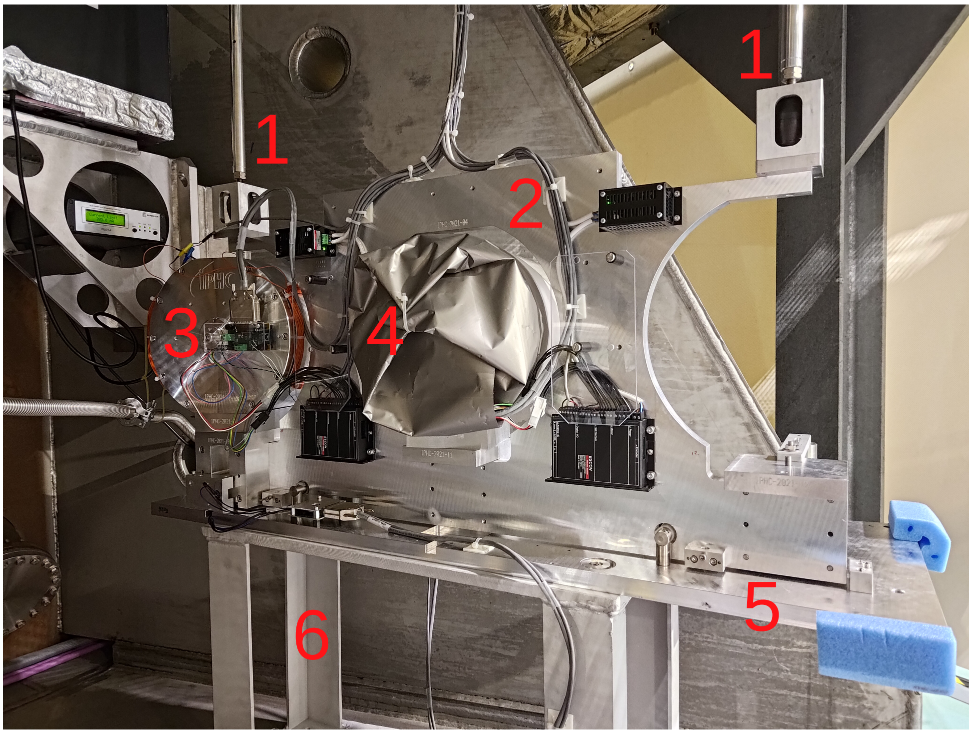

FIGURE 2.24: Picture of the North NCal setup at the start of O4b. From top to bottom of the picture, (1) the adjustable suspensions of the setup, (2) the suspended plate holding the near (3) and far (4) NCals, (5) the reference plate and (6) the support for the reference plate fixed at the base of the mirror tower.

2.5.7 NCal setup position monitoring

Six position sensors have been installed to monitor the displacement of the setups. A representation of a position sensor is shown in fig. 2.25, the left part is fixed on the reference plate (5) and provides real time data of the position of the magnet seen on the right which is fixed on the suspended plate (2). The position sensors used to monitor the displacement of the setups were characterized in [42]. It has been demonstrated that the position sensors reach a precision of better than 10% for setup displacement within 2 mm. As seen on fig. 2.26, where the data was collected for a month, with all rotors operating at a frequency around 18 Hz, the position sensors measurements show that the setup positions stayed within 0.3 mm along the mirror axis and sideways (left and middle plots). Therefore, the associated uncertainty from the position sensors on the NCal position in the plane of the interferometer is expected to be 0.03 mm.

The following sign convention was chosen for the position sensors:

- Axial: "+" moving away from the mirror
- Lateral: "+" clockwise seen from above, or similarly:
  NN: "+" moving away from the rib
  NE: "+" moving toward the rib
  NS: "+" moving away from the rib

- Vertical: "+" moving upward

where the rib is a part of the tower structure and can be seen in the background of fig. 2.24, four ribs are located around the vacuum chamber.

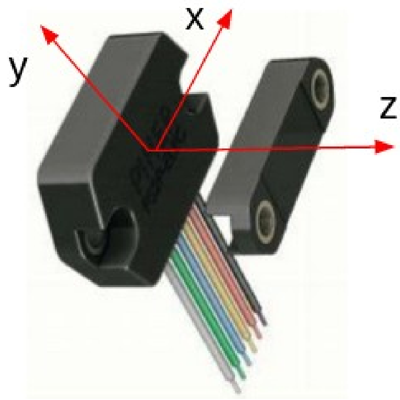

FIGURE 2.25: View of a position sensor and cartesian coordinates used in the study from [42].

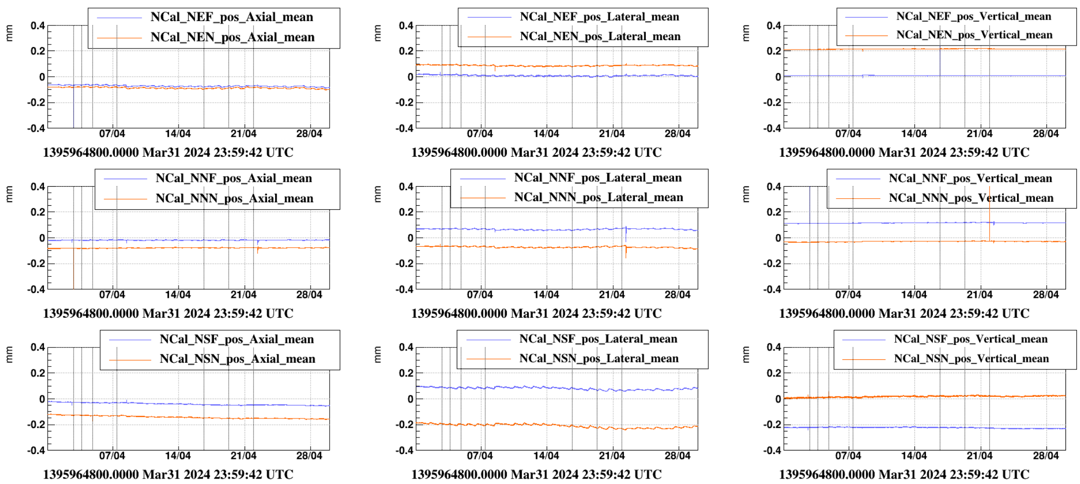

FIGURE 2.26: Position sensors measurements of each suspended setups for a month. From top to bottom, East, North and South setup. Left is the axial value, middle is the lateral value and right is the vertical value. A positive axial offset means away from the mirror. A positive vertical offset means away from the ground. A positive lateral offset means away from the rib for the North and South setup but towards the rib for the East setup.

Figure 2.27 shows the spectrum of the position sensors readout in the case of the NCals not operating (top plots) and operating at around 18 Hz (bottom plots). The lateral pendulum first resonance is around 0.6 Hz. The axial first resonance is around 0.8 Hz. The vertical resonance is not visible due to the poor quality factor of the rubber springs. The 18 Hz rotors lines and their harmonics can be seen on the bottom plots. The sensors are limited to 10^{-4} mm/$\sqrt{\text{Hz}}$ above 1 Hz.

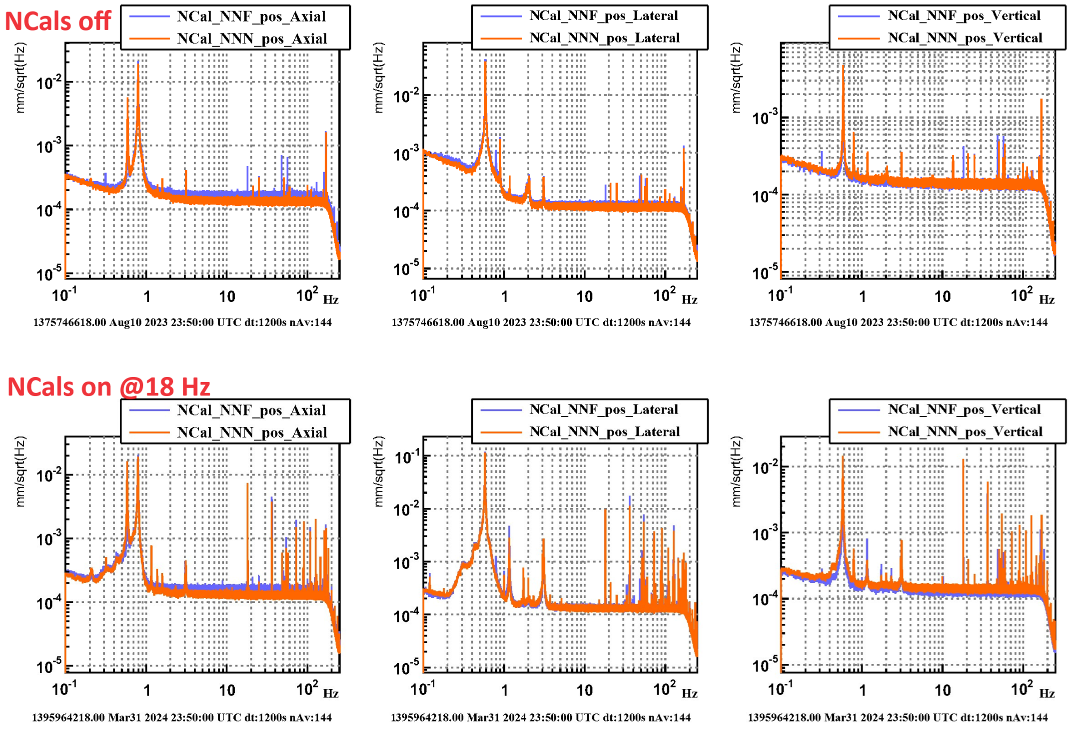

FIGURE 2.27: Spectrum of the position sensors placed on the East reference plate. From left to right, axial, lateral and vertical readouts. Top plots show when the NCals were not operating. Bottom plots show when the NCals were operating at 18 Hz. A day of data is represented in both cases.

2.5.8 Test setup at IPHC

A test configuration at IPHC was installed to replicate a NCal setup. A complete NCal setup was assembled at IPHC before starting the installation on Virgo. Then this configuration serves as a platform for submitting the rotors to various tests, including the task of rotor balancing. These tests help us to understand the NCals behavior under different conditions and validate their robustness. Figure 2.28 shows the IPHC NCal setup holding one NCal on the far slot of the suspended plate. This setup is equipped with the same real time control and data acquisition system as the installed setups around the NE Virgo mirror but on a local machine. Data are saved automatically for a few months. In the following chapters we will refer to this configuration as the IPHC NCal setup.

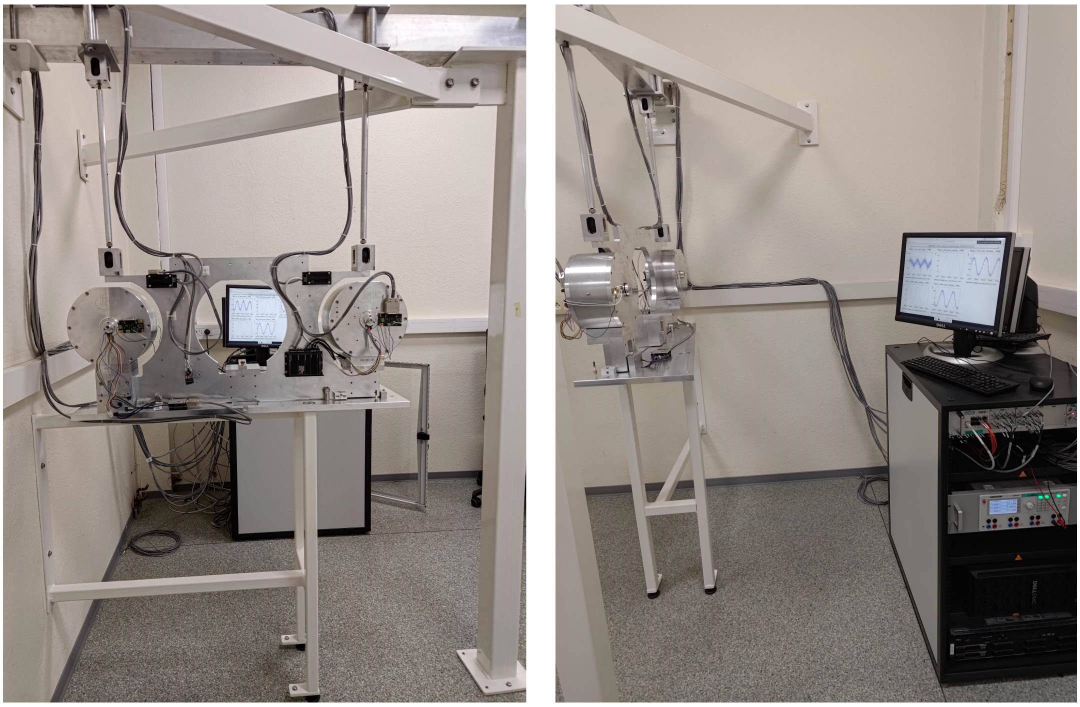

FIGURE 2.28: Left is a front picture of the NCal setup installed at IPHC, right is a back picture. The Near slot and Far slot are occupied by a NCal. Only the Far NCal is wired to the power supply and a motor controller.

Chapter 3

Density of the material used for the O4 NCal rotors

Contents

Introduction

In this chapter, we present the method used to measure the density of the NCal rotors material.

During the O3 tests, the rotor relative density uncertainty was taken from the literature. The corresponding uncertainty on the injected signal, 0.18% (see table 2.1 taken from [32]), was therefore fairly large. To reduce this uncertainty for O4, a careful set of measurement on the material used to machine the new rotors has been made. This measurement is simply the ratio between the mass, measured with a scale, and the volume of a sample, measured with metrology tools. To simplify the density measurements, blocks of material coming from the same longer cylinder have been machined in a simple cylindrical shape. These cylinders have later been machined into the O4 rotors. This process was accomplished with two different aluminum 7075 batches and for a PVC batch. The results for these respective materials will be discussed in the following sections.

3.1 Measurement tools used

The measurement tools used to measure the cylinders and determine their density are:

- A weighting scale located in the metrology room at IPHC, the model is a KFB 36K0.1 with an uncertainty of ± 0.3 g.
- A first measuring column (labeled as Column 1) located in the metrology room at IPHC. The model is a Garant 44 5350_600 HC1 with an uncertainty of 1.8+(L/600) µm at 95% CL (L is the measured length in mm).
- A second measuring column (labeled as Column 2) located in the mechanical workshop at IPHC. The model is a MAHR CX1 with an uncertainty of 2+(L/600) µm at 95% CL.
- A vernier caliper, the model is a TESA-CAL IP67 with a precision of 20 µm at 95% CL.

Steel reference blocks of 100.000 mm and 90.000 mm were used to check the accuracy of the measuring column. The observed standard deviation from the nominal values is of the order of the uncertainty of the measuring columns. The vernier caliper, which has an uncertainty eight times larger than the columns, has been used to check that no big mistake was made using the columns.

3.2 Measurement method of the rotor material density

This part describes the method used to compute the material density. This is done on simple cylinders which could be easily measured before machining them into rotors. The formula used to compute the density ρ of a cylinder is given as:

$$\rho = \frac{m}{\pi h(D^2/4)} \tag{3.1}$$

with D the diameter of the cylinder, h its height and m its mass.

Figure 3.1 shows an outline of the faces and side of the cylinders with each measurement points shown as colored dots. There is a total of 40 points on each cylinder to determine the volume. Points on one face are mirrored on the opposite face meaning for instance that "x_u" point on face up is associated to "x_d" on face down.

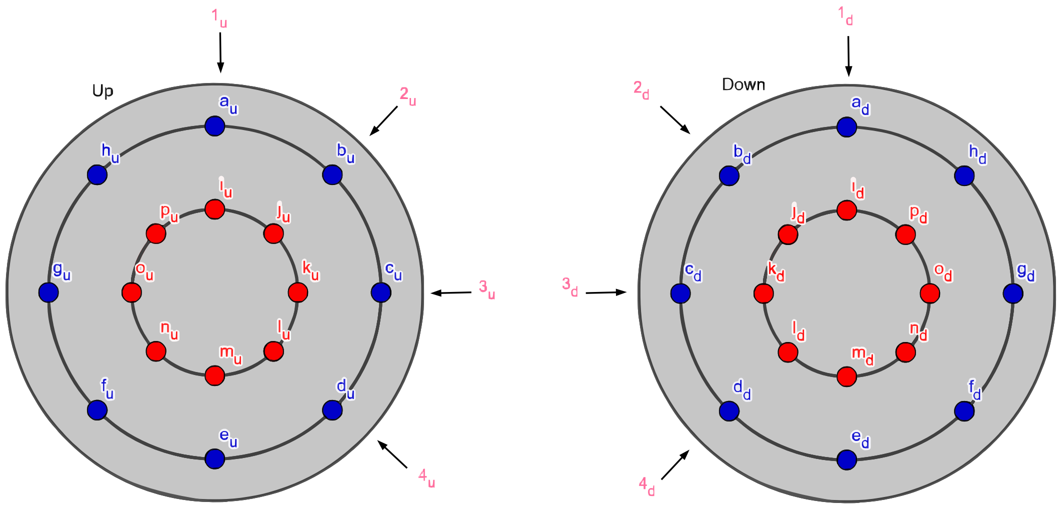

FIGURE 3.1: Outline of the faces and side of the cylinder, colored dots represent where the height measures are taken and arrows represent the diameter measures on each side. Left is face up, right is face down. The radius of the red inner points is r_{red}=44 mm and the radius of the blue outer points is r_{blue}=86 mm.

In fig. 3.1 we notice that the inner points (red colored points) are closer to each other than the outer points (blue colored points), the circle described by the outer points is twice larger than the inner circle. To not bias the mean height we will then apply a weight of 0.5 on the interior points when computing the mean height.

The mass of each cylinders was determined through several measurements using the weighting scale introduced in the beginning of this chapter.

3.3 Density of the Aluminum 7075

Figure 3.2 shows the first set of four aluminum cylinders machined. The cylinders have been machined to be 209 mm of diameter and 120 mm of height.

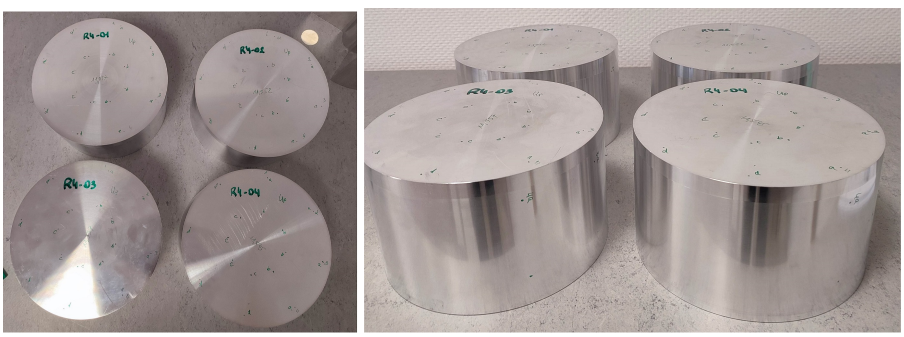

FIGURE 3.2: Aluminum cylinders machined. Left is a top view and right is a side view.

3.3.1 Raw density measurements

After machining the cylinders are not perfect. Tables 3.1 to 3.4 show the measurements and computed density made on each cylinder using the measuring columns and the scale. For each cylinder, three set of measurements have been performed on three different days. The yellow row shows the computed density (with weighted inner points) of the cylinders using the mean values for diameter and height and the mass measured. The mean density will be discussed later after taking into account thermal effects.

Parameter	15-12-21		16-12-21		04-01-22	
	Column 1	Column 2	Column 1	Column 2	Column 1	Column 2
Mean diameter D [mm]	209.047	209.045	209.045	209.045	209.044	209.043
Mean height h [mm]	119.916	119.916	119.915	119.916	119.913	119.914
Mass m [kg]	11.5578		11.5579		11.5583	
Density ρ [kg.m^{-3}]	2808.16	2808.21	2808.25	2808.24	2808.42	2808.44

TABLE 3.1: Measurements made on R4-01.

Parameter	16-12-21		04-01-22		18-01-22	
	Column 1	Column 2	Column 1	Column 2	Column 1	Column 2
Mean diameter D [mm]	208.986	208.986	208.984	208.983	208.980	208.983
Mean height h [mm]	119.916	119.917	119.914	119.916	119.913	119.917
Mass m [kg]	11.5521		11.5523		11.5522	
Density ρ [kg.m^{-3}]	2808.39	2808.38	2808.54	2808.53	2808.66	2808.49

TABLE 3.2: Measurements made on R4-02.

Parameter	15-12-21		16-12-21		04-01-22	
	Column 1	Column 2	Column 1	Column 2	Column 1	Column 2
Mean diameter D [mm]	209.023	209.021	209.022	209.022	209.020	209.019
Mean height h [mm]	119.936	119.936	119.935	119.935	119.934	119.935
Mass m [kg]	11.5580		11.5580		11.5583	
Density ρ [kg.m^{-3}]	2808.38	2808.43	2808.44	2808.42	2808.57	2808.60

TABLE 3.3: Measurements made on R4-03.

Parameter	15-12-21		16-12-21		04-01-22	
	Column 1	Column 2	Column 1	Column 2	Column 1	Column 2
Mean diameter D [mm]	208.985	208.985	208.985	208.985	208.984	208.982
Mean height h [mm]	119.858	119.858	119.856	119.858	119.856	119.857
Mass m [kg]	11.5459		11.5458		11.5464	
Density ρ [kg.m^{-3}]	2808.28	2808.29	2808.30	2808.26	2808.48	2808.50

TABLE 3.4: Measurements made on R4-04.

3.3.2 Uncertainties from the measuring tools

To compute the relative density uncertainty coming from the measuring tools we assume that the uncertainty on the mass and the distances are uncorrelated. Therefore we add the relative uncertainties quadratically. However the diameter and height values are correlated since we used the same measuring tool. The relative density uncertainty is then computed using eq. (3.2).

$$\frac{\delta_\rho}{\rho} = \sqrt{\left(\frac{\delta_m}{m}\right)^2 + \left(\frac{2\delta_D}{D} + \frac{\delta_h}{h}\right)^2} \tag{3.2}$$

with:

- δ_D the uncertainty on the diameter being the precision of the column
- δ_h the uncertainty on the height being the precision of the column
- δ_m the uncertainty on the mass of the cylinder being the linearity of the scale

Table 3.5 shows the relative uncertainties on the measurements.

Relative uncertainty	Column 1	Column 2
δ_D/D	1.03×10^{-5}	1.12×10^{-5}
δ_h/h	1.67×10^{-5}	1.83×10^{-5}
δ_m/m	2.60×10^{-5}	
δ_ρ/ρ	4.6×10^{-5}	4.8×10^{-5}

TABLE 3.5: Relative uncertainties associated to the measurement tools.

3.3.3 Combining measurements

The measurements have been taken during five different days, the temperature and humidity of the room where the cylinders were stored are shown in table 3.6.

Parameter	15-12-21	16-12-21	17-12-21	04-01-22	18-01-22
Temperature [°C]	21.9	21.8	21.8	21.2	21.0
Humidity [%]	37.70	35.90	36.10	47.00	34.90

TABLE 3.6: Temperature and humidity during the measurements at IPHC.

Given the thermal expansion coefficient of the Aluminum 7075 equal to 23.6 µm.m^{-1}.K^{-1} the 0.9°C observed temperature variation will induce a 4.3 µm of deformation on the 20 cm diameter on the cylinders. This is more than our measurement uncertainty and therefore we should correct for this effect.

The densities have been computed using measurements made at different temperatures. We have to check if a normalization at a reference temperature will correct the deviations of computed densities. The reference temperature is chosen to be 23°C since the average temperature in the North end building of Virgo is 21.5°C and we expect the rotor to be operating at a slightly higher temperature.

Figure 3.3 shows the mean density as a function of the temperature. The circles correspond to densities at different temperatures while triangles correspond to those same densities normalized at a reference temperature of 23°C. As expected, the temperature dependance of the density follows the theoretical slope for the measurements (below 22°C).

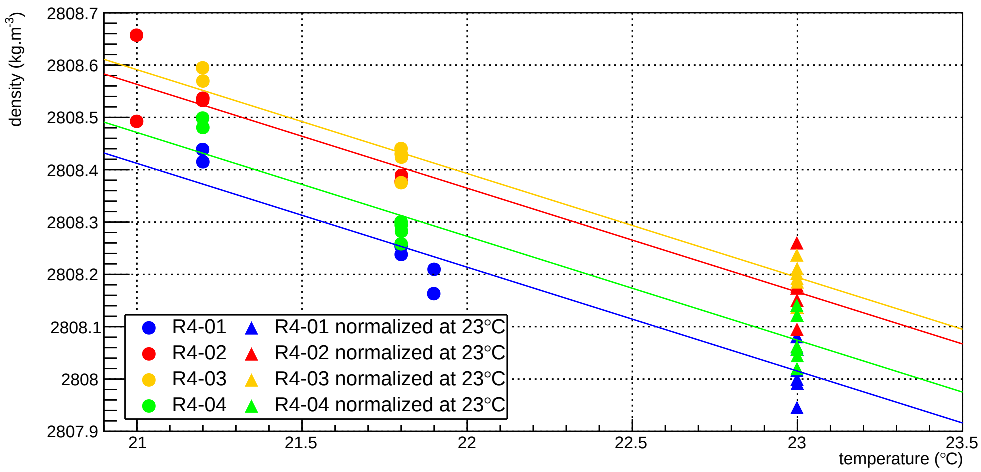

FIGURE 3.3: Correlation between the weighted density of the cylinders and the ambiant temperature. Each color corresponds to a cylinder and each line to its theoretical slope.

It is useful to check if the defects of the cylinders are responsible for the differences between the densities. Figure 3.4 shows a similar histogram as in fig. 3.3 with weighted values but removing the measurement points that were causing most of the shape defects for each cylinder (the eight worst points on the surface of the cylinder and the two worst points on the diameter). For this last figure, we notice that the density can change up to 0.5 kg.m^{-3} compared to fig. 3.3. This change is larger than the difference between cylinders which therefore are due to the difference in shape rather than density variation. Therefore the RMS of the rotor density observed in fig. 3.3 gives us the uncertainty due to the limitation of the number of points used to measure the shape of the cylinders: 0.1 kg.m^{-3}. This is of the same order as the uncertainty coming from the measuring tools (0.14 kg.m^{-3}). Overall the density uncertainty is the quadratic sum of these two numbers rounded to 0.2 kg.m^{-3}.

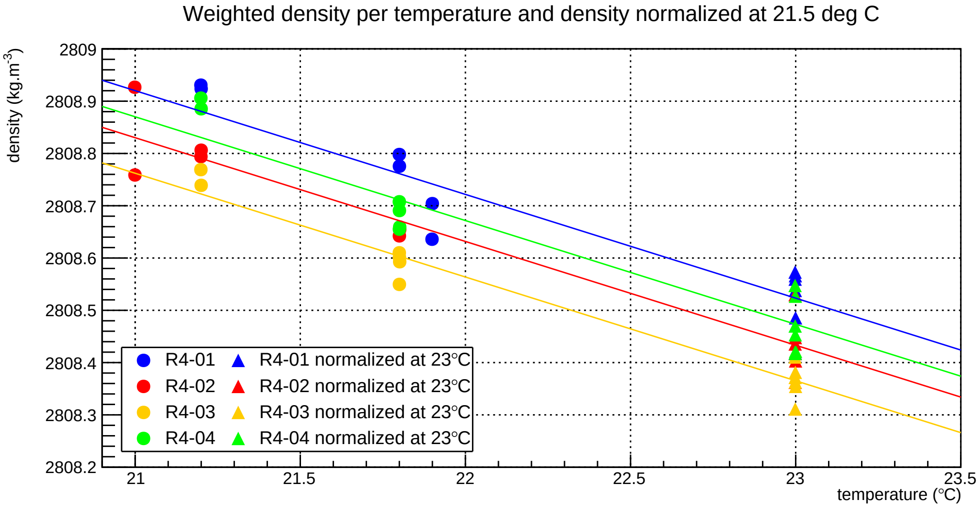

FIGURE 3.4: Correlation between the weighted density of the cylinders and the ambiant temperature excluding large deformations. Each color corresponds to a cylinder and each line to its theoretical slope.

3.3.4 Mean density of Aluminum 7075 at 23°C

First set of aluminum cylinders

Table 3.7 shows the mean density from the normalized data at 23°C for each cylinder of fig. 3.3. **This table gives a mean density of 2808.1 $\pm$ 0.2 kg.m^{-3} for the first set of aluminum 7075 cylinders at 23°C**. We reduced the density uncertainty by a factor 25 compared to the O3 value [32] which was just taken from the literature. This lowers its impact on the 2f signal from 0.18% to 0.007%. This could be further improved by making more measurement points of the cylinders geometry.

We must remember that these densities are measured in air. If the rotor is used under vacuum, the density should be increased by the air density (ρ_{air}=1.3 kg.m^{-3}).

Computation method	R4-01	R4-02	R4-03	R4-04
Density [kg.m^{-3}]	2808.0	2808.2	2808.2	2808.1

TABLE 3.7: Mean densities computed with weighted measures at a reference temperature of 23°C.

Another check has been made on the material that has been cut from a cylinder as shown in fig. 3.5. Both sectors have the same geometry and were cut from opposite sides of the cylinder and so they theorically have the same mass if the density is homogeneous in the material. The scale has given a mass of 1.1402 kg for both sectors meaning that the density is homogeneous at least at 10^{-4}.

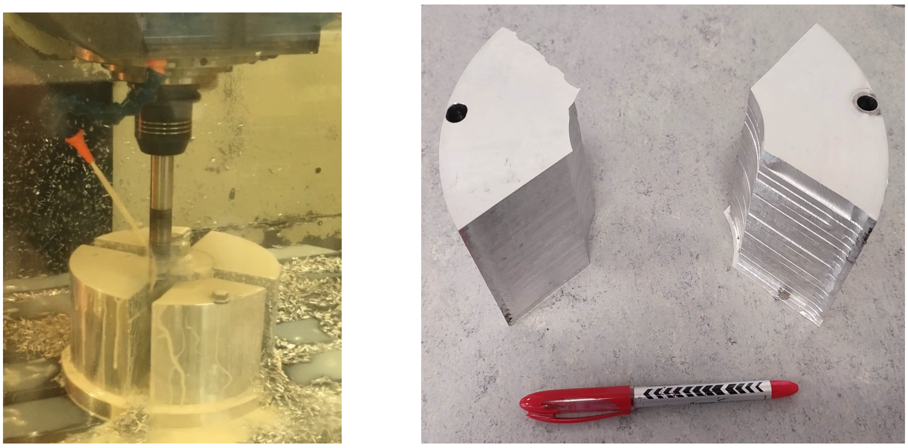

FIGURE 3.5: Material cut from one of the cylinders.

Second set of aluminum cylinders

For the second batch of aluminum, we measured the density of a reference cylinder labeled "R4-TEMOIN-2022" shown in fig. 3.6 using the same method.

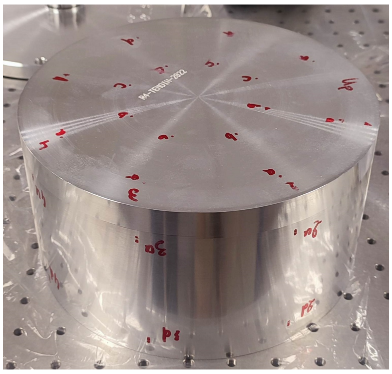

FIGURE 3.6: Picture of the up face and side of R4-TEMOIN-2022.

Measurements	Column 1 (21.2°C)	Column 2 (21.35°C)
Mean diameter D [mm]	210.028	210.023
Mean height h [mm]	109.864	109.865
Mass m [kg]	10.6998	
Density ρ (kg.m^{-3})	2811.0	2811.2
Density $\rho_{23°C}$ (kg.m^{-3})	2810.8	

TABLE 3.8: Measurements made at IPHC on R4-TEMOIN-2022. The mean density of the cylinder at 23°C is shown in yellow.

The density of the reference cylinder coming from the second aluminum 7075 cylinder block at 23°C is 2810.8 $\pm$ 0.2 kg.m^{-3}. This value was determined with one set of measurements with each measuring column as shown in table 3.8. We assumed that it is as homogeneous as the first cylinder block and therefore kept the same uncertainty value. This density is higher than for the first aluminum batch, by 10 times the measurement uncertainty. This could be due to small fluctuations of the aluminum alloy composition. It underlines the need of measuring the density of the material used to machine the rotors.

The reference cylinder was also used to check the consistency of the weighting scale, table 3.9 shows 5 measurements made on the reference cylinder more than one year later than the measurements made in table 3.8. The mean mass computed is 10.6992 kg giving a 0.6 g deviation from the value measured one year earlier. The dispersion of the measurements is of the order of $0.1 - 0.2$ g.

Scale measurements	1	2	3	4	5
Mass (kg)	10.6991	10.6993	10.6992	10.6994	10.6991

TABLE 3.9: Measurements made at IPHC on R4-TEMOIN-2022.

3.4 Density of PVC

This section describes the density measurements of the PVC. It follows the same method as for the aluminum rotors (see section 3.2). The same measuring tools were used as for the aluminum cylinders. Two sets of four cylinders were machined at IPHC from the same PVC block.

The technical data sheet of the PVC used is available at the end of the technical note [43].

3.4.1 Measurement of the four PVC cylinders

Figure 3.7 shows the four PVC cylinders machined and temporarily labeled 1, 2, 3 and 4 . The cylinders have been machined to be 211 mm of diameter and 114 mm of height. There is a total of 40 measurement points on each cylinder to determine the volume. In addition we measured the mass of each cylinder 4 times (turning back the cylinder upside down between each measure) and took the average value.

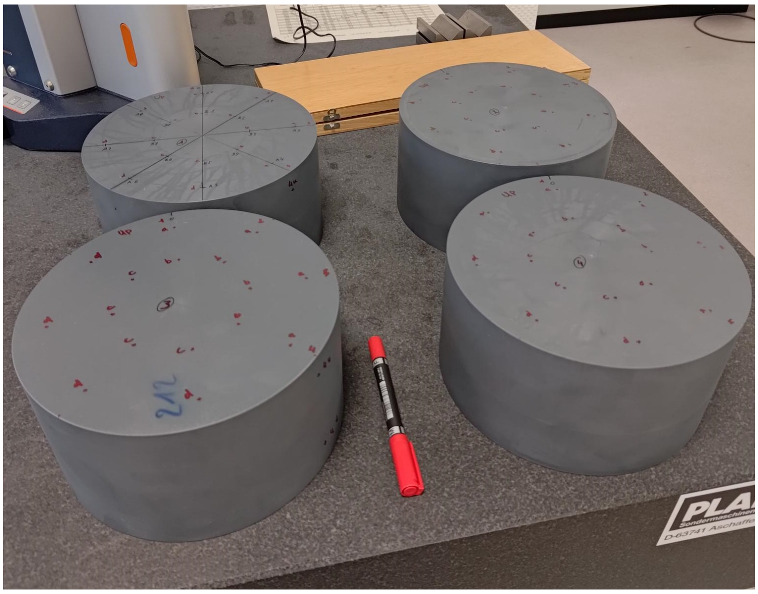

FIGURE 3.7: Picture of the four PVC cylinders machined at IPHC. The cylinders have been temporarily labeled 1, 2, 3 and 4.

As a side remark, one major concern with PVC was whether the machining of the material would produce uneven shapes. Table 3.10 shows the dispersion of the measurements made on the diameter and height of each cylinder. The dispersion is usually below the hundredth of a millimeter like the aluminum cylinders.

Parameter RMS	Cylinder 1	Cylinder 2	Cylinder 3	Cylinder 4
σ_D [µm]	4.9	15.4	15.3	9.8
σ_h [µm]	4.4	6.0	4.2	5.4

TABLE 3.10: RMS of the measurements made on the first set of PVC cylinders. Top row is for the diameter and bottom row is for the height.

3.4.2 Recalibration of the scale

To determine the mass of the cylinders we used the scale described in section 3.1. Since the PVC cylinders were produced almost two years after the purchase of the scale, the reference aluminum cylinder R4-TEMOIN-2022 (see fig. 3.6) was used to check the consistency of the scale. In September 2022 the measured mass was 10.6998 kg. In November 2023, a second set of measurements was made on this cylinder, the measured mass was 10.6992 kg or 0.6 g less than the previous year. In January 2024, when the first set of PVC rotors was machined, a third set of measurements gave 10.6983 kg or 0.9 g less than a few months earlier. But, between the second and third measurements, the scale was moved from the metrology room to another location for a few weeks then brought back. Therefore we decided to buy two reference weights from two different providers to check the scale.

In February 2024, we checked the scale calibration using the reference weights. Two 5 kg reference weights were used and are shown in fig. 3.8. The weight on the left of fig. 3.8 will be labeled test weight 1 (TW1) and the weight on the right will be labeled test weight 2 (TW2). The weights were given with a maximum tolerance of 0.25 g (with $k = 2$ i.e. 2σ), the calibration certificates are provided at the end of the technical note [43]. Since both weights come from different providers we assume that their calibration process is uncorrelated. When using them together, the uncertainty is then $0.25\sqrt{2} = 0.35$ g.

A set of 10 measurements was made on both weights (see table 3.11) and R4-TEMOIN-2022. The measurements on R4-TEMOIN-2022 gave an average value of 10.6983 kg with a RMS of 0.16 g. This value is compatible with the January 2024 measurement. The measurements on TW1 and TW2 gave a deviation of respectively -0.55 g and -0.38 g from the 5 kg theoretical value. If we consider a quadratic sum of the scale uncertainty (0.3 g) and the weight uncertainty (0.25 g) the 0.39 g total uncertainty barely covers the differences measured. When measuring both test weights at the same time (TW1 + TW2 in table 3.11) we observe an even larger -0.83 g deviation from the 10 kg theoretical value. It seems that for 5 kg the scale has an offset of about $(0.55 + 0.38)/2 = 0.47$ g. The measured mass of the PVC cylinders which weight about 5 kg, are therefore corrected (increased) by this amount when computing the density. We point out that the 0.9 g difference observed between 2022 and 2024 on R4-TEMOIN-2022 is compatible with the 0.83 g offset measured in last row of table 3.11 for a similar mass of about 10 kg. Therefore the measurements made on the aluminum cylinders in section 3.3 are correct and the offsets measured must be due to the aging and moving of the scale.

Object	Mean measurement [g]	RMS [g]	Difference from gauge [g]
TW1	4999.45	<0.1	-0.55
TW2	4999.62	<0.1	-0.38
TW1 + TW2	9999.17	0.2	-0.83

TABLE 3.11: Measurements made on both test weights TW1 and TW2. The TW1 + TW2 measurements were made with both test weights on the scale.

FIGURE 3.8: Reference weights used to calibrate the weighting scale. Left is from *Gram Precision*, right is from *AE Adam*.

3.4.3 Uncertainties for PVC density

The method to determine the uncertainty on the density of the PVC cylinders was the same as for the aluminum but using only column 1. Therefore the systematic part of the uncertainty is the same as eq. (3.2). The statistical part, for the aluminum, was taken from the dispersion of the densities measured. For PVC, we directly include the dispersion of the measurements (the maximum values from table 3.10) into a statistical part of the uncertainties. We chose to not divide by the square root of the number of measurement points to remain conservative. The statistical uncertainty on the density is then expressed in eq. (3.3).

$$\left(\frac{\delta_\rho}{\rho}\right)_{\text{stat}} = \sqrt{\left(\frac{2\sigma_D}{D}\right)^2 + \left(\frac{\sigma_h}{h}\right)^2} \tag{3.3}$$

The following parameters are used:

- δ_D the uncertainty on the diameter from the column 1 : 2.2×10^{-3} mm.
- σ_D the maximum RMS of the first row of table 3.10 : 1.54×10^{-2} mm.
- δ_h the uncertainty on the height from the column 1 : 2.0×10^{-3} mm.
- σ_h the maximum RMS of the last row of table 3.10 : 5.98×10^{-3} mm.
- δ_m the uncertainty on the mass of the cylinder. We still use the uncertainty of the scale : 0.3 g which was checked with the test weights as described in section 3.4.2.

Finally to compute the total uncertainty on the density we add quadratically the systematic and statistical uncertainty (eqs. (3.2) and (3.3)). Since the density is averaged over four cylinders, we divide the statistical uncertainty by the square root of four. The total uncertainty is then expressed in eq. (3.4).

$$\left(\frac{\delta_\rho}{\rho}\right)_{\mathrm{tot}} = \sqrt{\left(\frac{\delta_\rho}{\rho}\right)^2_{\mathrm{syst}} + \frac{1}{\sqrt{4}}\left(\frac{\delta_\rho}{\rho}\right)^2_{\mathrm{stat}}} \tag{3.4}$$

with $\left(\frac{\delta_\rho}{\rho}\right)_{\mathrm{syst}}$ defined by eq. (3.2).

Table 3.12 recaps the relative uncertainties on the measurements.

Relative uncertainty	Value
δ_m/m	5.22×10^{-5}
δ_D/D	1.90×10^{-5}
δ_h/h	2.63×10^{-5}
σ_D/D	7.30×10^{-5}
σ_h/h	5.25×10^{-5}
$(\delta_\rho/\rho)_{\mathrm{tot}}$	1.37×10^{-4}

TABLE 3.12: Relative uncertainties associated to the measurement tools.

3.4.4 Mean density of PVC at 23°C

First set of PVC cylinders

Table 3.13 shows the average measured values for the diameter, height and rescaled mass (see section 3.4.2) as well as the associated computed density for each cylinder. Since the measurements were taken in the metrology room at IPHC at a temperature of 21°C we must take into account the thermal expansion of the material. The material used is labeled as "PVC - U GREY" with a coefficient of linear thermal expansion of 80 µm/m/°C. This is taken into account when computing the density at the reference operating temperature of the rotors of 23°C (see last row of table 3.13).

Average value		Cylinder 1	Cylinder 2	Cylinder 3	Cylinder 4
D [mm]		211.040	211.047	211.029	211.034
h (weighted) [mm]		114.021	113.987	114.042	114.028
m_{rescaled} [kg]		5.7554	5.7535	5.7562	5.7554
ρ [kg.m^{-3}]	21°C	1443.0	1442.9	1443.1	1443.0
	23°C	1442.3	1442.2	1442.4	1442.3

TABLE 3.13: Average measurements made on the four PVC cylinders. From top to bottom: the diameter, the height, the mass and the density. The densities at 23°C are highlighted in yellow.

Using table 3.13 we compute the mean density of the PVC at 23°C with the associated uncertainty using last row of table 3.12 (rounded up to 0.2 kg.m^{-3}). The density of the material for the first set of O4 PVC rotors is then $\rho_{\mathrm{PVC}} = 1442.3 \pm 0.2$ kg.m^{-3}.

Second set of PVC cylinders

A second set of four PVC cylinders was machined three months later to produce a new set of rotors. The cylinders have been labeled R4-14, R4-15, R4-16 and R4-17. We determined its density following a similar method as the first set of PVC cylinders. The measuring tools used and their associated uncertainty are the same as for the first set of PVC cylinders. A series of 40 measurement was made on the thickness and diameter of each cylinder with the RMS of the measured values shown in table 3.14.

Parameter RMS	R4-14	R4-15	R4-16	R4-17
σ_D [µm]	10.9	9.4	13.7	20.6
σ_h [µm]	4.1	1.6	1.7	2.0

TABLE 3.14: Dispersion of the measurements made on the second set of PVC cylinders. Top row is the diameter and bottom row is the height.

To be more accurate we decided to change the scale correction with an improved value. This new scaling value is determined by fitting the mass difference to the gauge value of the reference masses (from table 3.15) using a linear function and extrapolating to the mass of each PVC cylinder.

Object	Mean measurement [g]	RMS [g]	Difference from gauge [g]
RW1	4999.22	<0.1	-0.78
RW2	4999.46	0.1	-0.54
RW1 + RW2	9998.82	0.1	-1.18

TABLE 3.15: Measurements made on both reference weights RW1 and RW2 at a room temperature of 18.0°C. The RW1 + RW2 measurements were made with both reference weights on the scale.

The rescaled mass m_{rescaled} is then expressed as :

$$m_{\text{rescaled}} = 1.04 \times 10^{-4} m + 0.14 \text{ g} \tag{3.5}$$

with m the average cylinder mass.

Average value		R4-14	R4-15	R4-16	R4-17
D [mm]		209.961	209.979	209.953	209.969
h (weighted) [mm]		106.032	106.038	106.015	106.023
m_{rescaled} from eq. (3.5) [kg]		5.3004	5.3016	5.2994	5.3009
ρ [kg.m^{-3}]	18.3°C	1443.8	1443.8	1443.9	1444.0
	23°C	1442.2	1442.2	1442.4	1442.3

TABLE 3.16: Average measurements made on the second set of four PVC cylinders. From top to bottom: the diameter, the height, the mass and the density. The densities at 23°C are highlighted in yellow.

Using table 3.16 we compute the mean density of the PVC at 23°C with the associated uncertainty using the method from section 3.4.3 (rounded up to 0.2 kg.m^{-3}). The density of the material for the second set of O4 PVC rotors is then $\rho_{\text{PVC}} = 1442.2 \pm 0.2$ kg.m^{-3}. This value is compatible with the density of the first set of PVC cylinders. It confirms that the two sets come from the same PVC batch.

Chapter 4

Predicting the signal emitted by the rotors

Contents

Introduction

In this chapter, we will discuss the geometry of the rotors machined from the cylinders discussed in chapter 3. We will start with the method used to get the geometrical parameters of the O4 rotors such as the thickness and radius. We then compare two parametrization models. The first model adopts a simplified approach, with averaged values for each parameter, while the second, the advanced model, incorporates multiple values per parameter. The advanced model will be used to compute with FROMAGE the gravitational signal emitted by a rotor. The last section presents the uncertainties on the injected signal coming from the rotor geometry.

4.1 Measurement tools used

The measurement tools used to determine the geometry of the rotors are:

- Column 1 discussed in section 3.1 with an uncertainty of 1.8+L/600 µm at 95% CL (L is the measured length in mm). The measuring column is operated on a metrology table. A total of 16 measurements were made to check the flatness of its surface. Their values range from 0 to 2 µm. The RMS is 0.9 µm.
- A video measuring microscope located in the metrology room at IPHC. The model is a "Garant MM2" given with an uncertainty of 2.9+L/100 µm at 95% CL.

4.2 Measuring the rotor geometry

In this section we study the geometry of the rotors.

Left and middle of fig. 4.1 shows pictures of both faces of the O4 rotor design. The rotors have been engraved with their serial number on a side and sandblasted on the other side as shown on the right picture of fig. 4.1. The sandblasting will be discussed in section 7.1.1.

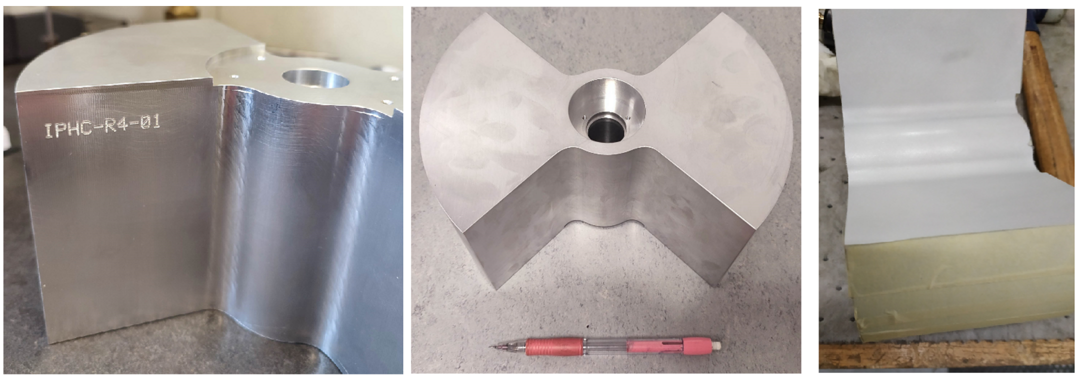

FIGURE 4.1: Left, up face with the engraving made on a side of the aluminum rotor R4-01. Middle, down face of the rotor. Right, other side of the rotor sandblasted.

4.2.1 Measurement method

To determine the geometry of the rotor, several measurement points were used to compute the thickness of the sectors as shown in fig. 4.2. The left sector of the rotor (labeled L in fig. 4.2) is set to be the sector with the serial number engraved. Since the strain on the mirror induced by the rotor will come from the sectors, we need to measure the thickness of both sectors as well as the outer and inner diameters. The central part is not affecting the signal because it is a full cylinder and its defects will have limited impact since they are at a small radius. The number of measured points has evolved with time:

- The first method (fig. 4.2a) uses 8*2*2 = 32 points for the outer thickness of the sector (red and blue colored points), 8 points for the inner thickness (orange colored points) and 8 points for the diameter (pink colored points). This method was used for the aluminum rotors R4-01 to R4-08.

- The second method (fig. 4.2b) uses 8*2*2 = 32 points for the outer thickness of the sector (red and blue colored points), 16 points for the inner thickness (orange colored points) and 12 points for the diameter (pink colored points). This method was used for the first batch of PVC rotors R4-10 to R4-13.

- The third method (fig. 4.2c) uses 17*2*2 = 68 points for the outer thickness of the sector (red and blue colored points), 16 points for the inner thickness (orange colored points) and 20 points for the diameter (pink colored points). This method was used for the second batch of PVC rotors R4-14 to R4-17.

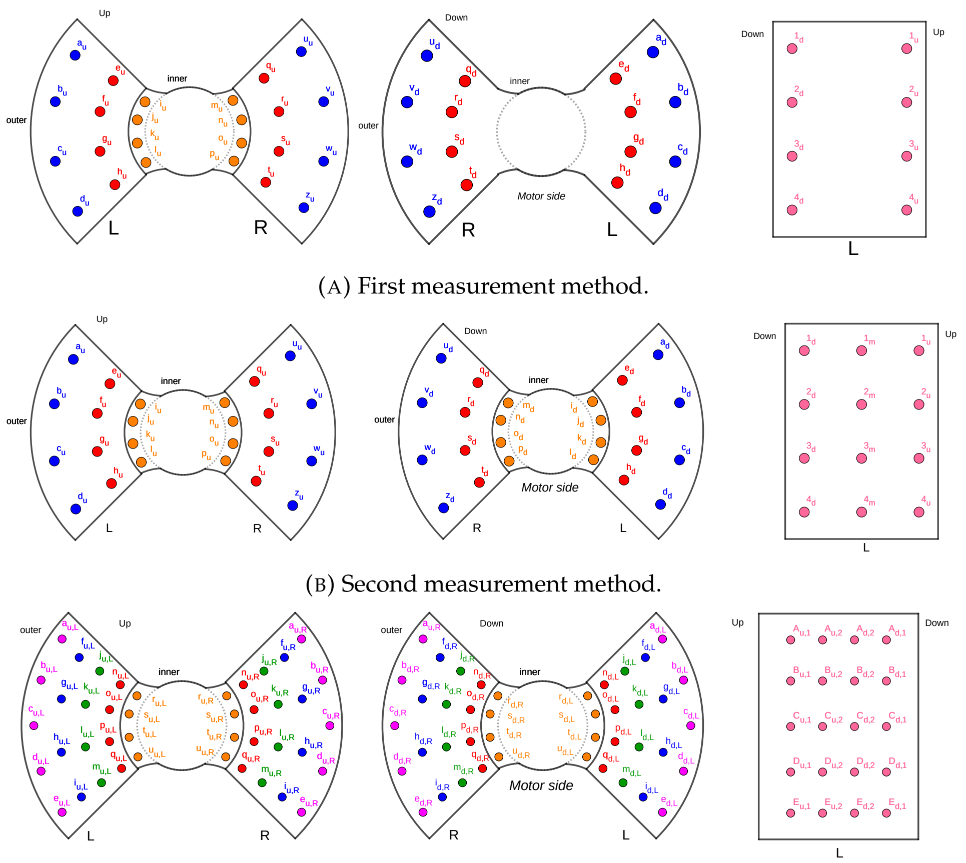

(A) First measurement method.

(B) Second measurement method.

(C) Third measurement method.

FIGURE 4.2: Outline of the faces of the rotor with the measurement points. (A) is the first set of points used for the aluminum rotors, (B) is the second set used for the first batch of PVC rotors and (C) is the third set used for the second batch of PVC rotors. For each figure, Left is face up, center is face down and right is the side view of the left sector. Sectors have been labeled L for left sector and R for right sector.

To measure the thickness and outer diameter of the rotor, the measuring column 1 was used. The vernier caliper (referenced in section 3.1 was used to check the inner diameter which was not accessible with the measuring column. We measured the opening angles of the sectors using the video measuring microscope.

For each rotor, a technical note, with the raw measurement points, was produced. These notes are available in the Virgo Technical Documentation System (TDS).

4.2.2 Getting the rotor thickness

The raw measured points are obtained when the rotor is on the metrology table. But since neither the rotor faces nor the metrology table are perfectly flat, we need to correct for the possible gap between the rotor and the metrology table. Since the metrology table is flatter than the rotor surface, the gap between the rotor and the table at a given point of the rotor's surface is mainly due to imperfections on the rotor's surface. To deduce this gap, measurements are taken on the top surface of the rotor (asking them to be on both sectors). By taking the highest points on this surface, a plane is obtained. By considering this tangent plane, the gap between the rotor and the table can be estimated, as the lower points on the rotor's face will create the gap when the highest points touch the table. This process is done for both faces of the rotor, allowing the thickness of the rotor to be determined. Using the raw measurements based on the method shown in fig. 4.2 we can compute a plane equation for each side of the rotor in cartesian coordinates. The coordinates of the 32 thickness measurement points represented in fig. 4.2a are shown in table 4.1 as x and y coordinates. As an exemple, the z coordinates shown in table 4.1 are the measured thicknesses of the aluminum rotor R4-07.

L sector	x [mm]	y [mm]	z (up) [mm]	z (down) [mm]	R sector	x [mm]	y [mm]	z (up) [mm]	z (down) [mm]
a	-73.18	48.89	104.349	104.353	q	46.55	31.11	104.348	104.355
b	-86.32	17.17	104.364	104.364	r	54.91	10.92	104.341	104.354
c	-86.32	-17.17	104.361	104.371	s	54.91	-10.92	104.343	104.356
d	-73.18	-48.89	104.346	104.373	t	46.55	-31.11	104.351	104.362
e	-46.55	31.11	104.357	104.371	u	73.18	48.89	104.337	104.331
f	-54.91	10.92	104.372	104.374	v	86.32	17.17	104.346	104.334
g	-54.91	-10.92	104.376	104.378	w	86.32	-17.17	104.353	104.340
h	-46.55	-31.11	104.371	104.381	z	73.18	-48.89	104.351	104.343

TABLE 4.1: Cartesian coordinates x and y of the points for each rotor R4-07 thickness z on each side of both L and R sectors.

Initially, the plane equations were computed using *Geogebra Classic*[1]. But using the highest points could result in negative gaps when the surface of the plane is convex. A new method was developped to ensure that all points remain below or on the plane defined by the previous requirements. However, there could be several planes fulfilling this requirement. For these cases we select the plane which minimizes the RMS of the gap values. As an exemple, for rotor R4-07 we obtain the plane equations eqs. (4.1) and (4.2) in cartesian coordinates. Using these equations the gap is computed and, as an example, reported in table 4.2. For this rotor, the maximum RMS of the gap for each sector is 11 µm, a typical value. The rotor thickness for each point is then computed by removing these gaps and converted to the reference temperature of 23°C. The value of each point is shown in table 4.3.

$$\text{Up plane equation} : z = -0.00017096x + -0.00018315y + 104.365 \text{ mm} \tag{4.1}$$

$$\text{Down plane equation} : z = -0.000171858x + -0.00016072y + 104.368 \text{ mm} \tag{4.2}$$

Measurement point	L sector		Measurement point	R sector	
	Up	Down		Up	Down
a	20	20	q	3	0
b	13	16	r	13	3
c	22	15	s	15	4
d	40	15	t	12	3
e	10	0	u	7	17
f	0	2	v	1	16
g	0	1	w	0	16
h	8	0	z	10	20

TABLE 4.2: The gap computed in µm on up and down sides of both sectors of R4-07.

[1]*Geogebra Classic* is a free online software used for geometry, algebra and other mathematical operations available at www.geogebra.org/classic

Measurement point	L sector	Measurement point	R sector
a	104.343	q	104.342
b	104.358	r	104.335
c	104.355	s	104.337
d	104.340	t	104.345
e	104.351	u	104.325
f	104.366	v	104.328
g	104.370	w	104.334
h	104.365	z	104.337

TABLE 4.3: Outer thickness in mm for each point of the L and R sectors of R4-07, at the reference temperature of 23°C.

4.2.3 Getting the rotor radius

Using the column we measured the diameter of a rotor on several points (given in fig. 4.2). We then computed the mean radius of the rotor for each level (up, middle or down). However, as the rotor is mounted on its axis which might be slightly off-centered, the local radius might be different from this mean value. Therefore, once the rotor was mounted on its axis, we used comparators to determine the deformation on both sectors and compute different radii values. The measurements were made using three comparators for a total of 5*3*2=30 points (the first and last points are near the edge of the sectors). These deformations were then added to the mean radius to get the radius of each measurement point.

This method was used for the aluminum rotors and the first batch of PVC ones. For the second batch of PVC rotors, we used the 40 points described in fig. 4.2c and replaced the comparators by the measuring column 1.

4.3 Parametrization of the rotors using a simple model

A simple model can be used to describe the geometry of the rotor and compute a first estimate of the signal emitted by the rotor. This model uses an average value of the measured thickness and radius.

4.3.1 Thickness

The 16 points listed in table 4.1 and shown in fig. 4.2 were used to compute the thickness of each sector. In this case we did not consider the inner points (orange points on fig. 4.2). We took the thickness as the mean value obtained using the method from section 4.2.2 at 23°C. Since we had a limited number of measurement points, to be conservative we took the thickness uncertainty as the RMS of the values to which we added linearly the metrology table uncertainty (0.9 µm) and the tool uncertainty (2.0 µm). The sector thickness of the simple O4 rotors geometry and uncertainties are shown in table 4.4.

Rotor	Thickness b at 23°C		
	mean value b [mm]	uncertainty δb [µm]	NCal 2f signal uncertainty [%]
R4-01	104.213	8	**0.008**
R4-02	104.292	21	**0.020**
R4-03	104.312	22	**0.021**
R4-04	104.347	18	**0.017**
R4-05	104.422	29	**0.027**
R4-06	104.340	14	**0.014**
R4-07	104.346	17	**0.016**
R4-08	104.236	14	**0.014**
R4-10	104.416	9	**0.009**
R4-11	104.409	11	**0.010**
R4-12	104.399	9	**0.009**
R4-13	104.416	9	**0.009**
R4-14	104.445	10	**0.010**
R4-15	104.422	7	**0.007**
R4-16	104.421	7	**0.007**
R4-17	104.415	7	**0.007**

TABLE 4.4: Thickness of the sectors from the simple O4 rotors geometry. The corresponding uncertainty on the gravitational signal at twice the rotor frequency is computed using the $\delta b/b$ derived from eq. (2.17).

4.3.2 Radius

For the radius we took the mean value obtained using the method from section 4.2.3 at 23°C. Like for the thickness we took the radius uncertainty as the linear sum of the RMS of the radius values and the tool uncertainty (2.2 µm). The sector radius of the simple O4 rotors geometry and uncertainties are shown in table 4.5.

Rotor	Radius r_{max} at 23°C		
	mean value r_{max} [mm]	uncertainty δr_{max} [µm]	NCal 2f signal uncertainty [%]
R4-01	103.996	12	**0.046**
R4-02	104.013	14	**0.053**
R4-03	104.019	13	**0.051**
R4-04	104.010	19	**0.072**
R4-05	103.964	22	**0.085**
R4-06	103.976	23	**0.088**
R4-07	103.983	23	**0.087**
R4-08	103.891	12	**0.046**
R4-10	103.839	5	**0.020**
R4-11	103.688	12	**0.046**
R4-12	103.912	12	**0.045**
R4-13	103.899	8	**0.032**
R4-14	104.068	15	**0.057**
R4-15	104.085	8	**0.040**
R4-16	*not yet assembled*		
R4-17	*not yet assembled*		

TABLE 4.5: Radius of the sectors from the simple O4 rotors geometry. The corresponding uncertainty on the gravitational signal at twice the rotor frequency is computed using the $4\delta r_{max}/r_{max}$ derived from eq. (2.17).

4.3.3 Simple rotor geometry in FROMAGE

The geometry used to describe the aluminum rotors as a simple model is represented in fig. 4.3a. Figure 4.3b shows the simple geometry used to describe the more recent PVC rotors. This second simple geometry takes into account the space for the counterweights on each side of the rotor as seen in fig. 2.15. Each counterbore is 3 mm thick and 40 mm of radius wide. For aluminum rotors, the signal variation induced by the presence of a counterweight counterbore in the simple model is 0.043%. For PVC rotors with two counterweight spacings, the value is 0.089%. Therefore, it was decided later to include the counterbores in the simple model described in the following section.

Using FROMAGE we implement the average values computed using the methods described in sections 4.3.1 and 4.3.2 and compute the corresponding 2f signal. An exemple of a simple rotor geometry implementation in FROMAGE is shown in Appendix A.1. The results are reported in table 4.9 where they are compared to the advanced model.

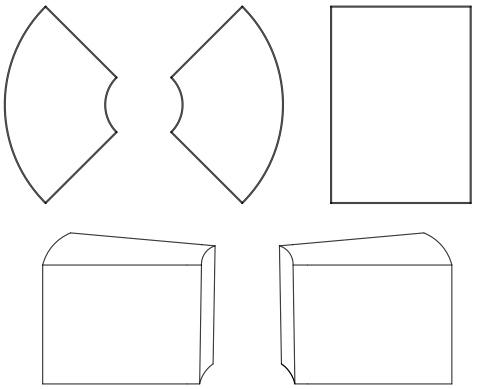

(A) Previous simple model geometry model with uniform sectors.

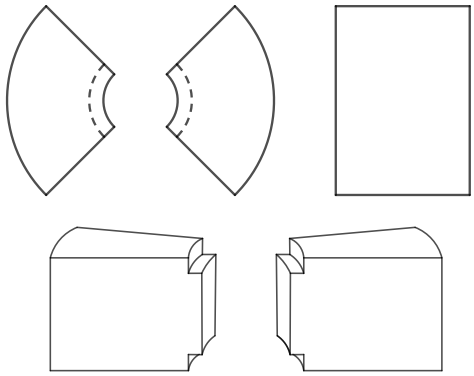

(B) New simple model geometry including the counterweight spacings.

FIGURE 4.3: (a) is the previously used simple geometry, (b) is the new version used for the PVC rotor. For each figure, left top is a top view, right top is a side view (external sector) and bottom is a tilted view of the rotor.

4.4 Parametrization of the rotors using an advanced model

A more advanced model includes the deformations on the surfaces of the sectors. It is expected to have a better accuracy and will be used to study the impacts and the defects of the rotor geometry.

4.4.1 Getting the thicknesses

Each measurement shown in fig. 4.2 can be considered as a sub-sector with its own thickness. The uncertainty on this value is more complex to evaluate. For the simple model we took used the RMS of the measured values. This could be an overestimation of the uncertainty when there is an overall surface deformation like a slight non parallelism of the two rotor faces as it has been observed on some rotors. Therefore, for this advanced model with several sub-sectors, we used the maximum deviation relative to the plane for each sector (see section 4.2.2) to which we added linearly the uncertainty on the flatness of the measurement table (0.9 µm) as well as the measurement tool (2.0 µm). The sectors thickness of the advanced rotors geometry and uncertainties are shown in table 4.6.

Rotor	Thickness b at 23°C			
	mean value b left sector [mm]	mean value b right sector [mm]	uncertainty δb [μm]	NCal 2f signal uncertainty [%]
R4-01	104.217	104.210	6	**0.006**
R4-02	104.279	104.305	11	**0.011**
R4-03	104.300	104.324	82	**0.082**
R4-04	104.349	104.345	10	**0.010**
R4-05	104.441	104.404	55	**0.052**
R4-06	104.337	104.342	33	**0.032**
R4-07	104.356	104.335	14	**0.013**
R4-08	104.237	104.236	15	**0.014**
R4-10	104.416	104.415	9	**0.008**
R4-11	104.407	104.411	12	**0.011**
R4-12	104.400	104.399	11	**0.010**
R4-13	104.418	104.414	10	**0.010**
R4-14	104.444	104.441	11	**0.010**
R4-15	104.422	104.418	9	**0.008**
R4-16	104.419	104.419	8	**0.008**
R4-17	104.416	104.410	9	**0.009**

TABLE 4.6: Thickness of the sectors from the advanced O4 rotors geometry. The corresponding uncertainty on the gravitational signal at twice the rotor frequency is computed using the $\delta b/b$ derived from eq. (2.17).

4.4.2 Getting the radii

On figs. 4.2a and 4.2b we divided the external sectors in 4 sub-sectors for each sector (blue points). We convert the 30 points from section 4.2.3 to 24 points by averaging the two consecutive values and converting them to 23°C. On fig. 4.2c we divided the external sectors in 5 sub-sectors for each sector (blue points). We take the 30 points from section 4.2.3 at 23°C. Like for the thickness we use a linear sum of the maximum radii RMS for both sector and the tool uncertainty (2.4 μm). The sectors radius of the advanced O4 rotors geometry and uncertainties are shown in table 4.7.

Rotor	Radius r_{max} at 23°C			
	mean value r_{max} left sector [mm]	mean value r_{max} right sector [mm]	uncertainty δr_{max} [μm]	NCal 2f signal uncertainty [%]
R4-01	104.006	103.987	12	**0.046**
R4-02	104.017	104.016	10	**0.039**
R4-03	104.023	104.021	11	**0.040**
R4-04	104.010	104.016	14	**0.052**
R4-05	103.971	103.968	14	**0.055**
R4-06	103.985	103.978	14	**0.059**
R4-07	103.990	104.987	16	**0.055**
R4-08	103.901	103.882	12	**0.046**
R4-10	103.840	103.838	5	**0.018**
R4-11	103.690	103.686	10	**0.039**
R4-12	103.922	103.903	12	**0.046**
R4-13	103.896	103.903	8	**0.031**
R4-14	104.047	104.071	15	**0.057**
R4-15	104.089	104.081	10	**0.040**
R4-16	*not yet assembled*			
R4-17	*not yet assembled*			

TABLE 4.7: Radius of the sectors from the advanced O4 rotors geometry. The corresponding uncertainty on the gravitational signal at twice the rotor frequency is computed using the $4\delta r_{max}/r_{max}$ derived from eq. (2.17).

4.4.3 Chamfers on the rotor

The rotor has been machined with four chamfers on the inner radius as shown on fig. 4.4. The presence of the chamfers on the rotor induces a variation of about 0.009% on the signal at twice the rotor frequency. This effect will be taken into account in the advanced model described in section 4.4.5.

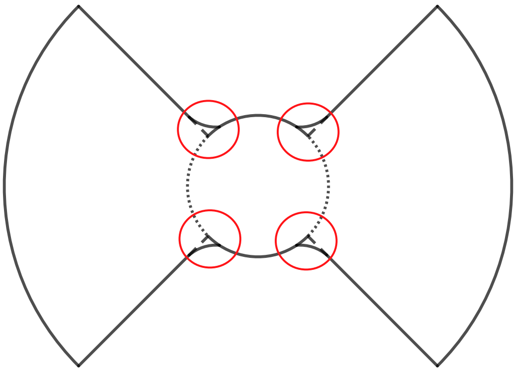

FIGURE 4.4: Outline of the rotor with the chamfers circled in red.

4.4.4 Opening angles and asymmetry of the sectors

The opening angles of the full and empty sectors have been measured for most rotors using the video microscope described in section 4.1. We measured four points to draw a line representing each side of the sectors and then the microscope interface computes the opening angle of each sector. The left sector (L) and the right sector (R) are defined in section 4.2.1. We define L-R the empty sector going clockwise from the left to the right sector and R-L the empty sector going clockwise from the right to the left sector when the "up" face is on the top. Since the microscope can only make the measurements on the up or down faces of the rotor, we took the average value between the up and down faces of each sector for the middle opening angle. The opening angles defects (corrected from the nominal $\pi/2$ value) for each rotor sector are shown in table 4.8. These measurements will be included in the advanced model described in section 4.4.5. The asymmetry offset between the L and R sector can be computed with a sum of the opening angles of the L-R, L/2 and R/2 sectors and compared to the theoretical value of π. For aluminum rotors, the largest mean opening angle defect is 0.89 mrad (R4-08) and the largest mean symmetry defects is 0.38 mrad (also R4-08). For PVC rotors, the largest mean opening angle defect is 2.01 mrad (R4-13) and the largest mean symmetry defects is 1.40 mrad (also R4-13).

Sector opening angle defect [mrad]												
Rotor	L			R			L-R			R-L		
	Up	Middle	Down	Up	Middle	Down	Up	Middle	Down	Up	Middle	Down
R4-01	0.10	0.38	0.67	0.25	0.36	0.48	-0.16	-0.30	-0.43	-0.22	-0.47	-0.73
R4-06	-0.08	0.11	0.29	0.12	0.11	0.11	0.08	0.05	0.03	-0.14	-0.29	-0.44
R4-07	0.04	-0.02	-0.07	-0.22	-0.14	-0.06	0.16	0.24	0.32	0.00	-0.11	-0.21
R4-08	0.35	0.45	0.55	0.68	0.79	0.89	-0.28	-0.82	-1.36	-0.76	-0.43	-0.10
R4-10	0.27	-0.34	-0.95	0.21	-0.33	-0.87	0.09	1.15	2.20	-0.58	-0.49	-0.40
R4-11	0.36	0.69	1.01	0.25	0.31	0.37	-0.10	0.65	1.40	-0.53	-1.66	-2.80
R4-12	0.22	0.48	0.74	0.17	0.61	1.04	-0.23	-0.43	-0.62	-0.18	-0.68	-1.17
R4-13	0.18	-0.25	-0.67	0.05	-0.98	-2.01	0.19	0.03	-0.14	-0.43	1.18	2.79
R4-14	0.21	0.30	0.40	0.18	0.20	0.22	-0.14	0.75	-0.37	-0.26	-0.27	-0.27
R4-15	0.22	0.20	0.19	0.31	0.33	0.34	-0.39	-0.22	-0.06	-0.16	-0.33	-0.49
R4-16	0.23	0.31	0.39	-0.10	-0.69	-1.28	0.01	0.59	1.16	-0.15	-0.21	-0.27
R4-17	0.31	0.43	0.55	0.16	0.44	0.73	0.18	-0.23	-0.65	-0.67	-0.65	-0.64

TABLE 4.8: Measured opening angles defect of the rotor sectors.

The uncertainty on the opening angle was computed with the method described by fig. 4.5. Using this method we found the uncertainty on the angle α and on the asymmetry η to be $(\alpha_+ - \alpha_-)/2 = 0.11$ mrad.

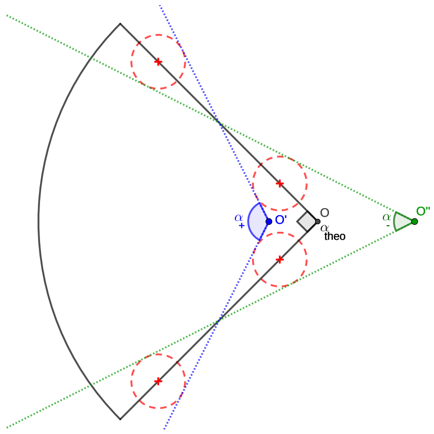

FIGURE 4.5: Method used to determine the uncertainty on the opening angles using the video microscope. The red points which are separated by $\sim$ 75 mm are used to determine the two lines for the opening angle computation. The red dotted circles represent their uncertainty ($\pm$ 4 µm). The theoretical angle α_{theo} is equal to $\pi/2$, α_+ and α_- are the maximum and minimum values of the angle. They differ from α by 4µm/(75 mm /2) $\sim$ 0.11 mrad. The proportions have been amplified for the visualization. This method combines the uncertainties in the most pessimistic way making them conservative.

4.4.5 Advanced rotor geometry in FROMAGE

The geometries used to describe the rotor as an advanced model are represented in fig. 4.6. The external parts of the sectors in fig. 4.6a are divided in 3 sub-sectors (4 in fig. 4.6b) corresponding to the measured radii. In addition we include the counterweights, the opening angles and asymmetry of the sectors. The screws and screw holes are not taken into account because they are not expected to generate a 2f signal thanks to their 180° pattern placement. An exemple of an advanced rotor geometry implementation in FROMAGE is shown in Appendix A.2.

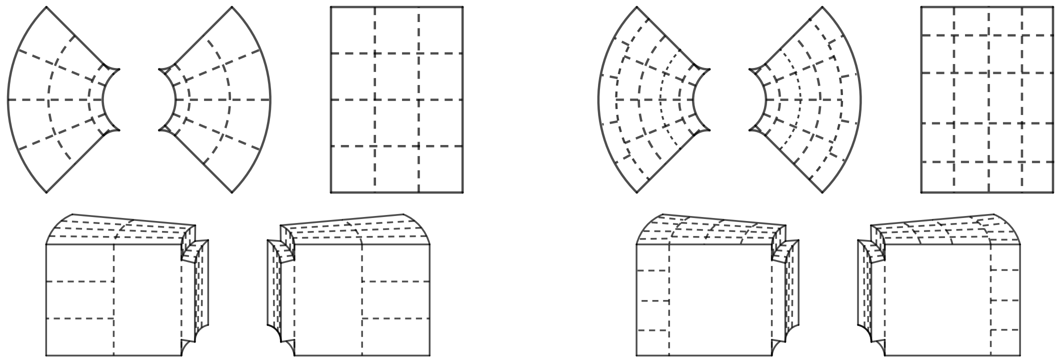

(A) First advanced model geometry.

(B) Second avanced model geometry.

FIGURE 4.6: Advanced model geometry used to describe the rotor. Top left is a front view, top right is a side view (external sub-sectors) and bottom is a tilted view of the sectors. Only the external sectors are divided in sub-sectors. The chamfers are visible on the inner radius. (A) is the geometry used for the first batch of PVC rotor, (B) is the version used for the second batch of PVC rotor. For each figure, left top is a top view, right top is a side view (external sector) and bottom is a tilted view of the rotor.

4.5 Signal emitted by the rotors

In this section we present the gravitational signal emitted by the rotors computed using the simple and advanced geometries in FROMAGE. These values, shown in table 4.9, are for the following position and orientation values: a distance $d = 1.7$ m to the mirror, an NCal to beam axis angle $\phi = 34.7°$ and a twist $\psi = 12°$. Their differences are well within the systematic uncertainties of the simple model.

Gravitational strain amplitude at twice the frequency $h\,[(2f)^2]$			
Rotor	simple model	advanced model	relative difference [%]
R4-01	$2.218\,16 \times 10^{-18}$	$2.217\,52 \times 10^{-18}$	0.029%
R4-02	$2.221\,30 \times 10^{-18}$	$2.220\,47 \times 10^{-18}$	0.037%
R4-03	$2.222\,24 \times 10^{-18}$	$2.221\,28 \times 10^{-18}$	0.043%
R4-04	$2.222\,21 \times 10^{-18}$	$2.221\,37 \times 10^{-18}$	0.038%
R4-05	$2.221\,97 \times 10^{-18}$	$2.221\,29 \times 10^{-18}$	0.031%
R4-06	$2.221\,27 \times 10^{-18}$	$2.221\,40 \times 10^{-18}$	0.006%
R4-07	$2.222\,00 \times 10^{-18}$	$2.221\,16 \times 10^{-18}$	0.038%
R4-08	$2.211\,76 \times 10^{-18}$	$2.210\,78 \times 10^{-18}$	0.044%
R4-10	$1.133\,56 \times 10^{-18}$	$1.133\,54 \times 10^{-18}$	0.002%
R4-11	$1.126\,85 \times 10^{-18}$	$1.126\,19 \times 10^{-18}$	0.059%
R4-12	$1.136\,59 \times 10^{-18}$	$1.136\,39 \times 10^{-18}$	0.018%
R4-13	$1.136\,20 \times 10^{-18}$	$1.136\,06 \times 10^{-18}$	0.012%
R4-14	$1.143\,90 \times 10^{-18}$	$1.143\,41 \times 10^{-18}$	0.043%
R4-15	$1.144\,41 \times 10^{-18}$	$1.143\,07 \times 10^{-18}$	0.117%
R4-16	*not yet assembled*		
R4-17	*not yet assembled*		

TABLE 4.9: Amplitude of the gravitational signal emitted by the rotors at twice the frequency for the simple and advanced models.

4.6 Rotor signal uncertainty

In this section we discuss the intrinsic NCal signal uncertainty, i.e., the uncertainty when the mirror location is perfectly known. Most of this uncertainty is coming from the rotor geometry already discussed in this chapter. We will first present the considered sources of uncertainty. As an example, the results are reported for the rotor R4-12 in table 4.12. Then we combine them to get the overall uncertainty per rotor. These overall uncertainties are reported in the last table of this chapter (table 4.13).

4.6.1 Uncertainty from the rotor geometry

In this part, we summarize the signal uncertainty from the geometrical parameters of the rotors.

Operating temperature of the rotors

As explained in section 3.3.3, the density has been computed anticipating an operating temperature of 23°C to account for a 1.5°C increase (due to the motor power dissipation) compared to the average building temperature (21.5°C). This has later been confirmed by measurements made with temperature sensors on the boxes. Figure 4.7 shows one month of data at the beginning of O4b with the NCals operating at their nominal frequency of 18 Hz with the temperatures within the expected boundaries. The gravitational strain h is therefore computed assuming the reference temperature $T_{\mathrm{ref}} = 23 \pm 1.5°\mathrm{C}$. Figure 4.8 shows one month of data with the NCals mostly turned off to compare the calibration of the sensors which is $\pm 0.2°\mathrm{C}$, much less than the 1.5° expected fluctuation.

Temperature variations will change rotor dimensions by a factor $(1 + C_T(T_{\mathrm{build}} - T_{\mathrm{ref}}))$. But the material density is reduced by a factor $(1 + C_T(T_{\mathrm{build}} - T_{\mathrm{ref}}))^3$. Therefore we could rewrite eq. (2.18) as:

$$h = h_0(1 + C_T(T_{\mathrm{build}} - T_{\mathrm{ref}}))^2 \approx h_0(1 + 2C_T(T_{\mathrm{build}} - T_{\mathrm{ref}})) \tag{4.3}$$

This lets us compute the relative uncertainty on the strain h due to the temperature variation:

$$\frac{dh}{h} = 2C_T(T_{\mathrm{build}} - T_{\mathrm{ref}}) \tag{4.4}$$

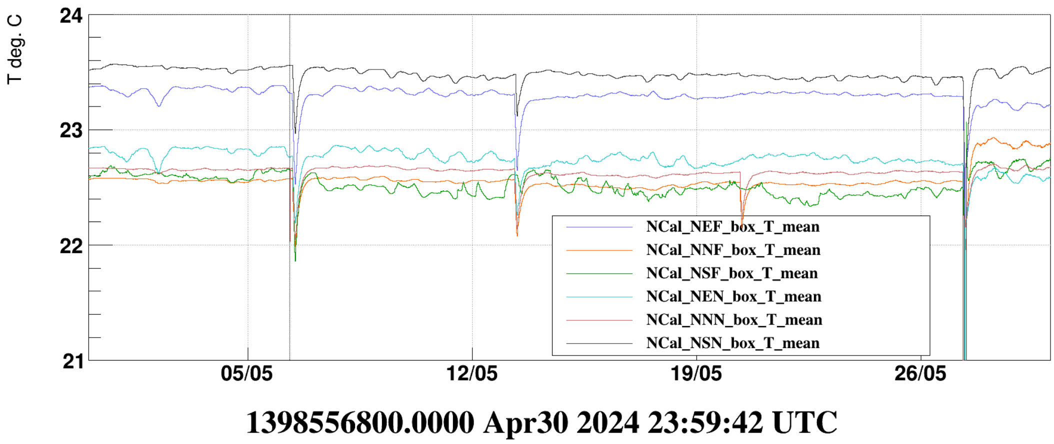

FIGURE 4.7: Temperatures of the rotor boxes in the Virgo NE building over the month of May 2024. Here the rotor were operated at 18 Hz with some maintenance breaks visible. The temperature differences between the rotors is due to the motor power dissipation differences coming from their respective ball bearing friction.

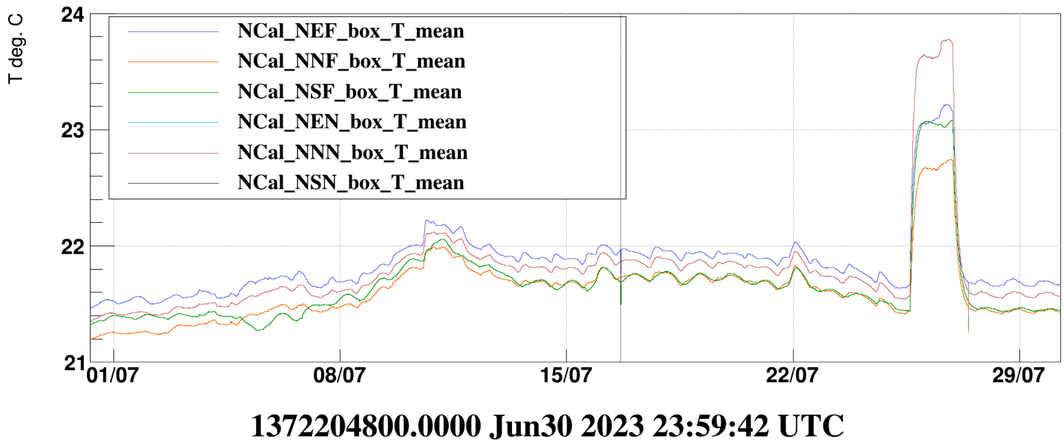

FIGURE 4.8: Temperatures of the rotor boxes in the Virgo NE building over the month of July 2023. The rotors were switched off during this month, except for two days (25/09 to 27/07). When the rotors are off, the NCal temperature probes are tracking the building temperature, around 21.5°C. Their relative calibration is within ±0.2°C.

Opening angle and sector asymmetry

We discussed the uncertainty on the opening angles and asymmetry of the sector in section 4.4.4, the value obtained is 0.11 mrad. In eq. (2.17), the opening angle contributes as $\sin(\alpha)$. Therefore, when adding a small opening angle uncertainty $\delta\alpha$, this equation becomes eq. (4.5). Using the largest value of the opening angle defect, 2.01 mrad (see section 4.4.4), the NCal signal uncertainty due to the opening angle uncertainty and defect is 2×10^{-5}%.

$$h(\alpha + \delta\alpha) = h(\alpha)\left(1 - \frac{\delta\alpha^2}{2} + \frac{\delta\alpha}{\tan(\alpha)}\right) \tag{4.5}$$

In eq. (2.12)), the asymmetry contributes as $\cos(2\eta)$. Therefore, when adding a small asymmetry uncertainty $\delta\eta$, this equation becomes eq. (4.6). Using the largest value of the symmetry defect, 1.40 mrad (see section 4.4.4), the NCal signal uncertainty due to the asymmetry uncertainty and defect is 2×10^{-5}%. To remain conservative we add linearly both uncertainties, the total uncertainty is 4×10^{-5}%.

$$h(\eta + \delta\eta) = h(\eta)\left(1 - \frac{\delta\eta^2}{2} - \delta\eta\tan(2\eta)\right) \tag{4.6}$$

Rotor flat surfaces offsets

The opening angle uncertainty described in the previous section assumes that the flat surfaces are pointing toward the center of the rotor. But that could be not the case as it is sketched in fig. 4.9 which corresponds to the rotor R4-01. This figure was made using the microscope to determine the center of each face of each sector compared to the axis center O. We notice that there is around 0.2 mm of offset between the center of each sector and the axis center. The offsets are also different face up to face down.

R4-01 was the first machined rotor which had the largest defect. This was improved for the following rotors. But we will use the parameter of this rotor to compute the maximum uncertainty due to this effect. To do so, we added in FROMAGE thin blocks of positive or negative mass to model these offsets. The thickness ϵ of the blocks is shown in table 4.10 corresponding to the axis offsets shown in fig. 4.9. Using this configuration, the 2f signal remains the same. The corresponding uncertainty is therefore below the FROMAGE precision of about $5 \times 10^{-4}\%$. This confirms the weak sensitivity to the exact position/shape of the flat surfaces defining the sectors, thanks to the 90° opening angles.

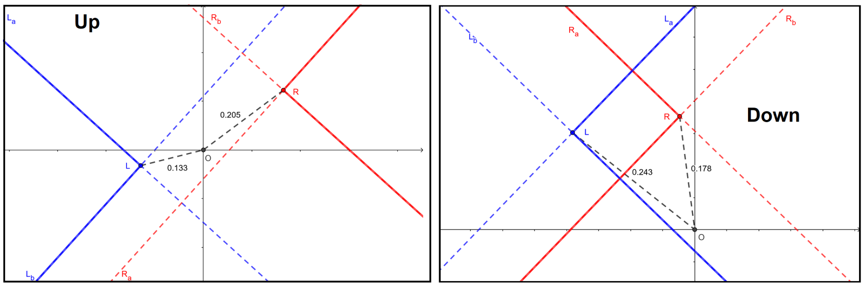

FIGURE 4.9: Offset of the centers to the axis center in mm. Left is face up, right is face down. L sector is shown in blue and R sector in red.

Side	Up thickness ϵ	Down thickness ϵ
L_a	(-) 111	(+) 242
L_b	(-) 74	(+) 24
R_a	(-) 40	(+) 111
R_b	(-) 201	(-) 139

TABLE 4.10: Thickness ϵ (in µm) of the positive/negative mass blocks added in FROMAGE. The sign (+) corresponds to a positive mass and (-) to a negative mass. The remaining dimensions of the blocks correspond to their associated sub-sector.

4.6.2 Modelling uncertainty

When initially computing the effects of the FROMAGE modelling method on the signal we compared the results of the simple and the advanced models simulations (see sections 4.3 and 4.4.5). The modelling uncertainty was taken as the difference between both models. This was reported in the technical notes describing each rotor, see for instance section 7.5.5 of [38] for the first aluminum rotor R4-01 and section 6.5.3 of [39] for the first PVC rotor R4-10. However, this approach overestimates the uncertainties, as the uncertainty in thickness and radius is already accounted for in the rotor geometry uncertainty.

A more detailed method was therefore developed and is described in this section. The results of this method were reported in the publication describing the NCal system at the start of O4b [44]. If we had a perfect knowledge of the rotor geometry with a very large number of measuring points, the NCal signal could be computed accurately using FROMAGE. But we use fairly large elements in FROMAGE, with only one measurement for the thickness and radius. To compute the NCal signal uncertainty, we make the assumption that the thickness and radius fluctuations within an element are not larger than the fluctuation measured between elements. Then we made 1000 FROMAGE simulations where the thickness and radius are randomly changed following the normal distributions:

- Thickness $X(b) \sim \mathcal{N}(\mu = b_{nom}, \sigma = \delta b)$, with $b_{nom} = 104.4$ mm the nominal thickness of the rotor and δb taken for each rotor from table 4.6.
- Outer radius $X(r_{max}) \sim \mathcal{N}(\mu = r_{max,nom}, \sigma = \delta r_{max})$, with $r_{max,nom} = 104$ mm the nominal rotor radius and δr_{max} taken for each rotor from table 4.7.

We use FROMAGE to include the machining imperfections which are expected to be correlated within each lathe pass. Therefore the elements within the colored sub-sectors represented in fig. 4.10 have the same fluctuation to the nominal value. The outer radius is computed independently for both sectors. The RMS of the 1000 simulated mirror displacement due to each rotor geometry is converted to the relative uncertainty shown in table 4.11. This value will be taken as the modelling uncertainty for each rotor, accounting for the radius and thickness uncertainties. They include the uncertainties of the measuring tools which are anyway small compared to the surface defects. This table has been made on June 2024. Of course any future machining of the rotors to reduce unbalances and surface imperfections would change these values.

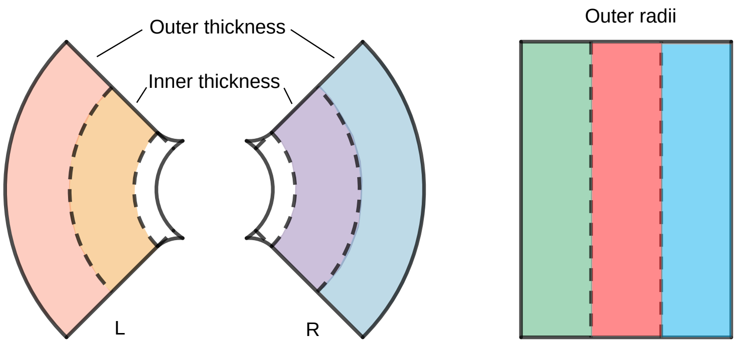

FIGURE 4.10: Left is a top view of the rotor model used in FROMAGE, right is a side view of a sector. Each colored sub-sector is expected to vary from the nominal value of thickness and radius following a normal distribution.

Rotor	NCal 2f signal modelling uncertainty [%]
R4-01	0.018
R4-02	0.018
R4-03	0.044
R4-04	0.023
R4-05	0.034
R4-06	0.026
R4-07	0.026
R4-08	0.019
R4-10	0.010
R4-11	0.017
R4-12	0.020
R4-13	0.013
R4-14	0.023
R4-15	0.016
R4-16	*to be computed*
R4-17	*to be computed*

TABLE 4.11: Relative uncertainty on the gravitational signal at twice the rotor frequency from the modelling method of each rotor.

4.6.3 Other parameters

FROMAGE grid uncertainty

The effect of the grid was already discussed at the end of section 2.3.5 and resulted in a variation of 0.005% on the asymptotic strain for the chosen rotor and mirror grid. This value is then taken as the grid uncertainty.

Gravitational constant G

The gravitational constant $G = 6.674\,30 \times 10^{-11} \pm 1.5 \times 10^{-15}$ m^3.kg^{-1}.s^{-2} [45] has been measured with an uncertainty that propagates in the signal to 0.002%. This value is not much smaller than some of the O4 rotor uncertainties.

4.6.4 Combining the uncertainties for a rotor

Based on the previous section, table 4.12 summarizes the uncertainties on the signal emitted by a PVC rotor (R4-12) for a mirror at 1.7 m. Since most of these uncertainties are uncorrelated, we add them quadratically to compute the overall uncertainty. The only correlated uncertainties are due to the measuring column which enter both in the density and modelling uncertainty. However, since their effects are anti-correlated, adding them quadratically is a conservative choice. The signal uncertainty for each rotor is presented in table 4.13. They depend on the measured geometry and therefore on the machining defects which are rotor dependent.

R4-12 rotor parameter advanced model (23°C)	2f signal uncertainty [%]
Density ρ	0.014
Temperature T	0.024
Opening angle and sector asymmetry	$<4 \times 10^{-5}$
Rotor flat surfaces offsets	$<5 \times 10^{-4}$
Modelling Uncertainty	0.020
FROMAGE grid uncertainty	0.005
Gravitational constant G	0.002
Total uncertainty from the rotor (quadratic sum)	0.035

TABLE 4.12: Uncertainties on the amplitude of the calibration signal at 2f from the R4-12 rotor advanced model geometry at 23°C.

Rotor	2f signal uncertainty[%]
R4-01	0.021
R4-02	0.021
R4-03	0.045
R4-04	0.026
R4-05	0.036
R4-06	0.028
R4-07	0.028
R4-08	0.019
R4-10	0.030
R4-11	0.033
R4-12	0.035
R4-13	0.031
R4-14	0.036
R4-15	0.032
R4-16	*to be computed*
R4-17	*to be computed*

TABLE 4.13: Uncertainties on the amplitude of the calibration signal at 2f for each rotor.

4.7 Conclusion

In this chapter, we outlined the method used to characterize the rotors geometry and assess the related uncertainties. We began by collecting measurement points and implementing them into FROMAGE to calculate the gravitational signal produced by each rotor. Then, we identified the uncertainties associated with the geometry of each rotor and evaluated their impact on the resulting gravitational signal. Thanks to these measurements, the uncertainty on the NCal signal coming the rotor parameters has been reduced by an order of magnitude for O4 compared to O3.

Chapter 5

Preparation of the rotors

Contents

Introduction

In this chapter we will discuss the different tests and operations performed on the rotors. We begin with the methodology employed for their balancing, aimed at minimizing vibrations transferred to the tower and mitigating wear on ball bearings. Followed by a safety check of the rotor to make sure that its material withstands the foreseen operating speeds. Finally, we discuss the elongation of the rotor material induced by the rotation speed.

5.1 Balancing of the rotors

One of the challenge of the NCal is to be a reliable system. This mainly concerns the ball bearings and their assembly with the rotor and the axis for a 24/7 use. To increase the reliability of the system we balance the rotor to minimize the vibrations.

To measure the slight asymmetry of the rotor we take advantage of the low resonance frequency of the NCal suspension. We set the rotor frequency at a value (14 Hz) larger than the suspension frequency and measure the recoil displacement using the position sensors on the reference plate. This section shows the method used to correct this unbalance and the results after a correction using a counterweight mounted on the rotor. The balancing was performed on the IPHC NCal setup (see section 2.5.8).

5.1.1 The balancing disk

A circular disk was foreseen to be mounted on the central part of the rotor (see fig. 5.1) to be machined as a counterweight. The dimensions of the disk are: an inner radius of 10 mm and an outer radius of 40 mm. This disk is fixed on the rotor using four metallic screws at a radius of 30 mm. The geometry of the screw holes on the rotor is shown on fig. 5.2. Considering the cartesian coordinate system, the angle from each screw to the horizontal axis x is $\theta = 30°$.

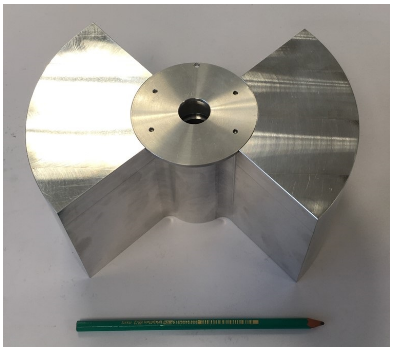

FIGURE 5.1: Disk layed on the up face of an aluminum rotor with four screw holes visible.

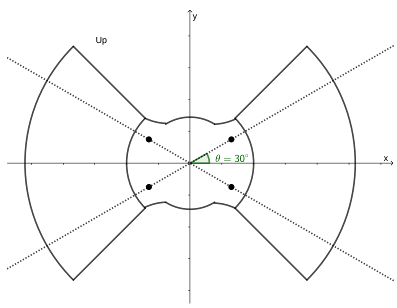

FIGURE 5.2: Layout of the screw holes on the face of the rotor. Each hole is 30° from the horizontal axis and at 30 mm from the center.

5.1.2 The counterweight

The balancing procedure starts by finding the masses which minimize the observed recoil motion of the suspended NCal. This is done by adjusting small masses mounted on the screw holes of the balancing disk (without the disk). At the end of this step, two masses m_1 and m_2 are respectively placed at angles α_1 and α_2 and at a radius r_m. We use the following formula to compute a single mass m, equivalent to the moment of the two masses located at an angle α_m:

$$m = \sqrt{m_1^2 + m_2^2 + 2m_1 m_2 \cos(\alpha_1 - \alpha_2)} \tag{5.1}$$

$$\alpha_m = \arctan \frac{m_1 \sin(\alpha_1) + m_2 \sin(\alpha_2)}{m_1 \cos(\alpha_1) + m_2 \cos(\alpha_2)} \tag{5.2}$$

Then the opening angle of the part cut (represented in fig. 5.3) in the balancing disk of density ρ is defined by asking to get the same moment as this equivalent moment. This gives:

$$\gamma_m = 2 \arcsin \left[\left(\frac{3}{2} \frac{m\, r_m}{\rho\, h\, R^3} \right)^{1/3} \right] \tag{5.3}$$

where h is the disk thickness and R its outer radius. The part cut is at an angle $\gamma_m + \pi$ since we are removing some mass.

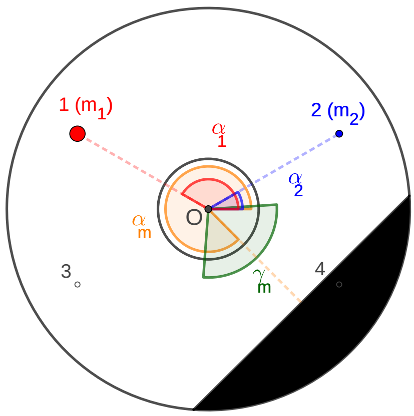

FIGURE 5.3: Outline of a disk to be used as a rotor counterweight with the material cut. In this case $m_1 = 5.9$ g and $m_2 = 1.6$ g.

The counterweight is then machined using these parameters. The counterweights for the aluminum rotors were made of aluminum. In February 2024 when PVC rotors were produced, the mass deduced from this method was divided into the two counterweights placed on each side of the rotor to reduce the possible lateral unbalance of the rotor. These counterweights were made of PVC disks as shown in fig. 5.4 or aluminum for the rotor R4-11 (see fig. 5.5) which could not be compensated by PVC disks.

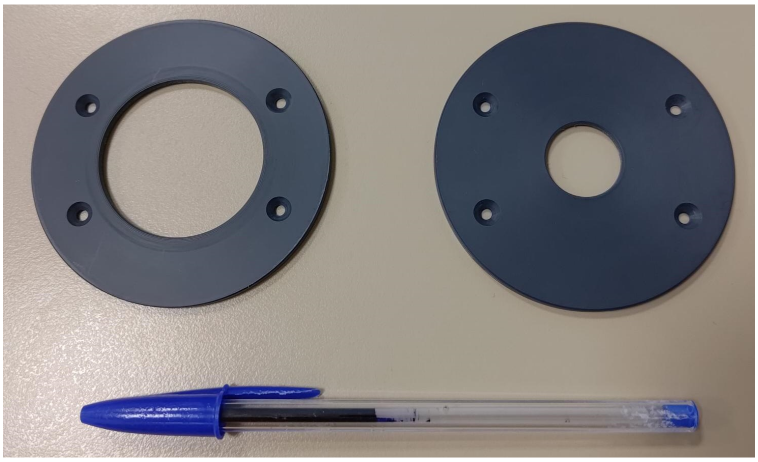

FIGURE 5.4: Picture of the PVC disks used as future counterweights for a PVC rotor.

FIGURE 5.5: Picture of the aluminum disks used as counterweights and placed on the PVC rotor R4-11. The disk on the left was designed so the motor would fit in its center, the disk on the right fits the axle of the rotor. On the motor side, the inner radius is 21.75 mm, while on the axle side, it measures 10 mm.

5.2 Safety checks of an aluminum rotor

A possible risk is the dislocation of the rotor when spinning at a relatively high speed. This risk was first studied at LAPP on the O3 NCal-200 rotor [37]. With a simple analytical model, the maximum stress was estimated to be 12 MPa when spinning at 100 Hz, much less that the 470 MPa elastic limit of the aluminum 7075 used. This result was confirmed with a full 3D ANSYS simulation of the rotor, showing maximum stress on the covers and external ring of the O3 rotor, but still very far from the elastic limit.

The rotor design has evolved for O4. Figure 5.6 shows the O3 and O4 design. The O4 design is much simpler. The external ring has been suppressed as well as the covers. We are left with only two sectors, and therefore, the evaluation of the stress with an analytical model is easier.

This section will first present this evaluation of the expected maximum stress on the rotor. It will show that again, the O4 design is safe. Then, a test performed on a modified rotor will be presented. The purpose of this test was to demonstrate that indeed, there is a large safety factor in the design of the O4 rotor and the risk of rotor dislocation is extremely small.

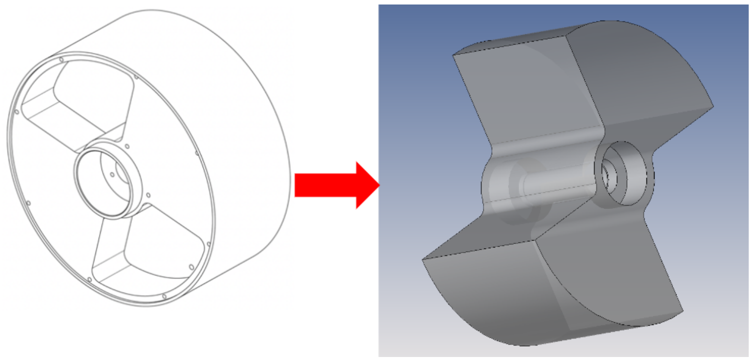

FIGURE 5.6: On the left is the O3 "NCal-200" rotor and on the right is the O4 rotor.

5.2.1 Analytic estimation of the stress for the O4 rotor

The surface where the stress is expected to be maximal is at the narrowest part of the rotor (see fig. 5.7). Since there are two similar areas we will only compute one of them. We use eq. (5.4) to compute the stress.

$$\mathrm{d}\sigma = \frac{\mathrm{d}F_{\mathrm{cent}}}{\mathrm{d}S} = \frac{\omega^2\, r\, \mathrm{d}m}{\mathrm{d}S} \tag{5.4}$$

- $\mathrm{d}F_{\mathrm{cent}}$ being the centrifugal force of the infinitesimal rotor sector
- $\mathrm{d}S$ is the infinitesimal surface where the stress is applied at radius r_S
- $\mathrm{d}m$ is the mass of the infinitesimal sector
- $\omega = 2\pi f$ is the angular velocity of the rotor
- and r is the radius to the center of gravity of the infinitesimal object considered

In cylindrical coordinates, the infinitesimal surface $\mathrm{d}S$ can be expressed as:

$$\mathrm{d}S = r_S\, \mathrm{d}\theta\, \mathrm{d}z \tag{5.5}$$

For the O4 rotor, assuming a constant density ρ, the mass $\mathrm{d}m$ is:

$$\mathrm{d}m = \rho\, r\, \mathrm{d}r\, \mathrm{d}\theta\, \mathrm{d}z \tag{5.6}$$

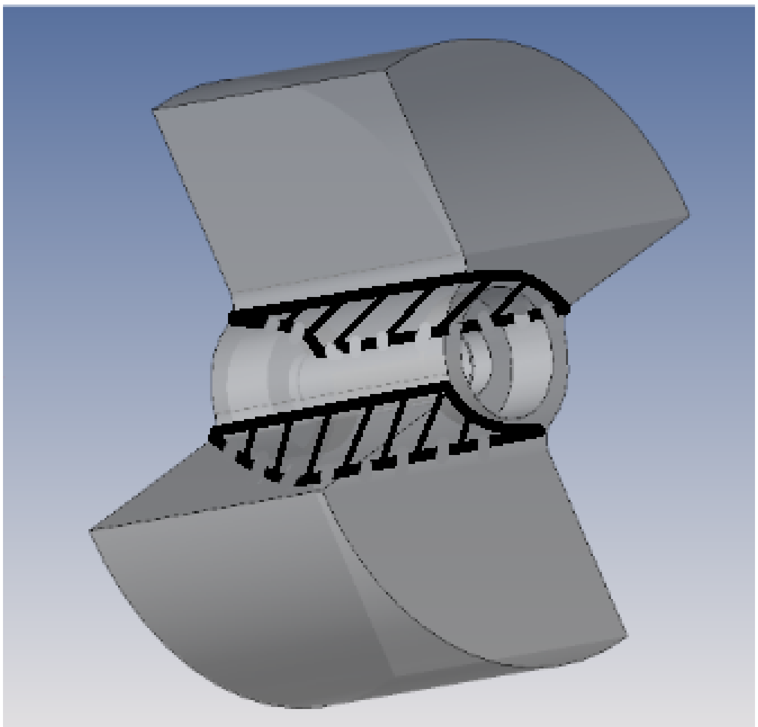

FIGURE 5.7: Surface stress on the O4 rotor shown in black hatched areas.

Using eq. (5.4), the infinitesimal stress expressed in eq. (5.7) is:.

$$\begin{aligned} d\sigma &= \frac{\rho\,\omega^2 dr d\theta dz}{d\theta dz}\frac{r^2}{r_S} \\ &= \rho\,\omega^2 \frac{r^2 dr}{r_S} \end{aligned} \tag{5.7}$$

Since R the radius of the sector (0.104 m) is much larger than r_S the radius to the surface stress (0.029 m), we can neglect the r_S^3 term while computing the integral over r, and therefore the stress is:.

$$\sigma = \frac{1}{3}\rho\,\omega^2 \frac{R^3}{r_S} \tag{5.8}$$

Using the O4 rotor parameters in table 5.1 we compute a stress of 14.3 MPa at an operating frequency of 100 Hz.

Parameter	O4 rotor value
ρ [kg.m^3]	$2808.1 - 2810.8$
ω [s^{-1}]	628.31
R [m]	1.04×10^{-1}
r_S [m]	2.9×10^{-2}

TABLE 5.1: Parameters considered for the O4 rotor stress computation.

This result is not very different from the analytic computations of the previous safety note about the O3 rotor since the main difference is a slight increase of the external radius. The stress induced by the rotation of the O4 rotor is far below the elastic limit of the material of 470 MPa with a safety factor of about 32. The full ANSYS FEM modeling was not re-done for the aluminum rotor because the safety factor was large enough. However, it was done for PVC rotors which are more likely to be deformed as described in the next section.

5.2.2 Experimental test of a weakened O4 rotor

To demonstrate that the safety factor is very large, one of the O3 rotor was modified to simulate the O4 rotor geometry, with a much larger stress. To increase the stress on the rotor, the connection between the sectors and the central part of the rotor was machined to reduce the surface S (from eq. (5.8)) on which the centrifugal force is acting. The red arrow on fig. 5.8 shows the small amount of material left (less than 11 mm of thickness) compared to the initial 82.4 mm. This modification increases the stress by a factor $82.4/11 = 7.5$.

Since we were using an O3 rotor for this test, the external radius was 102.5 mm instead of the foreseen 104 mm, reducing the stress by a factor 1.04 compared to the expected O4 geometry. Overall, this geometry increases the stress by a factor $7.5/1.04 = 7.2$. Therefore, the expected stress is $14.3 * 7.2 = 103$ MPa, still about a factor 4.5 away from the elastic limit.

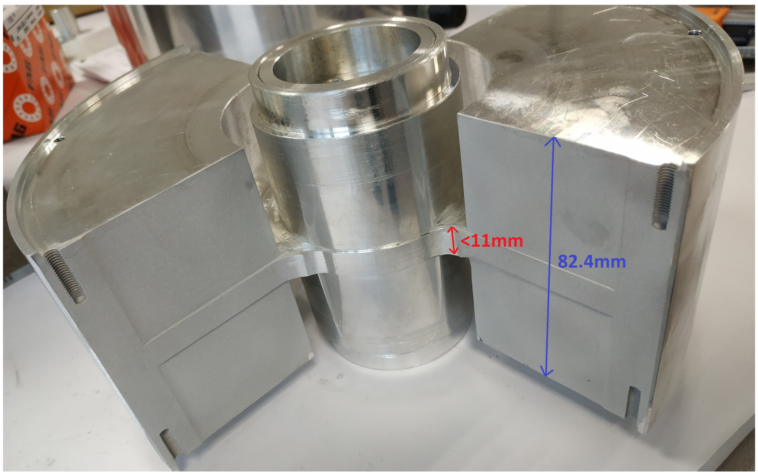

FIGURE 5.8: Weakened O4 rotor.

The rotating test with the weakened rotor has been made at IPHC on November 22, 2021. The goal was to increase the rotating speed as much as possible and check that the rotor would not break apart. The rotor reached a maximum frequency of 96 Hz for about 3 minutes.

Since the rotor could only reach 96 Hz during the experimental test and not 100 Hz as used for the stress computation, the stress was a factor $(100/96)^2$ weaker than the expected value. Therefore, taking into account the reduction of the central surface, the slight change of the rotor diameter and the maximum rotation speed reached during this test, the stress was enhanced by a factor $7.5/1.04 * (96/100)^2 = 6.6$. In other words, since the rotor was not damaged, this test demonstrates that the safety factor is at least 6.6.

5.2.3 Conclusion

We have first shown that the maximum expected stress is 14.3 MPa, well below the elastic limit of 470 MPa which is lower than the breaking stress of 535 MPa. Then we have prepared an O4 like rotor where the stress was increased by cutting material and making the rotor more fragile. We operated this rotor up to 96 Hz, without any damage, demonstrating that our safety factor is a least a factor 6.6 when operating at its maximum speed.

5.3 Safety checks of a PVC rotor

As PVC has a smaller elastic limit (45 MPa available in [43]) than the aluminum (470 MPa), more care is needed for PVC rotor operation. Using eq. (5.8) the stress for a PVC rotor operating at a frequency $f = 100$ Hz is expected to be 7.4 MPa thanks to the reduced PVC density compared to aluminum. This is almost twice less than the stress generated by the aluminum rotor (14.3 MPa). But due to the reduced PVC elastic limit, the safety factor is only a factor 6 at 100 Hz.

The full ANSYS FEM modeling was done for a PVC rotor. Figure 5.9 shows the map of the stress when operating at 50 Hz. The largest stress is observed on the front part of the image where the rotor is thinner due to the space reserved for the motor which was not included in this simulation. A more relevant comparison with our naive model is to look at the back of the rotor where the stress computed by ANSYS is around 2 MPa. This is compatible with the analytical model value, 7.4 MPa, which was computed at 100 Hz with therefore a stress $2 * 2 = 4$ larger.

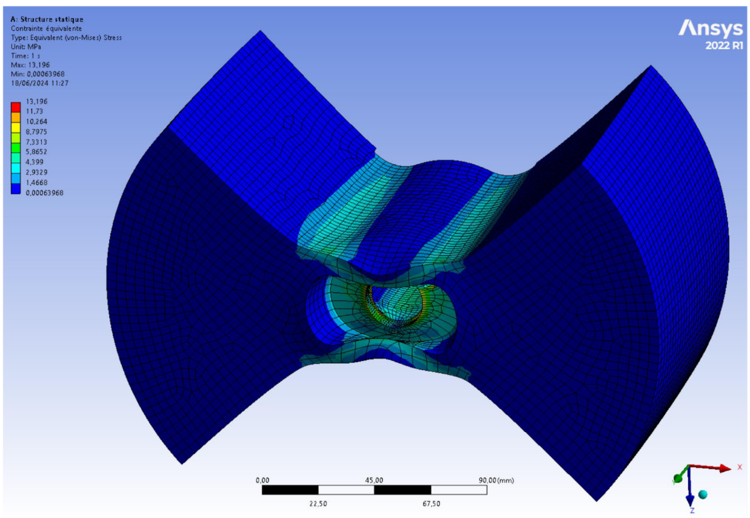

FIGURE 5.9: Stress map of a PVC rotor operating at 50 Hz made with ANSYS.

Since the rotor will be operating continuously at speed lower than 100 Hz, the safety factor should grow as the square of the ratio between 100 Hz and the desired operating frequency. We add that in the very unlikely scenario of a PVC rotor breaking apart, the aluminum box is designed to withstand the potential rupture of the aluminum rotors without breaking itself and should therefore withstand the PVC rotor.

5.4 Elongation of an operating rotor

When studying the sources of uncertainties, one concern was the elongation of the rotor caused by the centrifugal force induced by the rotation. We evaluated the elongation of a rotor through three methods: first, using a basic analytical model; second, with a finite element model; and finally, by conducting experiments with a PVC rotor.

5.4.1 Analytical model

To compute the elongation we first use a simple model that considers one sector of the rotor made of tiny springs being pulled by the outer mass of the sector such as shown in fig. 5.10.

The centrifugal force F_{c_i} exerted on a tiny spring i is expressed as :

$$F_{c_i} = \frac{\omega^2}{3}\rho\alpha h \left[R^3\right]_{R_0}^{R_i} \tag{5.9}$$

where ρ is the density of the material, α the opening angle of the sector and h the thickness of the sector.

The opposing force T_i of a tiny spring of size δ_x can be expressed as :

$$T_i = -k(x - \delta_x) \tag{5.10}$$

where $k = YA = Y\alpha h R_i$ the stiffness of the spring, Y the Young modulus of the material (71.7×10^3 MPa for the aluminum and 3 MPa for the PVC) and A the contact area between the spring and the outer sector.

Using the relation of equilibrium of the forces $F + T = 0$ on the first spring at $i = 0$ we have :

$$\begin{aligned}\Delta_{x_0} &= \frac{\omega^2}{3}\frac{\delta_x}{Y\alpha h(R_0+\delta_x)}\rho\alpha h\left[R_N^3 - (R_0+\delta_x)^3\right] \\ &= \frac{\omega^2}{3}\frac{\rho}{Y}\frac{\delta_x}{R_0+\delta_x}\left[R_N^3 - (R_0+\delta_x)^3\right]\end{aligned} \tag{5.11}$$

Which can be extended to any tiny spring i :

$$\Delta_{x_i} = \frac{\omega^2}{3}\frac{\rho}{Y}\frac{\delta_x}{R_0+i\delta_x}\left[R_N^3 - (R_0+i\delta_x)^3\right] \tag{5.12}$$

Finally we can express the total elongation Δ_x as the sum of all the Δ_{x_i} :

$$\Delta_x = \sum \Delta_{x_i} = \frac{\omega^2}{3}\frac{\rho}{Y}\sum_{i=1}^{N-1}\frac{\delta_x}{R_0+i\delta_x}\left[R_N^3 - (R_0+i\delta_x)^3\right] \tag{5.13}$$

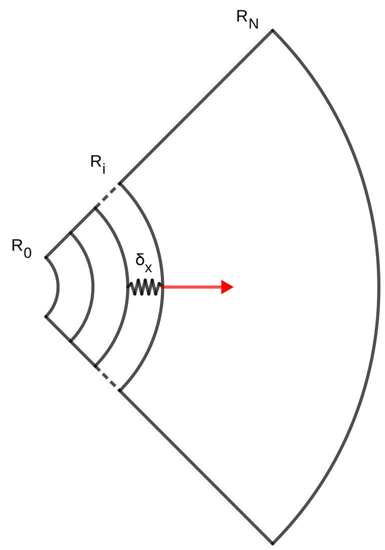

FIGURE 5.10: Drawing showing the centrifugal force exerted on a string of initial length x_0 by the external section of a sector.

The numerical integration of eq. (5.13) gives the elongation of a sector. Figures 5.11 and 5.12 show the result for respectively an aluminum ($\rho = 2810.8$ kg.m^{-3}) and PVC sector ($\rho = 1442.3$ kg.m^{-3}). The computation was made using the inner radius $R_0 = 12$ mm where the ball bearing is held in place, the outer radius of the sector $R_N = 104$ mm, the sector thickness $h = 104.4$ mm and an opening angle $\alpha = 90°$. As expected the PVC rotor undergoes more deformation than the aluminum. At 18 Hz, the aluminum elongation at the maximum radius R_N is 0.3 µm whereas the PVC elongation is 4.2 µm.

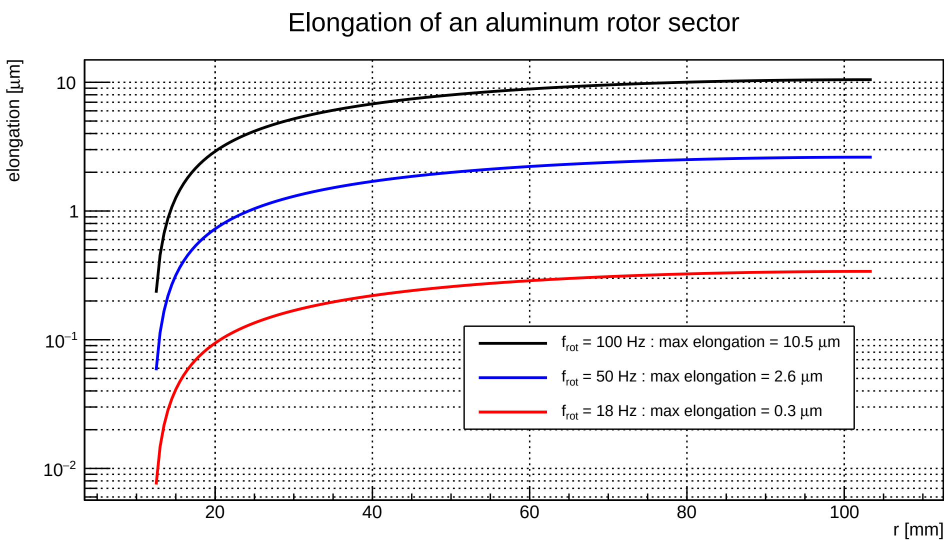

FIGURE 5.11: Elongation of an aluminum sector as a function of the radius. The red line shows the elongation curve for a rotation frequency of 18 Hz, the blue line at 50 Hz and the black line at 100 Hz.

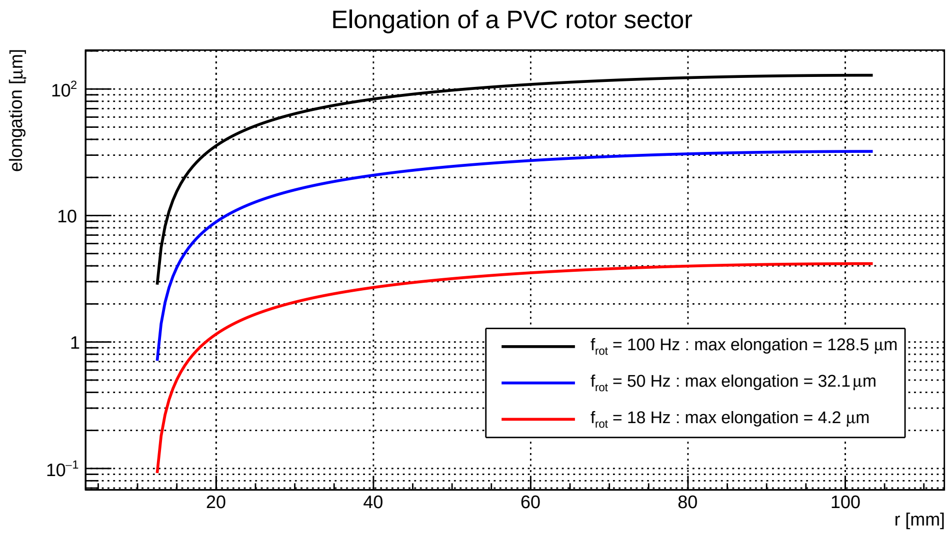

FIGURE 5.12: Elongation of a PVC sector as a function of the radius. The red line shows the elongation curve for a rotation frequency of 18 Hz, the blue line at 50 Hz and the black line at 100 Hz.

5.4.2 Finite element model

To confirm this simple model we use the results of an ANSYS simulation of the rotor geometry (using nominal rotor values with one counterweight spacing). This simulation was made at a rotation frequency of 50 Hz. As shown in fig. 5.13 individual nodes are used to describe the volume of the rotor where the stress and deformation due to the rotation frequency is computed. For an aluminum sector the maximum elongation is 3.5 µm and 43.0 µm for a PVC sector. These elongations are respectively 25% and 33% larger than our simple model. Extending these results to 18 Hz, we find an elongation of 0.5 µm for the aluminum and 5.6 µm for the PVC.

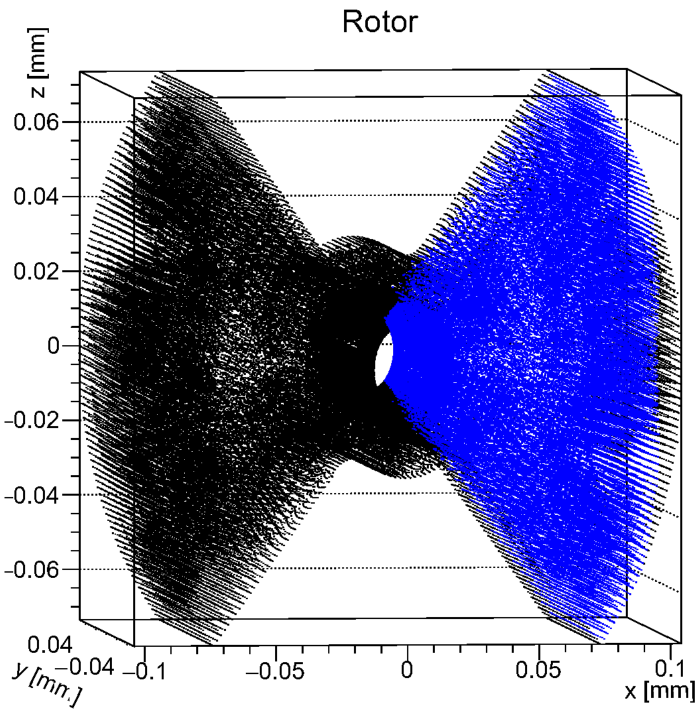

FIGURE 5.13: Visualization of the points used in the *ANSYS* simulation for the geometry of a O4 rotor.

Using the simulation results extended at 18 Hz and implementing the elongation as a shift of the sectors (along the x axis shown in fig. 5.13) in FROMAGE results in the following relative variations in the 2f strain signal (for nominal rotor values) :

- $\frac{\delta h}{h}(\mathrm{Al7075}_{\rho=2810.8}) = 0.002\%$
- $\frac{\delta h}{h}(\mathrm{PVC}_{\rho=1442.3}) = 0.020\%$

We note that for PVC, this value is comparable to the rotor's geometrical uncertainties, whereas for aluminum, it is an order of magnitude smaller. These values will be taken as our calibration uncertainties due to the elongation of the rotors for the O4 NCals.

5.4.3 Experimental check of a PVC rotor

Finally we made an experimental check using a PVC rotor (R4-13 in that case). The rotor radius was measured by monitoring the gap between the rotor and its box. This was done by placing a LED on the edge of the NCal box cover as shown in fig. 5.14. When the rotor spins, it extends, reducing the gap and the amount of light collected by a photodiode located on the other side of the box. Comparing the LED signal of a non spinning rotor with an operating rotor gives us the elongation value of both sectors individually. The zeroing of the photodiode was performed with the LED off, with an accuracy of 1×10^{-6} V.

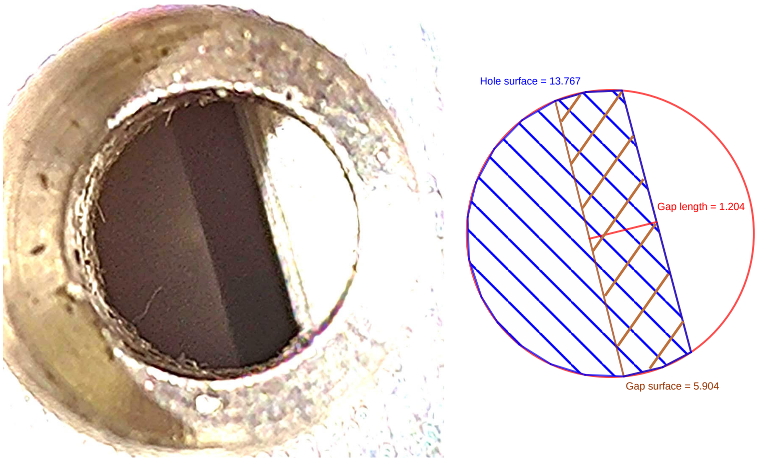

FIGURE 5.14: Left is a picture of the LED hole on the edge of the NCal box cover where the gap between the PVC sector and the box can be seen, right is a diagram of the left picture. The gap, 1.2 mm, has been computed by taking the ratio between the observed gap and the diameter hole assumed to be 5 mm.

Figure 5.15 shows the LED signal of the rotor operating at a frequency of 5 Hz (blue curve), 25 Hz (pink curve), 50 Hz (red curve) and 75 Hz (green curve). We chose a "rest" frequency of 5 Hz to be able to see the profile of the sectors when passing on front of the LED (areas labelled "Sector 1" and "Sector 2" in Figure 5.15). For readability purposes the 25, 50 and 75 Hz signals were stretched in time to superpose the 5 Hz signal. One can notice that all signals have the same value when no sector is passing in front of the LED. When a sector passes, the signal decreases when the spinning frequency increases. Table 5.2 shows the LED signal variation and the associated gap determined using the 1.2 mm gap value from fig. 5.14.

Frequency [Hz]		5	25	50	75	5
Signal variation [%]	Sector 1	0	0.70	2.95	7.13	0
	Sector 2	0	0.72	2.90	7.04	0
Gap variation [µm]	Sector 1	0	8.4	35.4	85.6	0
	Sector 2	0	8.6	34.8	84.5	0

TABLE 5.2: LED signal variation and corresponding gap as a function of the rotation frequency.

Taking the average value of both sector for each frequency from table 5.2 we then have an elongation of 8.5 µm at 25 Hz, 35.1 µm at 50 Hz and 85.0 µm at 75 Hz. The uncertainties from these values are coming from two parts. The first part is from the gap value which is our overall scaling factor. Given the nominal radius of the box (105.0 mm) and the measured rotor radius (103.9 mm see table 4.7), the expected gap is 1.1 mm. We can take the difference between this value and our measurement as a measurement uncertainty of about 10%. The second part is from the collected optical signal for which we assume another 10% to remain conservative as we might have parasitic reflections within the gap. The total uncertainty, 20%, is taken as the linear combination of these two values. The measured elongation values, compared to the analytical model and displayed in fig. 5.16, are consistent with the calculations performed using both an analytical and finite element model of the rotor.

In theory, using this method we could measure the elongation of each rotor when operating and correct the injected signal. But since this method requires some modifications on the NCal boxes and the elongation parameter is not dominant we chose to keep it as an uncertainty (see end of section 5.4.2).

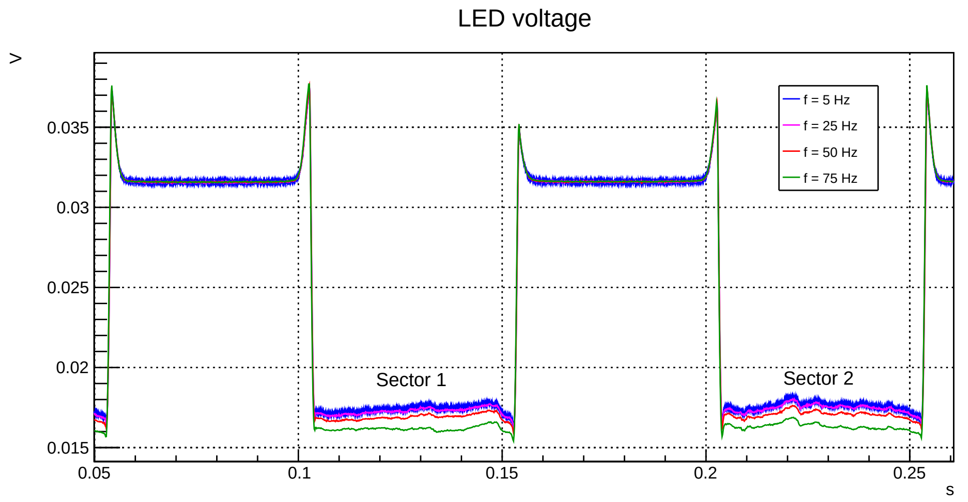

FIGURE 5.15: Signal of a LED through a rotor at 5 Hz (blue curve), 25 Hz (pink curve), 50 Hz (red curve) and 75 Hz (green curve). The signal is at the minimum when a sector passes by the LED hole. The 25, 50 and 75 Hz pulse signals have been stretched to be superposed to the 5 Hz signal.

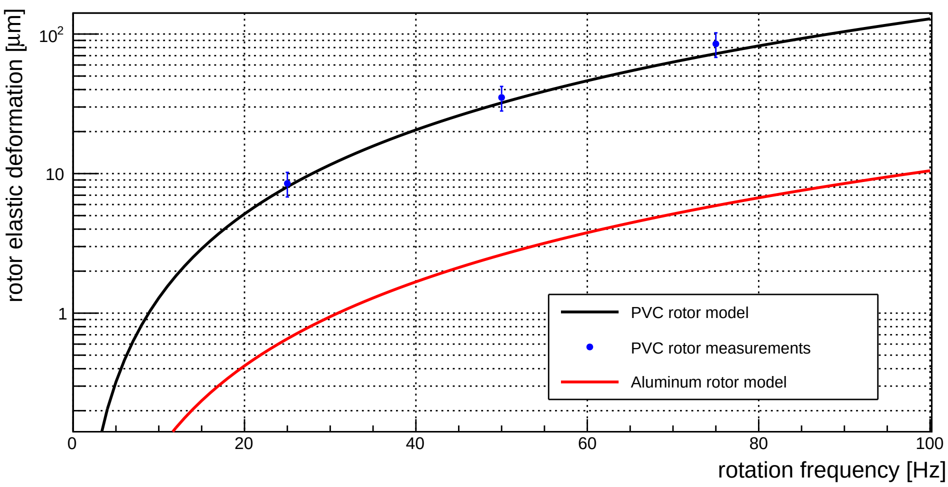

FIGURE 5.16: Elastic deformation of a section of PVC (in black) and aluminum (in red) rotors due to centrifugal force as a function of rotation frequency. The curves are computed analytically for nominal rotor values. The measurement points for the PVC rotor R4-13 are shown in blue with a 20% uncertainty.

Another check was made with R4-13 to study the effect of a long operating time at high frequency on a PVC rotor. For this test the rotor was first operated at 5 Hz for a few minutes, then at 75 Hz for approximately 8 hours, slowed down back to 5 Hz for a few minutes then stopped. Finally another measurement at 5 Hz was made the next morning. Figure 5.17 shows the LED signal at each frequency. We noticed that the LED signal suddenly changed after $\sim$ 5 hours of operating at 75 Hz, this event is labeled as "glitch" in the figure. The next morning, when operating the rotor at 5 Hz, the LED signal of the sectors are lower than the previous day, meaning that the sectors have been permanently elongated. The rotor R4-13 went through a plastic deformation when operated for $\sim$ 5 hours at 75 Hz, changing the rotor's properties.

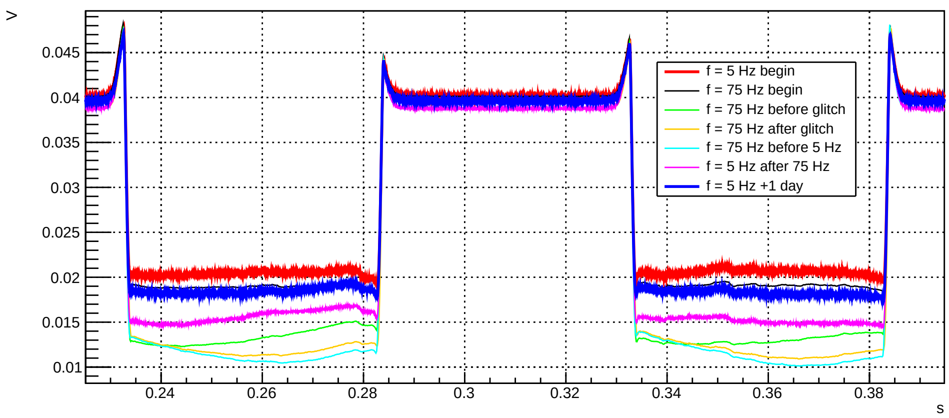

FIGURE 5.17: Pulse signal of a LED through a rotor. For a few minutes in the beginning at 5 Hz (red curve), then at 75 Hz (black curve), just before the "glitch" at 75 Hz (green curve), after the "glitch" at 75 Hz (yellow curve), at 75 Hz (light blue curve) just before changing back to 5 Hz for a few minutes (purple curve) and finally 5 Hz the next morning (blue curve). The signal is at the minimum when a sector passes by the LED hole. The 75 Hz pulse signals have been stretched to be superposed to the 5 Hz signal.

After the glitch, the pulse signal of an empty sector has also been shifted down, this effect is expected to be due to the temperature. Figure 5.18 shows the temperature of the box cover and the rotor. As we can see, the temperature gradually increased when the rotor operated at 75 Hz. It then dropped and came back slowly to the room temperature when the rotor was stopped. A small increase of the temperature can be seen in the morning when the rotor was operated back at 5 Hz. This shows that the temperature might be responsible of some of the signal variations seen. With the observed 15°C increase, the PVC rotor radius is expected to increase by 104 mm $*15°\text{C}*80\mu\text{m/m/K} = 125$ µm which corresponds to 0.02 V $*125$ µm /1.1 mm $= 2.5$ mV. This is what we observed in fig. 5.18 between the pink curve ("5 Hz after 75 Hz") and the blue curve taken one day later ("5 Hz + 1 day"). However, a plastic deformation was induced by the high speed operation of the rotor since the rotor has not returned to its initial radius. Therefore, we decided that the PVC rotors will be operated below 50 Hz.

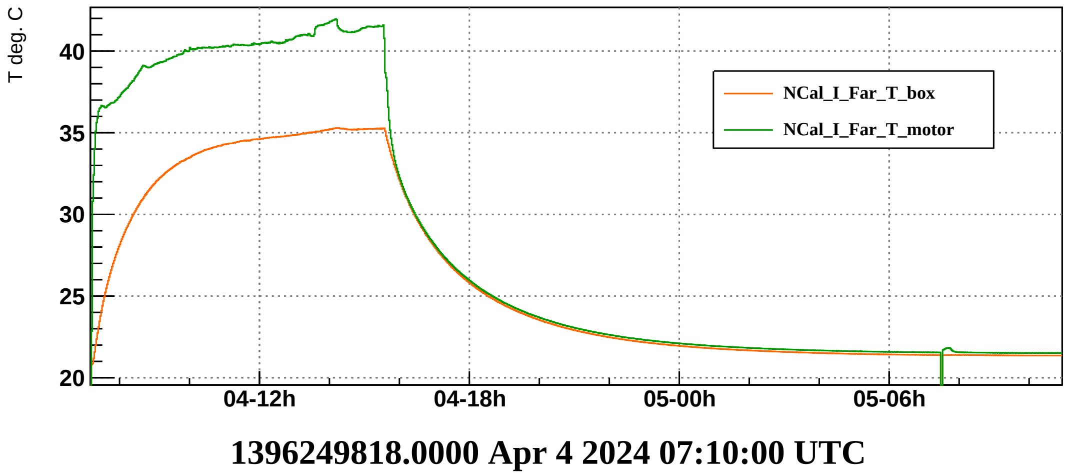

FIGURE 5.18: Temperature of the motor (green curve) and the box (orange curve) during the PVC rotor elongation test.

Chapter 6

Position of the NCals

Contents

Introduction

In this chapter we will discuss the method to determine the position of each NCal. This parameter is related to the NCal-to-mirror distance, a key parameter and the main source of uncertainty of the O3 NCal system. We begin with the determination of the position of the reference plates relative to the tower center based on geometrical surveys and mechanical measurements. Then we get the distance between each NCal and their associated reference plate. This allow us to compute the relative distances between NCals on the same setups. Finally we will provide the geometrical position of the NCal slots in the common reference frame. This study will focus on the NCal positions in the plane of the interferometer. But we will also discuss their vertical position.

6.1 Setups positions

The O4 NCal design calls for the installation of three sets of NCals on the NE tower as seen on fig. 2.23, one on the South side, one on the opposite side, the North location, and one on the East side.

Figure 6.1 presents a CAD view of the North NCal setup. The position of the suspended part, relative to the reference plates (in blue on figure fig. 6.1), is monitored using position sensors (see section 2.5.7). The reference plates are installed on top of frames (in green on figure fig. 6.1), attached to the tower base. The installation of these frames was made with a crude positioning, using the imperfect geometry of the tower base. The fine relative positioning of the three reference plates was made using a mechanical template to provide well-defined relative distances in order to create a local referential for the NCal system, and compute the mirror position relative to it.

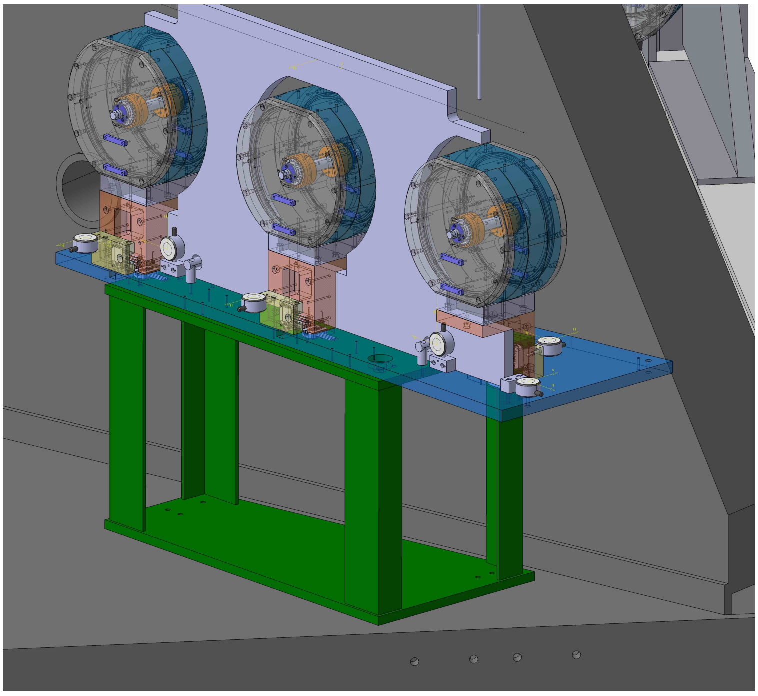

FIGURE 6.1: CAD view of the North NCal setup.

6.1.1 Mechanical template to position the setups

The template was made of four 5 mm aluminum plates of about 2 m long. Their size was a compromise between the transport constrains (smaller parts is better) and the precision (larger parts is better) as well as the need to go through the tower ribs. The 10 mm diameter assembling holes have been drilled using a computer numerical control (CNC) machine (having a range long enough) for the template parts and the reference plates.

The most important distance to know is the distance between the north and south reference plates, and especially the 10 mm H7 diameter reference hole located at the inner end of the references plates and aligned on the expected axis of the NCal (see the drawings and the pin inside the orange circle of fig. 6.2a.

We will start with a description of the expected relative position accuracy of the reference plates as well as the measurements made during the tests at the IPHC and the installation phase at the Virgo site. A mechanical drawing is shown in fig. 6.2b showing inner (within green circles) and outer reference holes (within orange circles).

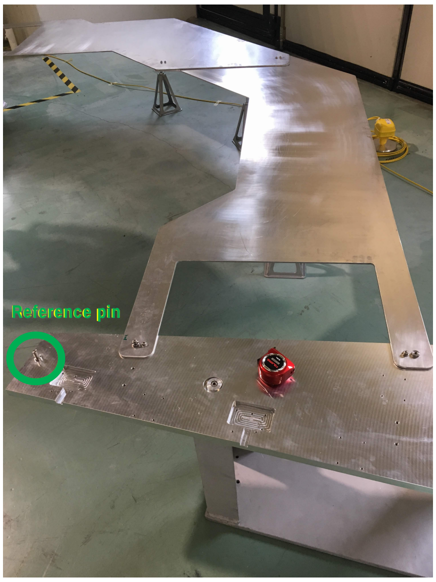

(A)

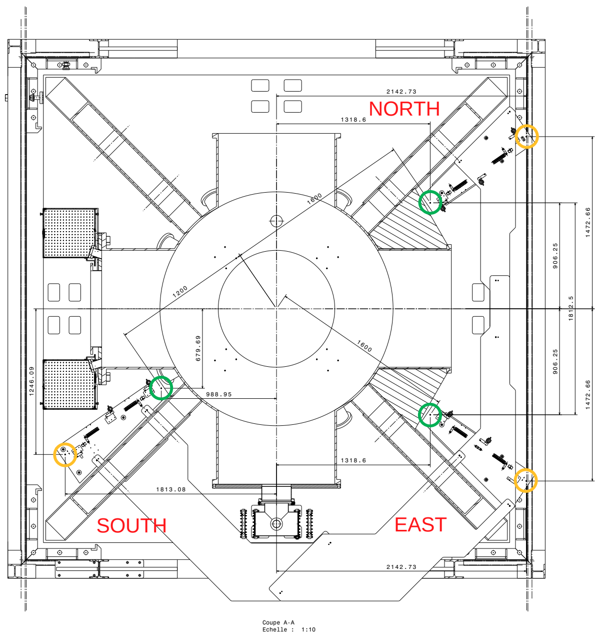

(B)

FIGURE 6.2: (A) Trial assembly of the frame, reference plate and template. (B) Top view drawing of the North, East and South reference plates with the template around the tower. The inner reference hole/pin is shown within the green circle and the outer reference within the orange circle.

Template design and expected accuracy

The uncertainty on the assembling holes diameter is expected to be between 0 and +18 µm (H7 tolerance). The uncertainty on the pins diameter is between −15 and 0 µm. Therefore, the clearance for the pins assembly is between 0 and 33 µm. This translate to a RMS of $= 33/\sqrt{12} = 10$ µm when assembling a pin. The uncertainty on the positioning of the assembling holes is expected to be less than 20 µm, thanks to the use of a CNC machining to drill them. To get the overall uncertainty on the relative positioning of two template part assembled with a pin, we add linearly (to be conservative) these two uncertainties and use 30 µm hereafter.

Since the two pins of the east plate are 0.61 m apart, the accuracy on the angle made by the two template parts is typically $30 \times 10^{-6}/0.61 = 0.05$ mrad. To get an uncertainty on the position at the end of the template relative to the east reference plate, we have to multiply this angle by the distance between assembling holes and the center of the tower (about 2 m). Since there are four template parts (some of them contributing with a smaller lever arm, but we conservatively ignore this), the overall expected mechanical accuracy between the north and south reference plates is 0.05 mrad $\times$ 2 m $\times \sqrt{4} = 0.2$ mm.

This number is close to the value coming from temperature variation. For instance, for a 5 degrees centigrade difference (that is the expected maximum difference between the workshop where the plates were machined and the NE building), over 2.8 m (the distance separating the two inner reference pins of the north and south reference plates) and the thermal expansion coefficient for aluminum (23 µm/m/K) we get 0.3 mm.

Adding linearly (to be conservative) the two numbers, the expected mechanical uncertainty on the 2.8 m distance of the two inner reference pins is about 0.5 mm.

In the case of the north and east reference plates that are less than 2 meters apart and positioned with only two reference template parts, the systematic uncertainty is estimated to 0.3 mm. For the south to east reference plates, since the distance is similar to the south to north reference plates, we will use 0.5 mm as systematic assembly uncertainty.

Precision of the measuring tapes used

To measure the distance, we use category 1 measuring tapes that are expected to have an accuracy of $\pm$ 0.4 mm at 3 m ($\pm$ 0.3 mm at 2 m and $\pm$ 0.6 mm at 5 m). The model used are Tajima H1630 MW (3 m) for most of the cases and sometimes Tajima H1550 MW (5 m) .

The reference holes are equipped with pin having a central slot to host the measuring tape. The reading is made by inserting the measuring tape inside one pin with an offset of 10 cm (see left image of fig. 6.3) and then reading the distance on the other pin after subtracting the 10 cm offset (right image of fig. 6.3). The reading is rounded to 0.5 mm. The reading uncertainty is therefore $0.5/\sqrt{12} = 0.15$ mm and fluctuate from one measurement to another. If the ruler is not perfectly straight, and have a deflection of 5 cm (maximum value during our measurements), the bias over 2.8 m is $2.8(1/2)(0.05/2.8)^2 = 0.44$ mm. Therefore the overall measurement uncertainty is $\sqrt{0.4^2 + 2 * 0.15^2 + 0.44^2} = 0.7$ mm for a 3 m distance.

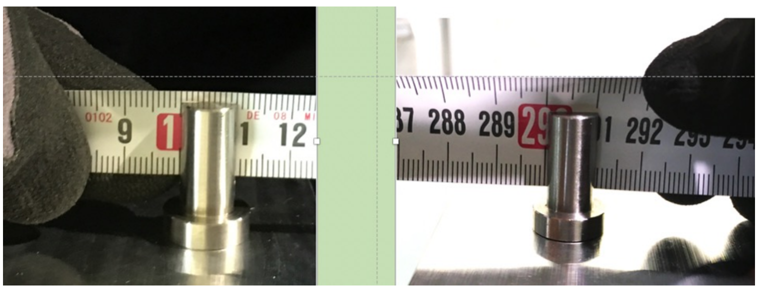

FIGURE 6.3: Example of distance reading. In this case, the distance between the two pins is 2900.5-100.0 = 2800.5 mm.

Template testing at IPHC - August 23, 2021

Before assembling the supports for the NCal at VIRGO, the system was assembled at IPHC for preliminary measurements as shown in fig. 6.4. Three distances needed to be measured labeled A, B and C and shown as plain black lines in fig. 6.4. Measurements are displayed in table 6.1. Their uncertainty was discussed in the previous section. The 5 m measuring tape was used. The "Expected" values are the distances from the CAD design. Their uncertainty is the assembly uncertainty. The measurements are in agreement with the expected values

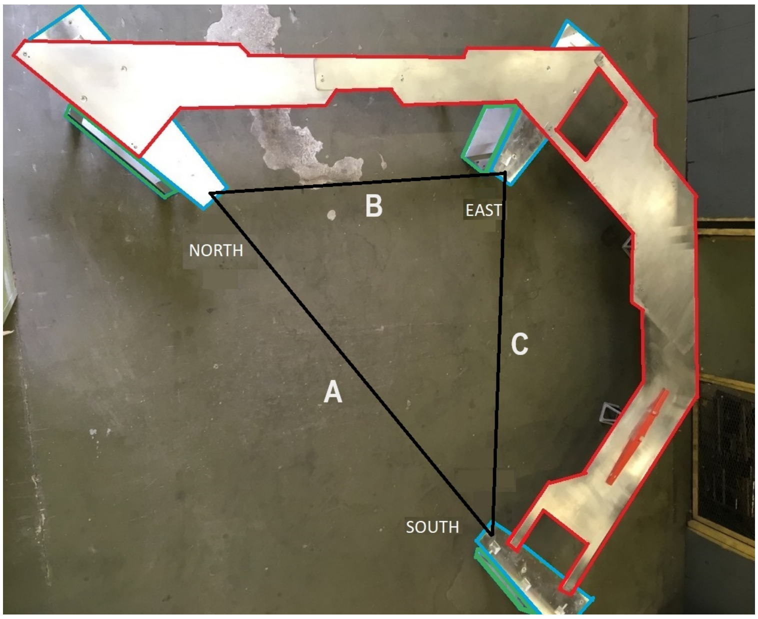

FIGURE 6.4: Top view of the complete assembly done at IPHC. The aluminum template made of four plates used for the positioning is outlined in red. The aluminum reference plates are in blue. The aluminum supports for the NCal are in green. The distances between the supports are shown as black lines labeled A, B and C

	Distance A [mm]	distance B [mm]	distance C [mm]
Measured	2800.5 ± 0.7	1812.0 ± 0.7	2318.0 ± 0.7
Expected	2800 ± 0.5 (1200+1600)	1812.5 ± 0.3	2318.6 ± 0.5

TABLE 6.1: Measurements made at IPHC.

On-site Assembly at Virgo NE - October 5, 2021

Once arrived at the site, the system was completely assembled in the NE building, next to the tower, to check again the distances between the reference plates just before the final assembly around the tower. Three sets of measurements were done using the 3 m and 5 m measuring tapes shown in table 6.2. Between each set, the template was disassembled and then assembled again. For the third and last set of measurements, the stacking order of the four plates composing the template was changed to see if there were some effect.

Measurement set	distance A [mm]		distance B [mm]		distance C [mm]
	3 m	5 m	3 m	5 m	3 m
1	2800.0 ± 0.7	2800.5 ± 0.7	1813.0 ± 0.7	1813.0 ± 0.7	2319.0 ± 0.7
2	2800.0 ± 0.7	2800.5 ± 0.7	1812.5 ± 0.7	-	2318.5 ± 0.7
3	2800.3 ± 0.7	-	1812.5 ± 0.7	-	2318.0 ± 0.7
Expected	2800 ± 0.5		1812.5 ± 0.3		2318.6 ± 0.5

TABLE 6.2: Measurement sets of the distance between the inner reference holes made at Virgo besides the tower using the 3 m and 5 m rulers.

Overall results and uncertainties

The averaged values of the measured distances are reported in table 6.3. These values agree with the expected values well within the mechanical systematic uncertainties. Therefore when considering the mechanical distance between the near reference holes we will use the last row of table 6.3.

	distance A [mm]	distance B [mm]	distance C [mm]
Average values	2800.3 ± 0.3	1812.6 ± 0.4	2318.4 ± 0.5
Expected values	2800.0 ± 0.5	1812.5 ± 0.3	2318.6 ± 0.5

TABLE 6.3: Average distances compared to the expected ones. The quoted uncertainties on the averaged values are just the RMS of the measurements, without the systematic uncertainty of the category 1 ruler (0.3 mm). The quoted expected uncertainty have been discussed in the template design section.

However, when positioning the references plates on top of their supporting frames, the foreseen 5 mm clearance of the assembling holes was not enough. Some holes on the supporting frames have been drilled again (for the north and east supports) with an offset approaching 1 cm in some cases. Because the installation on the tower was more difficult than the trial assemblies, the template could have been slightly distorted, introducing some shifts on the reference plates positions. In addition, the overall position of the NCal reference plates relative to the tower center is unknown by several millimeters. This confirms that the tower base is not an accurate reference frame.

6.1.2 Geometrical measurements in the Virgo reference frame

In October 2021 the reference plates for the NCal O4 system were installed and measurements were made during their assembly to mechanically check the distances between the near reference holes as described in the previous section.

In November 2021 the EGO infrastructure team made a survey on the position of the near and far reference holes on the reference plates around the NE tower.

In December 2023 the EGO infrastructure team made another survey on the position of the far reference holes on the reference plates around the NE tower. The near reference holes were no longer reachable due to the presence of the suspended vertical plates. The purpose of this last survey is to ensure that the relative distance between the NCals on the North to South axis remains consistent with the measurements taken two years prior to the first survey. One concern was whether the setups might have shifted slightly due to the ongoing work on the NCal system. This survey described hereafter allowed us to compute the NCal positions and relative distances.

Geometrical survey of November 16, 2021

The geometrical survey was made with a *LEICA laser tracker AT403* system using building reference points around the tower. The accuracy of this system is expected to be ±0.2 mm. Three stations were used to make the measurements, some of the points were measured through several stations. These points and the reference holes are displayed in table 6.4 as x and y coordinates in the Virgo Reference System (VRS) of the interferometer [46]. Notice that this reference frame swaps the x and y axis compared to the one used for the NCal study which is used everywhere in this document except when reporting the raw geometrical survey results.

Measurement point	Station 01		Station 02		Station 03	
	x [m]	y [m]	x [m]	y [m]	x [m]	y [m]
N201	2.5115	3000.4419				
N202	4.5120	3006.4206				
N204					-4.4878	3016.413
N205			-4.4919	3006.4162	-4.4918	3006.4162
N206					-4.4924	3000.4435
N208					-5.1473	2999.1256
N209			-5.7296	3012.4501	-5.7296	3012.4500
N210	4.6477	3012.3954	4.6481	3012.3959	4.6480	3012.3963
N211	3.3389	2996.7329				
North near			-0.8956	3007.1028	-0.8954	3007.1029
North far			-1.4642	3007.9254	-1.4640	3007.9255
East near			0.9161	3007.1075		
East far			1.4807	3007.9330		
South near	0.6935	3004.8000				
South far	1.2615	3003.9770				

TABLE 6.4: NCal geometrical survey measurements of November 16, 2021 (see logbook entry n°53883). Positions, in meters, are given in the global VRS frame of the interferometer.

Table 6.5 shows the distance between the near and far holes within each reference plates with geometrical survey values. The theoretical distance between the near and far reference holes is 1000.0 mm with a machining precision of 0.02 mm. The measured values are in agreement with the expected values within 0.1 mm compatible with the expected accuracy of a single station measurement. Furthermore the reference plates were machined during summer, without any tracking of the machining temperature which could have been up to 25°C, different from the 21.5°C of the NE building. The thermal expansion of the aluminum 7075 of 23.6 µm/m/°C and the 1 m distance translates to an uncertainty of about ± 0.08 mm, larger than the expected machining uncertainty of ± 0.02 mm and not very different from the observed difference of ± 0.1 mm.

Reference plate	Distance between near and far [mm]
North / station 02	1000.0
North / station 03	999.9
East / station 02	1000.1
South / station 01	1000.0

TABLE 6.5: Distance between the near and far reference holes on each reference plate based on the 2021 geometrical survey.

Geometrical survey of December 5, 2023

This survey was conducted two years following the initial one. The survey measurements are presented in table 6.6. Seven stations were used with different configurations compared to the four of the initial survey. Some points were measured using multiple stations. One can notice that the East far reference hole values have the largest fluctuation.

Measurement point	Station 1		Station 2		Station 3		Station 4		Station 5		Station 6		Station 7	
	x [m]	y [m]	x [m]	y [m]	x [m]	y [m]	x [m]	y [m]	x [m]	y [m]	x [m]	y [m]	x [m]	y [m]
N201					2.5117	3000.4421	2.5118	3000.4419						
N202					4.5121	3006.4206	4.5120	3006.4207	4.5118	3006.4204	4.5115	3006.4208		
N203									2.5117	3016.4154	2.5117	3016.4153		
N204	-4.4880	3016.4131	-4.4879	3016.4131							-4.4880	3016.4131	-4.4880	3016.4130
N205	-4.4921	3006.4165	-4.4918	3006.4162									-4.4921	3006.4162
N206	-4.4921	3000.4437	-4.4924	3000.4435										
N208	-5.1469	2999.1258	-5.1473	2999.1256										
N209			-5.7298	3012.4500									-5.7297	3012.4501
N210	4.6479	3012.3953	4.6483	3012.3962	4.6475	3012.3956	4.6476	3012.3956	4.6475	3012.3953	4.6477	3012.3957	4.6483	3012.3960
N211					3.3386	2996.7325	3.3386	2996.7326			3.3369	2996.7327		
North Far	-1.4647	3007.9252	-1.4640	3007.9255									-1.4642	3007.9253
East Far									1.4788	3007.9330	1.4793	3007.9331	1.4809	3007.9330
South Far					1.2609	3003.9769	1.2607	3003.9771						

TABLE 6.6: NCal geometrical survey measurements of December 5, 2023 (see logbook entry n°62657). Positions, in meters, are given in the global VRS frame of the interferometer.

Comparison between the surveys and the mechanical measurements

Table 6.7 brings together the measurements of the far reference holes made during both surveys. The difference between the surveys is less than a millimeter for the North and South far reference holes but just a bit more than 1 mm for the East far reference hole.

Date	Station	North far		East far		South far	
		x [m]	y [m]	x [m]	y [m]	x [m]	y [m]
06/11/21	01					1.2615	3003.9770
	02	-1.4642	3007.9254	1.4807	3007.9330		
	03	-1.4640	3007.9255				
05/12/23	1	-1.4647	3007.9252				
	2	-1.4640	3007.9255				
	3					1.2609	3003.9769
	4					1.2607	3003.9771
	5			1.4788	3007.9330		
	6			1.4793	3007.9331		
	7	-1.4642	3007.9253	1.4809	3007.9330		

TABLE 6.7: NCal measurements on the far reference holes from the November 2021 and December 2023 surveys. Positions, in meters, are given in the global VRS frame of the interferometer.

North to South far reference holes distance

In this section we combined the North far to South far reference hole distance measurements. Since each reference hole has been surveyed several times, we can combine the measurements to compute a set of distances for each survey as well as the combined of the two. The results are shown in fig. 6.5. The November 2021 survey made 2 measurements of the far North reference hole and 1 of the far South, we then compute 2 distances. The December 2023 survey made 3 measurements of the far North reference hole and 2 of the far South, we then compute 6 distances. A combination of both surveys can also be performed since the measurements should be compatible resulting in the computation of 15 measurements. The mean values are reported in table 6.8, where the RMS is only given for the combined results, since there are not enough values for the single surveys.

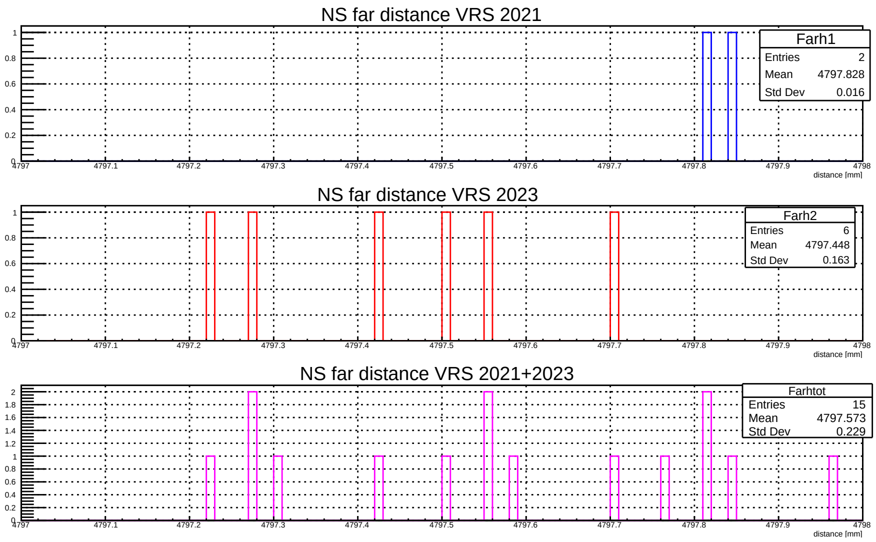

FIGURE 6.5: Distance between the North and South far reference holes using the combination of the VRS measurements. From top to bottom the 2021, 2023 and 2021+2023 combined measurements.

Survey	North to South far distance [mm]
2021	4797.83
2023	4797.45
2021+2023	4797.57 $\pm$ 0.23

TABLE 6.8: Mean values and RMS of the distance between the far reference holes along the North to South axis for different surveys.

The mechanical distance between the near reference holes is expected to be 2800 $\pm$ 0.5 mm (see the last row of table 6.3). Since the distance between the near and far reference holes on a plate is 1000.0 $\pm$ 0.1 mm (see table 6.5), the distance between the far reference holes translates to $2800 + 2 \times 1000 = 4800 \pm 0.5$ mm. This expected distance is 2.4 mm larger than the value of the combination of the 2021+2023 surveys. This is a bigger difference than the uncertainty on each value. Therefore we have to understand which is the more reliable value. The survey measurements are compatible between 2021 and 2023 within half a millimeter while the mechanical positioning using the metal template is less reliable due to the possible template deformation during the installation process. Therefore we decided to rely on the geometrical survey and use the position of the reference holes based on these measurements.

6.1.3 Geometrical position of the reference plates

Position of the NCal reference holes

As explained in the previous section, the new reference holes positions are from the average values of the 2021 and 2023 surveys. They are given in the VRS frame where the NE tower position center is at $x = 0.0129$ m and $y = 3005.7877$ m [46]. Table 6.9 shows the resulting average positions and RMS of the values converted to the NCal reference frame. The East near and South near positions were measured only once during the 2021 survey. Therefore, the displayed RMS value is selected as the maximum RMS among the position data for the reference holes and (if available) the tower measurements points across the surveys. Figure 6.6 shows a top view of the positions of the reference holes according to the mechanical center of the NE tower O(0,0). The angles ϕ between the setups axis and the beam axis are reported in this figure.

Object	x [mm]	y [mm]
North near	-1315.15 $\pm$ 0.34	-908.40 $\pm$ 0.35
North far	-2137.68 $\pm$ 0.34	-1477.12 $\pm$ 0.36
East near	-1319.80 $\pm$ 0.45	903.20 $\pm$ 0.35
East far	-2145.33 $\pm$ 0.45	1467.03 $\pm$ 1.10
South near	987.70 $\pm$ 0.45	680.60 $\pm$ 0.98
South far	1810.70 $\pm$ 0.45	1248.13 $\pm$ 0.98

TABLE 6.9: Average positions of each reference hole according to the values of the 2021 and 2023 geometrical surveys, relative to the tower center. The associated uncertainty is the maximum RMS among the reference holes and measurement points positions.

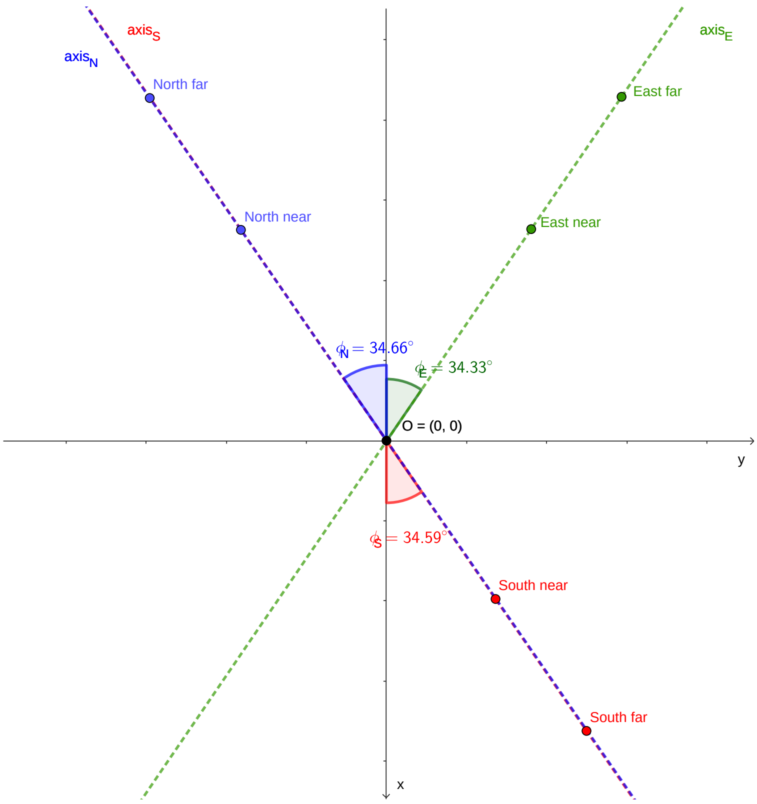

FIGURE 6.6: Top view of the position of the reference holes according to the average surveys measurements. The axis of each setup is the line drawn between the near and far reference holes of the setup as colored dashed lines. The center O is the mechanical center of the NE building. The beam axis is labeled as x.

The setup axes are not pointing to the center O but are slightly offsetted as seen on fig. 6.7. This results in a misalignment of the setup relative to the center O. The associated misalignment or "twist" angle ψ for each setup is between the setup axis and the line from the middle of each setup to the mechanical center O:

- $\psi_N = 0.02°$ towards -x.
- $\psi_E = 0.04°$ towards +x.
- $\psi_S = 0.01°$ towards +x.

These angles are well below the 0.1° expected mechanical twist uncertainty introduced in section 2.5.4 and will not be taken into account.

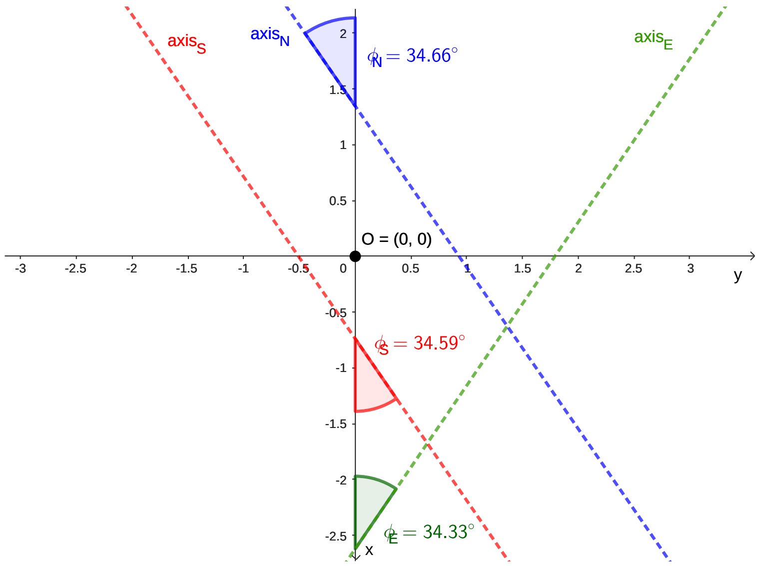

FIGURE 6.7: Zoomed in top view of the center of the mechanical center of the NE tower where the axis of each setup is shown as colored dashed lines. The beam axis is labeled as x.

Vertical offset of the reference holes

If the NCals are not in the ITF plane, their distance to the mirror is increased, leading to a change of the calibration that we will quantify. In addition to the NCal positions in the ITF plane, the 2021 and 2023 survey provided also the vertical offset relative to the tower center, a first order proxy for the mirror location. Table 6.10 shows the results of these measurements. Using the measurements of table 6.10 we compute the average elevation of each reference hole taking the maximum RMS of the measurement points as the uncertainty. The distance between the center of the reflector used by the survey and the reference plate is $25 + 10 = 35$ mm as shown in fig. 6.8. The dimensions of this reflector are shown in the drawing at the end of the technical note [47]. The previous value is then subtracted from the NE tower elevation (z=-0.902 m) provided by the EGO infrastructure [46]. The result is shown in table 6.11. Finally, the elevation of the NCals are computed using the drawing shown at the end of the technical note [48]. The NCal axis is elevated of $700 - 440 = 260$ mm from the reference plate. For each NCal we take the linear interpolation at the NCal position of the near and far reference hole elevation to which we add 260 mm. The resulting NCals axes elevation are shown in table 6.12, the uncertainties are taken as the same as in table 6.11.

Measurement Point	16/11/2021 z [m]			05/12/2023 z [m]						
	Station 1	Station 2	Station 3	Station 1	Station 2	Station 3	Station 4	Station 5	Station 6	Station 7
N201	-1.9632					-1.9631	-1.9631			
N202	-1.9995					-1.9991	-1.9992	-1.9992	-1.9992	
N203								-1.9979	-1.9979	
N204			-2.0023	-2.0023	-2.0024				-2.0023	-2.0024
N205		-1.9948	-1.9948	-1.9947	-1.9948					-1.9949
N206			-1.9924	-1.9926	-1.9925					
N208			-1.9916	-1.9915	-1.9915					
N209		-1.9938	-1.9938		-1.9937					-1.9937
N210	-1.9909	-1.9911	-1.9911	-1.9911	-1.9911	-1.9912	-1.9911	-1.9911	-1.9911	-1.9911
N211	-1.9989					-1.9992	-1.9991		-1.9976	
North Near		-1.1301	-1.1310							
North Far		-1.1303	-1.1314	-1.1298	-1.1298					-1.1299
East Near		-1.1310								
East Far		-1.1314						-1.1292	-1.1292	-1.1290
South Near	-1.1347									
South Far	-1.1344					-1.1363	-1.1363			

TABLE 6.10: NCal geometrical survey measurements of November 11, 2021 and December 5, 2023. Positions are in meters along the vertical axis.

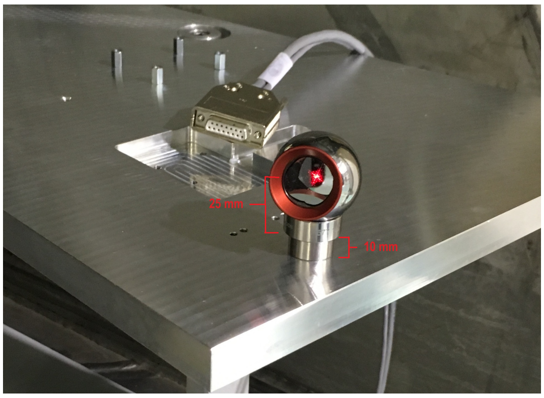

FIGURE 6.8: Picture of the reflector used to make the survey measurements on the reference plates with the support and the IPHC machined 10 mm spacer.

Object	z [mm]
North Near	-263.55 $\pm$ 0.64
North Far	-263.24 $\pm$ 0.78
East Near	-264.00 $\pm$ 0.12
East Far	-262.70 $\pm$ 0.12
South Near	-267.70 $\pm$ 0.90
South Far	-268.67 $\pm$ 0.90

TABLE 6.11: Average elevations of each reference hole according to the values of the 2021 and 2023 geometrical surveys, relative to the tower center. The associated uncertainty is the maximum RMS among the reference holes and measurement points positions.

NCal	axis elevation [mm]
NNN (1.7 m)	-3.52 $\pm$ 0.64
NNF (2.1 m)	-3.40 $\pm$ 0.78
NEN (1.7 m)	-3.87 $\pm$ 0.12
NEF (2.1 m)	-3.35 $\pm$ 0.12
NSN (1.7 m)	-8.18 $\pm$ 0.90
NSF (2.1 m)	-8.57 $\pm$ 0.90

TABLE 6.12: Axis elevation of each NCal.

6.1.4 Checking the setup to beam axis angle ϕ

As presented in section 2.5.5 the setup to beam angle was expected to be $\phi = 34.7°$ according to the drawing of the O4 NCal configuration. Using the survey positions of the reference holes we determined that each setup makes a respective angle relative to the beam axis different from the drawing value as shown in figs. 6.6 and 6.7.

To determine the uncertainty on the angle ϕ for each setup, we take the position of a reference hole and introduce an offset equal to the maximum uncertainty on these points from table 6.9. For all points, this uncertainty is along the y axis. Then, the difference between the setup axis draw with this offset and the setup axis (from figs. 6.6 and 6.7) is taken as the setup angle uncertainty $\delta\phi$. The results are shown in table 6.13.

Setup	ϕ	$\delta\phi$
North	214.66°	0.05°
East	145.67°	0.05°
South	34.59°	0.02°

TABLE 6.13: Uncertainty $\delta\phi$ on the setup to beam axis angle ϕ for each setup.

6.1.5 Checking the rotor twist ψ

In section 2.5.4 we discussed the method to determine the optimal twist value for the NCals with a rotor to beam angle $\phi = 34.7°$. Considering the new angles shown in figs. 6.6 and 6.7 we must check if the selected twist angle is still compatible with negligible signal uncertainties. Figures 6.9 to 6.11 show the maximum signal obtained using FROMAGE for a rotor on the North, East and South setup at respectively $\phi_N = 34.66°$, $\phi_E = 34.33°$ and $\phi_S = 34.59°$ with nominal distances from the mirror of 1.7 m and 2.1 m.

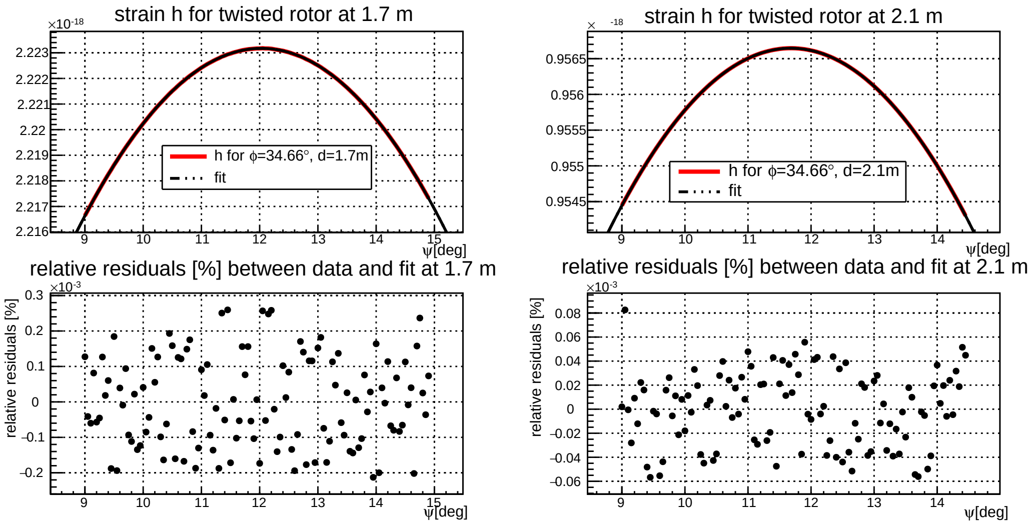

FIGURE 6.9: Top plots show the maximum signals for North NCal-to-mirror distances of (left to right) 1.7 m and 2.1 m at $\phi = 34.66°$, the red curves show the FROMAGE simulations and the black curve show quadratic fits. Bottom plots show the fit relative residuals which are usually the order of 10^{-4}%.

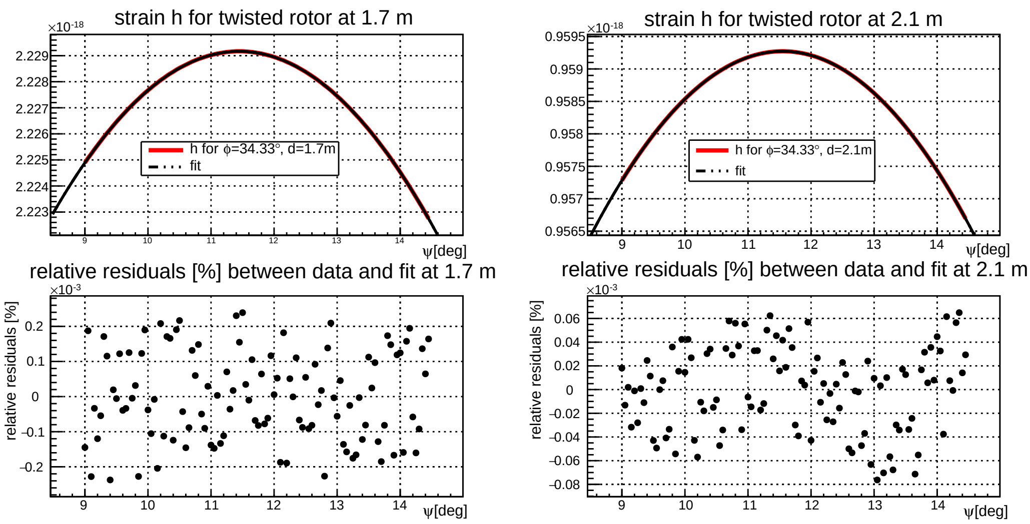

FIGURE 6.10: Top plots show the maximum signals for East NCal-to-mirror distances of (left to right) 1.7 m and 2.1 m at $\phi = 34.33°$, the red curves show the FROMAGE simulations and the black curve show quadratic fits. Bottom plots show the fit relative residuals which are usually the order of 10^{-4}%.

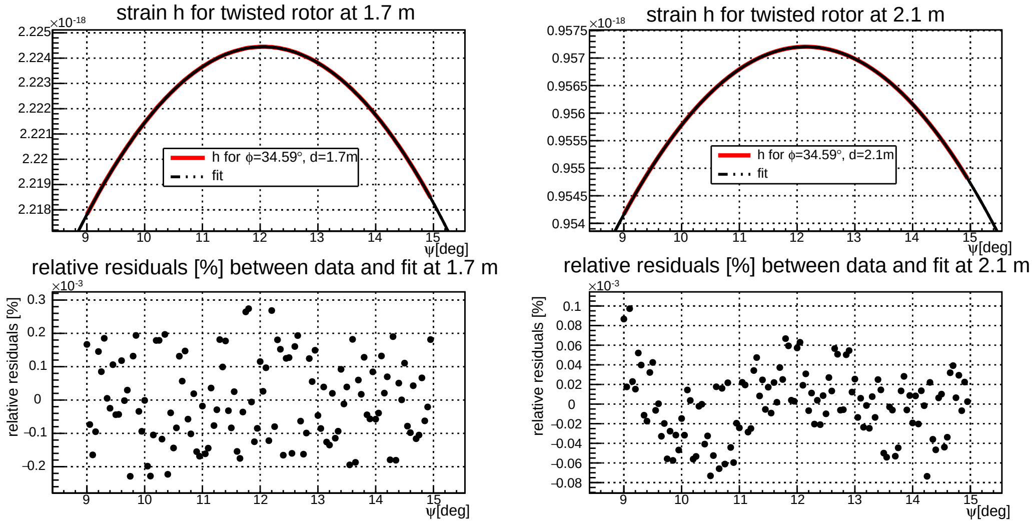

FIGURE 6.11: Top plots show the maximum signals for South NCal-to-mirror distances of (left to right) 1.7 m and 2.1 m at $\phi = 34.59°$, the red curves show the FROMAGE simulations and the black curve show quadratic fits. Bottom plots show the fit relative residuals which are usually the order of 10^{-4}%.

Using the fit results from figs. 6.9 to 6.11 we compute the twist $\psi_{\max}$ associated to the maximum signal for both NCal-to-mirror distances presented in table 6.14. These values are slightly different from 12.0° twist angle selected for all NCals as described in section 2.5.4. We can then use the fit of figs. 6.9 to 6.11 to evaluate the corresponding relative amplitude deviation of each NCal signal. These deviations are presented in table 6.14 and remain negligible.

Setup	$\psi_{\max}$ at 1.7 m	$\psi_{\max}$ at 2.1 m
North	12.03°	11.68°
East	11.45°	11.55°
South	12.05°	12.15°

TABLE 6.14: Twist $\psi_{\max}$ associated to the maximum signal for each setup distances.

Setup with $\psi = 12°$	Amplitude deviation [%] at 1.7 m	Amplitude deviation [%] 2.1 m
North	5.2×10^{-4}	2.4×10^{-3}
East	3.8×10^{-3}	3.2×10^{-3}
South	6.6×10^{-4}	1.3×10^{-3}

TABLE 6.15: Relative amplitude deviations for different NCal to mirror distances at a fixed $\psi = 12° \pm \delta\psi = 0.1°$.

6.2 Measurement of the NCals positions

Following the discussion made in section 6.1 to get the reference holes position, we now present the additional step to get the NCal positions. One NCal setup is composed of a reference plate and two NCals mounted on a suspended vertical plate.

To get the NCal position, we first have to go from the far reference hole to the far NCal rod, which correspond to the red dash line in fig. 6.12. Then we have to go to the other reference hole(s) (green dashed line), by measuring their distance. Finally, we have to go the NCal axis (black dashed lines). In addition, we have to evaluate the impact of a possible setup tilt. All these steps, which end by the NCal positions projected on the horizontal plane are described in this section.

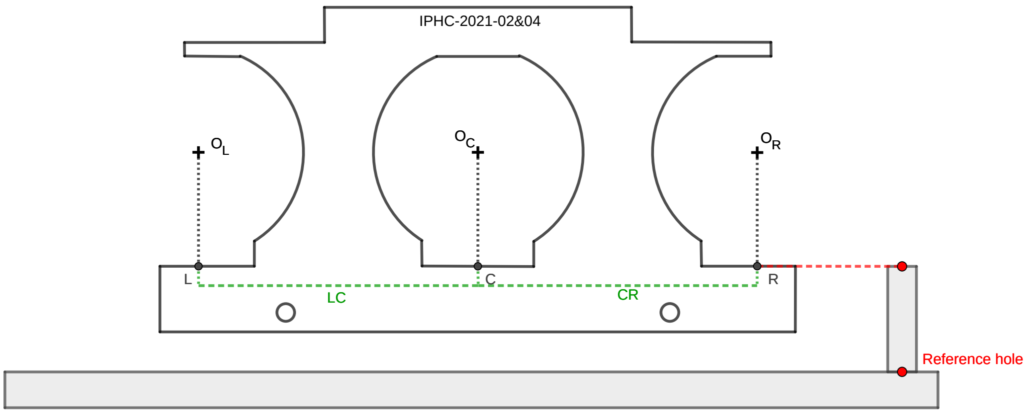

FIGURE 6.12: Outline of the front face of both North and South vertical plate suspended on a reference plate. The distances to be measured are represented as dashed colored lines.

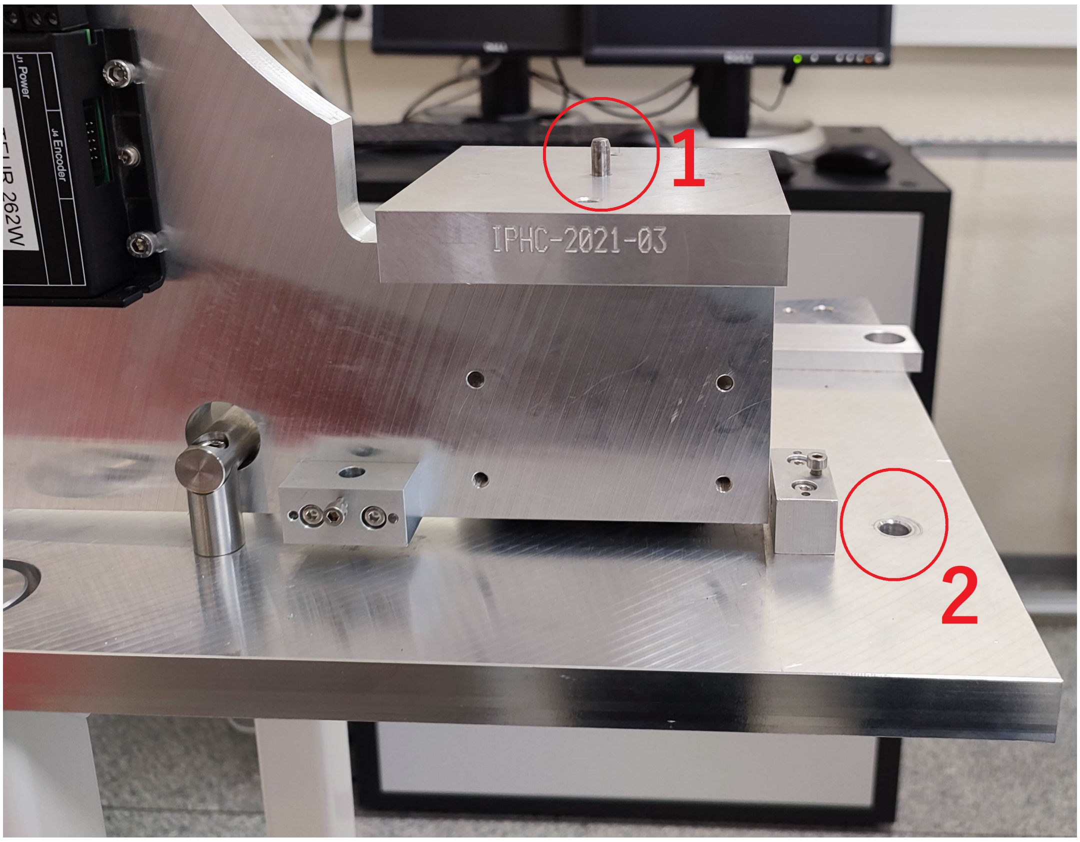

FIGURE 6.13: (1) is the right NCal rod of one of the suspended plate. (2) is a reference hole on a reference plate.

6.2.1 Distance between the reference hole and the far NCal rod

The NCal rods been on a suspended plate, their position is actually monitored by the suspended plate position sensors. Their zeros are made by setting the distance between the reference far hole (label 1 in fig. 6.13) and the far NCal rod (label 2), to the nominal 100 mm value. To do so, we used the tool presented in fig. 6.14 which is composed of a metal bar and a small aluminum plate which have two holes (100 ± 0.02 mm appart) to fit the metal bar and the NCal rod. For this measurement, three metal bars and small aluminum plates have been machined.

The installation process is shown in fig. 6.15. The metal bar has the purpose to place the small aluminum plate in an horizontal plane. We used small flat plates as spacers to hold the suspended plate still along the lateral and vertical directions as shown in fig. 6.16. They are 2.5 mm thick to fill the gap foreseen in the suspension drawing. Once the template is installed and the setup is still, the data coming from the position sensors is read. The channel bias is then adjusted to read zero.

After switching between the different templates and adjusting the setup back in a still position we observed that the greatest axial variation obtained for a single measurement was ± 0.1 mm around a mean value. Averaging several measurements, the uncertainty on the mean value is ± 0.05 mm. When swapping the vertical rod and/or the plate with the two holes, the results remain the same. The distance between the external NCal rod and the reference hole is then 100.00 ± 0.05 mm.

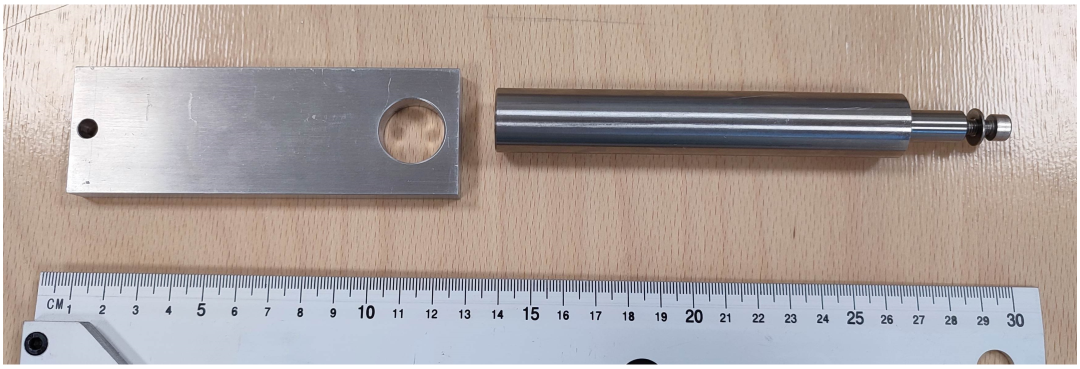

FIGURE 6.14: The two parts of a tool used. Left: the aluminum plate with the two holes of center distance = 100 mm. Right: the vertical bar.

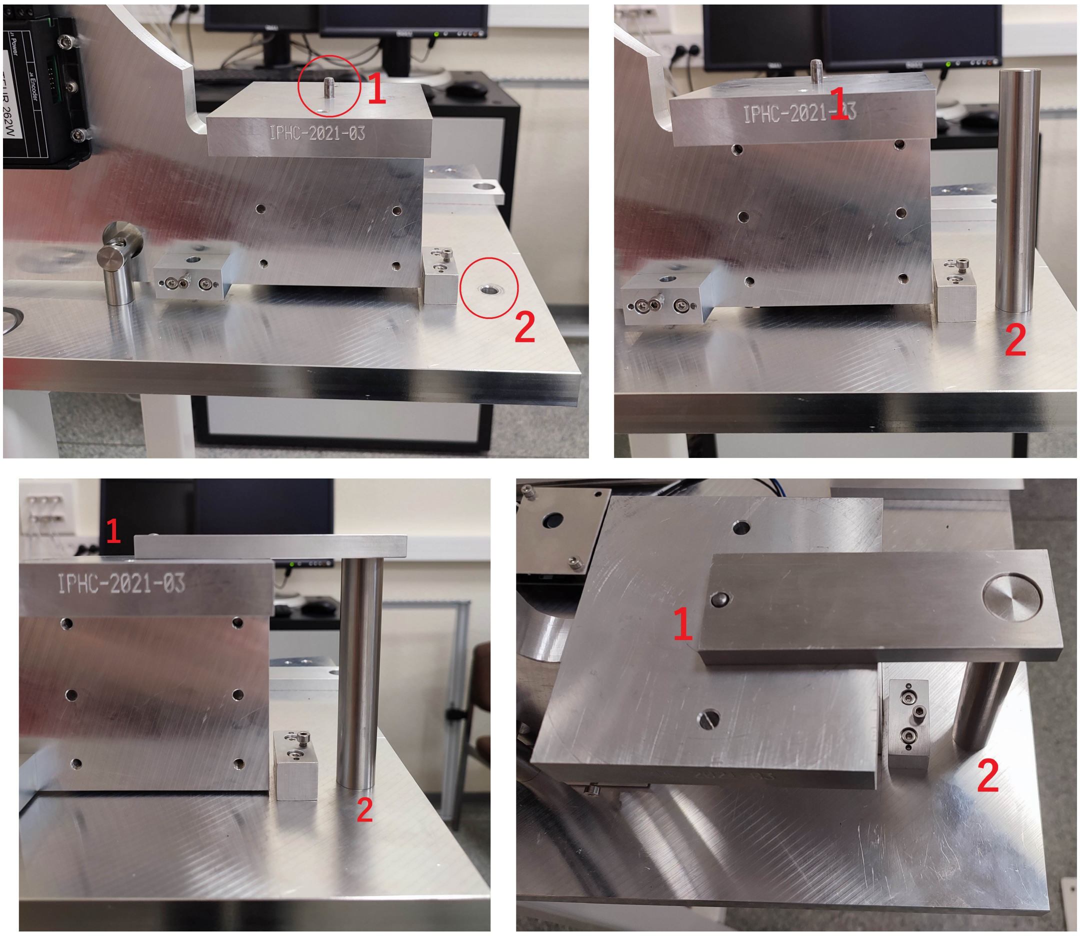

FIGURE 6.15: Installation of the template to set the distance between the NCal rod on the suspended plate (1) and the reference hole on the reference plate (2). The installation process is shown top to bottom and left to right.

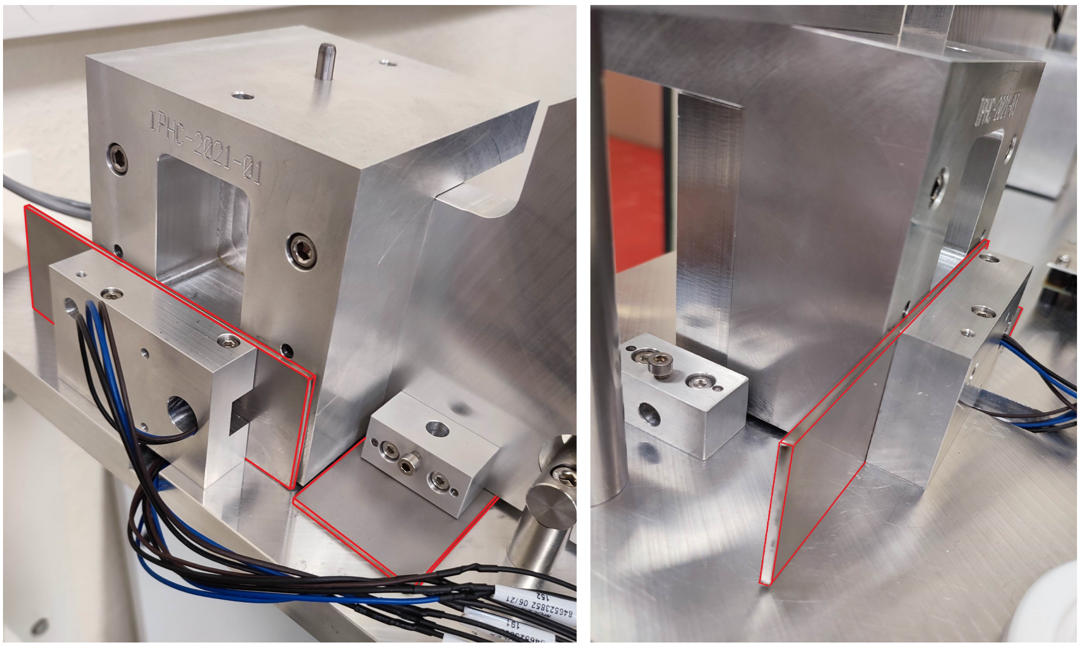

FIGURE 6.16: In red, the 2.5 mm metal plates used as spacers.

6.2.2 Distance between the NCal rods

Theorically there is 40 cm between each NCal rod on a suspended plate (see fig. 6.17). The rods are labeled L for left, C for center and R for right. These distances have been measured using a 1 m vernier caliper as shown in fig. 6.18. Several measurements of the NCal rods showed that they are approximately 6.04 mm in diameter (H7/g6 tolerance). This value is taken into account when computing the distance between each rod.

Table 6.16 shows the measured value of the distance between the NCal rods on the three suspended plates which are installed at the site. LC stands for left-center distance, CR for center-right and LR for left-right. In addition LC+CR refers to the addition of previously measured LC and CR, this distance should be the same as LR. The maximum difference is 60 µm meaning that the uncertainty of the measurements must be of the order of ± 30 µm on top of the vernier caliper precision of 20 µm. Therefore, we take the linear sum of the two values, 50 µm, as the overall uncertainty on the rod distances.

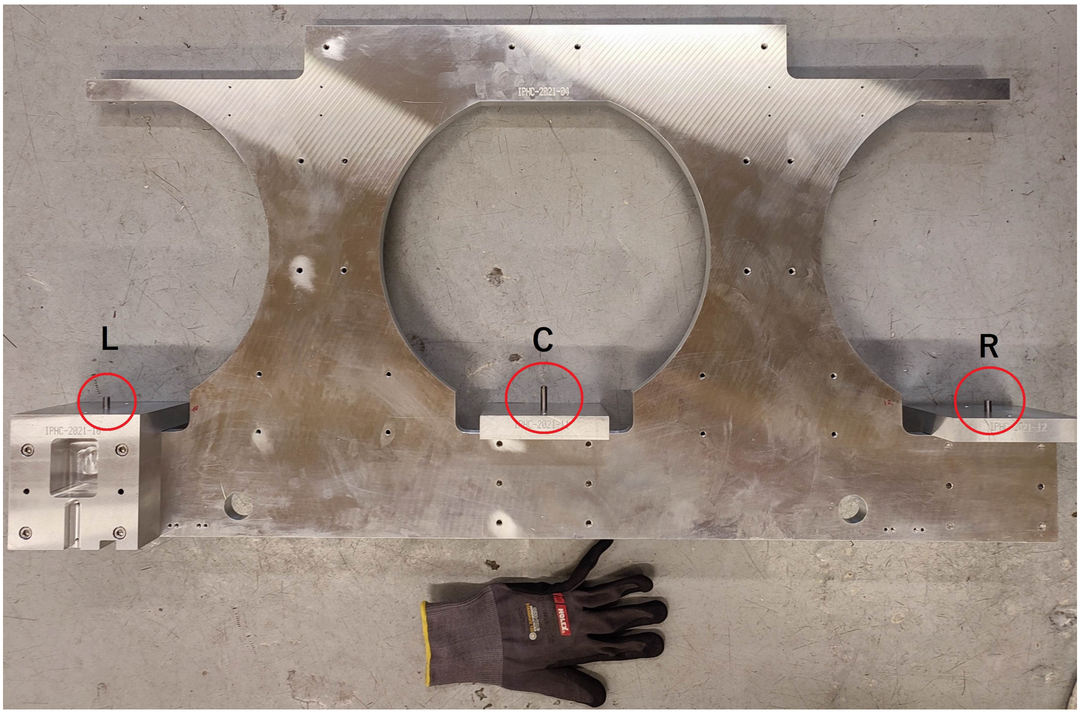

FIGURE 6.17: Front face of one of the suspended plates for O4. The labeled front face is marked "IPHC-2021-04". The NCal rods are circled in red and are labeled L for left, C for center and R for right. A drawing of a suspended plate is available at the end of the technical note [48].

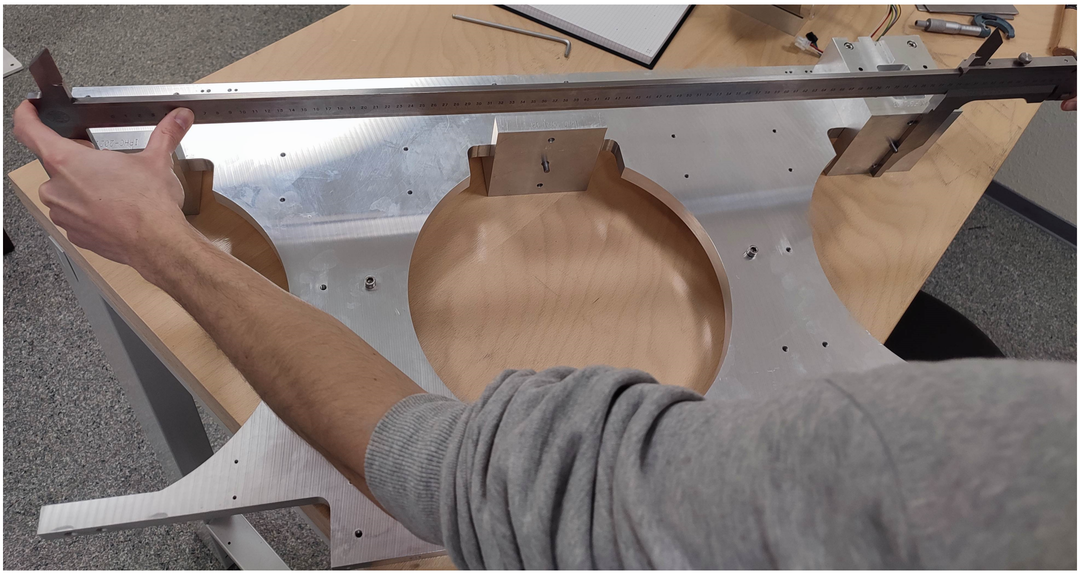

FIGURE 6.18: One of the suspended plates being measured using the vernier caliper.

Suspended plate	LC [mm]	CR [mm]	LR [mm]	LC+CR [mm]	(LC+CR) - LR [mm]
IPHC-2021-02 (South)	399.66	399.94	799.54	799.60	+0.06
IPHC-2021-03 (East)	400.18	399.78	799.96	799.96	0.00
IPHC-2021-04 (North)	399.76	400.46	800.24	800.22	-0.02

TABLE 6.16: Measurements on plates 02, 03 and 04 between the NCal rods. LC is left-center distance, CR is center-right, LR is left-right. The two last columns are derived from the first columns.

6.2.3 Determination of the NCal axis offset from the NCal rods

Due to the mechanical design of the NCal box, the NCal axis is not perfectly on top of the NCal rod of the suspended plates. This offset is measured by comparing two sets of measurements, with the NCal box turned by 180° around the NCal rod, as sketched on fig. 6.19. The NCal box has two different covers. One side is called S (side where there is a "small" metal part visible to hold the axis and the motor) and the other is called B (side where there is a "big" metal part holding the other side of the axis). The "Front" in fig. 6.19 label refers to the engraved side of the suspended plate. This method is performed four times per rotor with the 1 m vernier caliper. We then computed the average offset of each NCal box that is reported in table 6.17.

We compute the uncertainty on the measurement by taking the quadratic sum of $\sigma_{\text{measures}}/\sqrt{4}$ and the vernier caliper uncertainty (20 µm). The sign convention is taken as in fig. 6.19. These measurements are valid for a fully assembled NCal (rotor mounted with motor inside the NCal box and screwed), unmounting then mounting the NCal again is changing the offset. Therefore, when computing the uncertainty on the NCal position, we will use the conservative value of 300 µm, which is the largest measured offset.

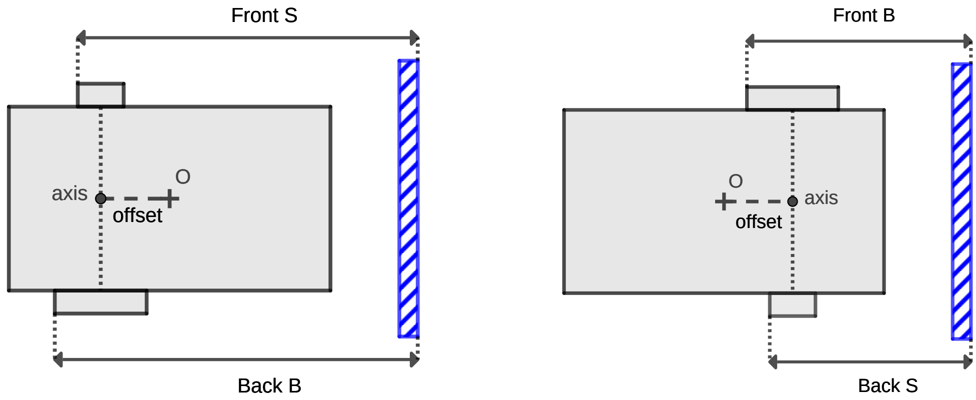

FIGURE 6.19: Top view of the two NCal positions used to determine the offset of the NCal axis relative to the NCal rod labeled as O. The NCal box, the "small" S and "big" B parts are shown in grey. S and B parts are used to measure the distance relative to a fixed screw shown in blue. By convention, this example has a negative offset.

NCal	Axis offset [µm]
01	+210 ± 30
02	+50 ± 30
03	-300 ± 30
04	+250 ± 40
05	+30 ± 20
06	+70 ± 20
07	-140 ± 70

TABLE 6.17: Axis offsets in µm of the NCals box.

6.2.4 Effects of possible horizontal tilts

During their installation, the reference plates were leveled better than 0.4 mrad according to the horizontal plane (this value was determined from the 2021 geometrical survey reported in section 6.1.2). When using the tool (see fig. 6.14) to set the axial distance we move by 125 mm along the vertical direction. The translation could give an uncertainty of $125 * 4 \times 10^{-4} = 0.05$ mm on the NCal position in the ITF plane.

The suspended plate may also be not perfectly leveled. The leveling of this plate was made using the 2.5 mm spacers (see fig. 6.16) and the position sensors on the reference plate. The total uncertainty is estimated to be 0.1 mm over 800 mm. When going from the plane of the NCal rods to the NCal axis, 135 mm above, this could give an uncertainty of $0.1 * 135/800 = 0.017$ mm.

To remain conservative we take the linear sum of both values, 0.067 mm, as the plane uncertainty on the distance between a NCal and a reference hole.

6.2.5 Distance between the NCals on the North to South axis

To compute the distance between two NCals on the North to South axis we use the distance between the North and South far reference holes of 4797.57 ± 0.23 mm from the last row of table 6.8. To this value we will subtract the distance between the considered NCals axes (which is taken as the NCals rods) and their associated far reference hole. Finally, the reading of the setup positions should be added when there is a significant offset.

The distance between an NCal rod and a far reference hole includes first the distance between the far reference hole and the closest NCal rod with a value of 100.00 ± 0.05 mm (see section 6.2.1). Then if the NCal is several slot away from the far reference hole we use the distance between the NCal rods on the corresponding suspended plate (see table 6.16) with an uncertainty of 0.05 mm. The NCals suffer a slight axis offset when mounted in their box varying from 0.03 to 0.30 mm depending on the NCal (see table 6.17). Since we plan to move the NCals throughout the O4 run, we chose to take 0.30 mm as the NCal axis offset uncertainty. Table 6.18 shows the distances of each NCal from the far reference hole and their uncertainty. For the East and North setups, the uncertainty is taken as the quadratic sum of all previous uncertainties with the setup position uncertainty of 0.03 mm (see section 2.5.7) for a total value of 0.31 mm.

Plate	NCal	Distance to reference hole [mm]
NN	Near	900.24 ± 0.31
	Far	499.76 ± 0.31
NE	Near	899.96 ± 0.31
	Far	500.18 ± 0.31
NS	Near	499.94 ± 0.31
	Far	100.00 ± 0.31

TABLE 6.18: Distances between each NCal to the far reference hole of the associated setup when the position sensor reading is zero.

The distance between two NCals on the same setup is also computed using table 6.16 and shown in table 6.19. The uncertainty is taken as the quadratic sum of the rod position uncertainty (0.05 mm) and twice the maximum axis offset of a NCal (0.30 mm) since two NCals are involved, making a total of 0.43 mm.

Plate	Near to Far NCal distance [mm]
NN	400.48 ± 0.43
NE	399.78 ± 0.43
NS	399.94 ± 0.43

TABLE 6.19: Distances between two NCals on a setup. The Near slots are at 1.7 m. The Far slots are at 2.1 m.

Using the results of table 6.18 we can compute the distance between two NCals on the North to South axis shown in table 6.20. The uncertainty on these distances is taken as the quadratic sum of the North to South far reference hole distance uncertainty (0.23 mm from last row of table 6.8), twice the table 6.18 uncertainty (0.31

mm) since two NCals are involved, and the plane uncertainty of 0.067 mm (see section 6.2.4) for a total uncertainty of 0.50 mm.

NCals	Distance [mm]
NNN-NSN	3397.39 ± 0.50
NNF-NSF	4197.81 ± 0.50
NNN-NSF	3797.33 ± 0.50
NNF-NSN	3797.87 ± 0.50

TABLE 6.20: Distances between two NCals on the North to South axis.

6.2.6 Geometrical position of the NCal slots

Using the measurements made in the previous sections, we can establish the geometrical position of the NCal slots on each setup in polar coordinates (d, ϕ) with d the distance to the center of the mechanical center of the tower and ϕ the angle of the NCal setup to the beam axis. The results are shown in table 6.21. To be accurate when computing the injected signal, we have to take into account the position sensors readout to correct for the axial and lateral offsets of the suspended setup.

The 0.36 mm uncertainty on the distance is the quadratic sum of:

- The distance uncertainty between an NCal and its far reference hole (0.31 mm).
- The distance uncertainty between the far reference holes and the mechanical center. This is taken as the North to South far uncertainty divided by $\sqrt{2}$ ($0.23/\sqrt{2}$ mm).
- The plane uncertainty (0.067 mm).

The uncertainty on the angle ϕ for each setup is given in table 6.13.

NCal slot	distance d [mm]	angle ϕ
NNN	1698.136 ± 0.36	$214.66 \pm 0.02°$
NNF	2098.616 ± 0.36	$214.66 \pm 0.02°$
NEN	1698.998 ± 0.36	$145.67 \pm 0.05°$
NEF	2098.778 ± 0.36	$145.67 \pm 0.05°$
NSN	1699.258 ± 0.36	$34.59 \pm 0.05°$
NSF	2099.198 ± 0.36	$34.59 \pm 0.05°$

TABLE 6.21: Polar coordinates of the NCals around the NE mirror relative to the mechanical center.

Chapter 7

NCal commissioning

Contents

Introduction

The NCal installation started in June 2021 by drilling holes in the tower base for the NCal reference plate supports. The commissioning phase started when one suspended NCal was available in June 2022. The installation of the six suspended NCals was completed on December 2022, allowing for few days of test from time to time. At the beginning of August 2023, the Virgo sensitivity started to be good enough to operate the NCal 24/7, providing a lot of interesting data and the opportunity to improve the system as we understood it better.

In this chapter, we will discuss the commissioning activities performed on the NCal system before Virgo joined the O4 run. We begin by introducing the process which controls the NCal rotations, focusing on the frequency and phase stabilization of the rotors. This is followed by the system's aging, primarily due to the friction of the ball bearings during rotor operation. Then, we explore the possible parasitic noises of the NCal system with the mirror. We discuss the process which monitors these calibration lines as well as the monitoring tools for the run. We then present the first measurement of the mirror position using the results of the monitoring tools after having mitigated the magnetic noise. Finally, we describe the choice of the frequencies for the NCal permanent calibration lines.

7.1 Real time control of the NCals

A major improvement of the O4 NCal system was to replace the commercial control system of the motor, which could be set to a given frequency, with a Virgo specific control system that could lock the NCal phase to the Virgo timing system slaved to a GPS clock. This allows long coherent integration time when doing the analysis of the NCal lines, as well as a more effective NCal lines subtraction for the $h(t)$ stream provided to the data analysis teams. This system combined two parts: the sensing and the actuation.

7.1.1 Sensing the NCal rotation

The sensing, i.e., the readout of the phase (and frequency) of a spinning NCal is done by an optical system. A LED is placed on one cover of the NCal box. A photodiode placed on the other side is monitoring the LED beam which is cut by the rotor at every half turn. Figure 7.1 shows the photodiode signal when a rotor makes a complete revolution. The two pulses correspond to the two sectors. The signal start at a low level, when the rotor prevents the light to reach the photodiode. When the sector moves away from the LED, a peak appears due to the LED reflection on the rotor flat side. Then, there is a plateau when no sector is in front of the LED followed by another peak when the next sector arrives. The cycle repeats with the following sector.

The aluminum rotors have been sandblasted on one side (i.e. painted white for the PVC rotors) so the reflectivity will change between each sector turn. This is why the two couple of spikes do not have the same amplitudes. This allow us to differentiate the sectors of the rotor.

The photodiode signal, sampled at 40 kHz, is analyzed every 100 µs by the real time process which controls the NCals. This process named "NEB_NCal" used the "Acl" framework developed for the real time control of Virgo. It measures the time of each new pulse, which could be converted to a rotor frequency when comparing to the time of the previous pulse, or to a phase for a given expected frequency.

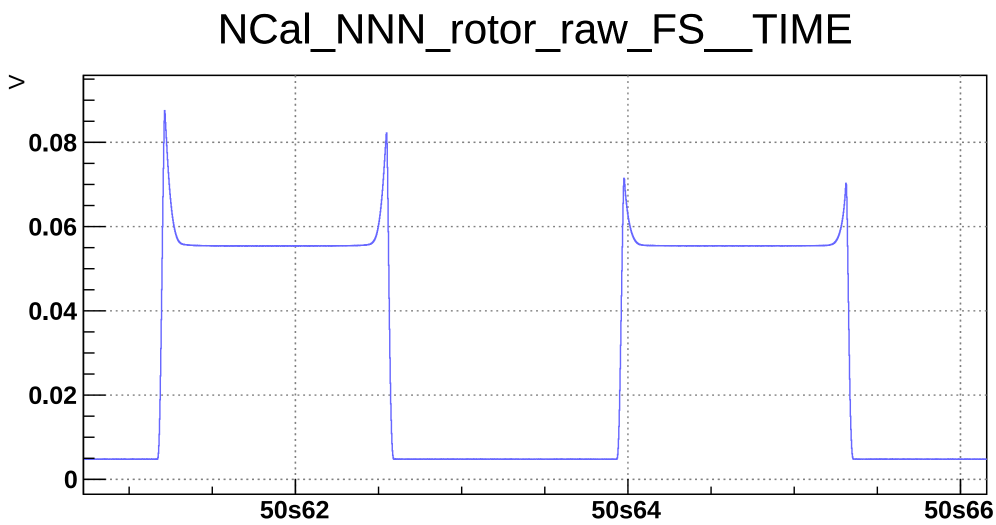

FIGURE 7.1: LED signal seen by the photodiode when a PVC rotor is operating at 18 Hz. The left pulse corresponds to the side painted white with a larger reflectivity.

7.1.2 Actuating the rotor

The rotor motor is driven by a controller, which, for a given input analogue value (voltage), sends the needed currents to achieve the expected rotor frequency. The NEB_NCal Acl process computes this analogue value based on the measured frequency or phase, depending on the control strategy used. At startup, the first strategy is to control the frequency. Two types of controls are used:

- The first type is called the *ON-OFF* mode which is used when the rotor is accelerating to achieve the required speed. In this mode, we first set the voltage sent to the motor controller to a large value for a fast acceleration. Then, we send 0 when the requested speed is reached. When the rotor frequency drops below the requested value, we return to the previous voltage value. This mode is not accurate but serves as the initial step in the frequency lock process.
- The second type, called *Smoothing* mode follows the *ON-OFF mode*. Instead of turning the voltage completely off and then back on, the voltage is computed by applying a control filter to the frequency readout to smoothly reach the requested frequency.

When the rotor is locked in frequency, the phase locking process is manually triggered. The frequency control is then disabled, allowing the phase to slowly drift. When the phase reaches 0, the process is similar to the *Smoothing Mode* presented before: the voltage is adjusted to reach the desired rotor phase by filtering the phase readout.

Figure 7.2 shows the frequency and phase during the locking process of the rotor control. Figure 7.3 shows that the rotor is stable once the phase loop control stabilizes. The phase fluctuates around 0 by ± 1 mrad. Further investigations will be presented on the NCal stability at the start of O4b in the next chapter.

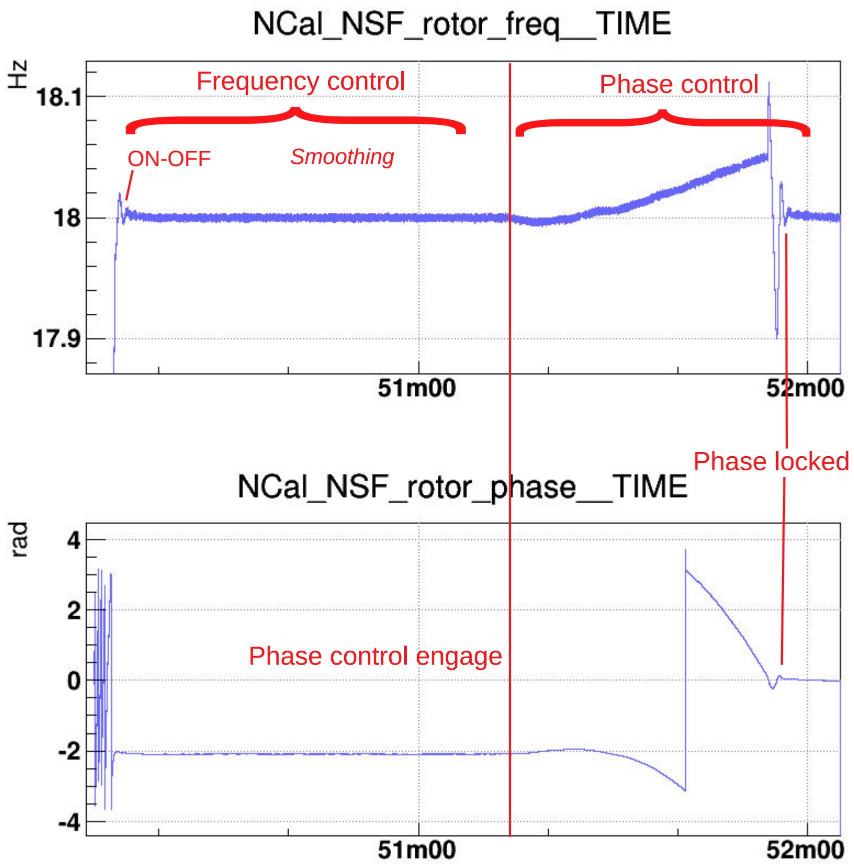

FIGURE 7.2: Top, frequency readout plot of the rotor NSF. Bottom, phase readout plot. The *ON-OFF* and *Smoothing* locking types are shown on the frequency readout. The phase control engage and locking is shown on the phase readout.

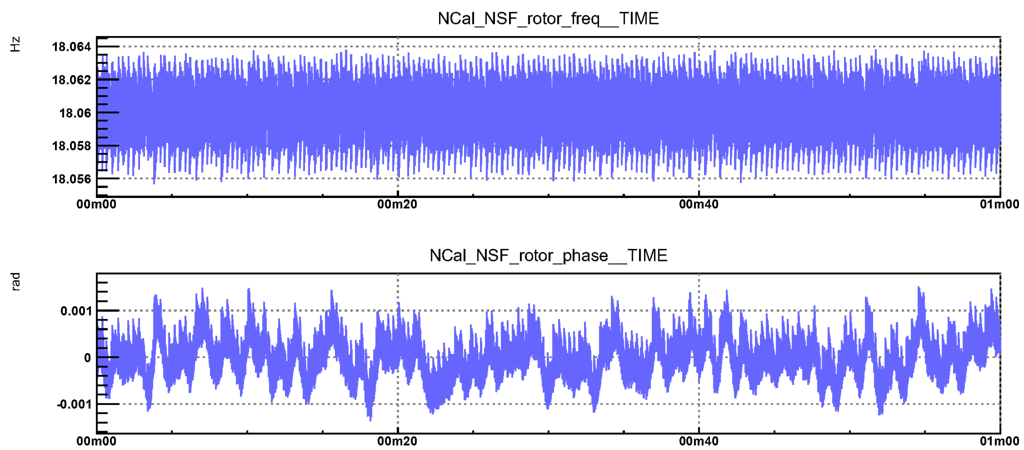

FIGURE 7.3: Frequency (top) and phase (bottom) readouts of a the rotor NSF for 60 s with the phase loop control closed.

7.2 NCal reliability pre-O4

One of the goals of the NCal is to maintain a reliable system over time. This reliability is primarily driven by the condition of the ball bearings impacted by small defects during their installation or possibly by aging after some time of operation.

7.2.1 Rotor friction

We first studied the rotor friction with the six NCals installed on December 2022. They were equipped with the following types of ball bearings:

- R4-02/04/05/06/07: Two single row bearings (ref: FAG 61802-2Z-HLC).
- R4-03: A double row bearing (ref: FAG 3802-B-2RSR-TVH-HLC) on the motor side and a single row on the other side.

We operated the six NCals at 70 Hz and stopped the motor to study the friction of each NCal. Figure 7.4 shows the observed slow down rate as function of the rotation speed. We notice that at the highest rotation speed close to 70 Hz, all rotors have the same slow down rate within less than a factor 1.5. Whereas at lower speed there is more than a factor 5 difference. Since the air friction is expected to be the same for all rotors, we deduce that at high rotating speed, the friction of the rotor is air dominated. On the contrary, at low rotating speed, solid friction becomes dominant, which is primarily induced by the bearings.

Figure 7.4 shows that rotors 04 and 07 have the largest friction. Therefore, we decided to replace them in June 2023. Once we remove the two worst rotors, the next one is the rotor equipped with a double row bearing (R4-03) which is expected to have a larger friction.

7.2.2 Detecting damaged bearings

The state of the operating rotors can be monitored using the microphones installed on each setups (see section 2.5.6). This is mostly an indicator of the condition of the NCals. That was our primary tool to detect the few NCals which had a problem. For these NCals, we observed an increase of the noise over time until we changed them. Figure 7.5 shows the RMS of the microphone readout installed on the Far location of the South NCal setup. In this case, the NCal NSF was replaced with another one as seen at around 8:00 UTC. The acoustic noise was reduced when the NCal was restarted. Figure 7.6 shows the microphone spectrum before the rotor swap (magenta curve) and after the swap (blue curve) with a reduction of the noise in the high frequency band.

We remark that most rotors have been operated for over a year without showing aging signs. Usually, when a rotor is diagnosed with a bearing issue, it is detected within a few weeks after its installation.

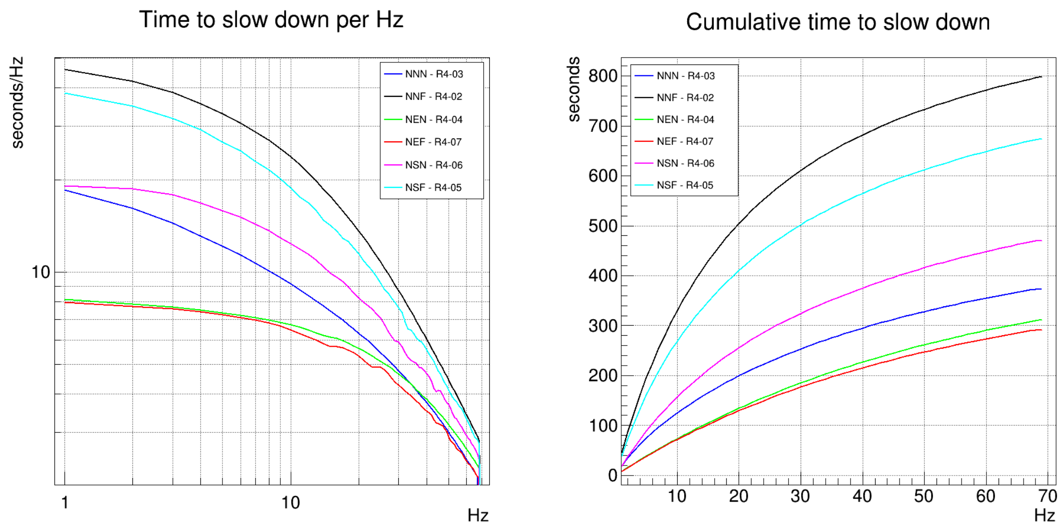

FIGURE 7.4: Friction measurements of the NCals. Left: slow down rate expressed as seconds per Hz as function of the rotor frequency. Right: cumulative time for the NCal to stop as function of the start frequency.

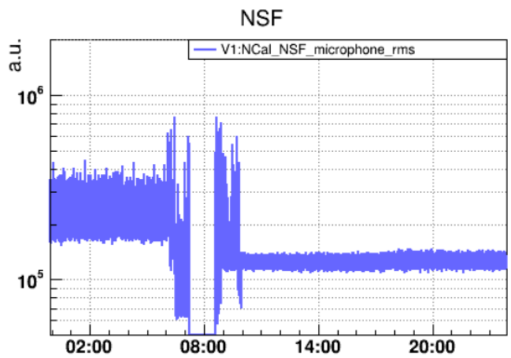

FIGURE 7.5: RMS of the microphone installed on the Far location of the South setup. The NSF rotor replacement occurred at around 8:00 UTC.

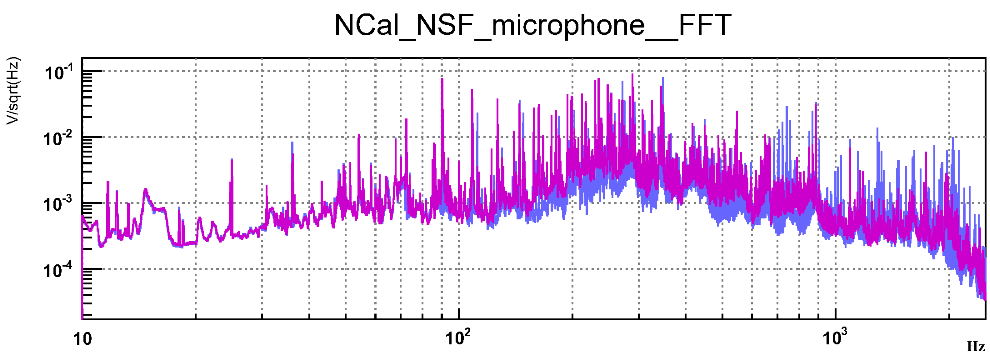

FIGURE 7.6: Spectrum of the microphone installed on the Far location of the South setup. Magenta curve: spectrum of the microphones before the NSF rotor replacement. Blue: after the replacement.

7.2.3 Motors aging

The motors have been changed since O3 so the rotors would achieve greater rotation speed. We now use 70 W EC frameless motors (reference n° 548270 from *maxon*). No motors have been changed since the O4 NCals have been assembled, there was no degradation in their performance even after months of continuous operation at Virgo.

7.3 Investigating parasitic noises

A parasitic noise is defined as any process that induces a signal in the interferometer other than the foreseen NCal signal. If this noise appears at twice the rotor frequency for a two-sector rotor (or three times the frequency for a three-sector rotor), it combines with the injected signal and biases it. Therefore, it is crucial to understand if such a noise exists to either mitigate it or account for it. Additionally, noise induced over a wider frequency band than the main NCal signal causes contamination in the online data $h(t)$.

The parasitic noise induced by the NCal in the interferometer is expected to be gravitational or magnetic.

The gravitational parasitic noise is expected to come from of a few sources. The suspended setup's motion acting on the mirror as they can move at twice the rotor's frequency. The rotor's induced motion on the suspension of the mirror, the *marionette*, transferring to the mirror. Another gravitational coupling that was already taken into account for O3 is the induced torque on the mirror. Since no specific commissioning activity was carried on for the gravitational parasitic noises, they will be discussed in the next chapter when evaluating the overall uncertainty on the NCal signal.

The magnetic noise would come from the operated rotor generating a magnetic field acting on the magnets on the mirror. Early during the commissioning of the NCal system, magnetic lines at twice the rotor frequency were observed by the environment monitoring probes. This triggered specific actions that will be described in this section.

The other commissioning activity was to search for an unexpected parasitic noise. The will be the second part of this section.

7.3.1 Magnetic noise

Observing the magnetic noise

As introduced in section 1.3.3, small magnets are attached to the mirror as part of the EM actuation process to control its position. These magnets are therefore sensitive to parasitic magnetic fields. For this reason, the magnetic field in the building is monitored by magnetic sensors. In april 2023, the NCals were started for a few days. The Virgo environment monitoring group searched for possible couplings and noticed in one of the magnetic probes (ENV_NEB_MAGV) a signal of about 0.1 nT (see fig. 7.7). This probe which was temporarily placed at the base of the vacuum chamber very close to the North NCal setup, was used to enhance the observed magnetic field. Figure 7.8 shows a zoom of the frequency band around the 2f NCal signal with a longer integration time. There are two orders of magnitude between the weakest and loudest signals, primarily due the different probe-to-NCal distances.

To investigate this magnetic issue, we designed dedicated coils and installed them on the extremities of the NCal setup structures. They have been placed at 1.7 m from the Near NCals such that the measured magnetic field at their location should be similar to the one at the mirror location. These measurement coils are made of copper with the following characteristics: an internal radius $R_{int} = 106$ mm, an external radius $R_{ext} = 116$ mm and ~ 760 turns. They have been tested and cross checked with the environment sensors.

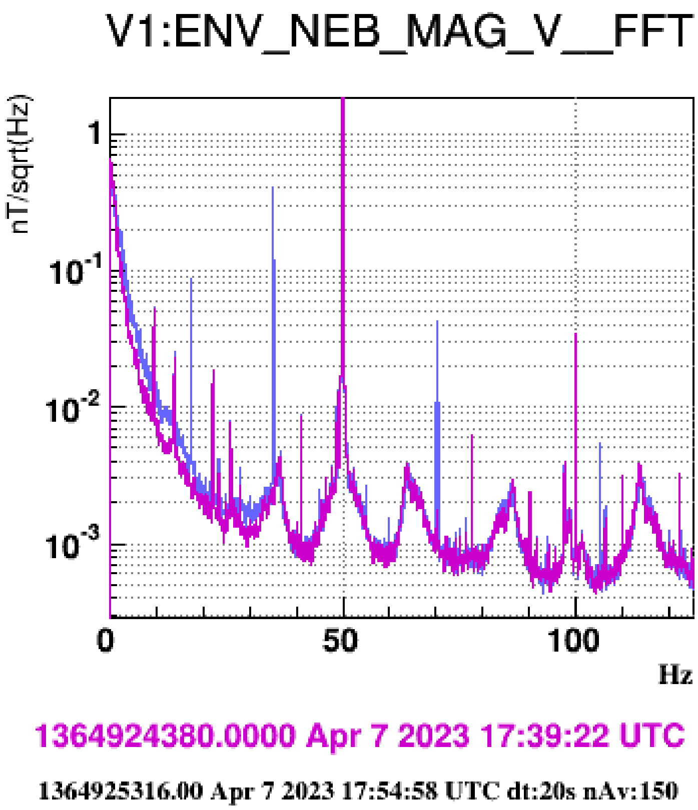

FIGURE 7.7: Magnetic field measurement with FFT of 20 s using ENV_NEB_MAGV sensor placed at the base of the NEB tower. Pink (resp. blue) curve corresponds to magnetic field with stopped (resp. rotating) rotors.

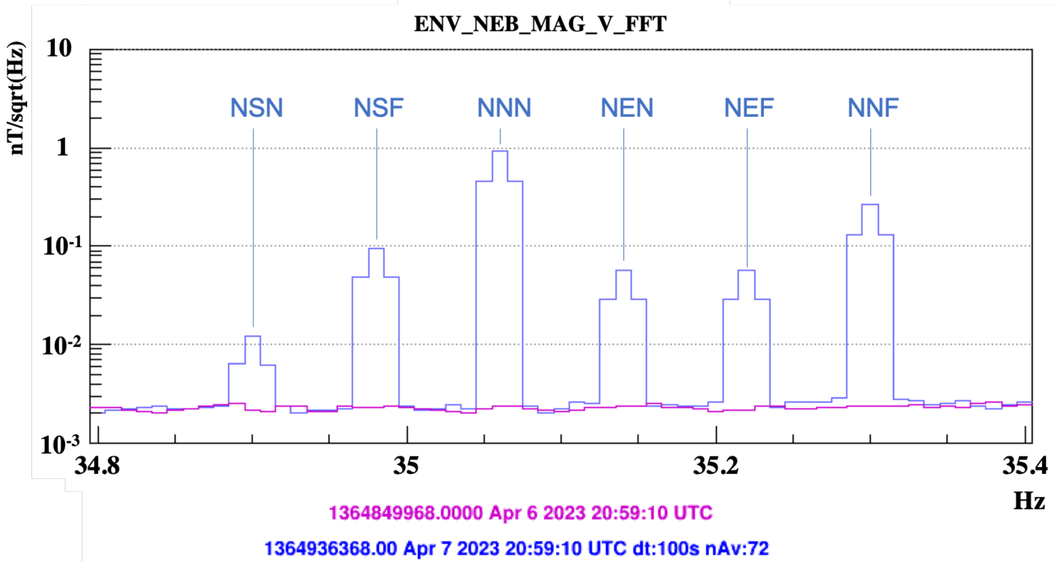

FIGURE 7.8: Zoom of the magnetic field measurement with FFT of 100 s using ENV_NEB_MAGV sensor placed at the base of the NEB tower. Pink (resp. blue) curve corresponds to magnetic field with stopped (resp. rotating) rotors.

Evaluating the magnetic noise

Then we decided to simulate the effect of NCal magnetic lines on the mirror with the NCal at rest. For this, we used small coils installed on some NCal housings (see fig. 7.9). These generating coils are made of copper with the following characteristics: a rectangular shape of $11 * 15 = 165$ cm^2 and ~ 50 turns. We generated a sinusoidal current of an amplitude equal to the magnetic field measured by the measurement coils. The resulting mirror displacement was measured and compared to the predicted NCal gravitational effect computed with FROMAGE. This magnetic noise resulted in a parasitic motion of 0.5% minimum.

The original O4 NCal setup, before February 2024, was composed only of aluminum rotors. However, as this material is known to be conductive, under the effect of the ambient magnetic field, Eddy currents could form in the moving rotor. These currents would then produce a variable field, opposite to that of the environment, which can explain the observed magnetic noise. If this is the case, using a different material can reduce magnetic noise.

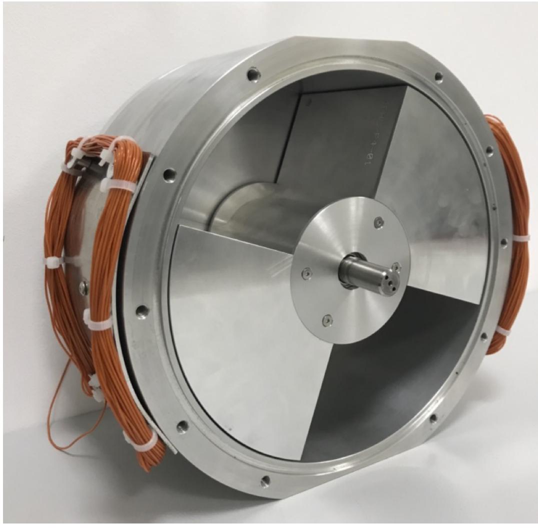

FIGURE 7.9: Side view of one opened NCal with a two branch aluminum rotor. The two generating coils are attached on each side of the box. The NCal box cover was removed for the picture.

Origin of the magnetic noise

A first test was performed to check that the magnetic field, measured at twice the rotor frequency, was not induced by the motor We measured the magnetic field produced by a three sector aluminum rotor (see fig. 7.10). For this we checked the spectrum at two and three times the rotor frequency. This is shown in fig. 7.11 for a three sector rotor operating at 21.2 Hz. We observed a magnetic field line only at three times the rotor frequency (63.6 Hz) and nothing at two times the rotor frequency (42.4 Hz). This confirms that the magnetic lines are not induced by the motor, but by the rotor sectors.

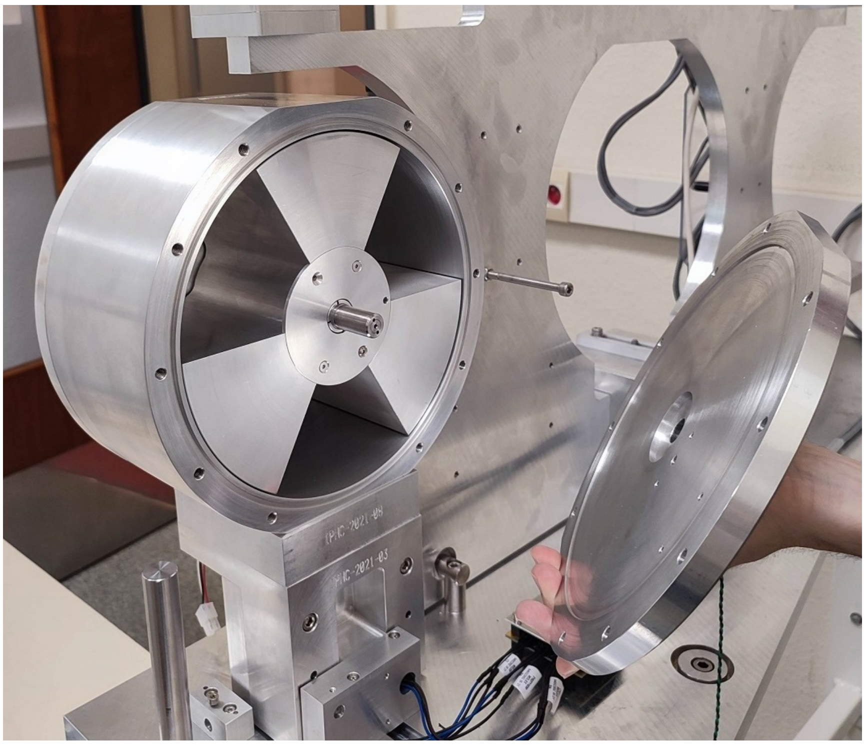

FIGURE 7.10: Three sector rotor in its box with the cover removed.

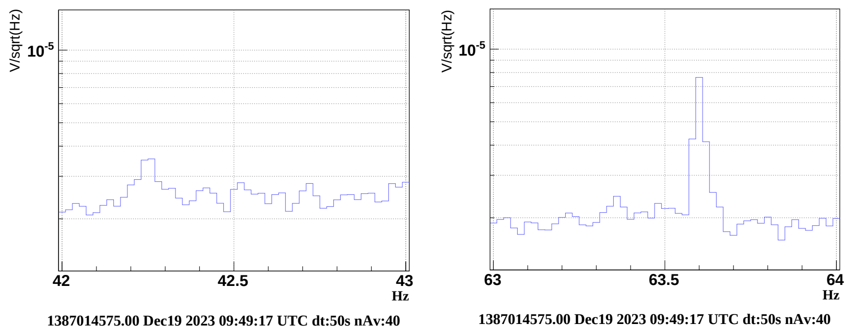

FIGURE 7.11: Magnetic signal generated by a three sector rotor. Left: zoom around twice the rotor frequency (21.2 Hz). Right: zoom around three times the operating frequency.

Mitigating the magnetic noise

A first simple solution tested during the commissioning phase was to wrap the NCals in magnetic shielding film (MCL61 from YSHILD®). This was done for the Far aluminum NCals in December 2023. The residual magnetic field measured by the coils was reduced by at least a factor 3. As a result, the magnetic noise of the Far aluminum NCals was reduced to less than 0.2%. Another option for future improvement could be to use iron boxes instead of aluminum ones to contains the magnetic field inside the NCal housing (iron is easier to machine than mu-metal).

A second solution was to replace some aluminum rotors with PVC rotors, a non conducting material. Measurements showed a reduction of the magnetic field by almost two orders of magnitude compared to aluminum rotors, making it negligible. As PVC rotors are about half as massive as aluminum ones, the induced gravitational amplitude is also reduced by a factor of 2. Therefore, in February 2024, we first installed them on the Near locations where the injected signal is about two times larger than for the Far location. One down side of PVC is its elasticity, already mentioned in section 5.4. Rotation speed larger than 50 Hz can lead to permanent deformation of the rotors. For these reasons, we kept some aluminum rotors for injections of NCal signals up to 150 Hz for the start of O4b, and continue the investigation to reduce their magnetic field.

Magnetic field compensation has also been tested. Using the two coils centered on a NCal (see fig. 7.9), we generated a magnetic field that compensates the one generated by the rotor. However, we observed that the magnetic field was not symmetrical, i.e when turning the NCal by 180°, the observed field value was not the same. This seemed strange, given the explanation of Eddy current coming from the ambient field. However, we noticed that the NCal axis (made of steel) is producing a magnetic field, similar to the terrestrial magnetic field. Therefore, when turning the NCal, the two fields either add or subtract, resulting in different Eddy currents. This fields changes from one rotor to another. Although the compensation seems attractive, it requires a precise knowledge of the field at the position of the mirror, something that is currently not possible.

7.3.2 Remaining parasitic noise

Possible other parasitic noises can induce an unpredicted mirror motion. Figure 2.21 shows that there is a value of twist ψ for which the induced gravitational signal becomes null. Therefore, at this angle, residual parasitic couplings to the mirror can be probed. For this purpose, we have set the twist of Near East NCal to $89.7 \pm 0.1°$ as shown in fig. 7.12. The remaining gravitational effect of the NCal is expected to be less than 0.1% of the nominal signal produced by a similar rotor with a 12° twist. In addition, for this value of twist, measurements in laboratories predict that the magnetic noise is less than 0.005%, and the parasitic signal due to displacement of the setup is expected to be below 0.001%.

At this twist value, we observed a signal of 0.1% of the nominal NCal signal in the spectrum of the interferometer, shown in fig. 7.13. We use this value as the upper limit for the remaining parasitic noise, excluding the magnetic noise. For aluminum rotors, the magnetic noise dominates over the other residual effects, raising this value to 0.2%.

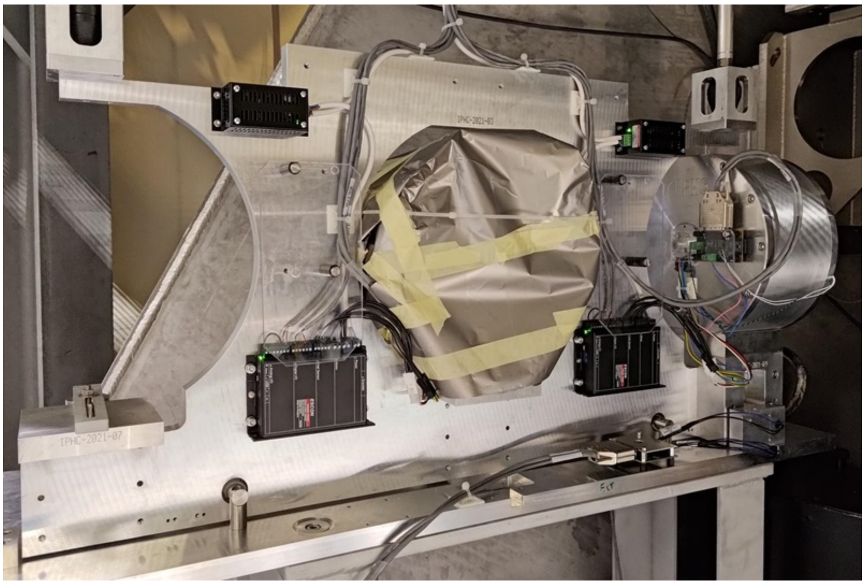

FIGURE 7.12: Picture of the East NCal setup. The left NCal (NEF) is wrapped in a magnetic shielding film. The right NCal (NEN) is twisted by 89.7°.

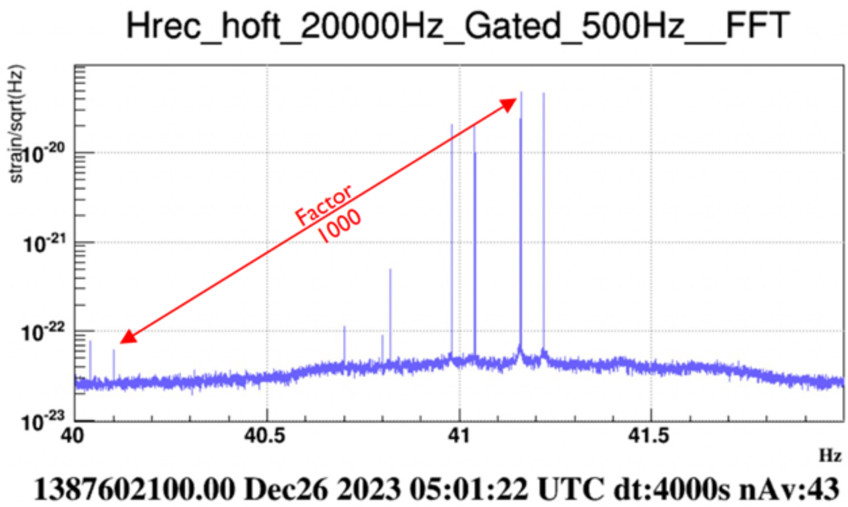

FIGURE 7.13: Spectrum of the interferometer showing NCal lines at twice the rotation frequency. The 89.7° twisted NEN NCal amplitude line is a factor 1000 less than the (12° twisted) NNN NCal line. The FFTs are 4000 s long.

7.3.3 Remark on the magnetic noise

The detection of the NCal magnetic noise became possible due to the increased accuracy of the NCal system compared to O3. This phenomenon was unexpected before the measurements presented here. We were able to reduce this noise by implementing PVC rotors and adding magnetic shielding to aluminum ones leading to respectively 0.1% and 0.2% upper limit couplings.

7.4 Preparing the monitoring of the NCal lines

During commissioning we have developed the principle of the NCal continuous operation. It is based on a set of permanent lines and a software to compute their amplitudes. In addition, diagnostic tools to monitor the NCal system were developed.

7.4.1 Example of injection lines during commissioning

As one of the O4 goals is to have a continuous NCal operation, the rotors have been permanently operating since August 2023. The injected lines are visible in the online version of the reconstructed strain, before the calibration lines subtraction, $h_{raw}(t)$. Figure 7.14 shows the spectrum of $h_{raw}(t)$ with the injected lines of the six NCals as of March 17, 2024. On this figure while studying parasitic noises, NEN was twisted by 90°, emitting no gravitational signal. The Near NCals were in PVC, the Far ones were in aluminum.

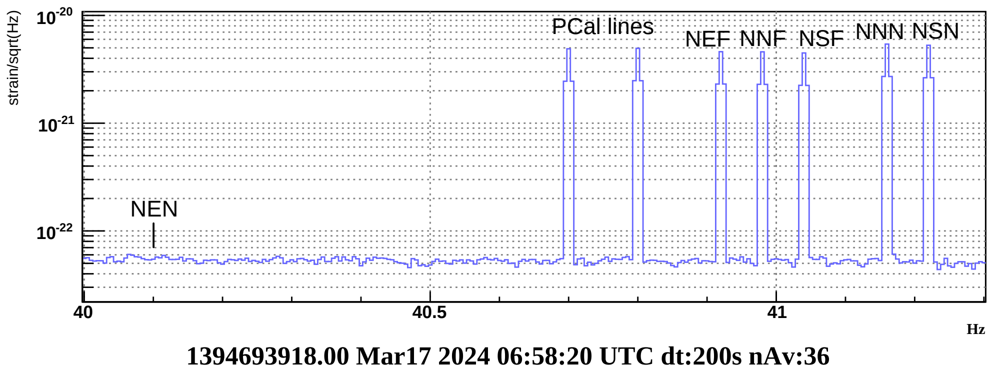

FIGURE 7.14: Injected NCal and PCal lines at around 40 Hz in the reconstructed strain before calibration lines subtraction, h_{raw}. Near NCals are in PVC, and Far NCals are in aluminum. NEN was twisted by 90°, emitting no gravitational signal. The FFTs are averaged over 200 seconds.

7.4.2 The *NCalMoni* process

After injecting NCal lines, they must be extracted from $h(t)$ to make calibration measurements. This section describes the method used to extract them.

The online process, called *NCalMoni*, is used to compute the amplitude of the NCal signals in $h(t)$ using 200 s FFTs. The following conditions are required for the amplitude to be computed:

- The rotor must be spinning ($f > 0$ Hz).
- The rotor phase must be stable within 0.03 rad.
- The interferometer must be in operation with a lock index above a threshold.

Once these conditions are fulfilled, the line amplitude and associated quantities are computed. Figure 7.15 shows the computation process of an NCal amplitude. Three bins at the rotor frequency are used to compute the line amplitude and five bins on each side are used to compute the noise floor. This allow us to compute the SNR of the recovered NCal line, characterizing the quality of the calibration measurement.

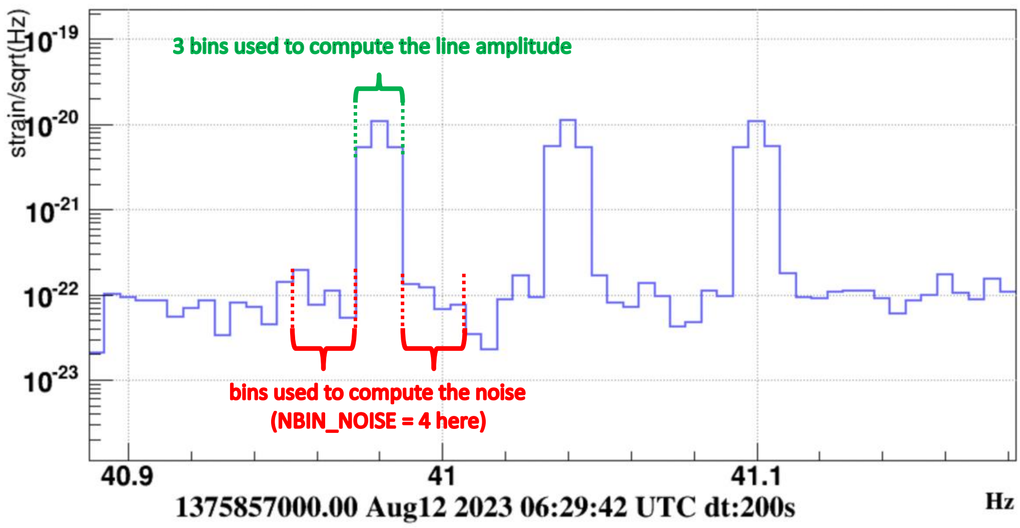

FIGURE 7.15: NCal line and noise extraction process performed by *NCalMoni* on the online data $h(t)$. The amplitude is computed using three bins. The noise is computed using bins around the line, four bins in this example but five bins in the online configuration.

7.4.3 The online monitoring and alert system

The monitoring of the NCal system, among various interferometer systems, is available online on the Virgo Interferometer Monitoring (VIM) page. The data to be displayed on this page can be modified to correspond to the monitoring needs. This page groups information such as:

- The frequency and phase of the NCals through the day.
- The position sensors, microphones and magnetic sensors readout.
- The signal to noise ratio (SNR) of the NCal lines in $h(f)$ and DARM.
- The h_{rec}/h_{inj} NCal ratios and the PCal comparison.

Additionnaly, a system of alerts was implemented through the Virgo Detector Monitoring System (DMS). DMS allow the operators to keep track of the interferometer's state and check issues. Systems are being monitored using quantities like the ones computed by the *NCalMoni* process. They are translated to a single summary page with colored boxes for each component of the Virgo detector. DMS sends emails to the NCal team in case of malfunction. This is triggered by any of the following conditions:

- The rotor is too slow, compared to the requested frequency, or is stopped.
- The phase drifts by more than 0.04 mrad.
- The temperature of the NCal box is too high, above 40°C.

It is common that frequency and phase alerts triggers during the maintenance time when the NCals stop due to small motion of the setup induced by people moving on the tower structure where they are attached.

7.5 Finding the mirror position offset using pairs of NCals

To use the NCal information, especially the h_{rec}/h_{inj}, we need to use a pair of NCals to reduce the uncertainty due to the NCal-to-mirror distance as explained in section 2.5.3. This uncertainty could be further reduced if we use the actual mirror position. This section will first present how this could be done with a pair of NCals.

On February 20, 2024, to mitigate the magnetic parasitic noise, two PVC rotors were installed on the North and South near slots. In addition, the Far NCals were wrapped with magnetic shielding. Therefore, we use the data of evening of February 20, 2024 to make a first clean measurement of the mirror position and adjust the h_{inj} value of the monitoring program. The results are presented in the second part of this section. The mirror position will be further discussed in the following chapters describing the ER16 data and the beginning of O4b.

7.5.1 Parametrizing the NCal signal in one dimension

We first compute with FROMAGE the equivalent NCal strain moving the mirror along the North to South axis. We call the result a one dimension "FROMAGE map". As we expect the mirror to be at the mechanical center of the NE tower within 50 millimeters, we can use this value for the limit of the 1D-maps. Then, we fit each map using a polynomial fit to get a parametrization of each NCal signal.

These parameters are function of the rotor's geometrical parameters determined in chapters 3 and 4 and its position determined in chapter 6 corrected from the axial and lateral offset read by the position sensors. The axial value is computed with the mean of the Near and Far values for each setup. The lateral value is associated to the NCal slot since the position sensors are on the Near and Far slots of each setups. By default, the NCals are twisted 12° with respect to the center of the reference frame (see section 6.1.5). We thus implement a correction on the twist angle ψ on each NCal to get the good orientation.

Figure 7.16 shows the FROMAGE 1D-map of a Far rotor (at $d = 2.1$ m from the mirror) on the South setup and the residues of a linear, quadratic and cubic fit. As a convention, a positive value translates to a mirror offset towards the North setup. The following cubic fit results are in agreement with FROMAGE within 10^{-4}%:

$$h(d) = p_0 + p_1 d_0 + p_2 d_0^2 + p_3 d_0^3 \tag{7.1}$$

with $p_{0,1,2,3}$ the fit parameters. As an example, the NSF 1D-map parameters from fig. 7.16 for an offset d_0 in millimeter are the following:

- $p0 = 9.582\,26 \times 10^{-19}$
- $p1 = -1.821\,18 \times 10^{-21}$
- $p2 = 2.166\,87 \times 10^{-24}$
- $p3 = -2.055\,22 \times 10^{-27}$

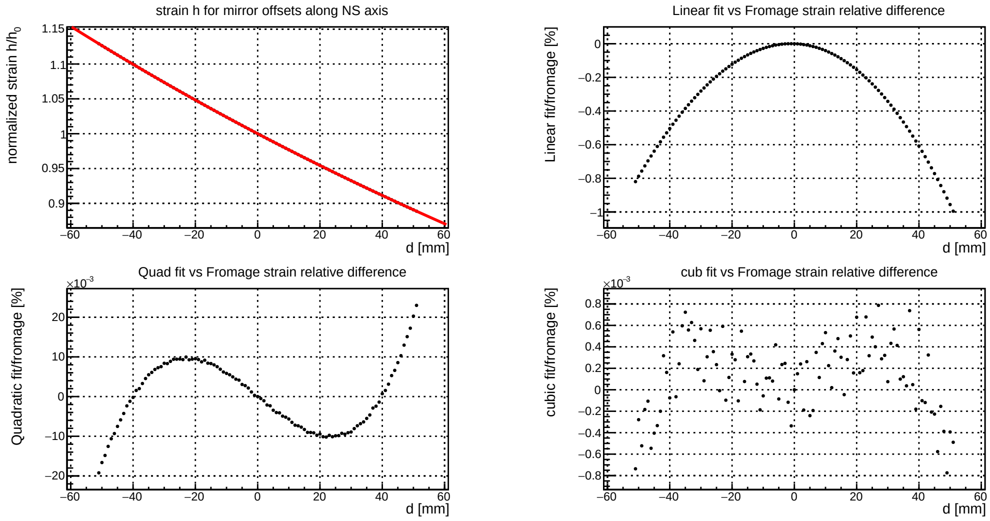

FIGURE 7.16: Top left is the FROMAGE 1D-map of the equivalent strain for a South Far NCal on the mirror for given radial distances. Top right, bottom left and bottom right show the relative residues between the FROMAGE 1D-map and respectively a linear, quadratic and cubic fit.

7.5.2 Measurements

Once we have the expected injected signal with the parametrization, we adjust it to the reconstructed signal by optimizing the d_0 value. We use the recovered NCal signal from the *NCalMoni* process computed with 200 s long FFTs. To minimize data pollution, we request a minimum SNR of 50 on the amplitude of one of the NCals. Using about 1.5 hours of data from February 20, 2024, we obtained the following mirror position with the NCals operating around 20.5 Hz:

- Near NCals $d_0 = 4.41 \pm 0.12$ mm
- Far NCals $d_0 = 4.19 \pm 0.34$ mm

Uncertainties are only statistical ($\sigma/\sqrt(n)$). We remark that both measurements are compatible. Therefore, we decided to take the average value, 4.30 mm, as the measured mirror offset during commissioning. We will discuss systematic uncertainties in the following chapters where more data are described.

7.6 Selecting the frequencies of the NCal permanent lines

The main goal of the NCal system is to continuously inject stable calibration lines. This section discusses the choice of the frequency of these lines. This choice is a trade-off between maximizing the SNR, minimizing the NCal aging (low frequencies are better) and avoiding frequency bands with known continuous astrophysical signals (pulsars). During commissioning, the Virgo sensitivity evolved as the noise reduced and changed the line SNR for a given frequency. The selection of the permanent lines for the run was made just before the start of the ER16 engineering run preceding the O4b start.

To find the band with maximum SNR, we compared the expected NCal line amplitude to the Virgo noise spectral density $h(f)$ (the sensitivity curve). This is shown in fig. 7.17 for an aluminum and a PVC rotor. The top plot shows the strain of the

Virgo interferometer with the frequency dependent rotor amplitudes. The NCal line amplitudes were computed using FROMAGE with the nominal rotor geometry at $d = 1.7$ m, $\phi = 34.7°$ and $\psi = 12°$, for 200 second integration time. The PVC rotor frequency domain was limited to 100 Hz in $h(t)$ (50 Hz operating frequency) due to risks of plastic deformation as explained in section 5.4. The aluminum rotor was limited to 150 Hz in $h(t)$ (75 Hz operating frequency) due to motor limitations. The bottom plot shows the SNR of the NCal lines. The SNR is maximum in the 35 to 60 Hz frequency band. To minimize the NCal aging we select frequencies in the lower part of this frequency band. We pick frequencies around 36 Hz which is free of known pulsars. This means that the NCal operating frequencies are around 18 Hz.

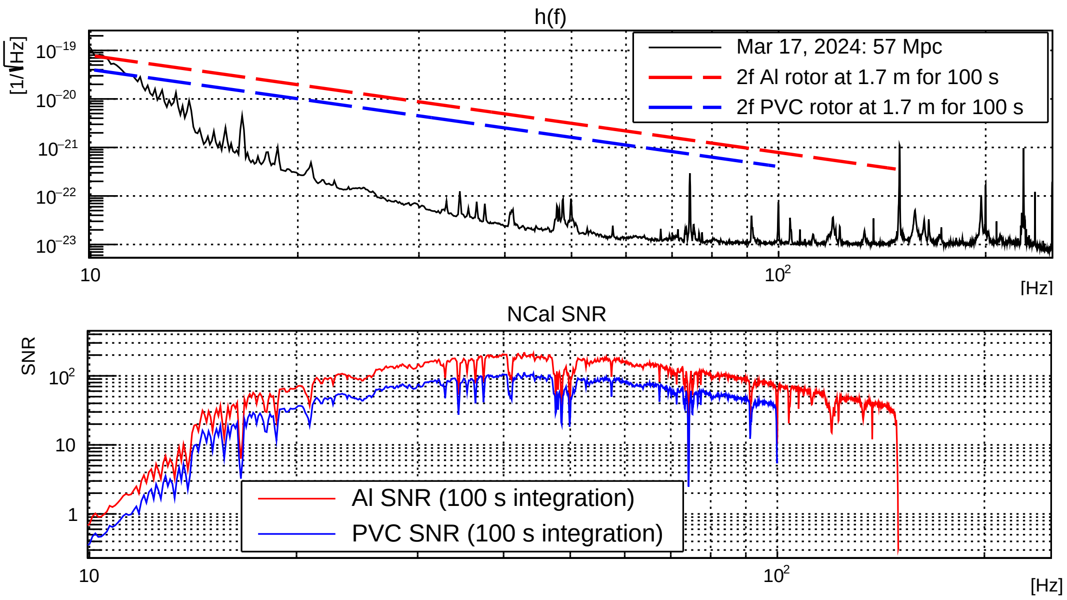

FIGURE 7.17: Top: spectrum of the Virgo strain during O4b on March 17, 2024 with the amplitude of an aluminum (red) and a PVC rotor (blue) calibration lines. Bottom: SNR.

Chapter 8

The engineering run ER16

Contents

Introduction

The engineering run number 16, ER16, started on March 20, 2024. It ends on April 10, 2024, with the start of the O4b observing run. During this period, the Virgo interferometer operated under similar conditions as at the start of the run with the aim of consolidating the duty cycle and carrying out pre-run measurements like detector calibration.

In this chapter, we discuss the NCal operations performed during ER16. We begin by presenting the status of the NCal system at that time. Next, we detail the measurements of the mirror position using multiple NCals, a key parameter for determining the injected signal. This is followed by a discussion on the parasitic couplings, continuing the section 7.3 on the NCal commissioning. We then provide a preliminary estimation of the NCal systematic uncertainty and compare the Near and Far NCals. Finally, we explain the decision to recalibrate the PCals using the NCals.

8.1 Calibration during ER16

8.1.1 Conditions of the NCal system

During ER16, the NCal configuration was the following:

- North setup: NNN was the PVC rotor R4-12 and NNF the aluminum rotor R4-02.
- East setup: NEN was the PVC rotor R4-11 twisted by 89.7° (see section 7.3.2) and NEF the aluminum rotor R4-06.
- South setup: NSN was the PVC rotor R4-14 and NSF the aluminum rotor R4-03.

Different operating frequencies were used during this period to perform various tests. They are shown in fig. 8.1, the resulting NCal signal in $h(f)$ was at twice the shown frequency. During the first four days of ER16, the NCals were operating around 20.5 Hz (i.e. 41 Hz in $h(f)$), frequencies which were selected months before, when the noise was larger at lower frequency. Then, for frequency scan checks with the PCal, they were shortly operating at higher frequencies, between 20.5 and 67.5 Hz (i.e. 41 Hz and 135 Hz in $h(f)$) and at lower frequencies around 15.5 Hz (31 Hz in $h(f)$). Finally, they have been set to their nominal O4b operating frequency around 18 Hz (36 Hz in $h(f)$), see section 7.6, for the remaining of the engineering run.

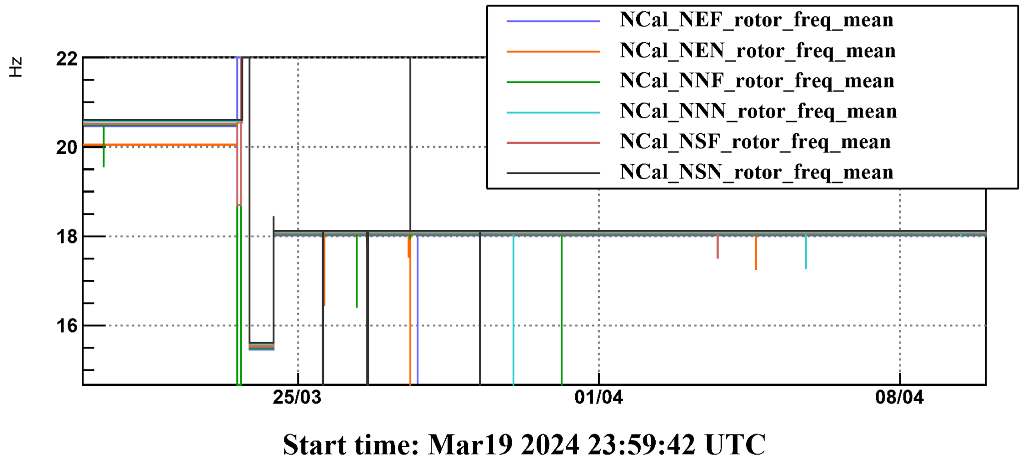

FIGURE 8.1: NCal operating frequencies during ER16.

8.1.2 Finding the mirror position offset using pairs of NCals

This section follows the method described in section 7.5. We introduce a simple analytical method to compute the mirror position offset presented in the first part of this section. New measurements of the mirror position were made during ER16, the results are shown in the second part of this section.

The simple analytical method

Using pairs of NCals on the North and South setups, we can compute the mirror position offset along their axis with a simple analytical model. Let's call a_i the amplitude of the mirror motion induced by the NCal i at the distance $d_i + d_0$ with d_i the nominal distance between the NCal and the mirror and d_0 the offset we want to measure. At first order, the amplitude can be expressed as a simple form of eq. (2.16):

$$a_i = C_i(d_i + d_0)^{-4} \tag{8.1}$$

with C_i the NCal coupling factor. We assume that $d_0 \ll d_i$ so we can write:

$$a_i \approx C'_i(1 - 4\frac{d_0}{d_i}) \tag{8.2}$$

Finally we can express the offset d_0 for a pair of NCals ($i = 1, 2$):

$$d_0 \approx \left(1 - \frac{a_1/C'_1}{a_2/C'_2}\right)\frac{d_1 d_2}{4(d_1 + d_2)} \tag{8.3}$$

In the case of $d_1 = d_2 = d$, it simplifies to:

$$d_0 \approx \left(1 - \frac{a_1/C'_1}{a_2/C'_2}\right)\frac{d}{8} \tag{8.4}$$

Measurements

We used the measurements of the recovered NCal lines amplitudes from April 1, 2024 when the inteferometer was locked with a BNS range of 55 Mpc for $\sim$ 19 hours. The mirror offset is then computed using the analytical method from eq. (8.3) and the

FROMAGE 1D-map from eq. (7.1). The measured mirror analytical and FROMAGE offsets are fitted using a gaussian distribution. The results are shown in table 8.1 and in fig. 8.2 for the FROMAGE 1D method.

The mirror position computed with the analytical and FROMAGE methods are compatible within their statistical uncertainties. However, the Near and Far NCals values disagree, given the low statistical uncertainty. Therefore, we have to evaluate the systematic uncertainties. For this, we use an NCal signal uncertainty of 0.21% for aluminum rotors and 0.12% for PVC rotors based on table 8.2 values (dominated by the residual couplings). This table does not include uncertainty from the mirror-to-NCal distance since this is what we are measuring. We implement them by introducing a variation, following a normal distribution, on one set of NCal amplitudes (to exclude statistical uncertainties). About one thousand samples are generated and we look for the RMS value of the resulting mirror distance distribution. The resulting systematic uncertainty on the mirror distance is presented in the last column of table 8.1. The Near and Far measurements are now compatible within their systematic uncertainties. But the Near NCal is providing the best measurement, due to the largest SNR and reduced parasitic coupling.

During ER16, to keep stable reference values, we continue to compute h_{inj} with the mirror offset from the commissioning time (4.30 mm). To evaluate the effect of this approximation, we recompute the expected injected NCal signal h_inj with the new mirror offset and obtain the Near and Far average values shown in table 8.3. Comparing the average injected signals h_{inj} computed using the ER16 mirror offsets to the commissioning value (4.30 mm), the relative variation is below 0.001% for the Near mirror distances (4.69 mm and 4.73 mm) and between 0.002% and 0.004% for the Far mirror distances (5.46 mm and 5.30 mm). These variations are small enough to justify continuing using the commissioning offset.

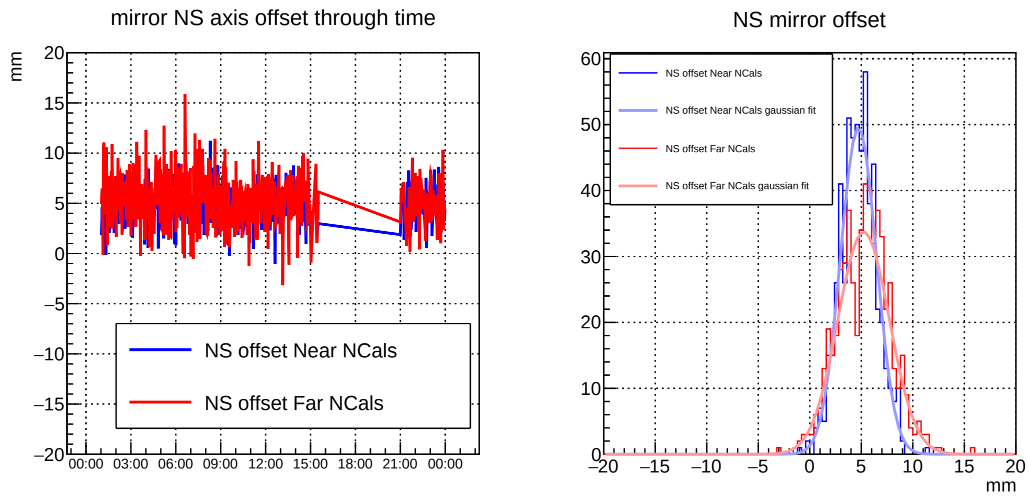

FIGURE 8.2: FROMAGE 1D-map measurements of the mirror offset with pairs of opposite Far aluminum and Near PVC rotors through April 1, 2024. The offsets are along the North-to-South (NS) NCal axis. Left are the measurements through time. Right are the distributions of these measurements with a gaussian fit. There is one measurement point every 100 s.

NS mirror offset			Systematic uncertainty [mm]
NCal pair	analytical [mm]	FROMAGE 1D-maps [mm]	
Near (PVC)	4.69 ± 0.08	4.73 ± 0.08	0.38
Far (Al)	5.46 ± 0.11	5.30 ± 0.11	0.81

TABLE 8.1: Mirror offset along the North to South (NS) NCal axis computed using the analytical and FROMAGE method. The dataset is from April 1, 2024. Uncertainties on the analytical and FROMAGE methods are statistical. The NCals were operating around 18 Hz (36 Hz in $h(f)$).

Parameter		Formula	NSF [%]	NNF [%]	NSN [%]	NNN [%]
Positioning	NCal supports to beam axis angle (ϕ)	$\delta\phi \tan(\phi)$	0.060	0.024	0.060	0.024
	NCal twist (ψ)	see table 6.15	≤ 0.003		≤ 0.001	
	NCal vertical position (z)	see section 8.3.2	0.011		0.017	
Rotor induced strain		see table 4.13	0.045	0.021	0.035	0.030
Rotor elastic deformation at 18 Hz		see section 5.4.2	0.002		0.020	
Residual coupling (including magnetic)		see section 7.3.2	0.200		≤ 0.100	
Total		quadratic sum	0.214	0.202	0.124	0.110

TABLE 8.2: Uncertainty on the injected NSF, NNF, NSN and NNN NCal signals at twice the rotor frequency, without the uncertainty from the NCal-to-mirror distance. The total uncertainty is computed as the quadratic sum of all the contributions.

Mirror offset measurement		$\|h_{inj}\|$ Far	$\|h_{inj}\|$ Near
Near (PVC)	Analytical $d_0 = 4.69$ mm	$9.584\,13 \times 10^{-19}$	$1.139\,18 \times 10^{-18}$
	1D-maps $d_0 = 4.73$ mm	$9.584\,14 \times 10^{-19}$	$1.139\,19 \times 10^{-18}$
Far (Al)	Analytical $d_0 = 5.46$ mm	$9.584\,31 \times 10^{-19}$	$1.139\,22 \times 10^{-18}$
	1D-maps $d_0 = 5.30$ mm	$9.584\,26 \times 10^{-19}$	$1.139\,21 \times 10^{-18}$
Commissioning $d_0 = 4.30$ mm		$9.584\,05 \times 10^{-19}$	$1.139\,17 \times 10^{-18}$

TABLE 8.3: Average injected signal h_{inj} of the Near and Far pairs of North-South NCals for different measured mirror offsets.

8.1.3 Finding the mirror position using triplets of NCals

This section follows the same method as in section 7.5 extended to the case of three NCals to compute the cartesian coordinates of the mirror in the plane of the interferometer. As discussed in section 2.5.3, this will further reduce the uncertainties on the NCal injected signal.

Parametrizing the NCal signal in two dimensions

To determine the position (x,y) of the mirror (see fig. 6.6 for the reference frame) using three NCals we use a two dimensional parametrization of the NCal equivalent strain. This is achieved for each rotor by running FROMAGE with mirror positions in a (x,y) grid. Then the 2D-map is fitted with a polynomial fit similar to the one used for the 1D-maps. In sections 7.5 and 8.1.2 we showed that the mirror offset was constrained well within 10 mm. Therefore, we chose this value as the 2D map size. Figure 8.3 shows this FROMAGE 2D-map of a Near rotor (at $d = 1.7$ m from the mirror) on the South setup and the relative residues of a linear, quadratic and cubic fit. The following cubic fit results are in agreement with FROMAGE within $10^{-4}\%$:

$$h(x,y) = p_0 + p_1 x + p_2 y + p_3 x^2 + p_4 y^2 + p_5 xy + p_6 x^3 + p_7 y^3 + p_8 x^2 y + p_9 x y^2 \quad (8.5)$$

with p_{0-9} the fit parameters.

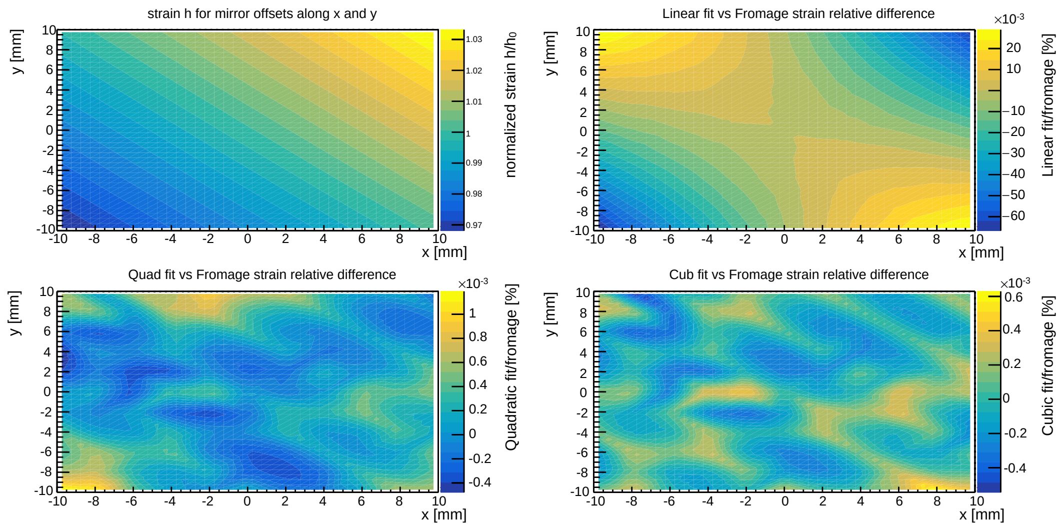

FIGURE 8.3: Top left is the FROMAGE 2D-map of the strain for a South Near NCal on the mirror for given cartesian coordinates (x,y). Top right, bottom left and bottom right show the relative residues between the FROMAGE 2D-map and respectively a linear, quadratic and cubic fit.

Measurements

We use the same day of data as in table 8.1, but with the triplet of Far NCals. This was the only triplet available during ER16, since the NEN NCal was twisted of 89.7° to continue the parasitic noise study. Figure 8.4 shows the measured mirror (x,y) positions over that day. We also translated the measurements as an offset along the North to South (NS) NCal axis to be compared with the measurements made with pairs of NCals. Since the setups are not perfectly aligned, the translated offsets are computed using the nominal NCal to beam axis angle $\phi = 34.7°$. The measured positions are fitted using a gaussian distribution and are shown in table 8.4. We remark that the translated NS mirror offset, 5.45 mm towards the North setup, is consistent with the measurement made with the pair of Far NCals, 5.46 mm from table 8.1.

Since the North-South axis is not at 90° of the East axis, there is a correlation between x and y, or in other words, the covariance matrix has a non-diagonal term. Therefore, to draw the error ellipse in the (x,y) plane, we use the method described in Appendix B. These parameters are also shown in table 8.4. The distributions for each day give the statistical uncertainties ($\sigma/\sqrt{n}$). To determine the effect of systematic uncertainties, we use the values shown in table 8.2 for NNF and NSF, and shown in table 8.5 for NEF. This is done with the same method as for the pair of NCals. Since the triplet is made of aluminum rotors, we take 0.21% as an upper limit. The resulting systematic uncertainty on the mirror position is presented in the last column of table 8.1. Figure 8.5 shows the measured mirror position in the plane of the interferometer with statistical and systematic uncertainties.

Here again, to evaluate the impact of a fixed mirror offset with the commissioning value (4.30 mm), we compute the expected injected NCal signal h_{inj} with the (x,y) mirror position of table 8.4 and obtain the Near and Far average values shown in table 8.6. Comparing the average injected signals h_{inj} computed using the ER16 mirror positions with the commissioning offset value, the relative variation is 0.007% for the Near mirror positions and 0.003% for the Far mirror positions.

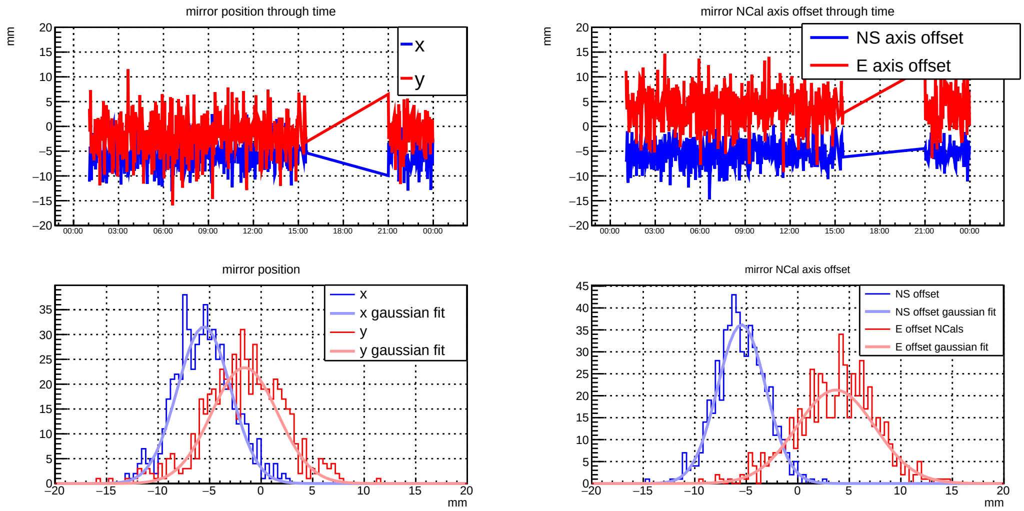

FIGURE 8.4: Measurements of the mirror position with the triplet of Far aluminum rotors through April 1, 2024. Top left and top right are the measurements of respectively the mirror position (x,y) and the translation on the NCal axes (NS is North to South NCal axis, E is East NCal axis). Bottom left and bottom right are the distributions of these measurements with a gaussian fit.

Mirror position		Translated mirror NS offset [mm]	Error ellipse parameter		
x_0 [mm]	y_0 [mm]		semi-major axis [mm]	semi-minor axis [mm]	rotation angle
-5.54	-1.61	-5.45	0.18	0.10	116.28°
Systematics			1.32	0.76	129.09°

TABLE 8.4: Mirror position and translated NS offset computed using 2D-maps of the Far NCal triplet with statistical and systematic error ellipse parameters.

Parameter		Formula	NEF [%]
Positioning	NCal supports to beam axis angle (ϕ)	$\delta\phi \tan(\phi)$	0.060
	NCal twist (ψ)	see table 6.15	$\lesssim 0.003$
	NCal vertical position (z)	see section 8.3.2	0.011
Rotor induced strain		see table 4.13	0.028
Rotor elastic deformation at 18 Hz		see section 5.4.2	0.002
Residual coupling (including magnetic)		see section 7.3.2	0.200
Total		quadratic sum	0.211

TABLE 8.5: Uncertainty on the injected NEF signal at twice the rotor frequency, without the uncertainty from the NCal-to-mirror distance. The total uncertainty is computed as the quadratic sum of all the contributions.

Mirror position measurement	$\lvert h_{inj}\rvert$ Far	$\lvert h_{inj}\rvert$ Near
Far (Al) 2D-maps $[x_0 = -5.54, y_0 = -1.61]$ mm	$9.583\,35 \times 10^{-19}$	1.1392×10^{-18}
Commissioning $d_0 = 4.30$ mm	$9.584\,05 \times 10^{-19}$	$1.139\,17 \times 10^{-18}$
Relative difference [%]	0.007%	0.003%

TABLE 8.6: Average injected signal h_{inj} of the Near and Far pairs of North-South NCals for different measured mirror positions. The relative difference with the commissioning mirror offset is shown. The NCals were operating around 18 Hz (36 Hz in $h(f)$).

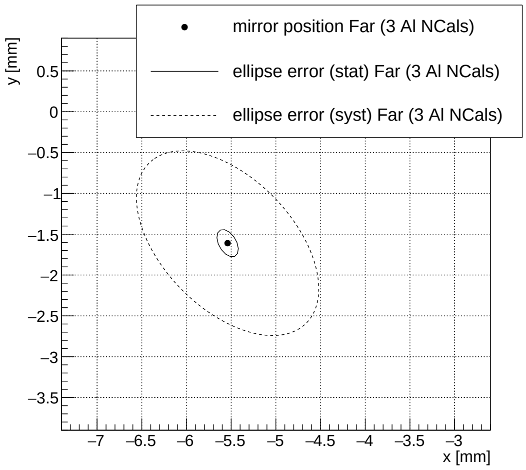

FIGURE 8.5: Measurement of the mirror position (x,y) with the Far NCal triplet on April 1, 2024. Plain ellipse: statistical uncertainties ($\sigma/\sqrt{n}$). Dashed ellipse: systematic uncertainties. See fig. 6.6 for the reference frame.

8.2 Induced coupling noise in the interferometer

This section continues the discussion started in section 7.3 on the parasitic noises induced by the NCals in the interferometer.

8.2.1 Gravitational coupling with the NCal supports

As the NCal setups are suspended from the Virgo infrastructure, the residual rotor unbalances can cause vibrations. These vibrations can induce a gravitational coupling between the setup and the mirror and therefore must be evaluated.

As seen in the previous chapters, we can track the setup's motion using the positions sensors. However, what is measured is the recoil motion of the NCal support due to the small unbalance of the rotor. But, for frequencies above 1 Hz, the center of mass of the rotor plus the full support is not moving because it is suspended. Since the masses distribution of the rotor and its axis, enclosure and suspending frame are not the same, we expect some gravitational effect on the mirror. To compute this effect we consider a model where the moving setup is divided in the Near, the Far part and the rotor. The Near part is composed of half the mass of the setup minus the mass of the rotor, the Far part is composed of the remaining half mass of the setup. The setup mass is moving in one direction of a quantity δ_a while the rotor mass is moving in the opposite direction, the center of mass of both does not move. Therefore, the movement of the rotor is:

$$\delta_r = -\delta_a \frac{m_{setup} + m_r}{m_r} \tag{8.6}$$

with m_{setup} the mass of the suspended setup and m_r the mass of the rotor. Summing the variable forces of each part on the mirror we can constrain the movement of the mirror with the following strain variation Δh:

$$|\Delta h| \sim \frac{G(m_{setup} + 2m_r)}{4\pi^2 f^2} \frac{\delta_a \cos(\phi)}{L} |d_N^{-3} - d_F^{-3}| \quad (8.7)$$

with G the gravitational constant, f the signal frequency, δ_a is the axial displacement read from the position sensors, ϕ is the NCal setup to beam axis angle, L is the interferometer arm's length, d_N is the distance between the center of mass of the Near part and the mirror (i.e. d_F for the Far part).

Based on the observed δ_a amplitude which is of the order of a few tenth of a micrometer as shown in fig. 8.6, δ_r is computed using eq. (8.6). Then, the first order model of the relative mass distribution predicts (eq. (8.7)) a coupling effect of about 10^{-4}% of the direct NCal signal at twice the rotor frequency ($f = 2f_{rot} = 36$ Hz). This model was validated at the rotor frequency ($f = f_{rot}$), where the NCal signal emitted by the rotors is negligible, and did not appear in the interferometer output.

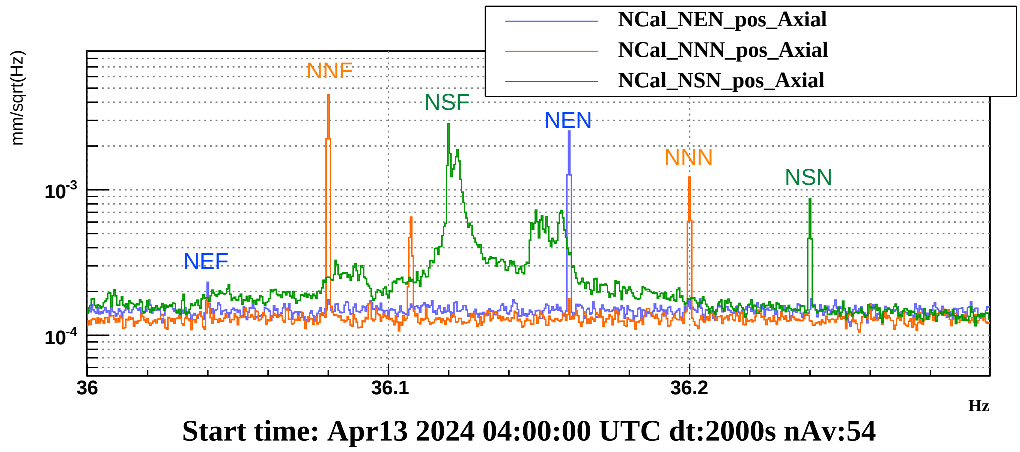

FIGURE 8.6: Spectrum of the Near axial position sensors at twice the NCal frequencies on April 13, 2024. FFTs are 2000 s long. Therefore, a $4\mu m/\sqrt{Hz}$ line (NNF) translates to a line amplitude of $4\mu m/\sqrt{2000} = 0.09$ µm.

8.2.2 Gravitational coupling with the *marionette*

The last stage of the mirror suspension, the so-called *marionette*, is also sensitive to the NCals. Since it is further away than the mirror, we can use the mirror motion as an upper limit of the marionette motion. This motion is filtered by marionette-to-mirror transfer function, which can be modelled by a simple pendulum with a resonance frequency of $f_0 = 0.6$ Hz. At 36 Hz, this results in a parasitic motion of 0.03% of the direct mirror's motion induced by the NCals. It is included as part of the residual coupling uncertainties.

8.2.3 Coupling with the induced torque

Due to the NCal positioning relative to the beam axis, all the mirror elements are not subjected to the same force. Therefore, the induced torque causes the mirror to rotate around its center of mass. As the interferometer beam is not perfectly centered on the mirror, this torque results in an optical path difference. Assuming an offset of 0.5 mm between the beam and the mirror center, using FROMAGE, we compute the torque produced by a Near NCal. The predicted signal variation is 0.03% for a Near NCal and 0.025% for a Far NCal.

However, this torque either increases or decreases the injected signal, depending whether the NCal is at the front or back of the mirror. Therefore, for a two NCal system, the torque effect cancels out, and the system is not sensitive to beam misalignment at first order. If the two NCal system is not perfectly centered on the mirror, the torques induced by each NCal are not anymore identical, leading to a residual effect. With our measured offset, this residual signal variation, considered as an uncertainty, is about 0.003%. As this value is small, it is also included as part of the residual coupling uncertainties.

8.3 Uncertainty on the injected signal during ER16

This section presents the NCal signal uncertainty during ER16. Most of the components have already been discussed in previous sections, except the effect of the distance and the vertical offset that are first discussed.

8.3.1 Uncertainties due to the NCal to mirror distance

Since we are using a couple of NCals along the North-South axis, the distance (D) between them (discussed in section 6.2.5 and table 6.20) is setting the scale for this couple of NCals. If the mirror is located exactly in the middle of the two NCal, the NCal to mirror distance is $d = D/2$ with an uncertainty of $\delta d = \delta D/2$. The corresponding relative uncertainty of a single NCal signal is $4\delta d/d = 4\delta D/D$. Since this uncertainty is fully correlated between the two NCals, the relative uncertainty of the average North + South NCals is still $4\delta D/D$. This means a $4 * 0.5/3400 = 0.06\%$ for the Near NCals and $4 * 0.5/4200 = 0.05\%$ for the Far NCal.

Then, in addition, the mirror offset relative to the center is adding another uncertainty (see section 2.5.3 and fig. 2.17a). If we use the measured mirror offset plus one sigma (i.e. 6.6 mm from fig. 8.5) as an uncertainty on the mirror position we can use fig. 2.17a to get the corresponding signal variation: 0.02% at 1.7 m. At 2.1 m, this uncertainty is slightly smaller but we keep the 1.7 m value.

8.3.2 Mirror elevation

For an elevation z of the NCals relative to the center of mass of the mirror, the NCal-to-mirror distance d increases by a factor $(1+\frac{1}{2}(z/d)^2)$. As a result, the induced force on the mirror is changed by a factor $(1+\frac{1}{2}(z/d)^2)^{-4}$ which can be written at the first order as $(1-\frac{4}{2}(z/d)^2)$. However, this force is not in the plane of the interferometer, its projection adds the term $(1-\frac{1}{2}(z/d)^2)$. Therefore, the force variation is $(1-\frac{5}{2}(z/d)^2)$, i.e. an error from the elevation z on the injected signal of $(5/2)(z/d)^2$.

In the worst case scenario of table 6.12 (8.57 mm with a 0.90 mm uncertainty), the elevation offset for an NCal is less than 9 mm. Since we are not (yet) including these vertical offsets when computing the NCal signal uncertainty, we take this value, 9 mm, as vertical offset uncertainty. In addition, the mirror is not exactly in the plane of the reference frame. We assume that this possible vertical offset is similar to the lateral offset, i.e., about 5 mm. Therefore, the total vertical uncertainty is $9 + 5 = 14$

mm. This offset translates to a signal variation of 0.017% at 1.7 m and 0.011% at 2.1 m. The results of a FROMAGE computation are very similar.

8.3.3 NCal uncertainty during ER16

One of the key calibration results is the ratio between the recovered and the injected calibration line amplitude (h_{rec}/h_{inj}). To minimize the effect of the NCal to mirror distance uncertainty, we use the average value of this ratio for the North and South NCals. Table 8.7 summarizes the calibration uncertainties using pairs of NCals during ER16. Except for the first three lines, all uncertainties for the averaged North and South NCals are the same as for an individual rotor. This means that we are taking the conservative approach of a linear sum of uncertainties rather than quadratic when filling each line of the table. However, the total uncertainty is defined as the quadratic sum of all these contributions that are uncorrelated. We note that further mitigating the residual coupling could reduce the uncertainty on h_{rec}/h_{inj} to below 0.1%.

Parameter		Formula	h_{rec}/h_{inj} Near [%]	h_{rec}/h_{inj} Far [%]
Positioning	NCal-to-NCal distance (D)	see section 8.3.1	0.060	0.050
	Mirror offset	see section 8.3.1	0.020	0.020
	NCal supports to beam axis angle (ϕ)	$\delta\phi \tan(\phi)/\sqrt{2}$	0.046	0.046
	NCal twist (ψ)	see table 6.15	≤ 0.001	≤ 0.003
	NCal vertical position (z)	see section 8.3.2	0.017	0.011
Rotor induced strain		see table 4.13	0.035	0.045
Rotor elastic deformation at 18 Hz		see section 5.4.2	0.020	0.002
Residual coupling (including magnetic)		see section 7.3.2	≤ 0.100	0.200
Total		quadratic sum	0.134	0.217

TABLE 8.7: Uncertainty budget, in percent, on calibration signal amplitude for the Near and Far North-South NCal pairs used during ER16.

8.4 NCal check during ER16

During ER16, we had two fairly independent NCal systems: the Near and Far NCals. Their rotors were made of different material, which fully decouples the uncertainty coming from the rotor and the uncertainty coming from the main part of the residual coupling. Therefore, comparing the Near and Far injected signals is an interesting test of the NCal system. Since the Near and Far signals are injected at slightly different frequencies, to avoid the slight bias of the frequency response, we compared the h_{rec}/h_{inj} signals of both couple of NCals. Figure 8.7 shows this comparison for Near PVC and Far aluminum rotors on the day of April 1, 2024. The ratio defect is around $0.14 \pm 0.01\%$ (statistical uncertainties), compatible with zero, given the systematic uncertainties of table 8.7. Both NCal systems are therefore in agreement.

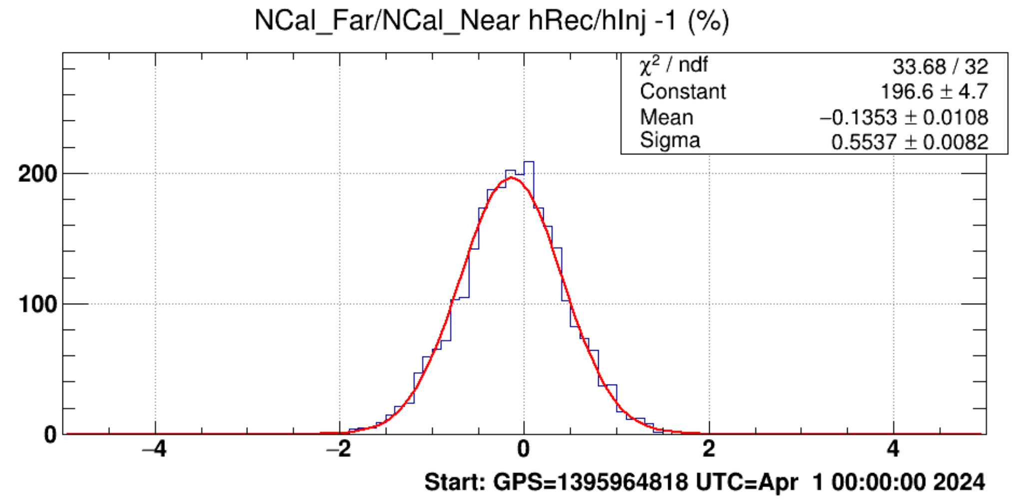

FIGURE 8.7: Comparison of the calibration ratios between the Near and Far NCal setups using data from ER16. Measured relative differences, in blue, correspond to a fitted normal distribution, in red. Calibration lines were spanning from 36.04 to 36.24 Hz for this measurement. This plot corresponds to one day of data.

8.5 Recalibration of the PCals using the NCals

The uncertainty on the mirror displacement induced by NE and WE PCals in preparation for the O4 run was estimated to be 0.56% [49, 50].

Actually, additional measurement during ER16 revealed that the West and North End PCals had a 0.8 to 0.9% discrepancy. The PCal system was therefore re-calibrated using the Near NCal system which has a smaller uncertainty of 0.13%, as discussed in the previous section.

Figure 8.8 shows an history comparing the PCal and the NCal calibration. One can notice the discrepancy of the NE and WE PCals (respectively blue and green data) before the re-calibration of the PCals based on the Near NCal.

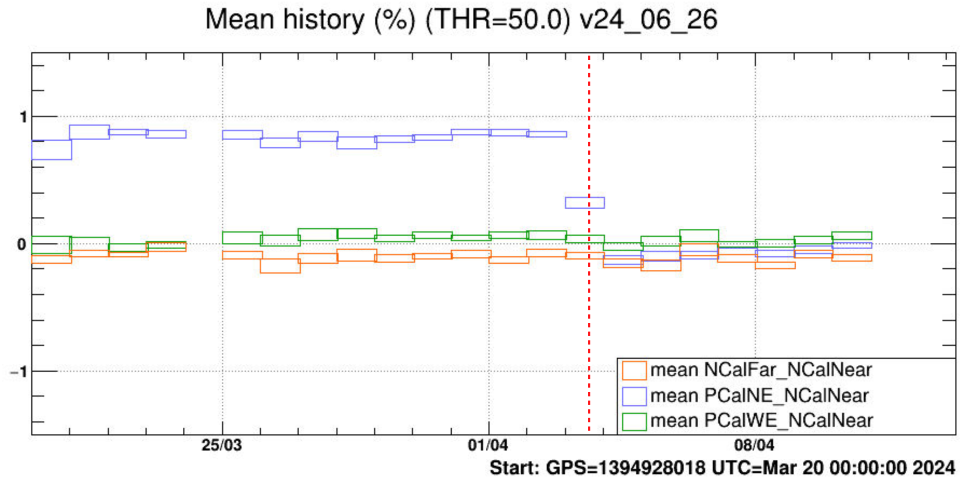

FIGURE 8.8: History for the three weeks of ER16 comparing ratio between the reconstructed and injected signal h_{rec}/h_{inj} for PCals and NCals. The values represented are expressed in ratio-1 (%). Orange: ratio between the Far and Near NCal. Green: ratio between the North end PCal and the Near NCals. Blue: ratio between the West end PCal and the Near NCal. The re-calibration of the PCal based on the NCal is represented with the red dashed vertical line. Uncertainties are only statistical.

Chapter 9

The first three months of O4b

Contents

Introduction

This chapter details the NCal operations for Virgo during the beginning of O4b, i.e. the first three months at the time of writing this document. The O4 run began on May 24, 2023, with the LIGO interferometers, and Virgo joined for the second part, O4b, on April 10, 2024. An important feature of the NCal system is to be reliable. Therefore, we will first present the NCal configuration and some monitoring plots for this period. Then we will discuss the mirror position recovery and its stability. We will continue with the estimation of the uncertainties. Finally, we will discuss the calibration stability and we will compare the PCals to the NCals.

9.1 The NCal system during O4b

9.1.1 NCal configuration

From the start of O4b until May 28, 2024, the NCal configuration was the same as during ER16:

- North Near (NNN): PVC rotor R4-12.
- North Far (NNF): aluminum rotor R4-02.
- East Near (NEN): PVC rotor R4-11 twisted by 89.7° (see section 7.3.2).
- East Far (NEF): aluminum rotor R4-06.
- South Near (NSN): PVC rotor R4-14 .
- South Far (NSF): aluminum rotor R4-03.

Then on May 28, 2024, two aluminum rotors were replaced by PVC ones with the following configuration change:

- North Far (NNF): PVC rotor R4-10.
- East Near (NEN): PVC rotor R4-11 twisted back to the nominal 12°.
- South Far (NSF): PVC rotor R4-15.

For the first three months of O4b, the NCals have been operating at their nominal frequencies, slightly above 18 Hz (36 Hz in $h(f)$) as shown in fig. 9.1.

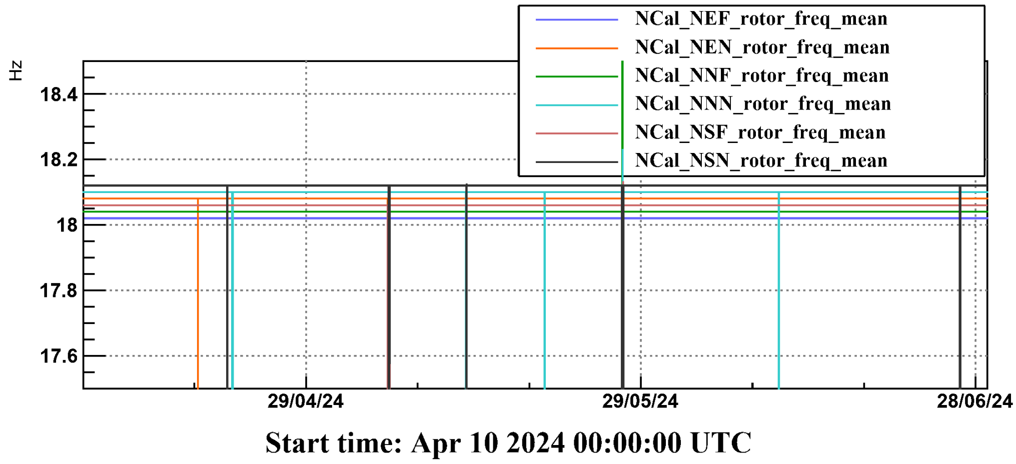

FIGURE 9.1: Measured NCal frequencies during the first three months of O4b.

9.1.2 NCal monitoring

During the first three months of O4b, the NCals have been operated continuously, without failure. There has been only short interruptions during the Tuesday morning maintenance period, when the NCals stopped because of nearby activity, or because of the change of two rotors on May 28.

Figure 9.2 show the temperatures of the NCal boxes during this period. The operating temperature is well within the expected $23 \pm 1.5°$C range used to predict the NCal signal amplitude. There are a few short glitches, due to the NCal stops for short times during the maintenance periods.

Figure 9.3 show the axial readout (i.e. along the NCal-mirror axis) of the position sensors placed on the Near location of each NCal setup. The offset value is around 0.1 mm without exceeding 0.2 mm. This is much less than the uncertainty on the NCal-to NCal distance. During the maintenance day of May 28, 2024, we changed the Far rotors on the North and South setup and twisted the Near East NCal. Then, we re-adjusted the setup positions. This explains the small jump of that day. Some maintenance days are visible with a displacement exceeding 0.25 mm due to activity near the NCals. Overall, the NCal system is stable.

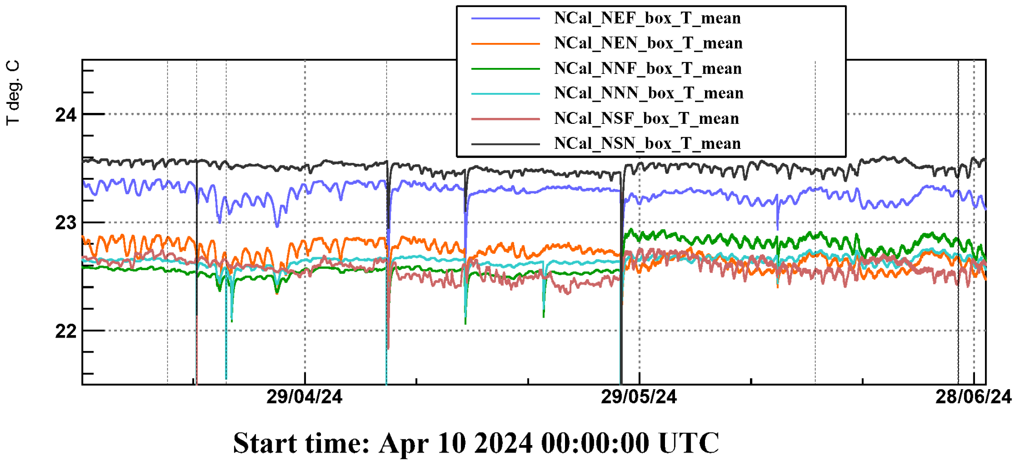

FIGURE 9.2: NCal temperatures during the first three months of O4b.

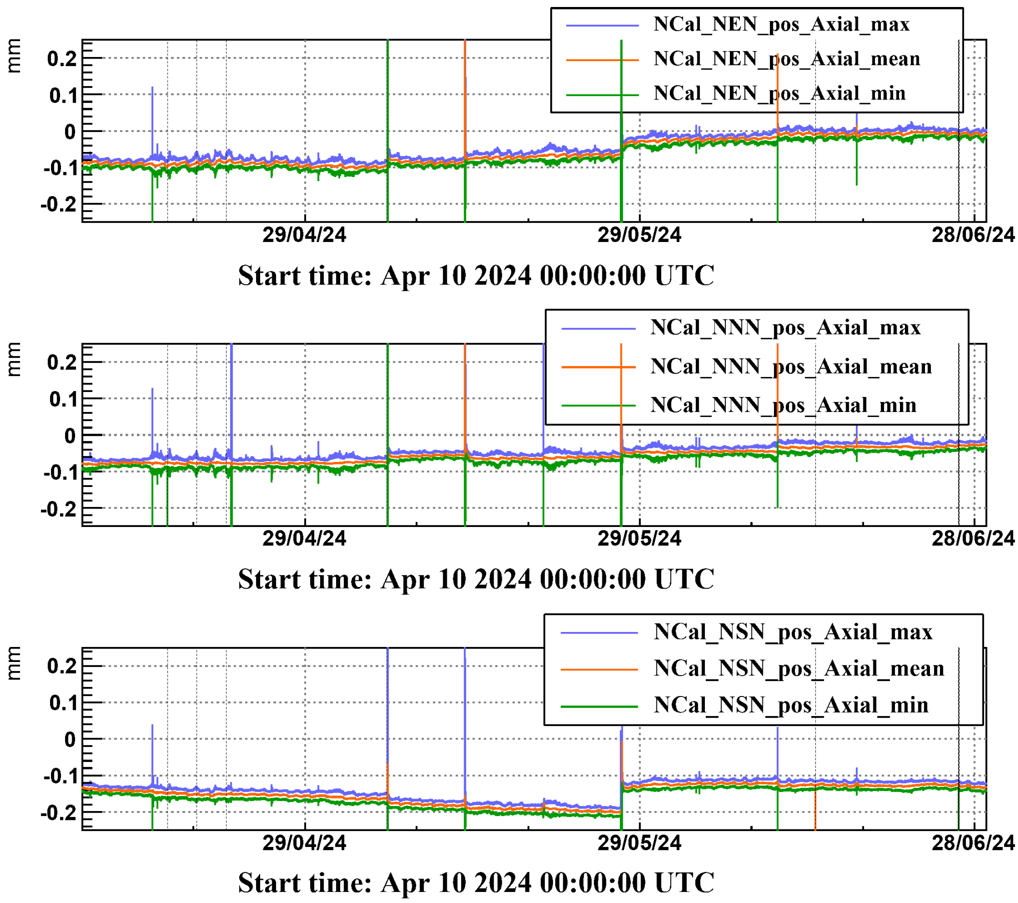

FIGURE 9.3: NCal axial position sensors readout during the first three months of O4b.

9.2 Finding the mirror position

9.2.1 Mirror position offset using pairs of NCals

This section presents new measurements of the mirror position offset made during O4b.

We first used the recovered NCal lines amplitudes from May 15, 2024 when the NCal configuration, described in section 9.1.1, was a mix of PVC and aluminum rotors, the same as during ER16. Therefore, the systematic uncertainties for the NCal lines are: 0.21% for aluminum rotors and 0.12% for PVC rotors based on table 8.2 values. The results are shown in the first part of table 9.1. As during ER16, the Near and Far NCals values disagree, given the low statistical uncertainty, but are compatible within their systematic uncertainties.

Then, on May 28, 2024, both Far aluminum rotors on the North and South setups have been changed to PVC ones as described in section 9.1.1. We thus used the measurements from June 12, 2024 with an NCal signal systematic uncertainty of 0.12% based on values of tables 8.2 and 9.2. The results are shown in the second part of table 9.1. The Near and Far values are now closer.

As for ER16, we compare the average injected signals h_{inj} computed using the O4b mirror offsets with the h_{inj} value computed with the commissioning offset (4.30 mm) shown in table 9.3. When the NCal configuration was identical to ER16, the relative variation for Near and Far was similar to what was computed using table 8.3. Once the Far rotors have been changed to PVC ones, this variation is less than 0.001% for both Near and Far mirror offsets (4.58 mm and 4.36 mm). Therefore, we chose to continue using the mirror offset commissioning value of 4.30 mm.

Measurement day	NS mirror offset			Systematic uncertainty [mm]
	NCal pair	analytical [mm]	FROMAGE 1D-maps [mm]	
15/05/24	Near (PVC)	4.81 ± 0.05	4.85 ± 0.05	0.38
	Far (Al)	5.57 ± 0.08	5.44 ± 0.08	0.80
12/06/24	Near (PVC)	4.57 ± 0.06	4.58 ± 0.06	0.37
	Far (PVC)	4.74 ± 0.15	4.36 ± 0.15	0.47

TABLE 9.1: Mirror offset along the North to South (NS) NCal axis computed using the analytical and FROMAGE method. Uncertainties on the analytical and FROMAGE methods are statistical.

Parameter		Formula	NSF [%]	NNF [%]
Positioning	NCal supports to beam axis angle (ϕ)	$\delta\phi \tan(\phi)$	0.060	0.024
	NCal twist (ψ)	see table 6.15	≤ 0.003	
	NCal vertical position (z)	see section 8.3.2	0.011	
Rotor induced strain		see table 4.13	0.036	0.032
Rotor elastic deformation at 18 Hz		see section 5.4.2	0.020	
Residual coupling (including magnetic)		see section 7.3.2	≤ 0.100	
Total		quadratic sum	0.124	0.110

TABLE 9.2: Uncertainty on the injected NSF and NNF PVC NCal signals at twice the rotor frequency, without the uncertainty from the NCal-to-mirror distance. The total uncertainty is computed as the quadratic sum of all the contributions.

Measurement day	Mirror offset measurement		$\|h_{inj}\|$ Far	$\|h_{inj}\|$ Near
15/05/24	Near (PVC)	Analytical $d_0 = 4.81$ mm	$9.584\,16 \times 10^{-19}$	$1.139\,19 \times 10^{-18}$
		1D-maps $d_0 = 4.85$ mm	$9.584\,16 \times 10^{-19}$	$1.139\,19 \times 10^{-18}$
	Far (Al)	Analytical $d_0 = 5.57$ mm	$9.584\,16 \times 10^{-19}$	$1.139\,22 \times 10^{-18}$
		1D-maps $d_0 = 5.44$ mm	$9.584\,30 \times 10^{-19}$	$1.139\,22 \times 10^{-18}$
Commissioning $d_0 = 4.30$ mm			$9.584\,05 \times 10^{-19}$	$1.139\,17 \times 10^{-18}$
12/06/24	Near (PVC)	Analytical $d_0 = 4.57$ mm	$4.933\,24 \times 10^{-19}$	$1.139\,18 \times 10^{-18}$
		1D-maps $d_0 = 4.58$ mm	$4.933\,24 \times 10^{-19}$	$1.139\,18 \times 10^{-18}$
	Far (PVC)	Analytical $d_0 = 4.74$ mm	$4.933\,26 \times 10^{-19}$	$1.139\,19 \times 10^{-18}$
		1D-maps $d_0 = 4.36$ mm	$4.933\,21 \times 10^{-19}$	$1.139\,17 \times 10^{-18}$
Commissioning $d_0 = 4.30$ mm			$4.933\,21 \times 10^{-19}$	$1.139\,17 \times 10^{-18}$

TABLE 9.3: Average injected signal h_{inj} of the Near and Far pairs of North-South NCals for different measured mirror offsets.

9.2.2 Mirror position using triplets of NCals

This section presents new measurements of the mirror position made during the first three months of O4b.

A first set of eight weekly measurements was obtained with the Far triplet of aluminum rotors from April 10 to May 27, 2024. This triplet was using the same aluminum rotors as during ER16. Therefore, the systematic uncertainty for each rotor was 0.21% based on tables 8.2 and 8.5 values. The results are shown in the first part of table 9.4.

Then, a second set of five weekly measurements was obtained with the Near and Far NCal triplets throughout June 2024 after the change of two aluminum rotors by PVC ones (see section 9.1.1). Therefore, the systematic uncertainty was 0.21% for the only aluminum rotor (NEF) and 0.12% for PVC rotors based on tables 8.2, 8.5 and 9.5 values. The results are shown in the second and third parts of table 9.4.

The measured mirror positions are presented in fig. 9.4. All these measurements, made over a three months period, are compatible within the systematic uncertainties. This demonstrates the good stability of the NCal system.

Here again, to evaluate the impact of a fixed mirror offset with the commissioning value (4.30 mm), we compute the expected injected NCal signal h_{inj} with the (x,y) mirror position of table 9.4 and obtain the Near and Far average values shown in table 9.6. Comparing the average injected signals h_{inj} computed using the O4b mirror positions with the commissioning offset value, the relative variation is 0.001% for the Near and Far NCals.

NCal triplet	Measurement day	Mirror position		Error ellipse parameter		
		x_0 [mm]	y_0 [mm]	semi-major axis [mm]	semi-minor axis [mm]	rotation angle
Far (3 Al)	13/04/24	-5.78	-1.79	0.14	0.08	121.42
	19/04/24	-5.81	-1.79	0.14	0.08	120.24
	24/04/24	-5.23	-1.70	0.13	0.08	125.02
	29/04/24	-5.63	-1.70	0.14	0.09	125.25
	05/05/24	-5.53	-1.79	0.13	0.08	123.60
	13/05/24	-5.59	-1.83	0.14	0.08	124.96
	19/05/24	-5.48	-1.89	0.13	0.08	120.27
	26/05/24	-5.53	-1.79	0.14	0.08	120.88
	Systematics	-5.57	-1.79	1.36	0.77	127.78
Far (2 PVC + 1 Al)	01/06/24	-4.05	-2.05	0.19	0.13	121.55
	07/06/24	-4.36	-1.68	0.21	0.14	116.46
	12/06/24	-4.31	-2.65	0.20	0.14	122.13
	16/06/24	-3.84	-2.39	0.18	0.13	119.82
	26/06/24	-3.85	-2.34	0.19	0.13	120.97
	Systematics	-4.08	-2.22	1.16	0.46	132.46
Near (3 PVC)	01/06/24	-4.02	-2.26	0.09	0.05	122.99
	07/06/24	-4.20	-2.21	0.11	0.06	120.22
	12/06/24	-4.12	-2.36	0.10	0.06	124.14
	16/06/24	-4.07	-2.49	0.09	0.06	125.72
	26/06/24	-4.18	-2.31	0.10	0.06	124.75
	Systematics	-4.12	-2.23	0.62	0.36	130.43

TABLE 9.4: Mirror position computed using 2D-maps with statistical error ellipse parameters for every measurement. The systematic error ellipse parameters are given in the grey rows.

Parameter		Formula	NEN [%]
Positioning	NCal supports to beam axis angle (ϕ)	$\delta\phi \tan(\phi)$	0.060
	NCal twist (ψ)	see table 6.15	≤ 0.001
	NCal vertical position (z)	see section 8.3.2	0.017
Rotor induced strain		see table 4.13	0.033
Rotor elastic deformation at 18 Hz		see section 5.4.2	0.020
Residual coupling (including magnetic)		see section 7.3.2	≤ 0.100
Total		quadratic sum	0.124

TABLE 9.5: Uncertainty on the injected NEN signal at twice the rotor frequency, without the uncertainty from the NCal-to-mirror distance. The total uncertainty is computed as the quadratic sum of all the contributions.

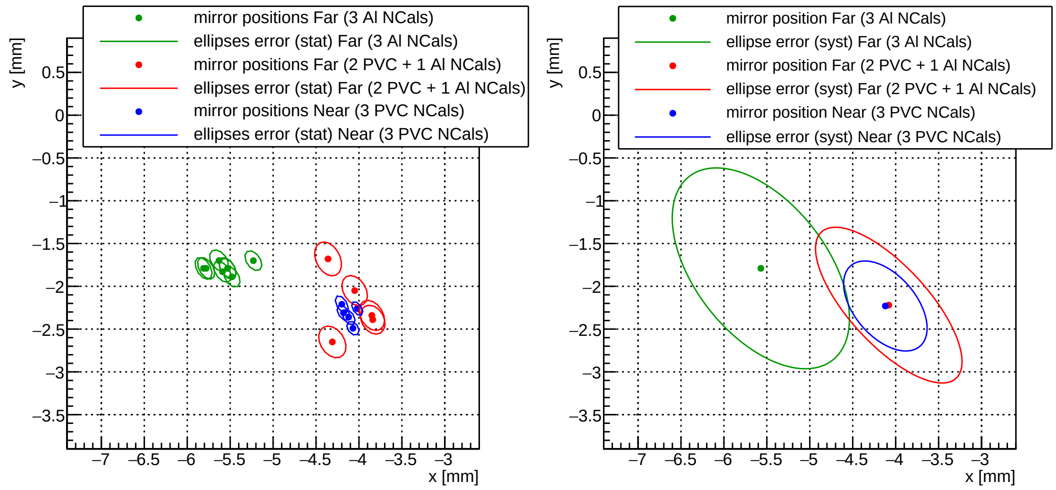

FIGURE 9.4: Measurements of the mirror position (x,y) with the Near and Far NCal triplets. Left: measurements with statistical error ellipses ($\sigma/\sqrt{n}$). Right: average measurement per triplet with systematic error ellipses.

Mirror position measurement	$\lvert h_{inj} \rvert$ Far	$\lvert h_{inj} \rvert$ Near
Far (Al) 2D-maps $[x_0 = -5.57, y_0 = -1.79]$ mm	9.58339×10^{-19}	1.13921×10^{-18}
Commissioning $d_0 = 4.30$ mm	9.58405×10^{-19}	1.13917×10^{-18}
Relative difference [%]	0.007%	0.003%
Far (2 PVC + 1 Al) 2D-maps $[x_0 = -4.08, y_0 = -2.22]$ mm	4.93323×10^{-19}	1.13918×10^{-18}
Commissioning $d_0 = 4.30$ mm	4.93321×10^{-19}	1.13917×10^{-18}
Relative difference [%]	< 0.001%	< 0.001%
Near (PVC) 2D-maps $[x_0 = -4.12, y_0 = -2.23]$ mm	4.93323×10^{-19}	1.13918×10^{-18}
Commissioning $d_0 = 4.30$ mm	4.93321×10^{-19}	1.13917×10^{-18}
Relative difference [%]	< 0.001%	< 0.001%

TABLE 9.6: Average injected signal h_{inj} of the Near and Far pairs of North-South NCals for different measured mirror positions. The relative difference with the commissioning mirror offset is shown.

9.3 Uncertainty on the injected signal during O4b

Table 9.7 summarizes the calibration uncertainties using pairs of NCals for O4b. Most of the components have already been discussed in chapter 8 during ER16. The Near and Far NCal calibration uncertainty during O4b is therefore 0.13%.

When combining the Near and Far NCals, we must take into account the correlations between their uncertainties. Some uncertainties are totally correlated: the mirror offset, the NCal supports to beam axis angle, the NCal vertical position and the rotor elastic deformation. Some are totally uncorrelated since they are rotor dependent: the NCal twist. Then, the following uncertainties are partially correlated:

- NCal-to-NCal distance: It is composed of the survey measurements (0.23 mm) and the plane uncertainty (0.067 mm) which are correlated. Then, the NCal to reference hole distance (twice 0.31 mm) which is uncorrelated.

- Rotor induced strain: It is composed of the material density (0.014%), the FROMAGE grid (0.005%), the gravitational constant (0.002%) which are correlated.

Then the temperature (0.024%), the modelling uncertainty (0.020% for Near and 0.016% for Far), the opening angle and asymmetry ($\leq 4 \times 10^{-5}$%) and the rotor flat surfaces offsets ($\leq 5 \times 10^{-4}$%) which are uncorrelated.

- Residual coupling: the correlation between the Near and Far pairs is unknown. Therefore we will use the most conservative assumption (fully correlated or fully uncorrelated) when combining the Near and Far signals.

We combine Near and Far in two cases: the mean value (Near+Far)/2 and the difference Near-Far. This results in the following combination of uncertainties:

- If the uncertainties are correlated, the mean value combines as $(d_{Near} + d_{Far})/2$ and the difference combines as $(d_{Near} - d_{Far})$.
- If the uncertainties are uncorrelated, the mean value combines as $\frac{1}{2}\sqrt{d_{Near}^2 + d_{Far}^2}$ and the difference combines as $\sqrt{d_{Near}^2 + d_{Far}^2}$.

The uncertainties on the Near and Far combinations are shown in the last two columns of table 9.7. The total uncertainty is still taken as the quadratic sum of all contributions.

Parameter		Formula	h_{rec}/h_{inj} [%]			
			Near	Far	(Near + Far)/2	Near - Far
NCal-to-NCal distance (D)	(corr)	see section 8.3.1	0.060	0.050	0.026	0.005
	(uncorr)				0.033	0.067
Mirror offset (corr)		see section 8.3.1	0.020	0.020	0.020	-
NCal supports to beam axis angle (ϕ) (corr)		$\delta\phi \tan(\phi)/\sqrt{2}$	0.046	0.046	0.046	-
NCal twist (ψ) (uncorr)		see table 6.15	≤ 0.001	≤ 0.003	≤ 0.002	≤ 0.003
NCal vertical position (z) (corr)		see section 8.3.2	0.017	0.011	0.014	0.006
Rotor induced strain	(corr)	see table 4.13	0.035	0.032	0.015	-
	(uncorr)				0.021	0.042
Rotor elastic deformation at 18 Hz (corr)		see section 5.4.2	0.020	0.020	0.020	-
Residual coupling (including magnetic) (uncorr)		see section 7.3.2	≤ 0.100	≤ 0.100	≤ 0.100	0.141
Total		quadratic sum	0.134	0.129	0.124	0.162

TABLE 9.7: Uncertainty budget, in percent, on calibration signal amplitude for the Near and Far North-South NCal pairs used during O4b.

9.4 Calibration stability during O4b and new reference

Figure 9.5 shows an history comparing the Near and Far NCal signals for the first three months of O4b. Before the change of Far aluminum rotors by PVC ones, the relative difference between the Far and Near NCals is -0.133 ± 0.003%. After this change, the relative difference is 0.081 ± 0.006%. This difference is within the systematic uncertainty : 0.162% (see last column table 9.7). It gives confidence in the NCal system and allows us to combine the Near and Far NCals instead of only using the Near NCal as reference as decided at the end of ER16. This is equivalent to shift the Near NCal calibration by $0.081\%/2 = 0.040\%$. The systematic uncertainty on the averaged result is 0.124%, see second to last column of table 9.7, which takes care of the correlation between NCal couples.

It is also interesting to check the calibration of the PCal system which was adjusted to the Near NCals during ER16. The PCal over the Near NCals relative difference are presented in fig. 9.6. The average values are:

- PCal NE = $-0.079 \pm 0.002(stat) \pm 0.132(syst)\%$.
- PCal WE = $-0.013 \pm 0.002(stat) \pm 0.132(syst)\%$.

After the change to PVC rotors on May 28, the Far NCal uncertainty has been reduced, letting us to combine their results. Therefore, we can use the average Near and Far NCals as a new reference to estimate the possible bias of the PCals which is:

- PCal NE = $-0.119 \pm 0.002(stat) \pm 0.122(syst)\%$.
- PCal WE = $-0.053 \pm 0.002(stat) \pm 0.122(syst)\%$.

The statistical uncertainties are negligeable when integrating over a long time. The uncertainties are dominated by the systematic contribution which are significantly smaller than the LIGO PCal uncertainty of 0.29% [50] or the Virgo PCal uncertainty of 0.56% [49].

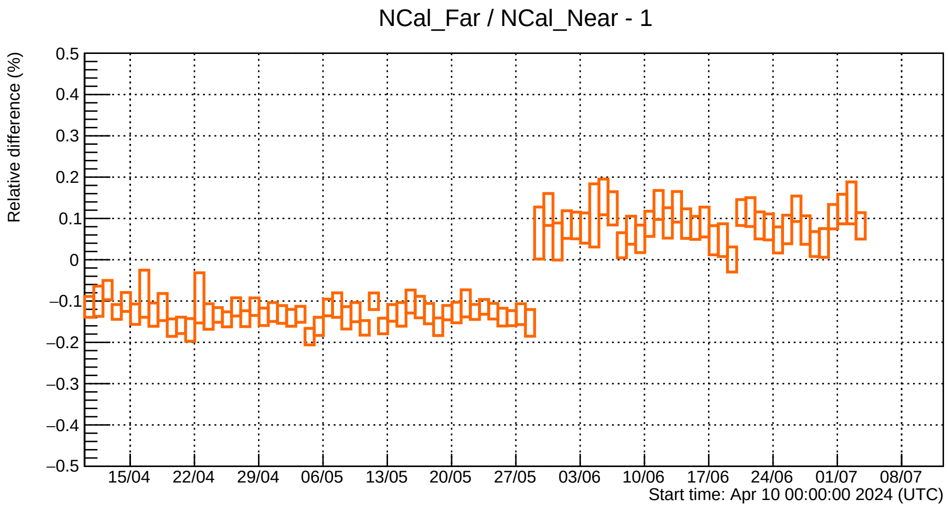

FIGURE 9.5: History for the first three months of O4b of the ratio between the reconstructed and injected signal h_{rec}/h_{inj} for the NCals. Uncertainties are only statistical.

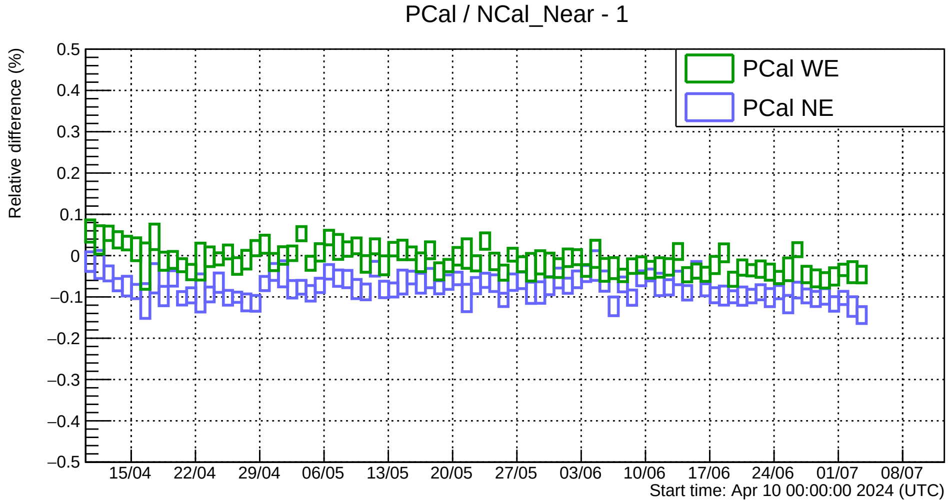

FIGURE 9.6: History for the first three months of O4b of the ratio between the reconstructed and injected signal h_{rec}/h_{inj} for the PCals and Near NCals. Green: WE PCal to Near NCals comparison. Blue: NE PCal to Near NCals comparison. Uncertainties are only statistical.

Chapter 10

Conclusion

The NCal is a new technology which was first tested for short times during a few calibration shifts of the previous observing runs. The main sources of uncertainty for the O3 NCal system were the rotor geometry (0.53%) and the rotor-to-mirror distance (1.31%) for an overall uncertainty of 1.4%. This result was similar to the reference calibration method which uses an auxiliary laser beam, the PCal.

Between the third and fourth observing runs, a new version of the NCal system was designed and installed around the North End mirror of the Virgo interferometer. I contributed to most of this work since my PhD began in October 2021, still during the design phase of some of its parts. The goal for O4 was to operate the NCal system continuously with a calibration accuracy of less than one percent. Many improvements have been done to achieve this.

For O4, more rotors were machined and their shape was simplified to improve the knowledge of their geometry. Two materials have been used for the rotors, aluminum 7075 and PVC. I did the metrology work on the material used for the rotors to determine their density and on the machined rotors to characterize their respective geometry. Then, using a finite element modeling program named FROMAGE, I computed the signal emitted by each rotor and their associated uncertainty. This work resulted in a rotor signal uncertainty between 0.019% and 0.045% depending on the rotor, an order of magnitude better than the O3 system.

For O4 a new support system was built so that multiple NCals could be operated around the mirror. Three suspended setups have been installed, each holding a pair of actuators for a total of six NCals around the mirror. The NCal triplet closest to the mirror, called Near, is at 1.7 m from the mirror and the Far triplet at 2.1 m. Using geometrical survey measurements made on the NCal system, I was able to compute the relative position of the NCals with an accuracy of 0.5 mm. This translates to a rotor-to-rotor distance uncertainty on the injected signal of 0.11% for the Near NCals and 0.09% for the Far ones.

The control of the NCal rotation has been improved and synchronized with the interferometer timing. A continuous online monitoring has been developed and made available on the Virgo Interferometer Monitoring (VIM) page.

During the commissioning phase of the NCal system, several tests were performed. As the sensitivity of the interferometer improved, more precise measurements have been made. We studied its stability over eight months of continuous operation and the parasitic couplings with the mirror that could induce a residual signal. This study led to a contribution to the signal uncertainty estimated to be 0.1% for PVC rotors and 0.2% for aluminum ones.

After the ER16 engineering run of three weeks, Virgo joined the second part of the fourth observing run, O4b, in April 2024. Using pairs and triplets of NCals and comparing their recovered signal, h_{rec}, retrieved from the online data $h(t)$ to the injected signal computed using FROMAGE, h_{inj}, I computed the position of the mirror inside the vacuum chamber. The NCal was also compared to the PCal method which was also improved for O4. During ER16, the two PCal systems differed by 0.9%, a bit more than their expected accuracy, but much more than the ER16 NCal overall uncertainty (0.13%). Therefore, the PCals were re-calibrated using the NCal, the absolute calibration reference for O4b.

The first three months of O4b operation confirm the stability of the NCal system. After a few weeks, two aluminum rotors were replaced with PVC rotors to further reduce the calibration uncertainty. Then, the Near and Far NCals reached a combined calibration systematic uncertainty of 0.12%, much smaller than the LIGO PCal uncertainty (0.29%). The development of the LIGO NCal tested during O3 was put on hold for O4.

Overall, the O4 NCal is a reliable system that is continuously operated. Its systematic uncertainty has been reduced by an order of magnitude compared to the O3 prototype. Improvements were made in every aspect of the system, and further enhancements are already being discussed for O5. Ongoing studies focus on reducing uncertainties such as parasitic couplings with the mirror, NCal positioning, and rotor geometry accuracy. As the sensitivity of detectors increases and next-generation ground-based detectors emerge, such as Einstein Telescope (ET) or Cosmic Explorer (CE), their calibration will become even more challenging, requiring a calibration precision below 0.1% in amplitude.

Appendices

Appendix A

Implementation of the rotor geometric parameters in FROMAGE

The measurements made on the rotors can be implemented in FROMAGE [35] using a configuration file loading the different parameters of the mirror and the rotor to compute the signal. The documentation of FROMAGE provides the information required to build the configuration files and compute the strain signal.

A.1 Nominal rotor model

The following lines show an example of a simple configuration file for a O4 rotor using nominal drawing values. In this instance, the mirror's definition segment corresponds to a cylindrical geometry of the mirror's parameters along with the ears and anchors situated on the mirror's side. The blue part is the rotor geometrical definition based on the nominal O4 rotor values. The values in this part can be adapted to the averaged value of a rotor simple model (see fig. 4.3). In this case, the rotor is placed at a distance $d = 1.7$ m, an angle to the beam axis $\phi = 34.7°$ and twisted by $\psi = 12°$.

```
### MIRROR DEFINITION
GRID_SIZE 12 30 8
CYLINDER 2202. 0 0.175 0.2 360 0 0 0

# Defining the flats on the edge of the mirror
CUT_CYL 2202. 0.175 0.2 0.05 0 0
CUT_CYL 2202. 0.175 0.2 0.05 0 180

# Defining the ears and anchors of the mirror
CUBOID 2202. 0.090 0.010 0.015  0     0.1782 -0.0125
CUBOID 2202. 0.090 0.010 0.015  0    -0.1782 -0.0125
CUBOID 2202. 0.039 0.008 0.008 -0.02 -0.1772 -0.024
CUBOID 2202. 0.039 0.008 0.008 -0.02  0.1772 -0.024
CUBOID 2202. 0.039 0.008 0.008  0.02 -0.1772 -0.024
CUBOID 2202. 0.039 0.008 0.008  0.02  0.1772 -0.024

### ROTOR DEFINITION
ROTOR_CYLINDRICAL 1.7 34.7 0 0 12

GRID_SIZE 8 65 40

# Left sector
```

```
CYLINDER 2808.1 0.029 0.04 0.0984 90 0 0 0
CYLINDER 2808.1 0.04 0.104 0.1044 90 0 0 0

# Right sector
CYLINDER 2808.1 0.029 0.04 0.0984 90 0 0 180
CYLINDER 2808.1 0.04 0.104 0.1044 90 0 0 180

### GENERAL PARAMETERS

# Number of steps used for the rotation
STEP 22.5 16

# Length of the interferometer arm
ARM_LENGTH 3000

# Number N up to which the Nf Fourier coefficient is computed
SIGNAL 2
```

A.2 Advanced rotor model

The advanced rotor model uses the same configuration file as the nominal model except for the blue part which is shown here. In this model, the rotor is divided in many sub-sectors, the grid is also adjusted to keep a similar total number of elements for the signal computation. The counterweights on both sides of the rotor are also modeled. For instance, the following part of the configuration file is used to simulate the geometry of the PVC rotor R4-14 (corresponding to fig. 4.6b). In this case, the rotor is placed at a distance $d = 1.7$ m, an angle to the beam axis $\phi = 34.7°$ and twisted by $\psi = 12°$.

```
### ROTOR DEFINITION
ROTOR_CYLINDRICAL 1.7 34.7 0 0 12

### COUNTERWEIGHT AXLE
GRID_SIZE 4 17 10
CYLINDER 1442.3 0.010 0.040 0.003 360 0 0.05077012356 0

### COUNTERWEIGHT MOTOR
GRID_SIZE 4 17 10
CYLINDER 1442.3 0.02175 0.040 0.003 360 0 -0.05077012356 0

### L sector
## Inner part
GRID_SIZE 8 17 10

OUTER_FILLET 1442.2 0.029 0.098519 0 0.01 -11.2522 146.2434
CYLINDER 1442.2 0.029 0.04 0.098519 22.5044 0 0 146.2434
CYLINDER 1442.2 0.029 0.04 0.098520 22.5044 0 0 168.7478
CYLINDER 1442.2 0.029 0.04 0.098521 22.5044 0 0 191.2522
CYLINDER 1442.2 0.029 0.04 0.098523 22.5044 0 0 213.7566
OUTER_FILLET 1442.2 0.029 0.098523 0 0.01 11.2522 213.7566

## Middle part
CYLINDER 1442.2 0.04 0.056 0.104451 22.5044 0 0 146.2434
CYLINDER 1442.2 0.04 0.056 0.104452 22.5044 0 0 168.7478
CYLINDER 1442.2 0.04 0.056 0.104455 22.5044 0 0 191.2522
```

```
CYLINDER 1442.2 0.04 0.056 0.104457 22.5044 0 0 213.7566

CYLINDER 1442.2 0.056 0.072 0.104446 22.5044 0 0 146.2434
CYLINDER 1442.2 0.056 0.072 0.104446 22.5044 0 0 168.7478
CYLINDER 1442.2 0.056 0.072 0.104448 22.5044 0 0 191.2522
CYLINDER 1442.2 0.056 0.072 0.104451 22.5044 0 0 213.7566

CYLINDER 1442.2 0.072 0.088 0.104437 22.5044 0 0 146.2434
CYLINDER 1442.2 0.072 0.088 0.104439 22.5044 0 0 168.7478
CYLINDER 1442.2 0.072 0.088 0.104441 22.5044 0 0 191.2522
CYLINDER 1442.2 0.072 0.088 0.104443 22.5044 0 0 213.7566

## Outer part
GRID_SIZE 2 13 10

CYLINDER 1442.2 0.088 0.104041 0.026107876574 18.0024 0 0.039161814861 143.9952
CYLINDER 1442.2 0.088 0.104046 0.026107876574 18.0031 0 0.013053938287 143.9937
CYLINDER 1442.2 0.088 0.104048 0.026107876574 18.0039 0 -0.013053938287 143.9923
CYLINDER 1442.2 0.088 0.104049 0.026107876574 18.0046 0 -0.039161814861 143.9908

CYLINDER 1442.2 0.088 0.104044 0.026107626568 18.0024 0 0.039161439852 161.9976
CYLINDER 1442.2 0.088 0.104044 0.026107626568 18.0031 0 0.013053813284 161.9969
CYLINDER 1442.2 0.088 0.104048 0.026107626568 18.0039 0 -0.013053813284 161.9961
CYLINDER 1442.2 0.088 0.104049 0.026107626568 18.0046 0 -0.039161439852 161.9954

CYLINDER 1442.2 0.088 0.104045 0.026107876574 18.0024 0 0.039161814861 180.0000
CYLINDER 1442.2 0.088 0.104045 0.026107876574 18.0031 0 0.013053938287 180.0000
CYLINDER 1442.2 0.088 0.104048 0.026107876574 18.0039 0 -0.013053938287 180.0000
CYLINDER 1442.2 0.088 0.104049 0.026107876574 18.0046 0 -0.039161814861 180.0000

CYLINDER 1442.2 0.088 0.104045 0.026109126604 18.0024 0 0.039163689906 198.0024
CYLINDER 1442.2 0.088 0.104045 0.026109126604 18.0031 0 0.013054563302 198.0031
CYLINDER 1442.2 0.088 0.104049 0.026109126604 18.0039 0 -0.013054563302 198.0039
CYLINDER 1442.2 0.088 0.104049 0.026109126604 18.0046 0 -0.039163689906 198.0046

CYLINDER 1442.2 0.088 0.104048 0.0261096338281865 18.0024 0 0.0391644507422798 216.0048
CYLINDER 1442.2 0.088 0.104047 0.0261096338281865 18.0031 0 0.0130548169140933 216.0063
CYLINDER 1442.2 0.088 0.104051 0.0261096338281865 18.0039 0 -0.0130548169140933 216.0077
CYLINDER 1442.2 0.088 0.104050 0.0261096338281865 18.0046 0 -0.0391644507422798 216.0092

### R sector
## Inner part
GRID_SIZE 8 17 10

OUTER_FILLET 1442.2 0.029 0.098529 0 0.01 11.2515 33.7541
CYLINDER 1442.2 0.029 0.04 0.098529 22.5029 0 0 33.7541
CYLINDER 1442.2 0.029 0.04 0.098529 22.5029 0 0 11.2512
CYLINDER 1442.2 0.029 0.04 0.098533 22.5029 0 0 348.7482
CYLINDER 1442.2 0.029 0.04 0.098540 22.5029 0 0 326.2453
OUTER_FILLET 1442.2 0.029 0.098540 0 0.01 -11.2515 326.2453

## Middle part
CYLINDER 1442.2 0.04 0.056 0.104461 22.5029 0 0 33.7541
CYLINDER 1442.2 0.04 0.056 0.104465 22.5029 0 0 11.2512
CYLINDER 1442.2 0.04 0.056 0.104467 22.5029 0 0 348.7482
CYLINDER 1442.2 0.04 0.056 0.104468 22.5029 0 0 326.2453
```

```
CYLINDER 1442.2 0.056 0.072 0.104450 22.5029 0 0 33.7541
CYLINDER 1442.2 0.056 0.072 0.104458 22.5029 0 0 11.2512
CYLINDER 1442.2 0.056 0.072 0.104462 22.5029 0 0 348.7482
CYLINDER 1442.2 0.056 0.072 0.104463 22.5029 0 0 326.2453

CYLINDER 1442.2 0.072 0.088 0.104445 22.5029 0 0 33.7541
CYLINDER 1442.2 0.072 0.088 0.104454 22.5029 0 0 11.2512
CYLINDER 1442.2 0.072 0.088 0.104459 22.5029 0 0 348.7482
CYLINDER 1442.2 0.072 0.088 0.104458 22.5029 0 0 326.2453

## Outer part
GRID_SIZE 2 13 10

CYLINDER 1442.2 0.088 0.104066 0.02610896505 18.0024 0 0.039163447575 36.0039
CYLINDER 1442.2 0.088 0.104067 0.02610896505 18.0031 0 0.013054482525 36.0042
CYLINDER 1442.2 0.088 0.104072 0.02610896505 18.0039 0 -0.013054482525 36.0045
CYLINDER 1442.2 0.088 0.104075 0.02610896505 18.0046 0 -0.039163447575 36.0048

CYLINDER 1442.2 0.088 0.104067 0.026110715232 18.0024 0 0.039166072848 18.0018
CYLINDER 1442.2 0.088 0.104068 0.026110715232 18.0031 0 0.013055357616 18.0020
CYLINDER 1442.2 0.088 0.104074 0.026110715232 18.0039 0 -0.013055357616 18.0021
CYLINDER 1442.2 0.088 0.104078 0.026110715232 18.0046 0 -0.039166072848 18.0022

CYLINDER 1442.2 0.088 0.104067 0.02611271544 18.0024 0 0.03916907316 359.9997
CYLINDER 1442.2 0.088 0.104069 0.02611271544 18.0031 0 0.01305635772 359.9997
CYLINDER 1442.2 0.088 0.104076 0.02611271544 18.0039 0 -0.01305635772 359.9997
CYLINDER 1442.2 0.088 0.104079 0.02611271544 18.0046 0 -0.03916907316 359.9997

CYLINDER 1442.2 0.088 0.104065 0.026113215492 18.0024 0 0.039169823238 341.9976
CYLINDER 1442.2 0.088 0.104068 0.026113215492 18.0031 0 0.013056607746 341.9974
CYLINDER 1442.2 0.088 0.104074 0.026113215492 18.0039 0 -0.013056607746 341.9973
CYLINDER 1442.2 0.088 0.104078 0.026113215492 18.0046 0 -0.039169823238 341.9971

CYLINDER 1442.2 0.088 0.104063 0.026109715128 18.0024 0 0.039164572692 323.9955
CYLINDER 1442.2 0.088 0.104066 0.026109715128 18.0031 0 0.013054857564 323.9952
CYLINDER 1442.2 0.088 0.104073 0.026109715128 18.0039 0 -0.013054857564 323.9949
CYLINDER 1442.2 0.088 0.104076 0.026109715128 18.0046 0 -0.039164572692 323.9946
```

Appendix B

Drawing an ellipse from a covariance matrix

The representation of a 2x2 covariance matrix as an ellipse is a useful way to visualize the correlations between the parameters of a minimization problem. The ellipse is characterized by parametric equations and formulas for radii and rotation, which are derived from the covariance matrix. We will consider the following 2x2 covariance matrix :

$$\begin{bmatrix} a & b \\ b & c \end{bmatrix}$$

The ellipse equation is:

$$ax^2 + 2bxy + cy^2 = 1$$

B.1 Radii and rotation

The parameters defining the radii and rotation of the ellipse are shown in fig. B.1. The parameter β is the angle in radians from positive x-axis to the ellipse's major axis r_1 in the counterclockwise direction. The parameter r_2 is the radius of the minor axis.

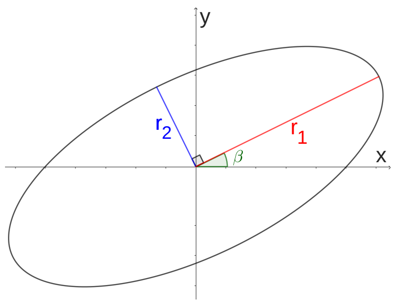

FIGURE B.1: Drawing of an ellipse.

$$r_1^2 = \frac{a+c}{2} + \sqrt{\left(\frac{a-c}{2}\right)^2 + b^2}$$

$$r_2^2 = \frac{a+c}{2} - \sqrt{\left(\frac{a-c}{2}\right)^2 + b^2}$$

$$\beta = \arctan\left(\frac{r_1^2 - a}{b}\right)$$

B.2 Parametric equation

The following describes the parametric equation to draw an ellipse as seen in fig. B.2.

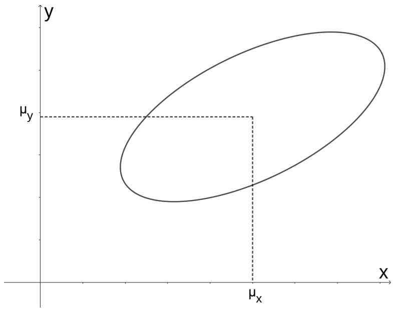

FIGURE B.2: Drawing of an ellipse with μ_x and μ_y offsets.

$$
\begin{aligned}
x(t) &= r_1 \cos(\beta)\cos(t) - r_2 \sin(\beta)\sin(t) + \mu_x \\
y(t) &= r_1 \sin(\beta)\cos(t) + r_2 \cos(\beta)\sin(t) + \mu_y \\
&\quad t \in \{0, 2\pi\}
\end{aligned}
$$

Bibliography

1. Einstein, A. Die Grundlage der allgemeinen Relativitätstheorie. *Annalen der Physik* **354,** 769–822 (Jan. 1916).
2. Le Tiec, A. & Novak, J. in *An Overview of Gravitational Waves: Theory, Sources and Detection* (eds Auger, G. & Plagnol, E.) 1–41 (2017). arXiv: `1607.04202 [gr-qc]`.
3. Abbott, R. *et al.* Search for Gravitational-wave Transients Associated with Magnetar Bursts in Advanced LIGO and Advanced Virgo Data from the Third Observing Run. *The Astrophysical Journal* **966,** 137 (Apr. 2024).
4. Abbott, R. *et al.* GWTC-3: Compact Binary Coalescences Observed by LIGO and Virgo during the Second Part of the Third Observing Run. *Phys. Rev. X* **13,** 041039. `https://link.aps.org/doi/10.1103/PhysRevX.13.041039` (4 2023).
5. Abbott, B. P. *et al.* Observation of Gravitational Waves from a Binary Black Hole Merger. *Phys. Rev. Lett.* **116,** 061102. `https://link.aps.org/doi/10.1103/PhysRevLett.116.061102` (6 2016).
6. Abbott, B. P. *et al.* GW170817: Observation of Gravitational Waves from a Binary Neutron Star Inspiral. *Phys. Rev. Lett.* **119,** 161101. `https://link.aps.org/doi/10.1103/PhysRevLett.119.161101` (16 2017).
7. Abbott, B. P. *et al.* First narrow-band search for continuous gravitational waves from known pulsars in advanced detector data. *Phys. Rev. D* **96,** 122006. `https://link.aps.org/doi/10.1103/PhysRevD.96.122006` (12 2017).
8. Abbott, B. P. *et al.* GW150914: Implications for the Stochastic Gravitational-Wave Background from Binary Black Holes. *Phys. Rev. Lett.* **116,** 131102. `https://link.aps.org/doi/10.1103/PhysRevLett.116.131102` (13 2016).
9. N V, K. & Ohme, F. Testing General Relativity with Gravitational Waves: An Overview. *Universe* **7,** 497 (Dec. 2021).
10. Abbott, B. P. *et al.* Gravitational Waves and Gamma-Rays from a Binary Neutron Star Merger: GW170817 and GRB 170817A. *The Astrophysical Journal Letters* **848,** L13. `https://dx.doi.org/10.3847/2041-8213/aa920c` (2017).
11. Vartanyan, D., Burrows, A., Wang, T., Coleman, M. & White, C. Gravitational-wave signature of core-collapse supernovae. *Physical Review D* **107** (May 2023).
12. Vivanco, F. *et al.* Measuring the neutron star equation of state with gravitational waves: The first forty binary neutron star merger observations. *Physical Review D* **100** (Nov. 2019).
13. Riess, A., Casertano, S., Yuan, W., Macri, L. & Scolnic, D. Large Magellanic Cloud Cepheid Standards Provide a 1Foundation for the Determination of the Hubble Constant and Stronger Evidence for Physics beyond ΛCDM. *The Astrophysical Journal* **876,** 85 (May 2019).
14. Aghanim, N. *et al.* Planck 2018 results: VI. Cosmological parameters. *Astronomy and Astrophysics* **641** (Sept. 2020).

15. Abbott, B. *et al.* A gravitational-wave standard siren measurement of the Hubble constant. *Nature* **551** (Nov. 2017).
16. Abbott, B. *et al.* A Gravitational-wave Measurement of the Hubble Constant Following the Second Observing Run of Advanced LIGO and Virgo. *The Astrophysical Journal* **909,** 218 (Mar. 2021).
17. The Virgo Collaboration. *Advanced Virgo Plus Phase I - Design Report* `https://tds.virgo-gw.eu/ql/?c=14430`. VIR-0596A-19. 2019.
18. Accadia, t. *et al.* Virgo calibration and reconstruction of the gravitationnal wave strain during VSR1. *Journal of Physics: Conference Series* **228,** 012015 (July 2010).
19. Accadia, T *et al.* Calibration and sensitivity of the Virgo detector during its second science run. *Classical and Quantum Gravity* **28,** 025005. `https://dx.doi.org/10.1088/0264-9381/28/2/025005` (2010).
20. Acernese, F *et al.* Calibration of advanced Virgo and reconstruction of the detector strain h(t) during the observing run O3. *Classical and Quantum Gravity* **39,** 045006 (Feb. 2022).
21. Acernese, F *et al.* Calibration of advanced Virgo and reconstruction of the gravitational wave signal h(t) during the observing run O2. *Classical and Quantum Gravity* **35** (Oct. 2018).
22. Lagabbe, P. *Improving the Advanced Virgo+ calibration with the photon calibrator for the O4 run* PhD thesis (Nov. 2023).
23. Sinsky, J. & Weber, J. New Source for Dynamical Gravitational Fields. *Physical Review Letters - PHYS REV LETT* **18,** 795–797 (May 1967).
24. Sinsky, J. Generation and Detection of Dynamic Newtonian Gravitational Fields at 1660 cps. *Physical Review - PHYS REV X* **167,** 1145–1151 (Mar. 1968).
25. Suzuki, T., Tsubono, K., Kuroda, K. & Hirakawa, H. Calibration of Gravitational Radiation Antenna by Dynamic Newton Field. *Japanese Journal of Applied Physics* **20** (July 1981).
26. Ogawa, Y., Tsubono, K. & Hirakawa, H. Experimental test of the law of gravitation. *Physical Review D* **26** (Aug. 1982).
27. Astone, P. *et al.* Long-term operation of the Rome "Explorer" cryogenic gravitational wave detector. *Physical review D: Particles and fields* **47,** 362–375 (Feb. 1993).
28. Astone, P. *et al.* Experimental study of the dynamic Newtonian field with a cryogenic gravitational wave antenna. *European Physical Journal C* **5,** 651–664 (Oct. 1998).
29. The Virgo Collaboration. *VIRGO final conceptual design Part I-II* (1992).
30. Inoue, Y. *et al.* Improving the absolute accuracy of the gravitational wave detectors by combining the photon pressure and gravity field calibrators. *Phys. Rev. D* **98,** 022005. `https://link.aps.org/doi/10.1103/PhysRevD.98.022005` (2 2018).
31. Estevez, D. *et al.* First tests of a Newtonian calibrator on an interferometric gravitational wave detector. *Classical and Quantum Gravity* **35,** 235009. `https://dx.doi.org/10.1088/1361-6382/aae95f` (2018).
32. Estevez, D., Mours, B. & Pradier, T. Newtonian calibrator tests during the Virgo O3 data taking. *Classical and Quantum Gravity* **38,** 075012. `https://dx.doi.org/10.1088/1361-6382/abe2da` (2021).

33. Ross, M. *et al.* Initial results from the LIGO Newtonian calibrator. *Physical Review D* **104** (Oct. 2021).
34. Estevez, D. *Virgo O3 NCal update and FROMAGE* `https://tds.virgo-gw.eu/ql/?c=15890`. VIR-0765A-20. 2020.
35. Estevez, D., Mours, B. & Pradier, T. *Numerical simulations for Virgo O3 NCal using FROMAGE* `https://tds.virgo-gw.eu/ql/?c=15884`. VIR-0759B-20. 2020.
36. Estevez, D., Mours, B. & Pradier, T. *Virgo NCal update; March LVK meeting* `https://tds.virgo-gw.eu/ql/?c=16517`. VIR-0269A-21. 2021.
37. Aimard, B., Lieunard, B. & Mours, B. *NCal-200 safety study* `https://tds.virgo-gw.eu/ql/?c=13160`. VIR-0270A-18. 2018.
38. Dangelser, E. *et al. Characteristics of the rotor R4-01 for the O4 NCal system* `https://tds.virgo-gw.eu/ql/?c=18237`. VIR-0591C-22. 2022.
39. Aubin, F., Dangelser, E., Mours, B., Syx, A. & Van Hove, P. *Characteristics of the rotor R4-10 for the O4 NCal system* `https://tds.virgo-gw.eu/ql/?c=20263`. VIR-0203A-24. 2024.
40. Ross, M. P. *et al.* Pseudoplane-wave gravitational calibrator for gravitational wave observatories. *Phys. Rev. D* **107,** 062003. `https://link.aps.org/doi/10.1103/PhysRevD.107.062003` (6 2023).
41. Dangelser, E. *et al. Design and installation of the NCal reference plates for O4* `https://tds.virgo-gw.eu/ql/?c=17372`. VIR-1123A-21. 2021.
42. Estevez, D., Mathieu, C. & Mours, B. *NCal position sensors characterization* `https://tds.virgo-gw.eu/ql/?c=16801`. VIR-0553A-21. 2021.
43. Aubin, F. *et al. Density of the PVC used for the O4 NCal rotors* `https://tds.virgo-gw.eu/ql/?c=20253`. VIR-0193A-24. 2024.
44. Aubin, F. *et al. The Virgo Newtonian calibration system for the O4 observing run* 2024. eprint: `arXiv:2406.10028`.
45. *CODATA Value: Newtonian constant of gravitation — physics.nist.gov* `https://physics.nist.gov/cgi-bin/cuu/Value?bg`. [Accessed 12-06-2024].
46. Paoli, A., Marsella, M., Nardinocchi, C., Vittuari, L. & Zanutta, A. *Geodetic Reference Frame for the Virgo Interferometer* in *14th International Workshop on Accelerator Alignment* (2016).
47. Aubin, F., Dangelser, E., Mours, B., Syx, A. & Van Hove, P. *Distance between NCals on the North to South axis for O4* `https://tds.virgo-gw.eu/ql/?c=20088`. VIR-0029A-24. 2024.
48. Dangelser, E. *et al. Position of the NCals relative to the reference plates for O4* `https://tds.virgo-gw.eu/ql/?c=18655`. VIR-1009C-22. 2022.
49. Aubin, F. *et al. Calibration and reconstruction update (talk at the Virgo week)* `https://tds.virgo-gw.eu/ql/?c=20582`. VIR-0522A-24. 2024.
50. Betzwieser, J. *et al. Calibrating the global network of gravitational wave observatories via laser power calibration at NIST and PTB* LIGO DCC P2300412 `https://dcc.ligo.org/LIGO-P2300412` (to be published in Metrologia). 2024.

Université de Strasbourg

Antoine SYX

ECOLE DOCTORALE pcp

Calibration of the Virgo gravitational waves detector using a Newtonian Calibrator for the observing run O4

Résumé

Depuis la première détection d'ondes gravitationnelles en 2015, la collaboration LIGO-Virgo-KAGRA a vu son taux de détection d'événement augmenter au fur et à mesure des périodes d'observation. Avec leurs améliorations successives, l'étalonnage précis de ces détecteurs est essentiel.

Jusqu'à la fin de la période d'observation O3, Virgo utilisait le *Calibrateur* à Photons (PCal). Pour O4, un nouveau système, le *Calibrateur* Newtonien (NCal) a été développé. Il génère un champ gravitationnel variable à l'aide de masses en rotation. Cette thèse présente le développement et les résultats du NCal. Mes travaux, commencés en 2021, ont porté sur la métrologie, l'installation, la mise en service des NCals et la réduction des incertitudes du système.

Au début de O4b, l'incertitude d'étalonnage du NCal a été estimée à 0.12%, bien plus précise que celle du PCal de Virgo (0.56%) et le PCal de LIGO (0.29%), faisant du NCal la nouvelle référence absolue pour Virgo.

Mots clés : *ondes gravitationnelles, interféromètre, étalonnage, Virgo, calibrateur Newtonien*

Abstract

Since the first detection of gravitational waves in 2015, the LIGO-Virgo-KAGRA collaboration has seen an increasing detection rate with each observation period. With their successive improvements, increasingly precise calibration of these detectors is necessary.

Until the end of the O3 observation period, Virgo used the Photon Calibrator (PCal). For O4, a new system, the Newtonian Calibrator (NCal), was developed. It generates a variable gravitational field using rotating masses. This thesis presents the development and results of the NCal. My work, which began in 2021, focused on metrology, installation, commissioning of the NCals, and reducing system uncertainties.

At the start of O4b, the NCal's calibration uncertainty was estimated at 0.12%, much more precise than that of Virgo's PCal (0.56%) and LIGO's PCal (0.29%), making the NCal the new absolute reference for Virgo.

Keywords : *gravitational waves, interferometer, calibration, Virgo, Newtonian calibrator*